DOCTOR OF PHILOSOPHY

Recent irreversible retreat phase of Pine Island Glacier

Reed, Brad

Award date:
2023

Awarding institution:
Bangor University

Recent irreversible retreat phase of Pine Island Glacier

Bradley C. Reed

PRIFYSGOL
BANGOR
UNIVERSITY

A thesis presented for the degree of
Doctor of Philosophy

School of Ocean Sciences
Bangor University
Wales, UK
2023

Declaration

I hereby declare that this thesis is the results of my own investigations, except where otherwise stated. All other sources are acknowledged by bibliographic references. This work has not previously been accepted in substance for any degree and is not being concurrently submitted in candidature for any degree unless, as agreed by the University, for approved dual awards.

Acknowledgments

Firstly, a big thank you must go to my main supervisors Professor Mattias Green and Professor Hilmar Gudmundsson for their guidance and patience throughout my PhD research. I am sure they thought that I would never finish! I would also like to express my gratitude to my supervisory committee, Dr Peter Robins and Dr Martin Austin for their advice and interest over the past four years.

Thank you to the Envision Doctoral Training Partnership and the Natural Environment Research Council whose funding and support made this work possible. I would like to thank the organising committee and instructors of the Karthaus summer school on Ice Sheets and Glaciers in the Climate System for an inspiring introduction to glaciology and the cryosphere. A special thanks must go to Supercomputing Wales, including lead engineer Ade Fewings and research software engineer Aaron Owen for their invaluable technical support.

And finally, a huge thank you must go to my friends and family. In particular, my parents, Cheryl and Mike, and my sister Nikki, thank you for your support and patience as always. I look forward to being able to see you all more often and spending some quality time with you after the PhD. Lastly, thank you to Nia, for looking after me during this write up period, and throughout the rest of the PhD. I hope I can pay you back as you finish yours.

Abstract

Pine Island Glacier (PIG) is one of the fastest flowing outlets in the Antarctic Ice Sheet. In recent decades the glacier has undergone substantial changes including speed up, thinning and grounding-line retreat. Between the 1970s and early 1990s, despite comprising just 1.5 % of the overall area, PIG contributed almost 13 % of the total mass loss, adding 0.34 mm to global mean sea level rise. Situated in the Amundsen Sea Embayment in West Antarctica, it has long been considered that PIG is close to an unstable state owing to its underlying bed profile. This has prompted fears about its future and the fate of the wider region. Historic records show the glacier underwent a period of mass loss and retreat after a 1940s climate anomaly, causing PIG to unground from a long term position on a subglacial ridge. The initial cause of retreat and the ongoing transition until the 1990s remains poorly understood. The aim of this thesis is to gain a better understanding of the transient evolution of PIG after it retreated from the ridge 80 years ago, and determine whether it was subjected to an instability mechanism.

In the first research chapter, an ice flow model is used to investigate how the behaviour of an idealized buttressed ice sheet is affected by changes in external forcing. It is found that ocean induced sub shelf melting leads to thinning and retreat of the ice sheet from a stable position on a retrograde slope. The choice of basal friction within the model impacts the rate of mass loss, with the commonly used Weertman law causing the least retreat. Further experiments show that the ice sheet undergoes a hysteresis in response to changes in ice softness. In the second research chapter, ice flow modelling results show that a sustained increase in basal melting beneath PIG ice shelf leads to a loss of buttressing, which is sufficient to cause a retreat from the subglacial ridge to an upstream ice plain. The formation of glacial features prior to and after the retreat, together with the evolution of mass loss are all in agreement with observations. A stability analysis indicates that an unstable region is present upstream of the ridge suggesting PIG crossed a tipping point in its retreat by the early 1970s. In the third research chapter, further modelling of PIG shows that a short period of increased basal melt is sufficient to cause irreversible retreat from the ridge to the next bed high point; a much greater decrease in forcing, compared to the initial perturbation, is needed to stop and reverse the retreat. Once there is sufficient melting upstream of the ridge, after a connection is established between the inner and outer cavities, only extreme cold conditions, or near-zero melt, can stop the retreat to the next bed high point.

The results in this thesis suggest that PIG could have experienced an unstable response to a warm anomaly in the 1940s. Periods of cool ocean conditions were unable to affect the retreat until it stabilized at an ice plain in the 1990s. We provide new insight into

how future glaciers in the Amundsen Sea may respond to more prevalent warm conditions that have been predicted for the region.

Contents

List of Figures

List of Tables

Chapter 1

Introduction

1.1 Research context

The Antarctic Ice Sheet (AIS, Fig. 1.1) holds the largest reservoir of freshwater on Earth, with the capacity to raise global sea levels by 58 m, if it was to completely melt (Morlighem et al., 2020). Between 1992 and 2017 the ice sheet lost $2,720 \pm 1,390$ Gt of mass, contributing 7.6 ± 3.9 mm to global mean sea-level rise, and the rate of mass loss has increased since 2012 (Shepherd et al., 2018). Over the next century, AIS is likely to continue losing mass in response to rising anthropogenic emissions (DeConto and Pollard, 2016; DeConto et al., 2021; Fox-Kemper et al., 2021). However, the nature of this response is highly uncertain due to poorly understood ice sheet instability processes (Bulthuis et al., 2019; Robel et al., 2019).

Most of the current mass loss in Antarctica is occurring on the West Antarctic Ice Sheet (Shepherd et al., 2018), particularly in the Amundsen Sea Embayment (ASE; see Sect. 2.1) (Rignot et al., 2019), where glaciers have undergone substantial acceleration (Mouginot et al., 2014) and retreat (Rignot et al., 2014) in recent decades. Much of the ice here is grounded on bedrock below sea level (Morlighem et al., 2020) and it flows toward the coastline where it forms floating ice shelves (Fig. 1.2). These ice shelves are vulnerable to ocean-induced melting from below, which is believed to be the primary cause of mass loss in this region (Paolo et al., 2015; Pritchard et al., 2012). Although a change in the mass of an ice shelf does not directly contribute to sea level rise, the shelves can restrict the flow of upstream grounded ice, and therefore a change in their geometry affects their buttressing ability. Hence, ocean-induced thinning of these shelves, particular in confined regions, can lead to the accelerated ice flow and increased mass loss (Gudmundsson et al., 2019).

Pine Island Glacier (PIG) is one of the largest and fastest flowing ASE glaciers (Rignot et al., 2011). Between 1979 and 2017 it contributed more to global sea level rise than any

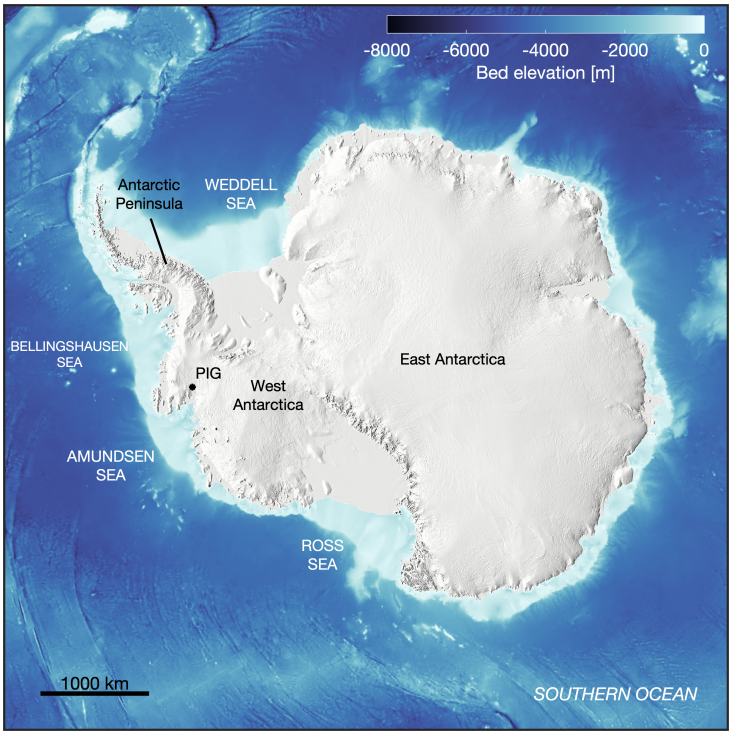

Fig. 1.1: Antarctic Ice Sheet. The bed elevation is shown on the seaward side of the ice shelves. The approximate location of Pine Island Glacier (PIG) is also shown.

other Antarctic outlet (Rignot et al., 2019). The glacier has recently undergone episodes of rapid thinning and retreat (Konrad et al., 2017; Park et al., 2013), and evidence from sub-ice shelf sediment cores suggest that it has been out of balance since the 1940s (Smith et al., 2017). Beneath the ice shelf is a bedrock ridge (Jenkins et al., 2010), which prior to the 1940s, had been its long term grounding position (Smith et al., 2017). However, following a notable climate anomaly in West Antarctica (Schneider and Steig, 2008), possibly caused by the strong 1939–42 El Niño event, the ice shelf started to retreat from the ridge and an ocean cavity developed upstream (Smith et al., 2017). In the subsequent years, despite cooler ocean conditions (Dutrieux et al., 2014), the glacier has failed to recover its original position on the ridge.

Beneath PIG, from the landward side of the ridge to the present day grounding line position, there are several sections of retrograde bed (sloping upwards in the direction of ice flow) that lie below sea level (Morlighem et al., 2020). Ice sheets in equilibrium grounded on this type of bed are vulnerable to the marine ice sheet instability (MISI), where a perturbation in grounding line position could cause an unstable response and runaway retreat (Schoof, 2007a; Weertman, 1974). It has long been considered that the West Antarctic Ice Sheet is vulnerable to destabilization and collapse, whether it is caused by an instability mechanism, anthropogenic causes or a combination of both

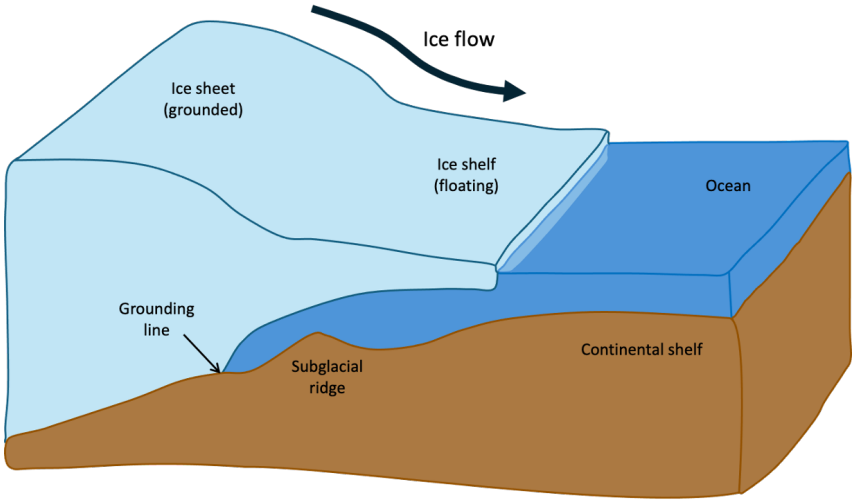

Fig. 1.2: A schematic of an ice shelf showing key terminology that is used throughout this thesis.

(Mercer, 1978; Thomas and Bentley, 1978). However, the presence of ice shelf buttressing can be sufficient to permit stable equilibrium and stabilize an ice sheet on retrograde beds (Gudmundsson et al., 2012).

Without direct observations of MISI occurring, ice sheet models have been relied on to predict when this instability mechanism will occur, especially in the presence of ice shelf buttressing. Studies have suggested that MISI may already be underway for the biggest ASE glaciers and could be responsible for their current and future mass loss (Favier et al., 2014; Joughin et al., 2014; Rignot et al., 2014). Furthermore, an idealized version of PIG has been shown to undergo an irreversible retreat from a topographic high when forced with changing ocean conditions (Rydt and Gudmundsson, 2016).

It is possible that PIG was initially forced off its subglacial ridge in the 1940s due to a change in climate or ocean forcing, and its ongoing retreat until the 1990s may have been an unstable response due to its underlying bed topography. There is observational evidence which suggests a rapid retreat occurred from the ridge, but it is yet to be determined whether this was due to MISI. Knowledge of whether MISI has occurred in the recent history of one of Antarctica's biggest glaciers, especially in the presence of ice shelf buttressing, would help to improve the understanding of the AIS future evolution, which is the largest uncertainty in sea level rise projections (Fox-Kemper et al., 2021).

1.2 Aims and objectives

The overall aim of this thesis is to gain a better understanding of the transient evolution of PIG after it retreated from the subglacial ridge 80 years ago. To achieve this, I will combine ice sheet modelling with historical observations to answer the following questions: (1) How are buttressed ice sheets affected by a change in external forcing? (2) Could a change in ocean forcing have been responsible for the retreat of PIG from a subglacial ridge? (3) After PIG retreats from the ridge, why does it not recover in the following years? (4) What is the impact of different ocean forcing when PIG is grounded on the ridge?

To answer these questions, a series of time dependent modelling experiments will be carried out using the two-dimensional ice flow model Úa. The first set of model simulations will be using an idealized representation of PIG to assess the impact of basal melting and changes in other model parameters on the ice shelf buttressing capabilities. The next set of experiments will investigate the stability regime of PIG as it retreats from the subglacial ridge. This will determine the long term equilibrium positions that PIG would move to under prolonged forcing. The final experiments will study the impact of shorter, more realistic timescales of forcing on the retreat of PIG.

1.3 Thesis structure

This section outlines the thesis structure and describes each chapter in detail. Firstly, there is an introduction and background to the research, this is followed by the methods that are common throughout. Then, three research chapters are presented, followed by a summary of the main conclusions.

Chapter 2 gives the relevant scientific background for this thesis and highlights the knowledge gaps that will be addressed here. Firstly, there is an overview of AIS to establish the wider importance of this research. This includes information about its current mass balance and recent changes, with a particular focus on the geographic area that has contributed the most to sea level rise in recent decades. There is a description of the ocean conditions, which is important for this particular region of Antarctica, and how this is driving mass loss for PIG. This is followed by an introduction to MISI and the capabilities of ice sheet models.

Chapter 3 introduces the ice flow model Úa that will be used in this research. It will outline and derive the governing ice flow equations and the modelling methods that are used in all of the experiments in this thesis.

Chapter 4 presents the first set of time-dependent modelling experiments, which ex-

plore the impact of changing forcing on an idealized representation of PIG. This chapter will primarily follow the methodology of two recent ice sheet model intercomparison projects.

Chapter 5 will show a stability analysis of the recent history of PIG. It will use a depth dependent melt rate parameterization, which represents local ocean conditions, to investigate how increased melt beneath PIG impacts its position on the subglacial ridge. Individual model simulations with different basal melt are run until a steady state is reached to establish whether the glacier experiences threshold behaviour. This will provide insight into why PIG has not recovered its position on the ridge after it started to retreat in the 1940s.

Chapter 6 gives the final set of time-dependent ice sheet modelling experiments, which explore the transient reversibility of PIG when forced with different basal melting. The depth dependent melt rate is used on decadal timescales to show the impact on retreat under more realistic conditions.

Chapter 7 summarises the key findings from the research presented in this thesis and discusses the limitations and potential directions for future work.

1.4 Submitted manuscripts

The research presented in **Chapter 5** is being revised for Nature Climate Change with the following details:

> Reed, B., Green, J. A. M., Jenkins, A., and Gudmundsson, G. H. (2023), Recent irreversible retreat phase of Pine Island Glacier

The research presented in **Chapter 6** is to be submitted to The Cryosphere with the following details:

> Reed, B., Green, J. A. M., Jenkins, A., and Gudmundsson, G. H. (2023), Melt sensitivity of irreversible retreat of Pine Island Glacier

The following manuscript is published in the Journal of Geophysical Research: Oceans, but is not included in this thesis:

> Anselin, J., Reed, B., Jenkins, A., and Green, J. A. M. (2023), Ice Shelf Basal Melt Sensitivity to Tide-Induced Mixing Based on the Theory of Subglacial Plumes

Chapter 2

Scientific background

This chapter gives the scientific background that is relevant for this thesis and outlines the work that has been built on in the subsequent research chapters. Firstly, an overview is given of the whole Antarctic Ice Sheet (AIS), with its current status and recent changes. Then, a more in-depth look is given to its western region, with a particular focus on ocean conditions and the fast flowing Pine Island Glacier (PIG). Following this, the marine ice sheet instability is explained and why this ice dynamic feedback mechanism is important for the future of the ice sheet. A brief section is then given on the capabilities of ice sheet modelling and how they help us understand ice processes and responses to changing forcing. At the end of the chapter is a summary of the knowledge gaps regarding the recent history of PIG and where they are addressed in this thesis.

2.1 Antarctic Ice Sheet

The AIS is the largest mass of ice on the planet, and holds enough water to raise global sea levels by 58 m, if it was to completely melt (Morlighem et al., 2020). Although the AIS may sometimes be referred to as one body of ice, it is generally thought of as comprising three distinct ice sheets (Fig. 2.1a), each with their own characteristics and behaviour: the East Antarctic Ice Sheet (EAIS), the Antarctic Peninsula (AP), and the West Antarctic Ice Sheet (WAIS).

The EAIS is the largest of the three ice sheets, containing over 22 million km^3 of ice and the potential to raise global sea level by 52 m (Morlighem et al., 2020). However, this ice sheet is considered to be the most stable due to its cold and dry atmospheric conditions and being mostly grounded on bedrock above sea level (Fig. 2.1b). In the interior of EAIS there are vast regions of thick, slow moving ice which creep towards the coastline via ice deformation. At the outer margins of the ice sheet, fast-flowing ice streams are formed, which generally slide over the bed along deep bedrock channels. These ice streams flow

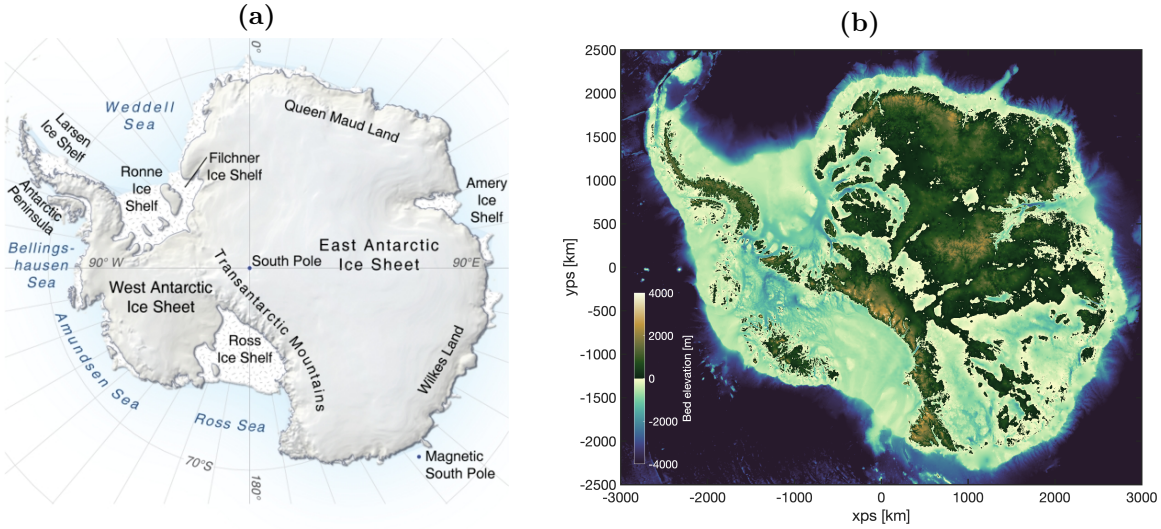

Fig. 2.1: (**a**) Antarctic Ice Sheet is comprised of the three separate ice sheets: East Antarctic Ice Sheet, Antarctic Peninsula, and the West Antarctic Ice Sheet. Image from: Hugo Ahlenius, UNEP/GRID-Arendal, https://www.grida.no/resources/5231. (**b**) Antarctic bed elevation using the Bedmachine dataset (Morlighem et al., 2020).

towards the ocean where they eventually thin and form floating ice shelves as the ice loses contact with the bedrock beneath. This point of transition between grounded and floating ice is known as the grounding line. The ice streams and ice shelves around the EAIS are generally slower and smaller than their western counterparts (Rignot et al., 2011).

The AP is the smallest of the three ice sheets, with 131,000 km^3 of ice or a 0.27 m sea-level equivalent, SLE (Morlighem et al., 2020). However, this region experiences the warmest atmospheric temperatures on the continent, which has led to considerable ice shelf changes in recent decades, including thinning and collapse (Shepherd et al., 2003). Ice in this region is fed from the interior mountain range via a number of smaller ice streams. At the coastline, on one side of the peninsula, they form one of the largest ice shelves around Antarctica, the Larsen C ice shelf, which is fringed by the cold waters of the Weddell Sea. On the other side of the peninsula, ice flows into the much warmer waters of the Bellingshausen Sea.

The WAIS is also much smaller than the EAIS and holds just 13 % of the total ice volume (3.4 million km^3, 5.3 m SLE) (Morlighem et al., 2020). It is mostly grounded on bedrock below sea level which generally slopes downward towards the interior (Fig. 2.1b) and is thus termed a "marine ice sheet". This bed configuration makes the WAIS vulnerable to ice dynamic instabilities, as will be discussed in Sect. 2.3. The ice sheet is separated from the EAIS by the Transantarctic Mountains, and has several large, fast moving ice streams that flow into the Filchner-Ronne and Ross ice shelves, in the cold

Weddell and Ross seas respectively. Along the coastline between these two large bodies of floating ice are several ice streams that feed into smaller ice shelves in the warm waters of the Amundsen and Bellingshausen Seas. The focus of this thesis will be on the WAIS, and in particular, Pine Island Glacier, which flows into the Amundsen Sea.

2.1.1 Mass balance

To make accurate predictions about the future state of AIS we need to know its current condition and past changes. The mass balance of an ice sheet informs us of whether it is gaining or losing mass overall, and can help us gauge the "health" of the ice sheet. The mass balance is largely determined by the difference between the accumulation of mass, via snowfall across the upper surface, and the loss of ice through discharge at its coastal margins. Several studies have attempted to estimate the mass balance by using one of three main methods (Hanna et al., 2020): mass budget or component method (Rignot et al., 2019), satellite altimetry (McMillan et al., 2014), and gravitational measurements (Schrama et al., 2014). Shepherd et al. (2018) used a combination of 24 independently derived estimates of mass balance, which used these different methods, to derive a mean estimate and uncertainty range. In agreement with earlier work, they conclude that the AIS continues to lose mass, with $2,720 \pm 1,390$ Gt of ice lost between 1992 and 2017 (Fig. 2.2), which equates to 7.6±3.9 mm SLE; the average annual rate was 109±56 Gt yr^{-1}. Within these 25 years, there was an increase in the rate of mass loss, from 49 ± 67 Gt yr^{-1} between 1992–1997, to 219 ± 43 Gt yr^{-1} in 2012–2017.

Many studies show that the mass loss is not spatially uniform (Gardner et al., 2018; Shepherd et al., 2018), and others also highlight the short-term temporal variability (Rignot et al., 2019). Despite the EAIS containing 90 % of the total ice volume, the mean estimate shows it being close to balance (Fig. 2.2). However, this region has the largest uncertainty of mass loss (Shepherd et al., 2018), and is therefore sometimes shown as losing mass (Rignot et al., 2019). There is a small contribution to the mass loss from the AP, where the break up of ice shelves has caused an increase in the rate of mass loss from 7 ± 13 Gt yr^{-1} to 33 ± 16 Gt yr^{-1} between the first five and last five years of the Shepherd et al. (2018) study. By far, the largest contribution to mass loss comes from the WAIS, where the rate has increased from 53 ± 29 Gt yr^{-1} in 1992–1997, to 159 ± 26 Gt yr^{-1} in 2012–2017 (Shepherd et al., 2018). Other studies that calculate surface elevation changes and coastal thinning rates also show that the WAIS, and in particular the Amundsen Sea Embayment (ASE), has been the main contributor to mass loss in recent decades (Fig. 2.3).

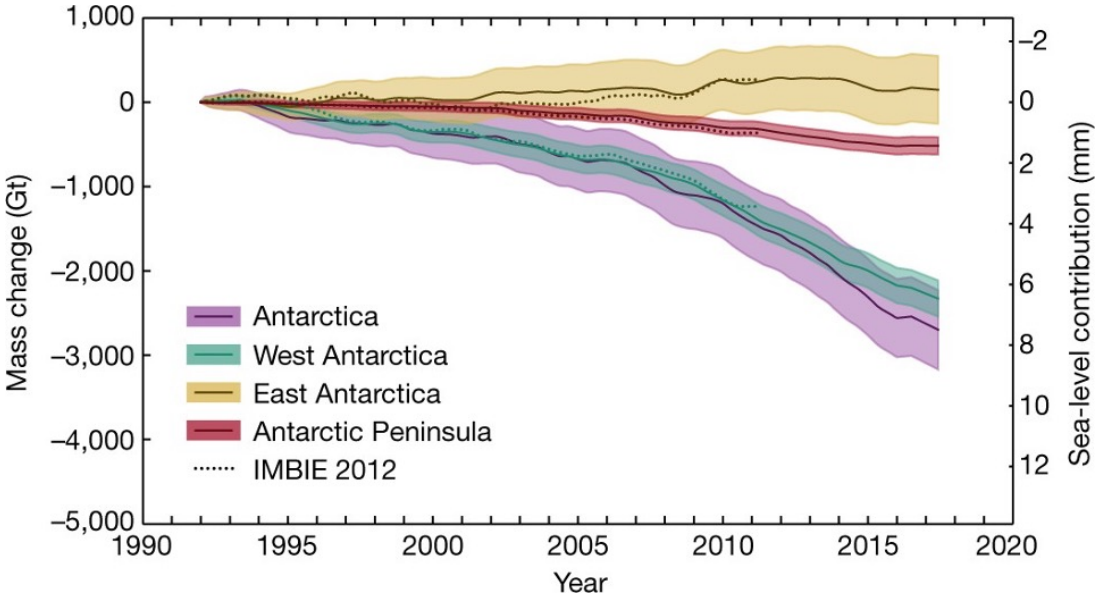

Fig. 2.2: The cumulative change in Antarctic Ice Sheet mass (solid lines) for each ice sheet. The shaded region shows the uncertainty of the cumulative change. Dashed lines show the results from an earlier study. Figure is from Shepherd et al. (2018).

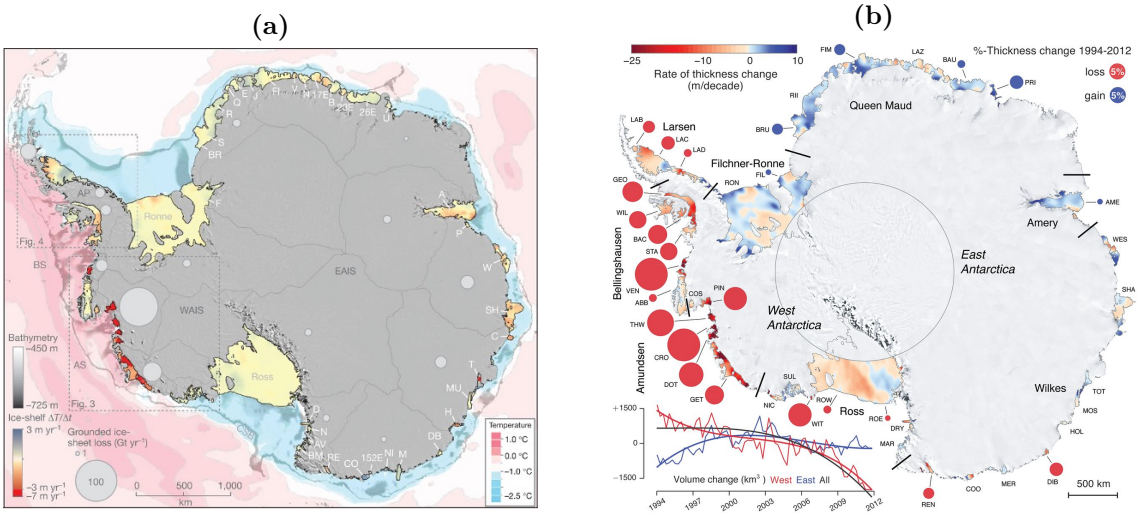

Fig. 2.3: (**a**) Ice shelf thickness change rate for 2003–2008. The average ocean bottom temperatures are shown on the seaward side of the ice shelves, overlaid on the coastal bathymetry. Figure is from Pritchard et al. (2012). More details are available in the original paper figure. (**b**) Rate of ice shelf thickness change and percentage of thickness lost for 1994–2012. Figure is from Paolo et al. (2015).

2.2 Amundsen Sea Embayment

As shown in the previous section, most of the mass loss across Antarctica comes from the WAIS (Rignot et al., 2019; Shepherd et al., 2018), and this has been attributed to the high rates of thinning (Paolo et al., 2015; Pritchard et al., 2012) and acceleration (Mouginot et al., 2014) of the glaciers flowing into the Amundsen Sea (Fig. 2.4). Here, glaciers have undergone a rapid increase in ice discharge (Mouginot et al., 2014) and inland thinning (Konrad et al., 2017; Shepherd et al., 2001; Wingham et al., 2009) in recent decades, which has led to a widespread retreat of grounding lines across the major ASE glaciers (Rignot et al., 2014). These glaciers are also susceptible to the marine ice sheet instability (MISI) (Sect. 2.3), where a small perturbation in grounding line position could lead to irreversible retreat across their deep retrograde sloping beds (Schoof, 2007a; Weertman, 1974). Some observational and modelling studies suggest this could already be underway for the large glaciers of Pine Island and Thwaites (Favier et al., 2014; Joughin et al., 2014; Rignot et al., 2014).

It is now widely accepted that the imbalance of ASE glaciers is due to incursions of warm Circumpolar Deep Water (CDW) onto the continental shelf and beneath the floating ice shelves. This has led to enhanced basal melting and increased ice shelf thinning (Jacobs and Hellmer, 1996; Jacobs et al., 2011; Paolo et al., 2015; Pritchard et al., 2012; Shepherd et al., 2004). The weakening of confined ice shelves, through basal melt or calving, reduces the buttressing of upstream ice, which can lead to a speed-up of ice flow, grounding line retreat and mass loss (Dupont and Alley, 2005; Fürst et al., 2016; Goldberg et al., 2009; Gudmundsson, 2013; Gudmundsson et al., 2019). The future state and stability of ASE glaciers will likely depend on their exposure to warm ocean waters.

The flow of CDW onto the continental shelf is affected by the strength of westerly winds at the shelf break (Steig et al., 2012; Thoma et al., 2008), leading to ocean conditions that can vary on a range of timescales, from seasonal to interannual to decadal (Dutrieux et al., 2014; Jenkins et al., 2016; Kimura et al., 2017). Changes in CDW volume and heat content on the shelf influence the rate of basal melting (Dutrieux et al., 2014; Jacobs et al., 2013) and this could explain the intermittent nature of mass loss observed since the 1970s (Mouginot et al., 2014). The variability of ocean conditions, and subsequent mass loss, has been linked to tropical (Paolo et al., 2018; Steig et al., 2012), local (Thoma et al., 2008; Webber et al., 2017), and anthropogenic (Holland et al., 2019) forcing.

In the rest of this ASE section is a more in depth review of the recent glaciological changes, including glacier acceleration, thinning and retreat, and the intermittent mass loss over the observational period. This is followed by a description of the ocean conditions in the Amundsen Sea and how these affect ice shelf basal melting, with detail about the

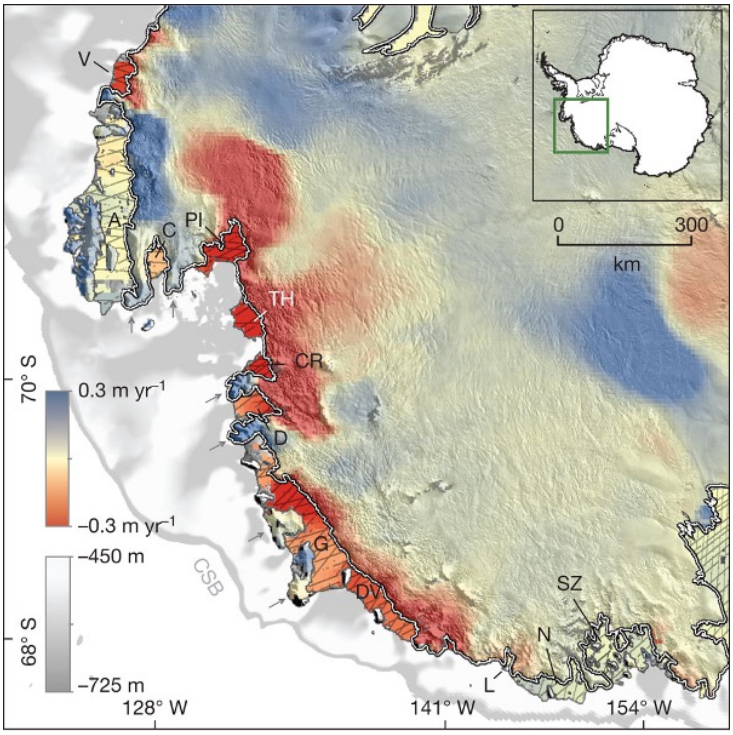

Fig. 2.4: Ice shelf elevation change rate for the ice shelves and grounded ice in the ASE for 2003-2008. The large glaciers of Pine Island and Thwaites are labelled PI and TH respectively. Figure is from Pritchard et al. (2012).

temporal variability and link to Pacific drivers. Lastly, a review is given of PIG with a historical perspective of its ocean conditions and glaciological changes.

2.2.1 Glaciological changes

Glacier acceleration

Several studies (Konrad et al., 2017; Mouginot et al., 2014; Rignot et al., 2014) have shown that in the last few decades, there have been substantial and widespread changes occurring in the ASE. Early observations of PIG and Thwaites Glacier velocities showed an acceleration of both glaciers in the 1990s (Joughin et al., 2003; Rignot et al., 2002). These results were later extended by Mouginot et al. (2014) using a combination of data from Landsat imagery in 1973 to radar observations in 2013. They showed that floating and grounded ice for all of the major ASE glaciers had accelerated in those four decades, albeit at different rates, with speedup being detected up to 150 km inland (Fig. 2.5).

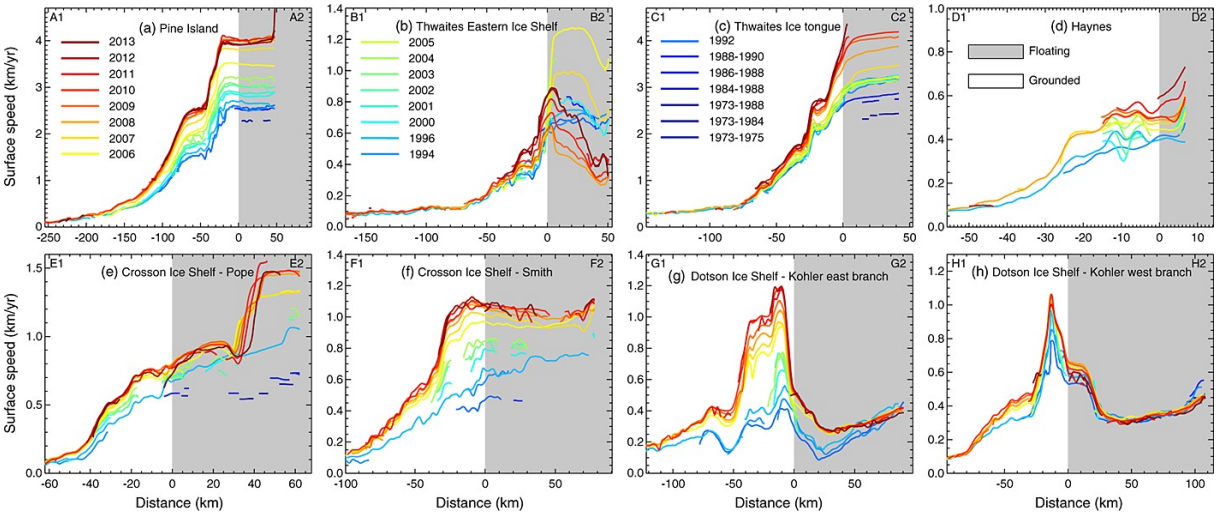

Fig. 2.5: Flow line ice speed for ASE glaciers and ice shelves between 1973 and 2013. Figure is from Mouginot et al. (2014).

Thinning of grounded ice

The increased flow speed observed across the glaciers has led to a dynamical imbalance in the sector and subsequent thinning of grounded ice (Flament and Rémy, 2012; Sutterley et al., 2014). It was estimated that between 1992 and 1996, PIG was thinning upstream of the grounding line by 2.1 m yr^{-1}, and then in 1992–2000 by 1.9 m yr^{-1} (Rignot, 2002). Neighbouring glaciers were also thinning but at varying rates, with Thwaites and Smith thinning by 0.55 m yr^{-1} and 3.21 m yr^{-1}, respectively (Shepherd et al., 2002). Thinning of ASE glaciers was also propagating inland, where it was detected 150 km upstream from the grounding line.

Thinning of floating ice

There has also been a change in the thickness of floating ice shelves in the ASE in recent decades. Pritchard et al. (2012) used satellite laser altimetry data across the whole of the AIS and found rapid thinning occurring along the Amundsen Sea coastline in 2003–2008, of up to 6.8 m yr^{-1} (Fig. 2.3a). By ruling out firn compaction and changes in surface mass balance or ice influx, they concluded that this thinning was due to increased basal melting beneath the ice shelves. They found that all cases of ocean-driven ice shelf thinning corresponded with dynamical thinning and acceleration of grounded ice. Another pan-Antarctic study by Paolo et al. (2015) showed that mass loss of ASE ice shelves was accelerating in the period of 1994–2012 and was experiencing the highest rates of thinning compared to the rest of AIS (Fig. 2.3b).

Glacier retreat

The acceleration and thinning of grounded ice has led to widespread retreat across ASE glaciers (Konrad et al., 2018; Rignot et al., 2014). The earliest estimates of retreat were made by Rignot (1998) who found that the hinge line of PIG was retreating at 1.2 km yr^{-1} between 1992 and 1996. This was similar to the 1.5 km yr^{-1} rate of retreat that Park et al. (2013) calculated along the center line of PIG between 1992 and 2011, where the glacier had retreated by as much as 28 km. This agreed with a later study by Rignot et al. (2014) who document a 31 km PIG grounding line retreat in the same time period. They also highlighted a substantial retreat of 35 km of Smith/Kohler glaciers further along the coast, a 14 km retreat of the fast flowing part of Thwaites Glacier, and 10 km retreat of Haynes Glacier. More recent observations of these glaciers show continued retreat since 2011, with the fastest rate of 11.7 km yr^{-1} in 2017 when Pope Glacier retreated 3.5 km in three and a half months. There has also been fast rates of retreat for Smith West with 2 km yr^{-1} and Kohler at 1.3 km yr^{-1} (Milillo et al., 2022).

Intermittent mass loss

Although there have been widespread changes across ASE glaciers, the pattern has been spatially and temporally variable. Konrad et al. (2017) show that thinning of grounded ice across the sector was initiated during different periods between 1992–2015 and the thinning propagated inland at different rates. Furthermore, grounding line retreat has been episodic in nature (Rignot et al., 2014), with some glaciers experiencing temporary advances and others undergoing rapid retreat (Milillo et al., 2022; Scheuchl et al., 2016). In the study by Mouginot et al. (2014), they use a number of flux gates to show that between 1973 and 2013, although the average ice flux increased almost monotonically across all ASE glaciers, there are some temporary periods of stabilization between acceleration phases (Fig. 2.6). The near-synchronous changes in ice mass across the sector suggests there is a forcing link between the glaciers, with the ocean being the main contender.

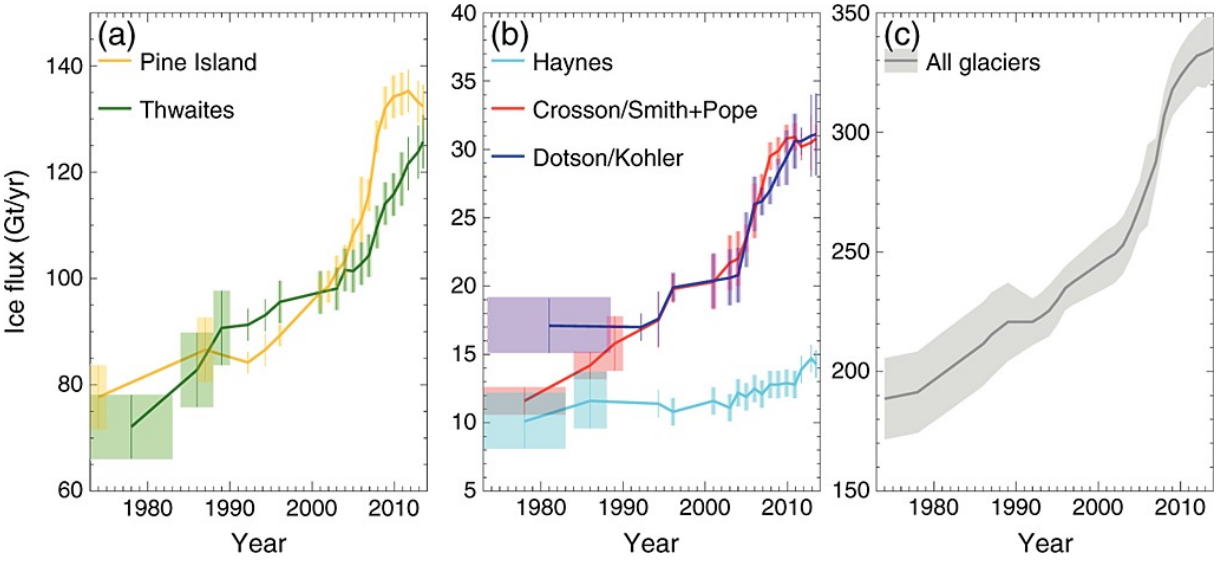

Fig. 2.6: Average ice discharge at the grounding line for the major ASE glaciers between 1973 and 2013. Figure is from Mouginot et al. (2014).

2.2.2 Ocean conditions

The previous sections highlighted the important role that ocean conditions play in the mass balance of the AIS. Most of the mass loss from the AIS occurs through ice discharge along the coastline, where iceberg calving and basal melting each account for roughly half of the overall ice loss (Depoorter et al., 2013; Rignot et al., 2013). However, this ratio varies spatially around Antarctica, which is mainly due to the adjacent ocean conditions and available water masses.

Flowing clockwise around Antarctica is the wind-driven Antarctic Circumpolar Current (ACC), which is a vast ocean current that connects the Southern Ocean with the other three major ocean basins (Indian, Pacific and Atlantic). The core of the ACC consists of CDW, which is the warmest water mass in the Southern Ocean, with a temperature that is typically 3 °C warmer than the in situ freezing point (Jacobs and Hellmer, 1996). Around much of the continent, CDW is found close to the shelf break and in some regions it can flow onto the shelf via a number of different mechanisms, including wind forcing, Ekman dynamics and topographically controlled flows (Thomas and Bentley, 1978; Wåhlin et al., 2013; Walker et al., 2013). In the ASE, deep glacial troughs facilitate the transport of CDW from the break to the deep grounding lines beneath ice shelves (Wåhlin et al., 2010; Walker et al., 2007). However, depending on local meteorological conditions, and the thickness of the overlying layer of cold and fresh surface waters, CDW may be restricted from accessing the ice shelf cavities.

Ice shelf water masses

Basal melting beneath Antarctic ice shelves can generally be characterised by three different modes (Fig. 2.7), or similarly, three distinct water masses (Jacobs et al., 1992; Jenkins et al., 2016).

Mode 1 melting occurs when dense, cold and saline Shelf Water (SW), produced during sea ice formation, flows into the cavity beneath the ice shelf. The temperature of this water is close to the surface freezing point (−1.9 °C) and can melt ice at the deep grounding lines, where higher pressures decrease the melting point. This process of melting is sometimes referred to as thermohaline convection. This water mass can also be divided into Low Salinity Shelf Water (LSSW) and High Salinity Shelf Water (HSSW) as shown in Fig. 2.8.

In mode 2 melting, relatively warm CDW (1 °C), occupying intermediate offshore depths, intrudes into the ice shelf cavity and can cause rapid melting at the deep grounding lines. CDW might mix with other cold water masses when flowing from the ACC to the shelf which leads to the formation of modified CDW (MCDW, Fig. 2.8). The presence of CDW flowing along the base of the cavity, and the associated warming, can be referred to as bottom-dominated warming (Naughten et al., 2018).

Mode 3 melting occurs when Antarctic Surface Water (AASW), which has a cold core of Winter Water and is formed from melting sea ice, flows into the ice shelf cavity. During the winter, the AASW has a temperature close to the surface freezing point (−1.9 °C), and acts similar to mode 1 melting, but during the summer its upper layer is warmed from atmospheric interaction and can therefore lead to higher melt rates. This is referred to as surface-dominated warming (Naughten et al., 2018).

Atmospheric forcing

Atmospheric and meteorological conditions over the continental shelf and shelf break can influence the degree of basal melting in ice shelf cavities. In areas of strong sea ice formation, deep convection allows SW to descend to the base of the cavity. If there are sufficiently strong winds then downwelling of AASW creates an Antarctic Slope Front (ASF), which separates the colder on-shelf waters from the warmer off-shelf CDW (Gill, 1973; Jacobs, 1991). The level of sea ice production and the strength and position of the ASF influence the flow of CDW onto the continental shelf (Schmidtko et al., 2014). Therefore, strong wind or buoyancy forcing can depresses the thermocline (Sverdrup, 1954), leading to a smaller volume of CDW flowing onto the continental shelf. This is typical for the cavities beneath the Filchner-Ronne and Ross ice shelves, and therefore these are classed as “cold” cavities.

In the Amundsen and Bellingshausen Seas, weaker buoyancy and wind forcing result

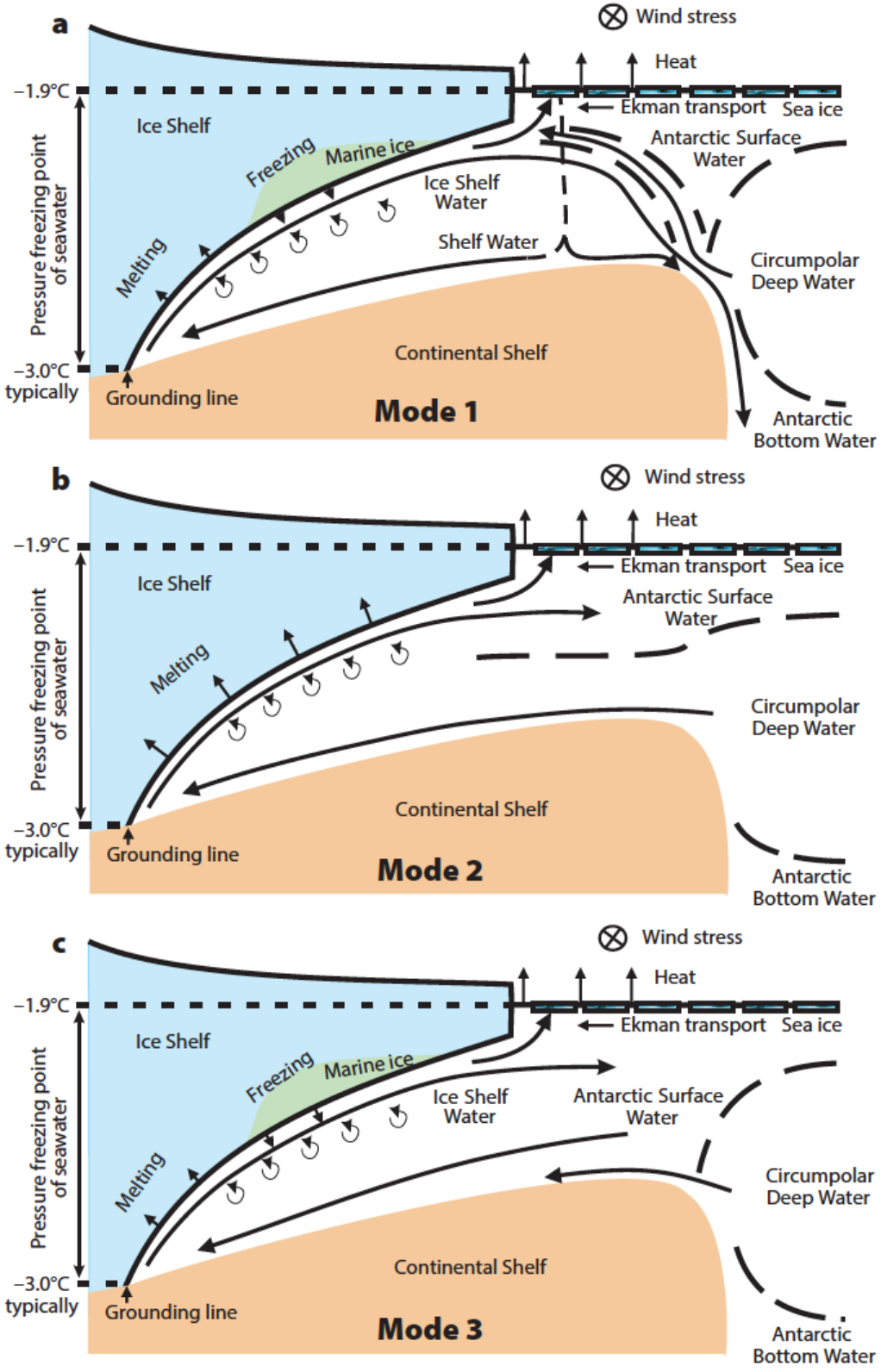

Fig. 2.7: Three modes of ice shelf basal melting for Antarctic ice shelves. Figure is from Jenkins et al. (2016).

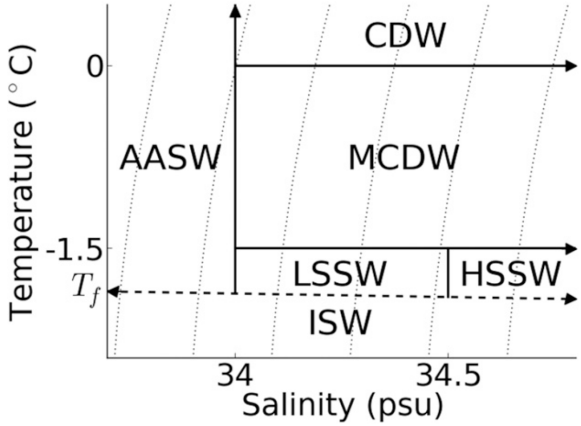

Fig. 2.8: Temperature and salinity of the different water masses found in ice shelf cavities. The dashed line indicates the surface freezing point, T_f, and the dotted curves show potential density contours. AASW=Antarctic Surface Water, CDW=Circumpolar Deep Water, MCDW=Modified Circumpolar Deep Water, LSSW=Low Salinity Shelf Water, HSSW=High Salinity Shelf Water, ISW=Ice Shelf Water. Figure is from Naughten et al. (2018).

in a less distinguishable ASF and a shallower thermocline. This allows warm CDW to flow onto the continental shelf and into the sub-ice shelf cavities via deep troughs (Jacobs et al., 2011; Wåhlin et al., 2010). This leads to much higher melt rates compared to their cold counterparts (Dutrieux et al., 2014; Thoma et al., 2008). These ice shelf cavities are classed as "warm". The location of these cold and warm cavities around Antarctica can be shown by their bottom water temperature in Fig. 2.3a and by their corresponding melt rates in Fig. 2.9.

Basal melting

The cold cavities beneath the large Filchner-Ronne and Ross ice shelves have inflowing waters close to the surface freezing point and experience low average melt rates, between $0.1 - 1.0$ m yr^{-1} (Depoorter et al., 2013). For these ice shelves, over 80 % of their mass loss is instead due to calving. In contrast, water flowing into the warm ice shelf cavities along the Bellingshausen and Amundsen Sea coastline have a temperature above the in situ freezing point, causing average melt rates of 10s of metres per year (Depoorter et al., 2013; Rignot et al., 2013). This leads to two-thirds of the mass loss from these ice shelves being due to basal melting.

In both cold and warm cavities, the basal melting that occurs beneath an ice shelf causes fresh meltwater to be released into the saltier ocean. The meltwater cools and freshens the adjacent waters leading to a buoyant plume of Ice Shelf Water (ISW) that flows up along the base of the ice shelf (Fig. 2.7). This turbulent ISW plume entrains

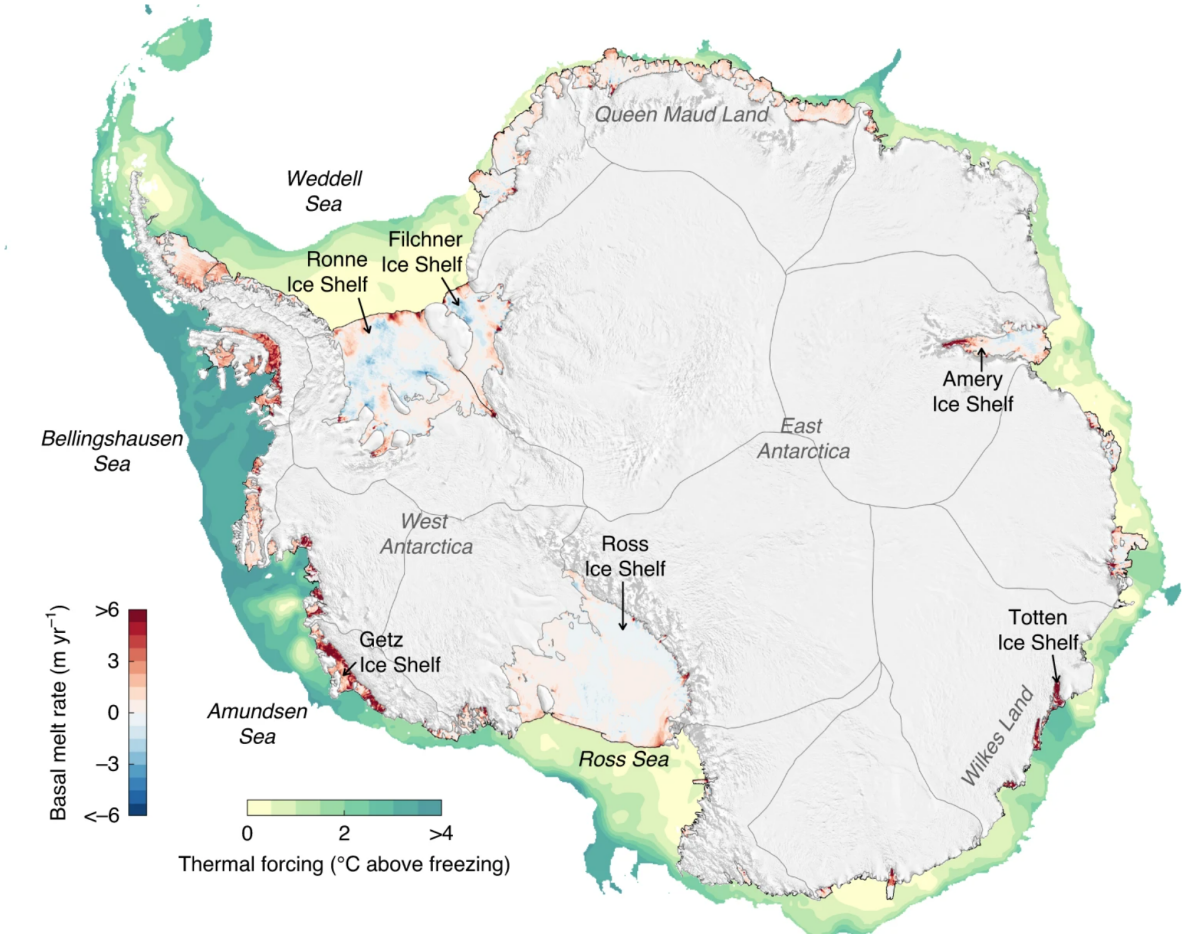

Fig. 2.9: Average basal melt rates of Antarctic ice shelves during 2010–2018. The temperature above the in situ freezing point of seawater is shown for water depths <1,500 m. For water depths less than 200 m, the seafloor thermal forcing is shown, and for water depths >200 m, the maximum thermal forcing between 200 m and 800 m is shown. Figure is from Adusumilli et al. (2020).

ambient cavity waters below and can induce an inflow of warmer ocean water, leading to a sustained or further increase in basal melting. Ice shelf thinning due to basal melting can also cause geometric feedbacks whereby an increased water column thickness alters the circulation of ocean currents and therefore location of warm waters and high melting (Holland et al., 2023).

Ocean tides can also affect the degree of basal melting beneath an ice shelf (Padman et al., 2018). This can happen through two different mechanisms: tidal currents can modify ambient waters in the cavity, which therefore alters the thermohaline properties of water coming into contact with the ice base; tidal currents can also influence the turbulent mixing in the ice-ocean boundary layer. However, the impact of tides on basal melting differs for cold and warm cavities. In cold ice shelf cavities, basal melting is low which causes a weak plume flow which can be dominated by tidal currents. In contrast, for warm cavities, meltwater plumes are stronger and therefore the impact of tidal currents is less.

Oceanic variability

The previous sections show the role that different water masses can play in controlling the amount of basal melting that occurs beneath floating ice shelves. This then impacts the mass balance of glaciers and the fate of upstream grounded ice. In the Amundsen Sea, observations of temperature profiles show a seasonal to decadal variability, where the depth of the thermocline can fluctuate up to 200 m from year to year (Fig. 2.10a). This then drives large changes in basal melt beneath the ASE ice shelves as the amount of heat available for melting varies (Dutrieux et al., 2014; Jenkins et al., 2018). The level of melting is further complicated by the presence of topographic highs, for example, the bedrock ridge beneath Pine Island Glacier, which can act as a barrier against the deepest warm waters (Fig. 2.10b).

Modelling results show that changes in the thermocline depth are impacted by the strength of CDW inflow onto the continental shelf, which is influenced by zonal winds at the shelf edge (Jenkins et al., 2016; Thoma et al., 2008). Cool ocean conditions are caused when strong easterly winds promote polynya growth and downwelling on the shelf, which suppresses the thermocline and the inflow of CDW (Fig. 2.11a). In contrast, warm conditions are caused when there are weaker easterlies and reduced polynya activity, which leads to less downwelling, and a shallower thermocline with enhanced inflow of CDW (Fig. 2.11b).

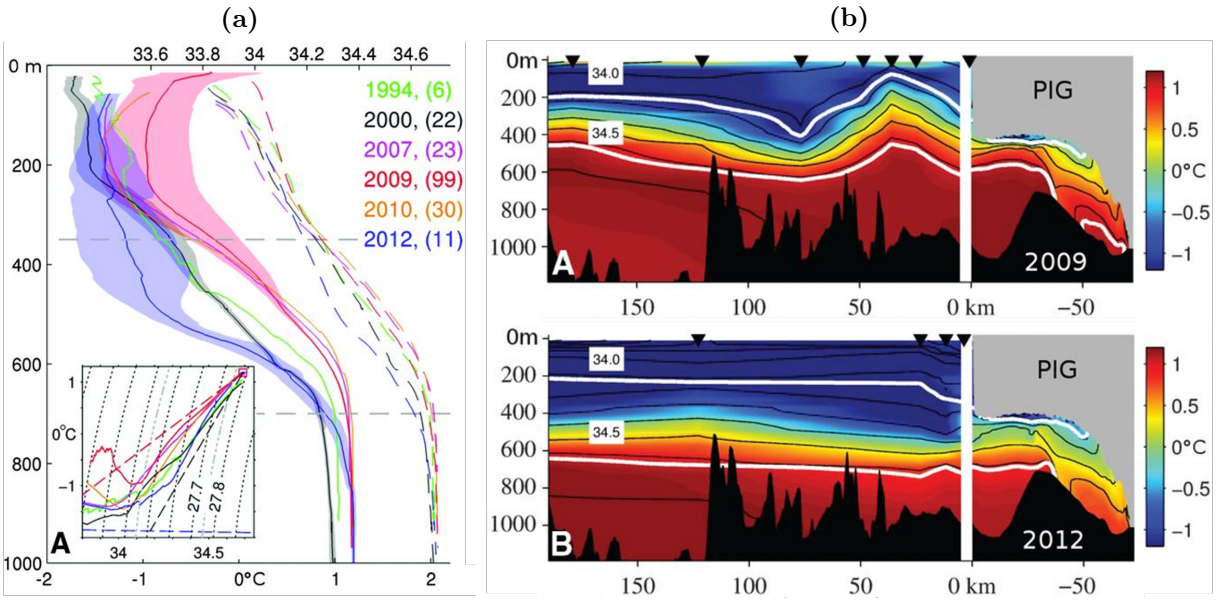

Fig. 2.10: (**a**) Average ocean temperature profiles from Pine Island Bay between 1994 and 2012. Numbers in brackets denote the number of profiles per year. Inset: the same data but in potential temperature-salinity space. Figure is from Dutrieux et al. (2014). (**b**) Vertical section of observed (in front of shelf) and modelled (beneath shelf) temperatures from Pine Island Bay for 2009 (warm year) and 2012 (cold year). Figure is from Dutrieux et al. (2014).

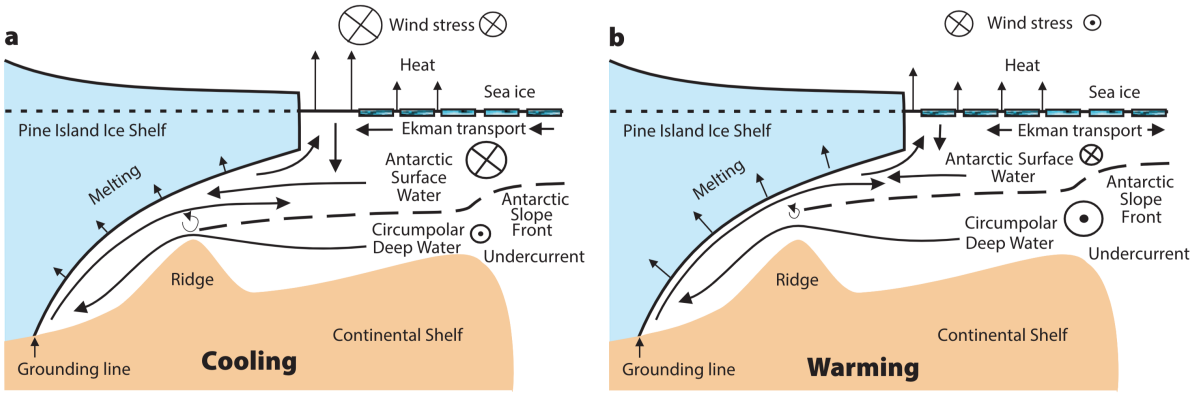

Fig. 2.11: Schematic showing the oceanic and atmospheric processes that lead to (**a**) cooling and (**b**) warming of Amundsen Sea continental shelf near Pine Island Glacier. Figure is from Jenkins et al. (2016).

Tropical Pacific drivers

The strength of easterly winds at the continental shelf break has been linked to variability of sea surface temperatures in the tropics. Modelling results from Steig et al. (2012) suggest that an increase in westerly wind stress near the shelf edge is caused by a change in sea level pressure in the ASE. This pressure anomaly is caused by a Rossby wave response to warming in the central tropical Pacific Ocean (Lachlan-Cope and Connolley, 2006). Hence, strong El Niño/Southern Oscillation (ENSO) events can lead to weakened easterlies, and therefore a shallower thermocline and greater flow of CDW onto the ASE continental shelf. The opposite happens during strong La Niña periods. These easterly winds have been shown to be weakened by anthropogenic forcing throughout the twentieth century, with warm anomalies becoming more prevalent (Holland et al., 2019; Naughten et al., 2022). Future projections show a possible switch to mean westerly winds under a high-emissions scenario (Holland et al., 2019), which suggests further warming in the Amundsen Sea.

A time series of ASE thermocline depth for the past 160 years was estimated by Jenkins et al. (2016) using various observations and indirect proxies. They found a decadal variability in ocean conditions that is in phase with central tropical Pacific sea surface temperature anomalies. A shallow thermocline and high basal melting in the late 2000s followed a warm anomaly between 2005 and 2010, whilst the deepest thermocline and lowest melting on record in 2012 followed a strong La Niña in 2011 (Dutrieux et al., 2014). Jenkins et al. (2018) suggest the retreat of ASE glaciers is driven by these tropically forced decadal changes in ocean conditions (Fig. 2.12). This is explored further for Pine Island Glacier in the next section (Sect. 2.2.3).

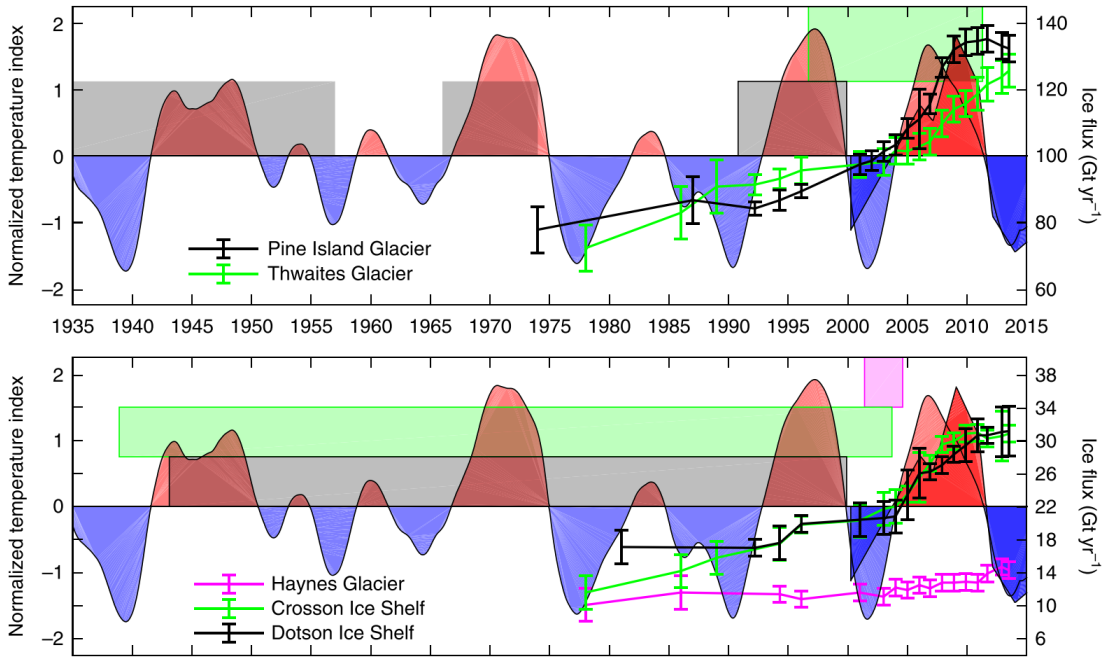

Fig. 2.12: Time series of ocean forcing (left axis) and ASE glacier ice flow (right axis) between 1935 and 2015. Ocean conditions show warm periods (red) and cool conditions (blue) from observations and inferred from central tropical Pacific sea surface temperatures anomalies. Outlined coloured boxes indicate the estimated initiation times of retreat for the most recent phases of grounding line thinning of ASE glaciers. Other grey boxes show the estimated times of initial retreat and final ungrounding of Pine Island Glacier from a subglacial ridge. Figure is from Jenkins et al. (2018).

2.2.3 Pine Island Glacier

Pine Island Glacier (PIG), which is one of the largest and fastest flowing glaciers in ASE, has contributed more to global sea level rise in recent decades than any other Antarctic outlet (Rignot et al., 2019). Together with its neighbour, Thwaites Glacier, they drain a third of the WAIS and have been collectively known as the "weak underbelly" of the ice sheet since the 1980s (Hughes, 1981). The bedrock beneath both glaciers makes them susceptible to MISI (Sect. 2.3), which if initiated, could result in huge mass loss and possibly a collapse of the WAIS via interaction between different basins (Feldmann and Levermann, 2015a; Feldmann and Levermann, 2015b). This collapse would most likely be initiated by ocean forcing, as PIG experiences some of the highest basal melt rates across Antarctica (Rignot et al., 2013). A notable episode of mass loss and period of retreat within the last century has been linked to tropically forced ocean changes (Smith et al., 2017), which has implications for future events as warm anomalies become more prevalent (Holland et al., 2019; Naughten et al., 2022).

Recent changes

As mentioned in Sect. 2.2.1, PIG has undergone substantial changes since at least the start of the satellite observation period in the early 1970s. There are two notable periods of increased ice discharge, in the mid 1990s and mid to late 2000s (Fig. 2.6), which are also indicated by a marked acceleration of grounded and floating ice (Fig. 2.5). The earlier period of acceleration (1994–2001) coincided with the most recent onset of upstream thinning (Konrad et al., 2017). This dynamical imbalance led to a gradual retreat across a localised bed rise (Rignot et al., 2014). During the later, more enhanced period of acceleration (2006–2010), the highest rates of inland thinning were observed for PIG (Konrad et al., 2017) and there was further retreat across an ice plain (Fig. 2.13). The onset of these changes have been linked to tropically forced ocean changes in the Amundsen Sea.

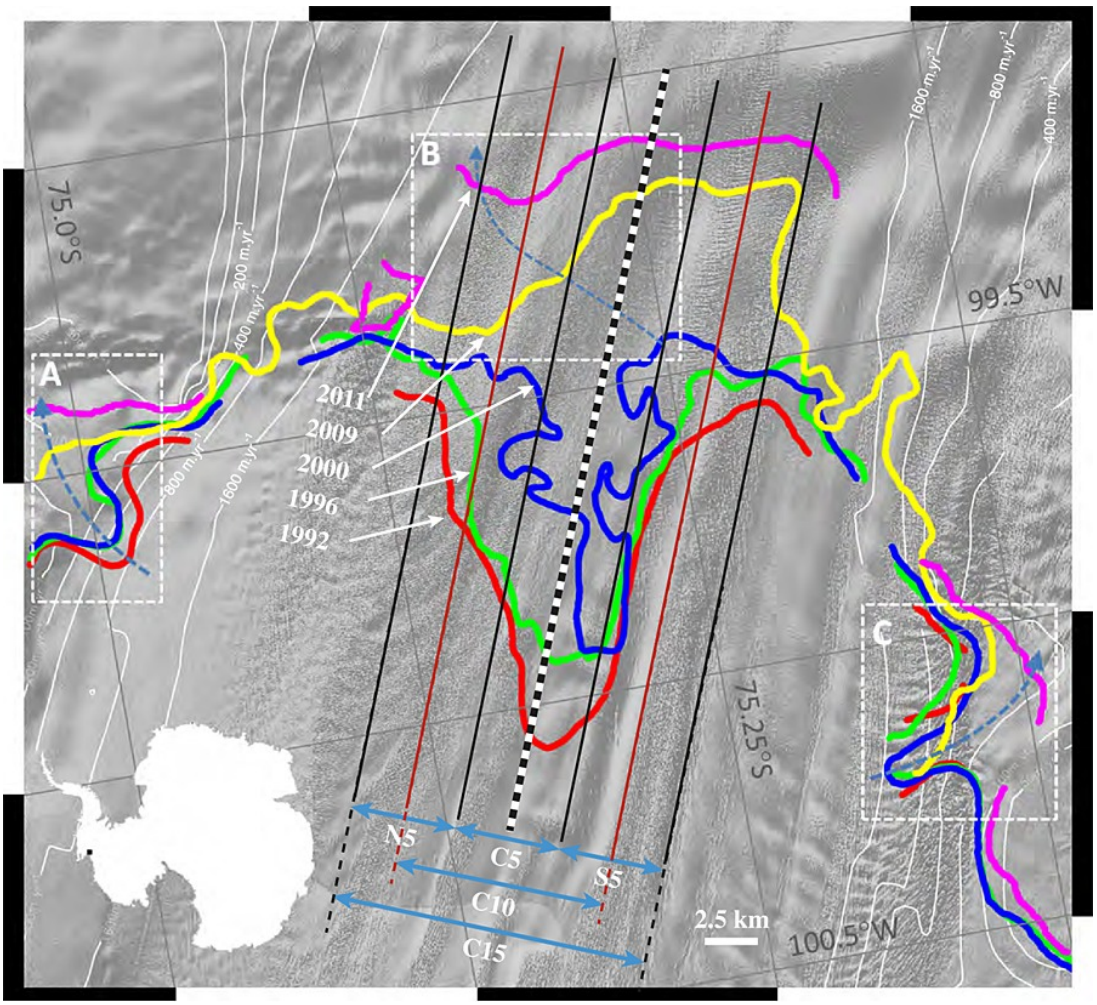

Fig. 2.13: Hinge-line positions of PIG for 1992 (red), 1994 (green), 2000 (blue), 2009 (yellow) and 2011 (magenta). Figure is from Park et al. (2013).

Ocean forcing

The mass loss in the late 2000s happened during a period of warm ocean conditions in the Amundsen Sea, where there was a shallow thermocline and thicker layer of CDW (Fig. 2.10). The shoaled thermocline allowed the warmest waters to access the ice shelf cavity, despite the presence of a subglacial ridge, leading to the highest PIG melt rates on record (Dutrieux et al., 2014). Although there are limited oceanographic observations in the mid 1990s, modelling studies (Naughten et al., 2022; Thoma et al., 2008) and an estimated thermocline depth (Jenkins et al., 2016) suggest there may also have been warm conditions during the earlier acceleration period. This link between ocean forcing and mass changes may also account for the periods of stabilization around 1990 and 2011. Oceanographic observations show a cooling in 2012 following the strong 2011 La Niña (Dutrieux et al., 2014; Jenkins et al., 2016), whilst a deep thermocline and weakened inflow of CDW during the early 1990s (Thoma et al., 2008) would both have reduced the heat available for melting.

Despite the apparent link between ocean forcing and fluctuations in ice discharge, this does not hold all of the time. If there was a decrease in available heat in the early 2000s, as predicted by Jenkins et al. (2016) and Naughten et al. (2022), this did not affect the ongoing mass loss of PIG (Fig. 2.6), as it continued to retreat across the ice plain (Fig. 2.13). It is possible that PIG was undergoing an episode of unstable retreat from a local topographic high, forced by the warm conditions in the mid 1990s, and was unaffected by a decrease in ocean temperature and subsequent drop in basal melting (Rydt and Gudmundsson, 2016).

Historic perturbations

The earliest direct observations of PIG from 1947 indicate that the ice shelf was not that much larger than its present day size, and very similar to the pre-2013 configuration (Arndt et al., 2018; Rignot, 2002). Although the ice front fluctuated in position between 1947 and 2013, the mean ice front remained in a similar location. Sediment cores recovered from a subglacial ridge beneath the present day ice shelf show that prior to the 1940s, the glacier was grounded on the ridge, 40 km downstream of its present-day position (Smith et al., 2017). The sediment cores show two distinct regimes: (1) before 1945, a deposition of coarse-grained sediments close to the grounding line; (2) between 1945 and 1970, deposition of fine-grained sediment far from the grounding line. In the period between 1945 and 1970, an ocean connection was established between the outer main cavity and upstream of the ridge (Fig. 2.14). The ice shelf then completely ungrounded from the ridge between the 1970s and 80s (Jenkins et al., 2010; Smith et al., 2017), with

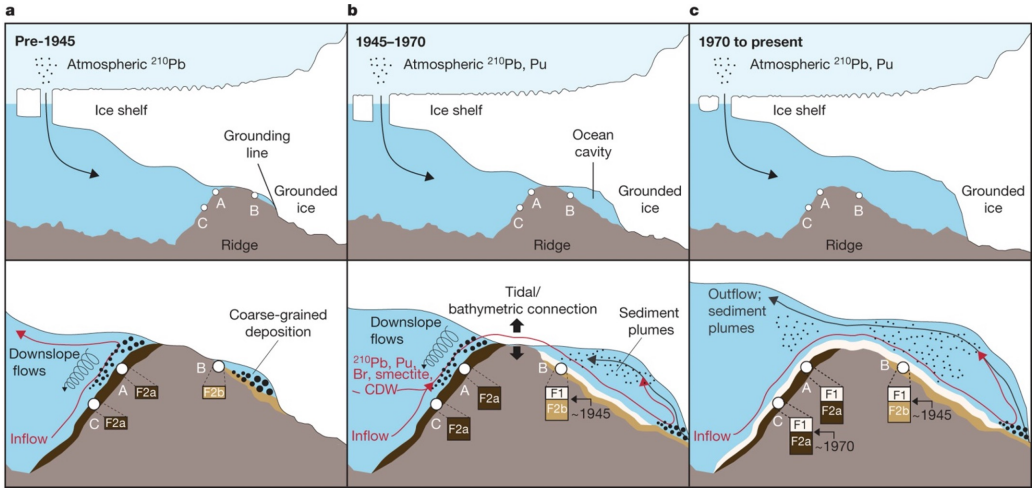

Fig. 2.14: Schematic of the sedimentation and processes beneath PIG ice shelf over the last 80 years, inferred from sediment cores. Figure is from Smith et al. (2017).

only a temporary light re-grounding in 2011 (Rignot et al., 2014), possibly due to thicker advected ice from the deep retreating grounding line.

Ice cores from WAIS indicate a climate anomaly in the 1940s (Schneider and Steig, 2008), following the 1939–42 El Niño event. A composite of stable isotope records, representative of surface temperatures in West Antarctica, show an extreme positive anomaly between 1936 and 1945, compared to the background warming trend. This suggests that the initial opening of the present day ice shelf cavity may have been caused by a tropically forced perturbation in ocean conditions (Jenkins et al., 2018). Although there are no direct observations of ASE ocean conditions prior to 1994, modelling results show a similar variability in temperature and basal melt that we see today (Naughten et al., 2022). Therefore, we can expect that a period of cold ocean conditions followed the warm anomaly in the years after. However, despite this, and similar to the irreversible retreat observed in the early 2000s, the cavity remained open with the grounding line retreating down the landward, retrograde side of the bedrock ridge back to its 1990s position at the ice plain.

2.3 Marine Ice Sheet Instability

2.3.1 Early MISI theory

The previous sections have discussed the ongoing mass loss in West Antarctica, and how ocean forcing is driving changes in ASE glaciers. However, the bed geometry beneath these glaciers also plays a big role in the present and future stability of the WAIS. The first mention of a connection between a possible WAIS collapse and a warming climate came

in the late 60s. Mercer (1968) claimed that western Antarctica is "the most vulnerable to a rise in temperature" and a "possible catastrophic disintegration of the West Antarctic Ice Sheet" could have been responsible for the rapid rise in sea level during the Sangamon Interglacial, some 120,000 years ago. According to Mercer, it was the marine based (grounded below sea level) parts of the ice sheet that would disintegrate into the sea. The concept of a possible Marine Ice Sheet Instability (MISI) was first suggested by Hughes (1973), who further stated that the bedrock configuration made the WAIS unstable in a warming climate.

However, the first theoretical studies that explored MISI were done by Weertman (1974) and Thomas and Bentley (1978). Weertman proposed that for an ice sheet in one horizontal dimensional (i.e., where lateral flow variations are ignored), ice flux at the grounding line increases with the local ice thickness. Therefore, if a steady state grounding line is located on bedrock that deepens inland (retrograde), a small retreat will lead to an increase in ice thickness at the grounding line and therefore increased ice flux. This increase in ice discharge across the grounding line would cause a negative mass balance (i.e. more mass lost at the fringes than gained in the interior), and therefore thinning and further retreat would occur (Fig. 2.15). Hence, in the absence of lateral stresses, marine ice sheets resting on retrograde slopes are inherently unstable. The same conclusion was derived by Thomas and Bentley (1978) who studied a retreat of the WAIS during the Holocene. In their work they also highlight the importance of ice shelves in slowing down the flow of grounded ice and potentially stabilising the grounding line.

The theoretical work done by Weertman (1974) and Thomas and Bentley (1978) showed that due to ice dynamic instabilities and a positive feedback mechanism it was possible for the WAIS to undergo a runaway retreat without the need for additional for-

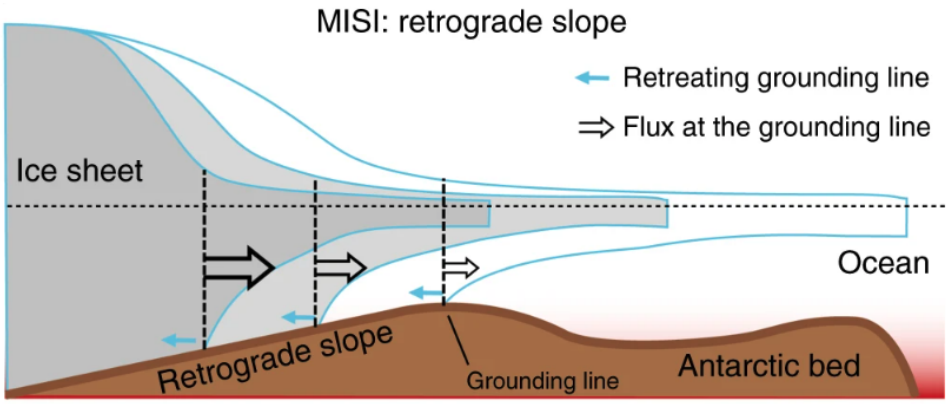

Fig. 2.15: Schematic of marine ice sheet instability (MISI): ice flux increases with ice thickness for a 1-D ice sheet (no lateral variation) as the grounding line retreats down a retrograde sloping bed. Figure is from Pattyn (2018).

cing. Mercer (1978) claimed that instead of instability mechanisms, a collapse of the WAIS would likely result from "man-made climate warming" leading to the break up of ice shelves and grounded ice. He had also made this remark in his earlier work suggesting that polluting the atmosphere could lead to future warming, which would then threaten the WAIS (Mercer, 1968). It seems likely that both claims are correct, where anthropogenic global warming will lead to ocean driven mass loss and retreat at the ice sheet fringes, thereby possibly initiating an unstable retreat. This was discussed by Thomas (1979) who further expressed the important buttressing effect of ice shelves. He stated that thinning of these ice shelves due to warmer atmospheric or oceanic temperatures would lessen their backpressure and could lead to increased flow from the ice sheet.

2.3.2 Analytical and modelling results

More recently, Schoof (2007a, b) provided the mathematical proof to support the earlier theoretical argument of Weertman (1974). By using a boundary layer theory for the sheet-shelf transition zone, he confirmed that ice flux at the grounding line of a rapidly sliding unbuttressed ice sheet (i.e., no lateral stresses) is an increasing function of ice thickness. Schoof (2007a) reaches three conclusions: (1) marine ice sheets have only a finite number of steady state profiles; (2) steady state grounding lines on retrograde slopes are not stable and (3) marine ice sheets with overdeepened beds can undergo hysteresis behaviour under perturbation of various parameters.

Later, an intercomparison project of ice sheet models was set up to determine whether the community of flow-line models could replicate MISI behavior (Pattyn et al., 2012). By perturbing a viscosity parameter, some models were able to produce an advancing and retreating ice sheet across an overdeepened bed, with equilibrium solutions that agreed with the semi-analytical solution from Schoof (2007a). However, other models that had insufficient resolution around the grounding line or those that used a simplified model approximation failed to advance the ice sheet across the overdeepened bed or reproduce the hysteresis behaviour (Pattyn et al., 2012). Further details on different modelling approximations and numerical methods are given in Section 2.4.

2.3.3 Buttressed ice sheets

The analytical (Schoof, 2007a) and modelling (Pattyn et al., 2012) results are now widely accepted. However, the theory only applies to the one horizontal dimensional ideal case where there is no flow variation in the transverse direction. This means that lateral stresses exerted from the ice shelf through contact with the seabed and coastal features, such as ice rises and rumples, are ignored. A number of studies have investigated the

buttressing effect of ice shelves either by prescribing a lateral drag at the boundaries or by modelling both horizontal directions, and they have shown that a stable grounding line can exist on a retrograde sloping bed (Dupont and Alley, 2005; Goldberg et al., 2009; Gudmundsson, 2013; Gudmundsson et al., 2012). This means that the stability of marine ice sheets is not just dependent on the bed topography but is also affected by their fringing ice shelves and the buttressing they provide. Other processes may also impact ice sheet stability such as ice front calving (Nick et al., 2010) and solid-earth feedbacks (Barletta et al., 2018; Kachuck et al., 2020), which may depend on the local geometry and long timescales.

2.4 Ice sheet modelling

Numerical models can be used to simulate the current state of ice sheets and predict their future behaviour in response to various forcing. These models can range from large continental scale simulations to smaller, individual glacier studies, and can be run in a diagnostic or prognostic way. All of these models are based on Stokes flow equations (Sect. 3.1), but due to the complexity and computational effort that is required to solve the full 3D set of equations, some form of approximation is often used.

The ice flow equations are then solved on a discretized grid, where the accuracy of the solution can depend on the grid resolution and how grounding line migration is specified (Vieli and Payne, 2005). In addition to the approximation of the 3D ice flow equations, ice sheet models also parameterize various physical processes which are difficult to observe or quantify directly, such as basal melting, upper surface accumulation, ice stiffness and conditions between the bed and the ice base.

2.4.1 Approximations

Depending on the problem that is being modelled, assumptions can be made so that components of the full set of equations can be neglected. This gives rise to a number of different approximations. The simplest approximation used in models, and the first that was developed, is the shallow ice approximation (SIA, Hutter, 1983). This assumes that the horizontal flow of the ice sheet is due to vertical shearing (deformation) alone, and neglects longitudinal (stretch and compression) and transverse stresses. This gives a balance between the basal shear stress of the grounded ice and the gravitational driving stress. This is appropriate for ice sheets with a small aspect ratio, where the thickness is much smaller than its length scale, and where there is a small ratio of strain-rate at the bed to strain-rate in the ice. This approximation is useful for simulating the creeping

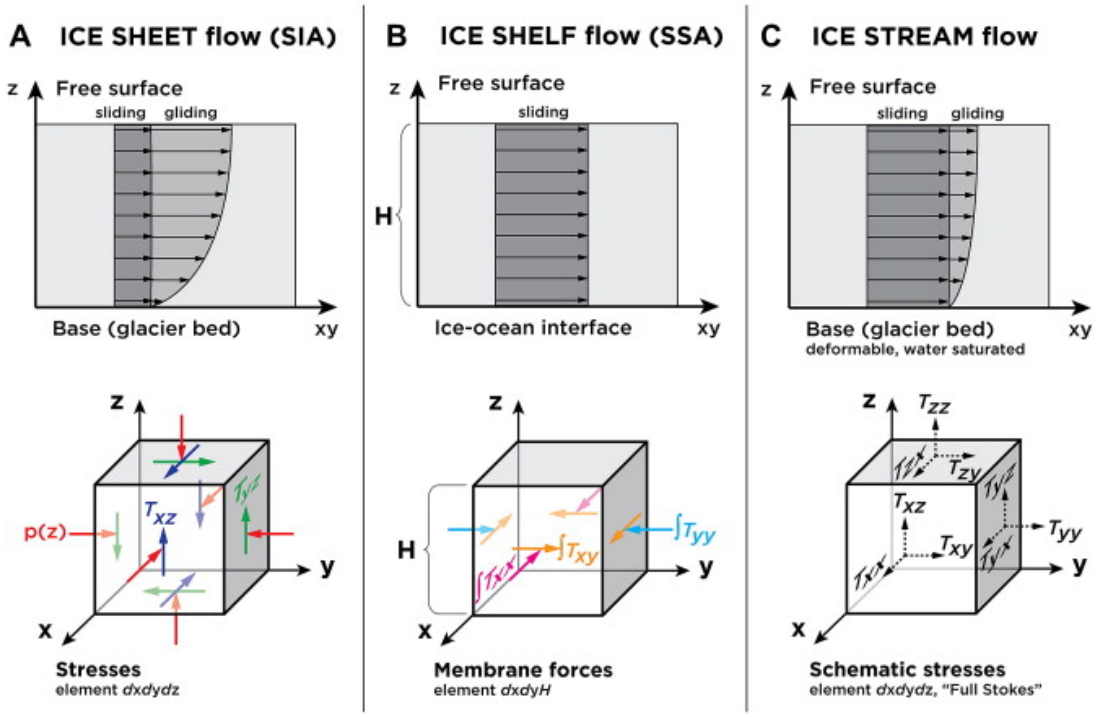

Fig. 2.16: Schematic of velocity profiles stress states for three different types of ice flow. Figure is from Kirchner et al. (2011).

flow of large, slow moving bodies of grounded ice in the interior of the ice sheet, over timescales of millennia. However, this approximation is not appropriate for fast flowing ice at the margins. The model intercomparison project (Pattyn et al., 2012) found these types of models could not replicate the MISI behaviour described in Sect. 2.3.

The next method is more complex but is most commonly used and is known as the shallow ice-stream approximation, or sometimes referred to as "SSTREAM" or "shelfy-stream" (SSA, Macayeal, 1989). This approximation is used for the coupling of fast flowing ice streams and ice shelves at the margins and therefore assumes that vertical shear is negligible compared to longitudinal and transverse stresses. This flow is sometimes referred to as "plug flow". The balance of horizontal stresses can be vertically integrated as described in Sect. 3.1. This approximation was capable of producing MISI behaviour in the MISMIP experiments (Pattyn et al., 2012) and is used for all the modelling shown later in this thesis.

A schematic of the velocity profiles for the SIA and SSA approximations is shown in Fig. 2.16. There are also other approximations such as Higher Order models (Blatter, 1995; Pattyn, 2003), hybrid SIA and SSA (Pollard and Deconto, 2009), SSA+SIA (Bueler and Brown, 2009), and L1L2 (Schoof and Hindmarsh, 2010). More details about the different stress approximations is given in Hindmarsh (2004) and Kirchner et al. (2011).

2.4.2 Numerical methods

To solve the governing equations for the above approximations, models can use a number of different numerical methods: finite-volume, finite-difference, finite-element, or a mixed approach. The equations are solved on a computational domain that has been discretized into some form of grid or mesh. The size or resolution of the mesh has been shown to impact the accuracy of model results (Durand et al., 2009; Vieli and Payne, 2005), especially in the important grounding line area where there is a transition from grounded to floating ice. To accurately model the grounding line migration with models that use a fixed size mesh requires very high computational costs. Therefore, a number of different modelling schemes have been developed to overcome this problem.

An adaptive approach, or *h-refinement*, refines the mesh around the grounding line, using extra points, whilst coarsening elsewhere (Cornford et al., 2013; Santos et al., 2019). The mesh size is usually determined in a trade-off between computational limitations and model accuracy, and this is done by carrying out a sensitivity analysis. In moving grid models, or *r-refinement*, the grounding line is modelled explicitly at grid points, which can be clustered closely together, and is followed continuously by moving the points, whilst the overall number of points remains constant (Goldberg et al., 2009). Alternatively, a less common refinement approach is a *p-refinement* of the mesh, which uses higher order polynomial basis functions around the grounding line, instead of moving or changing mesh grid points.

There are also other schemes to model grounding line migration which include either parameterizing the ice flux across the grounding line as a function of ice thickness (Pollard and Deconto, 2009; Schoof, 2007a), or by using a sub-grid or sub-element interpolation of the basal friction (Feldmann et al., 2014; Seroussi et al., 2014).

2.4.3 Friction law

Conditions between the base of the ice and the underlying bed are difficult to observe and quantify, but it is an important area which affects the movement of ice sheets. Therefore, ice sheet models usually use a friction law to parameterize the process. The general form of a friction law relates the basal drag to the sliding velocity. As there are different bed types, from hard bedrock to soft sediments, and water filled cavities, there are several different friction laws (e.g., Budd et al., 1979; Schoof, 2005; Tsai et al., 2015; Weertman, 1957). The choice of which friction law to use depends on the expected type of bed and glacier flow, and these laws have been shown to impact the mass balance differently (Brondex et al., 2017, 2019; Joughin et al., 2019; Yu et al., 2018). More details about the different laws that are used in experiments throughout this thesis are given in Sect. 3.1.4.

2.4.4 Other physical processes

Another physical process that is difficult to measure directly is ocean-driven basal melting beneath floating ice shelves. As basal melting is a major contributor to mass loss in Antarctica (Pritchard et al., 2012), it is a crucial component that needs to be accounted for in the ice flow equations. Basal melting is affected by the hydrographic properties of the water column and ocean circulation within the ice shelf cavity. Therefore, the most complete way to apply basal melting is with the use of coupled ice-ocean models (Naughten et al., 2021; Rydt and Gudmundsson, 2016), but these are computationally expensive for large scale simulations. Therefore, ice sheet models rely on basal melt parameterizations which can be in the form of simple linear or quadratic relationship, or more complex such as the plume, box or PICOP parameterizations (Burgard et al., 2022). There has also been a recent novel approach of using machine learning to predict basal melt rates (Rosier et al., 2023). Models also differ on how basal melt is applied close to the grounding line, which can affect the overall mass loss (Seroussi and Morlighem, 2018).

In addition to the mass balance of the ice-ocean interface, processes at the upper ice-atmosphere interface must also be included. The upper surface mass balance in ice sheet models is often provided by regional climate models (Wessem et al., 2018) but large scale Antarctic simulations may instead use global climate models (Nowicki et al., 2020; Seroussi et al., 2020).

2.5 Summary

A summary of the key points and knowledge gaps are:

- The largest contribution to the ongoing AIS mass loss is from the glaciers flowing into the Amundsen and Bellingshausen Seas. In recent decades, ocean-driven thinning of ASE ice shelves has reduced their buttressing capacity and led to an imbalance in the sector. One of the largest and fastest of these is PIG, which is considered to be part of the "weak underbelly" of the WAIS. This is due to its underlying bedrock being below sea level and retrograde sloping.

- Existing and longstanding work has shown that an unbuttressed marine ice sheet exhibits hysteretic behaviour in response to changes in ice softness. Whereas, in the presence of sufficient ice shelf buttressing, MISI can be avoided and a stable grounding line can be established on retrograde sloping beds. However, it has not yet been shown how a buttressed ice sheet responds to changes in ice softness, and whether it displays unstable behaviour. Research exploring the impact of changes in ice shelf thickness and other forcing on a buttressed ice sheet is given in Chapter 4.

- Observations show that until 80 years ago, PIG was grounded on a subglacial ridge 40 km downstream from its current position. Existing studies have linked a 1940s climate anomaly in West Antarctica with the retreat of PIG from the ridge. However, no study has yet shown that a tropically forced change in ocean conditions could have been responsible for the initial ungrounding. This research question is investigated in Chapter 5.

- Once PIG was retreating from the ridge, observations suggest that it did not stop until the early 1990s, when it stabilized at the next seabed rise. An idealized modelling study has shown that the retreat could have become irreversible after 20 years of melting, despite ocean conditions reverting to normal. This has been shown to happen when upstream cavities become connected with the ocean. However, this has yet to be confirmed for a realistic PIG configuration. Furthermore, several studies have shown the impact of varying ocean conditions on the future evolution of ASE glaciers, but none have assessed this for the recent PIG retreat. These questions have been explored in Chapter 6.

Chapter 3

Model description (Úa)

Throughout this thesis, the open-source numerical ice flow model Úa (Gudmundsson et al., 2012; Gudmundsson, 2020) is used to solve the shallow ice-stream approximation (SSA) (see Sect. 2.4.1). In this approximation the continuity and momentum equations are reduced to two horizontal dimensions by using a vertically integrated form (Sect. 3.1). This means that Úa is capable of simultaneously modelling the behaviour of the fast flowing grounded ice streams and floating ice shelves.

Úa is a finite element model which has been used in a wide range of studies which include the pan-Antarctic model comparison project (Levermann et al., 2020), idealized intercomparison projects (Cornford et al., 2020; Pattyn et al., 2012; Pattyn et al., 2013), ice-ocean coupled simulations using MITgcm on the Filchner-Ronne ice shelf (Naughten et al., 2021) and an idealized geometry (Rydt and Gudmundsson, 2016), comparison of model inversion techniques (Barnes et al., 2021; Ranganathan et al., 2020), grounding line dynamics, buttressing and stability theory using idealized geometries (Gudmundsson, 2013; Gudmundsson et al., 2012), ice shelf buttressing in diagnostic (Gudmundsson et al., 2019; Hill et al., 2018; Mitcham et al., 2022; Reese et al., 2018a; Rydt et al., 2015) and transient (Hill et al., 2021) simulations for Greenland and Antarctica, tipping point analysis for Pine Island Glacier (Rosier et al., 2021), rift propagation (Rydt et al., 2018), transient Holocene simulations (Jones et al., 2021), and data assimilation simulations (Rydt et al., 2021).

In this chapter a derivation of the vertically integrated SSA equations will be presented. This is followed by details about the boundary conditions, and the sliding laws that are used in the later research experiments. A brief description is then given of the numerical methods, inversion technique and basal melt parameterization.

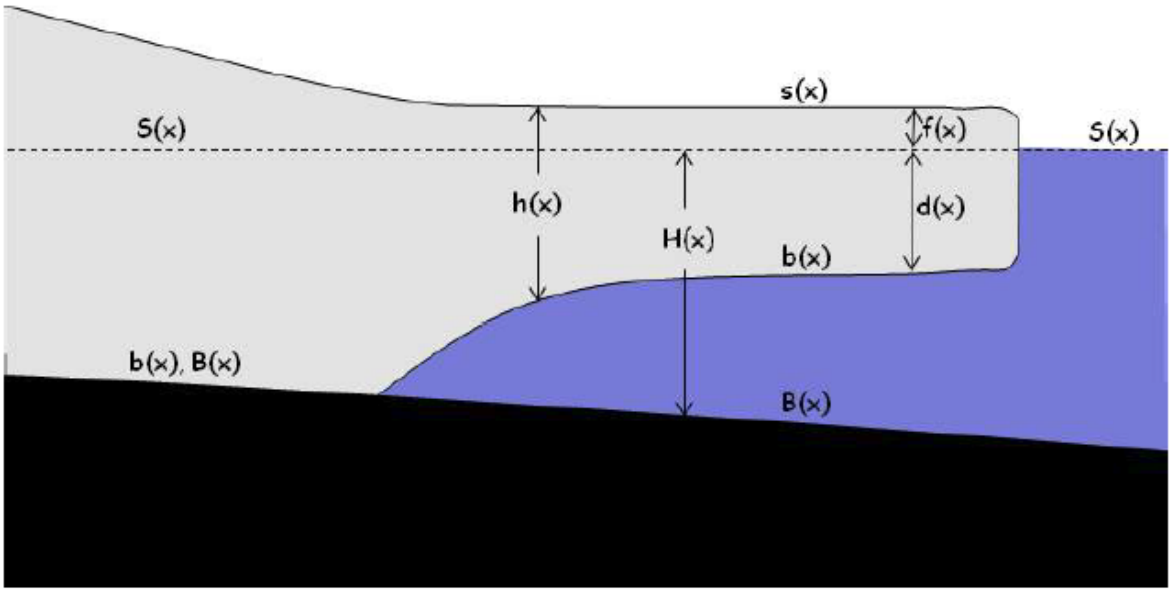

Fig. 3.1: Schematic of Úa model variables. Figure is from the Úa compendium (Gudmundsson, 2020).

3.1 Governing equations

The governing equations of ice flow in Úa are obtained from the conservation of momentum, conservation of mass, a constitutive law and boundary conditions. The ice geometry model variables that are used below are shown in Fig. 3.1.

3.1.1 Conservation of momentum

Firstly, the Navier-Stokes conservation of momentum equation can be written in convective form as

$$\rho \frac{D\boldsymbol{v}}{Dt} = \nabla \cdot \boldsymbol{\sigma} + \rho \boldsymbol{F}, \tag{3.1}$$

where $\boldsymbol{v}$ is the three-dimensional ice velocity, ρ is the ice density, $\boldsymbol{F}$ is a body force and $\boldsymbol{\sigma}$ is the Cauchy stress tensor.

For ice flow, it can be assumed that the inertial forces are dominated by viscous forces (small Reynolds number, $Re \ll 1$), and the only body force acting is due to gravity (i.e., neglecting the Coriolis force). Therefore, neglecting the inertial terms on the left hand side of Eq. 3.1 gives the equation for Stokes flow:

$$\nabla \cdot \boldsymbol{\sigma} + \rho \boldsymbol{g} = 0, \tag{3.2}$$

where $\boldsymbol{g}$ is gravitational acceleration. The Cauchy stress tensor, $\boldsymbol{\sigma}$, can be expressed in

terms of the deviatoric stress tensor, $\boldsymbol{\tau}$, and pressure, p, as

$$\boldsymbol{\sigma} = \boldsymbol{\tau} - p\boldsymbol{I}, \tag{3.3}$$

where $p = -\frac{1}{3}tr\boldsymbol{\sigma}$ and $\boldsymbol{I}$ is the identity matrix. Therefore, Stokes flow (Eq. 3.2) can be written in full as

$$\partial_x\tau_{xx} + \partial_y\tau_{xy} + \partial_z\tau_{xz} = \partial_x p \tag{3.4}$$

$$\partial_x\tau_{yx} + \partial_y\tau_{yy} + \partial_z\tau_{yz} = \partial_y p \tag{3.5}$$

$$\partial_x\tau_{zx} + \partial_y\tau_{zy} + \partial_z\tau_{zz} = \partial_z p + \rho g \tag{3.6}$$

where τ_{ij} are the components of the deviatoric stress tensor, and it is assumed that the z-axis is orientated upwards, against the direction of the gravity vector.

Shallow ice-stream approximation

As mentioned in Sect. 2.4, some models solve the full three dimensional Stokes flow equations, but this is computationally expensive, so most models use some form of approximation. In Úa, either the SIA or SSA can be implemented, however, the experiments that are presented in this thesis all use SSA as we focus mainly on the floating part of the ice sheet. In SSA, it is assumed that the ice thickness is much smaller than the horizontal extent, and that vertical shear is negligible compared to longitudinal and transverse stresses. A full derivation of the SSA can be found in (Macayeal, 1989), and for the model used here in the Úa Compendium (Gudmundsson, 2020). Based on the above assumptions, and expressed in terms of ice velocities, the full set of Stokes equations in Eqs. (3.4)–(3.6) can be reduced to two-dimensions and written as

$$\nabla_{xy} \cdot (h\boldsymbol{R}) - \boldsymbol{t}_{bh} = \rho g h \nabla_{xy} s + \frac{1}{2} g h^2 \nabla_{xy} \rho, \tag{3.7}$$

where $\boldsymbol{R}$ is the resistive stress tensor defined as

$$\boldsymbol{R} = \begin{pmatrix} 2\tau_{xx} + \tau_{yy} & \tau_{xy} \\ \tau_{xy} & 2\tau_{yy} + \tau_{xx} \end{pmatrix} \tag{3.8}$$

and $\nabla_{xy} = (\partial_x, \partial_y)^T$, h is the ice thickness, s is the ice upper surface elevation, ρ is the vertically averaged ice density (spatially variable), and $\boldsymbol{t}_{bh}$ is the horizontal component of the bed-tangential basal traction.

3.1.2 Constitutive law

The most commonly used flow law in ice sheet modelling relates deviatoric stresses τ_{ij} to the strain-rates $\dot{\epsilon}_{ij}$ in Glen's flow law:

$$\dot{\epsilon}_{ij} = A\tau^{n-1}\tau_{ij}, \tag{3.9}$$

where $\tau = \sqrt{\tau_{ij}\tau_{ij}/2}$ is the second invariant of the deviatoric stress tensor, and the strain-rate tensor $\dot{\epsilon}_{ij}$ is given by

$$\dot{\epsilon}_{ij} = \frac{1}{2}\left(\frac{\partial u_i}{\partial x_j} + \frac{\partial u_j}{\partial x_i}\right). \tag{3.10}$$

and A is an ice rate factor (representing ice properties such as temperature, damage or ice "softness") and $n = 3$ is a creep exponent that is used for the experiments throughout this thesis. The rate factor A can vary in time and space, but is often assumed to be constant for ease of use and to represent isothermal ice. A spatially varying A can be determined through an iterative optimization (or an inverse methodology) using data assimilation (Sect. 3.3).

3.1.3 Boundary conditions

The following boundary conditions are required:

Upper surface

At the upper surface it is assumed that wind and atmospheric pressure are negligible compared to ice stresses, and therefore a stress free condition is applied

$$\boldsymbol{\sigma} \cdot \boldsymbol{n}_s = 0, \tag{3.11}$$

where $\boldsymbol{n}_s$ is the unit normal pointing outward from the upper surface.

Lower surface (floating)

Under a floating ice shelf, it is assumed that the only stress is exerted by water pressure

$$\boldsymbol{\sigma} \cdot \boldsymbol{n}_b = -p_w \boldsymbol{n}_b, \tag{3.12}$$

where $\boldsymbol{n}_b$ is the unit normal pointing outward from the lower surface, $p_w = \rho_w g(S - z)$ is the ocean pressure, ρ_w is the ocean density and $S = 0$ is the ocean surface.

Lower surface (grounded)

Between grounded ice and the bed, a sliding law is used for the basal shear stress (see Sect. 3.1.4). There is also a kinematic boundary condition that assumes no ice ablation or accumulation can happen at the base

$$\boldsymbol{u} \cdot \boldsymbol{n}_b = 0, \tag{3.13}$$

where $\boldsymbol{n}_b$ is the unit normal pointing outward from the lower surface.

To determine whether the ice is grounded or afloat, Úa uses a floatation condition which compares the ice thickness h with the floatation thickness h_f, which is the maximum possible ice thickness without grounding:

$$h_f = \frac{\rho_w}{\rho}(S - B). \tag{3.14}$$

The ice grounds if ice thickness h exceeds h_f, i.e., $h > h_f$. The floatation condition is applied on the grid nodes and this produces a floating/grounding mask for the entire domain. The grounding line can pass through the grid elements, where its position is calculated through interpolation from the floating/grounding mask.

Calving front

At the calving front, similar to the lower surface of the floating ice shelf, the stress boundary condition is given by

$$\boldsymbol{\sigma} \cdot \hat{\boldsymbol{n}} = -p_w \hat{\boldsymbol{n}}, \tag{3.15}$$

where $\hat{\boldsymbol{n}}$ is the unit normal pointing horizontally outward from the ice front. In Úa this is expressed as the 'natural' boundary condition in the form

$$\boldsymbol{R} \cdot \hat{\boldsymbol{n}} = \frac{g}{2h}(\rho h^2 - \rho_w d^2)\hat{\boldsymbol{n}} \tag{3.16}$$

where $\hat{\boldsymbol{n}}_{xy} = (n_x, n_y, 0)^T$. For a floating calving front, which applies to the experiments presented in this thesis, $\rho h = \rho_w d$, and Eq. 3.16 becomes

$$\boldsymbol{R} \cdot \hat{\boldsymbol{n}} = \frac{1}{2}\varrho g h \hat{\boldsymbol{n}}, \tag{3.17}$$

where $\varrho \coloneqq \rho(1 - \rho/\rho_w)$.

3.1.4 Sliding law

Basal sliding is an important process in glacial flow, but it is difficult to prescribe in ice sheet models. A sliding law is used by models to parameterize the conditions at the bed, which relates the basal velocity to the basal shear traction. However, there is not a universal law that represents all types of motion or bed conditions, and one must be selected depending on the expected scenario. In Úa, there are a number of sliding laws that can be implemented, including: Weertman, Budd, Coulomb, Tsai, Schoof and Umbi. The derivation for each of these can be found in the Úa Compendium (Gudmundsson, 2020) but because some of these laws will be used later in the thesis, their definitions are given below:

Weertman

The power-law type sliding law (Weertman, 1957) is the most commonly used and gives the basal traction in terms of bed roughness and basal velocity. This law is appropriate for sliding over hard bedrock, where the basal traction is affected by the roughness of the bed. It is given by

$$\boldsymbol{t}_b = \beta^2 \, \boldsymbol{v}_b, \tag{3.18}$$

where

$$\beta^2 = C^{-1/m} \|\boldsymbol{v}_b\|^{1/m-1} \tag{3.19}$$

and C is the basal slipperiness, $m = 3$ is a stress component, $\boldsymbol{t}_b$ is the horizontal component of the tangential basal traction and $\boldsymbol{v}_b$ is the horizontal component of the tangential basal velocity. Similar to the parameter A in Glen's flow law (Eq. 3.9), the basal slipperiness, C, can vary spatially and temporally but is often kept constant. A spatially varying C can be determined through an iterative optimization (or an inverse methodology) using data assimilation (Sect. 3.3).

Budd

A generalized Weertman sliding law where basal traction additionally depends on effective pressure, N, at the bed (Budd et al., 1979) is given by

$$\boldsymbol{t}_b = N^{q/m} \beta^2 \, \boldsymbol{v}_b, \tag{3.20}$$

where q is derived from laboratory experiments and is generally set to $q = 3$. In this formulation the basal traction becomes zero ($t_b \to 0$) as the grounding line is approached ($N \to 0$).

Coulomb

In regions close to the grounding line, the underlying bed may be softer or weaker and saturated with water. In this case a Coulomb-type sliding law may be more appropriate, which assumes the basal traction does not depend on the velocity, and this is sometimes referred to as *plastic* friction. This is given by

$$\boldsymbol{t}_b = \mu_k N \frac{\boldsymbol{v}_b}{\|\boldsymbol{v}_b\|}, \tag{3.21}$$

where μ_k is the coefficient of kinetic friction and is typically set to $\mu_k = 0.5$.

Tsai

The Tsai sliding law (Tsai et al., 2015) is a modified power law which combines the Weertman and Coulomb laws, so that basal traction is prevented from exceeding some fraction of the effective pressure. The Weertman part of the law is appropriate where the bed is hard, whilst the Coulomb law is more appropriate for soft sediments or water filled cavities close to the grounding line. The Tsai law is given by

$$\boldsymbol{t}_b = \min(\beta^2 \|\boldsymbol{v}_b\| \boldsymbol{v}_b, \mu_k N) \frac{\boldsymbol{v}_b}{\|\boldsymbol{v}_b\|}. \tag{3.22}$$

Schoof

The Schoof sliding law (Schoof, 2005) is another modified power law which places a limit on the basal traction but has a smoother and continuous transition between the two limits, compared to the Tsai law. The Schoof law is given by

$$\boldsymbol{t}_b = \frac{\beta^2 \|\boldsymbol{v}_b\| \mu_k N}{((\mu_k N)^m + (\beta^2 \|\boldsymbol{v}_b\|)^m)^{1/m}} \frac{\boldsymbol{v}_b}{\|\boldsymbol{v}_b\|}. \tag{3.23}$$

Umbi

The Umbi sliding law is similar to the Schoof law, and is given by

$$\boldsymbol{t}_b = \frac{\beta^2 \|\boldsymbol{v}_b\| \mu_k N}{\mu_k N + \beta^2 \|\boldsymbol{v}_b\|} \frac{\boldsymbol{v}_b}{\|\boldsymbol{v}_b\|}. \tag{3.24}$$

3.1.5 Conservation of mass

To model the evolution of ice geometry over time in the SSA approximation, the conservation of mass and kinematic boundary conditions on the lower and upper surfaces must be taken into account. The local form of conservation of mass is given by

$$\partial_t \rho + \nabla \cdot (\rho \boldsymbol{v}) = 0, \tag{3.25}$$

where ρ is assumed to be horizontally spatially variable. The kinematic boundary conditions related to the evolution of the lower (b) and upper surface (s) are

$$\partial_t b + u_b \partial_x b + v_b \partial_y b - w_b = -a_b \tag{3.26}$$

$$\partial_t s + u_s \partial_x s + v_s \partial_y s - w_s = a_s, \tag{3.27}$$

where u_b, v_b and w_b are the x, y and z ice velocity components at the lower surface, and similarly, the s subscript components at the upper surface. a_b and a_s are the lower and upper surface mass balance and are measured in meters of water equivalent per time

(m yr^{-1}). There are different signs for a_b and a_s because mass flux into the ice is defined as positive, irrespective of surface. Therefore, accumulation on the upper surface is positive whilst basal melting from the lower surface is negative.

In most ice sheet models, the ice density is assumed to be constant in time and space. However, in Úa for the SSA approximation, the density is free to vary in the horizontal and is assumed constant in time. Therefore, the assumption is

$$\partial_t \rho = 0. \tag{3.28}$$

Equation 3.25 then becomes

$$\nabla \cdot (\rho \boldsymbol{v}) = 0. \tag{3.29}$$

From the above equations, the vertically integrated form of the mass conservation can be derived as

$$\rho \partial_t h + \nabla_{xy} \cdot \boldsymbol{q} = \rho a, \tag{3.30}$$

where $\boldsymbol{q} = \rho h \boldsymbol{v}$ is the ice flux, $\boldsymbol{v} = (u, v)^T$ is the horizontal ice velocity and $a = a_s + a_b$.

3.2 Numerical methods

Úa is a finite element model capable of solving the nonlinear system of equations on an unstructured mesh with spatially varying element sizes. Mesh refinement can be based on specific criteria such as high velocities or strain-rates, and a time-dependent adaption can be made around the grounding line as it moves. For the experiments presented in this thesis, a number of different refinement methods are used depending on the problem, and more details are given in the methods section of each research chapter. The coordinate system used for the model runs in chapters 5 and 6 is the WGS84 Antarctic Polar Stereographic projection (EPSG:3031). The figure axis labels in those chapters show the x and y polar stereographic coordinates as xps and yps, respectively.

To calculate the transient evolution of the geometry Úa uses a fully implicit method, which simultaneously solves for the unknowns of velocity and ice thickness at each time step. The resulting non-linear system is solved using the Newton-Raphson method. All experiments shown in this thesis use linear six-node triangular elements and a minimum ice thickness of 1 m is imposed using a reset method.

All model simulations presented in this thesis were carried out using Supercomputing Wales facilities, with the help of lead engineer Ade Fewings and research software engineer Aaron Owen. Each simulation was run on two cores, which resulted in completion times of between a few hours for short transient runs, and up to several days for steady state simulations.

3.3 Model initialization

In this thesis the model is initialized in two different ways. The most simple approach, which is done for the idealized case in Chapter 4, is to spin the model up from a constant ice thickness over the bedrock topography until an approximately steady state is reached. In this approach, spatially constant fields are generally used for the model parameters A (Eq. 3.9) and C (Eq. 3.19). The basal slipperiness, C, can be estimated using typical values of basal traction and velocity in Eq. 3.19, and the ice rate factor, A, can be approximated through ice temperature evolution.

An alternative approach for initializing a model is to use a dataset of observed ice geometry as a starting configuration, as shown in Chapters 5 and 6. In this approach, spatially variable fields A and C values are used and these are generally determined through an inversion process, as they are too difficult to measure directly.

The optimization (or inversion) process is a commonly used method in glaciology (e.g., MacAyeal, 1993), where unknown model parameters, such as the ice rate factor and slipperiness, are found through an iterative process, starting from some initial guess. In Úa, this involves minimizing a cost function, $J = I + R$, which is constructed from the misfit, I, between modelled and observed surface velocities, and an additional regularization term, R, as this is an ill-posed problem. Úa uses the adjoint method to determine the gradient of the cost function, with respect to A and C.

For the experiments given in Chapters 5 and 6, the misfit term is given by

$$I = \frac{1}{2\mathcal{A}} \int \left(\frac{\boldsymbol{v} - \boldsymbol{v}_{\text{obs}}}{\boldsymbol{v}_{\text{err}}} \right)^2 d\mathcal{A} \tag{3.31}$$

and a Tikhonov regularization is used on the amplitudes and slopes of A and C:

$$\begin{aligned} R = \frac{1}{2\mathcal{A}} \int \Bigg[& \gamma_{sA}^2 \left(\nabla \log_{10} \left(\frac{A}{\hat{A}} \right) \right)^2 + \gamma_{sC}^2 \left(\nabla \log_{10} \left(\frac{C}{\hat{C}} \right) \right)^2 \\ & + \gamma_{aA}^2 \left(\log_{10} \left(\frac{A}{\hat{A}} \right) \right)^2 + \gamma_{aC}^2 \left(\log_{10} \left(\frac{C}{\hat{C}} \right) \right)^2 \Bigg] d\mathcal{A}. \end{aligned} \tag{3.32}$$

In Eq. 3.31, the velocity observations ($\boldsymbol{v}_{\text{obs}}$) and measurement errors ($\boldsymbol{v}_{\text{err}}$) are taken from the MEaSUREs Annual Antarctic Ice Velocity Maps dataset (Mouginot et al., 2017a,b) for 2014/15 and $\mathcal{A}$ is the total domain area. In Eq. 3.32, $\hat{A}$ and $\hat{C}$ are prior estimates for A and C, where we used spatially uniform values $\hat{A} = 5 \times 10^{-9}$ yr^{-1}kPa^{-3}, which corresponds to an ice temperature of -15 °C, and $\hat{C} = 1.46 \times 10^{-3}$ m yr^{-1}kPa^{-3}, which was derived from Eq. 3.18 using $\boldsymbol{t}_b = 80$ kPa and $\boldsymbol{v}_b = 750$ m yr^{-1}.

The regularization parameters ($\gamma_{sA}, \gamma_{sC}, \gamma_{aA}, \gamma_{aC}$) in Eq. 3.32 control the relative size of the regularization terms, where s refers to slope and a refers to amplitude. An L-

curve approach was initially used to find optimal values for the parameters. This involves plotting the regularization against the misfit for different parameter combinations, which produces an L-shaped plot. The optimal parameters tend to be near the corner of the L-shape, which minimizes the velocity misfit whilst limiting any overfitting. In our experiments however, more smoothing was required to avoid artefacts appearing when the model was advanced forward.

During the inversion process, the spatially varying basal slipperiness (C) is determined for grounded areas only, using the present day geometry. However, as will be shown in Chapters 5 and 6, to derive a 1940s PIG configuration the present day geometry is advanced forward to the ridge. Therefore, slipperiness values are required for the region downstream of the present day grounding line. Without any velocity information for the 1940s period, a constant C value representative of fast flowing regions was chosen. Whilst a more realistic field may alter the timescales of retreat, we do not expect this to change the overall outcome of this study.

The optimal A and C fields that were found through inversion are used in Chapters 5 and 6 and are shown in Fig. 3.2. When using these fields there is a good fit between modelled and observed ice surface velocities, with only large differences where there were missing measurements near the ice front. The mean difference, excluding these large discrepancies, is 0.94 m yr^{-1}, with typical differences within 30 m yr^{-1} in all the main tributaries. The highest rate factor values are found along the shear margins of the fast flowing trunk, which suggests the presence of softer or damaged ice (Lhermitte et al., 2020). The highest slipperiness values are found along th fast flowing tributaries. Although this is an ill-posed problem with a non-unique solution, the features shown in these inversion results have also been demonstrated in other PIG studies (Barnes et al., 2021; Rydt et al., 2021), which gives us confidence in these A and C fields.

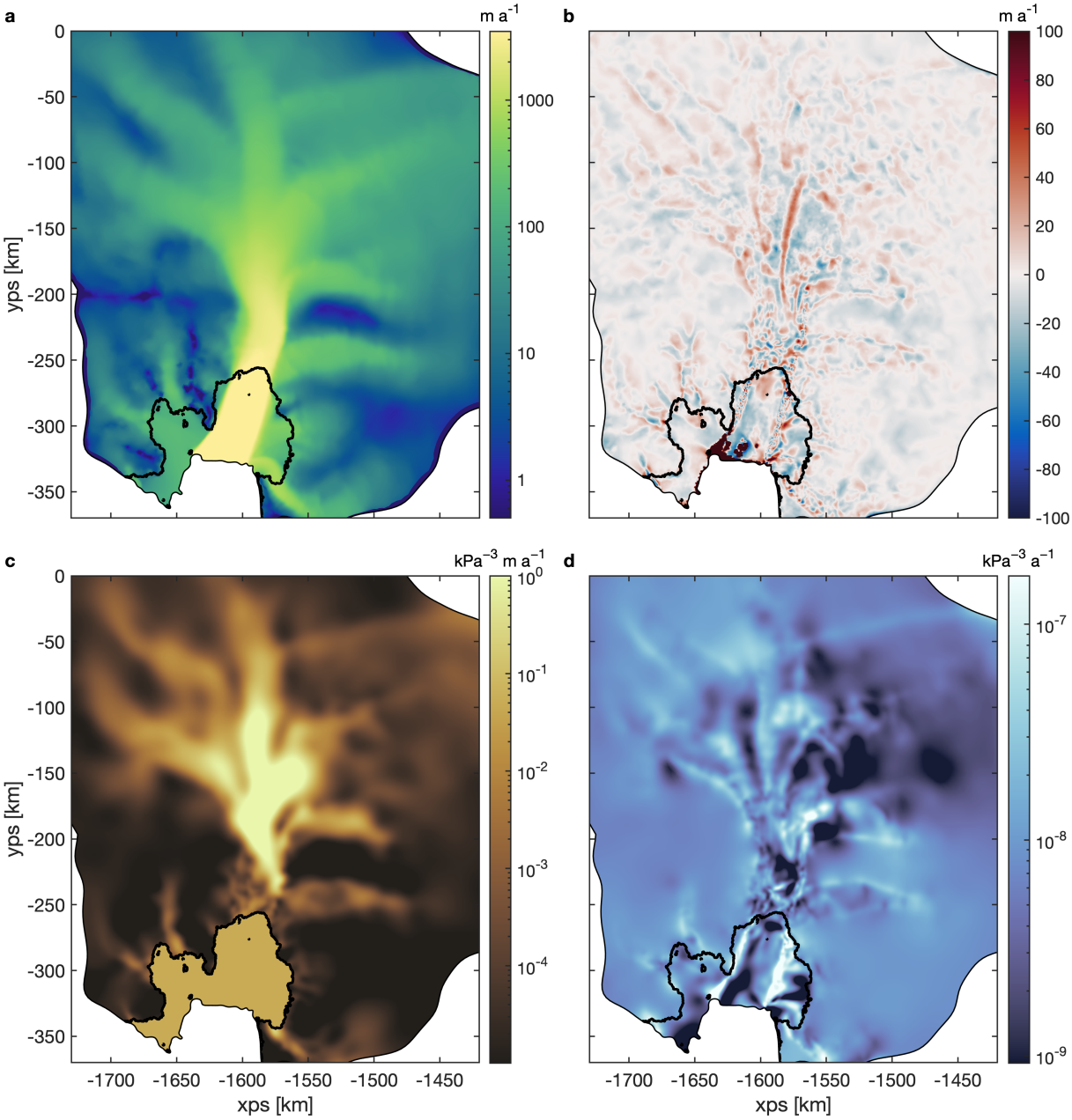

Fig. 3.2: **(a)** Modelled ice speed after the inversion process. **(b)** Difference between modelled and observed ice speeds (mod minus obs). **(c)** Basal slipperiness (C), where lighter colours indicate high slipperiness. Downstream of the grounding line the slipperiness is set to a constant value to allow an advance to the subglacial ridge. **(d)** Rate factor (A) on a colour scale equivalent to depth-averaged ice temperatures from -35°C (darker colours) to 0°C (lighter colours). The model boundary and grounding line are shown as thin and thick black lines respectively. Note the log-scale colour maps for **(a)**, **(c)** and **(d)**.

3.4 Melt rate parameterization

As mentioned in Sect. 2.4.4, ice sheet models often use a parameterization for the basal melting beneath an ice shelf. In this thesis, two simple parameterizations are used and these are described below.

3.4.1 MISMIP+ melt rate

The first basal melt rate parameterization is from a recent marine ice sheet model intercomparison project, MISMIP+ (Asay-Davis et al., 2016). This parameterization depends on ice shelf draft and water column thickness, and has a coefficient that takes into account the thermal driving and ocean friction velocity. It is given by the following equation

$$m_i = \Omega \tanh\left(\frac{H_c}{H_{c0}}\right) \max(z_0 - d, 0), \tag{3.33}$$

where $\Omega = 0.2$ yr^{-1} is a melt rate coefficient corresponding to an ocean temperature of ~ 1.0°C, $Hc = b - B$ is the water column thickness, $H_{c0} = 75$ m is a reference ocean-cavity thickness, $z_0 = -100$ m is the depth above which melt is zero and d is the ice draft. The parameterization is shown in Fig. 3.3 and was loosely developed based on results from the Parallel Ocean Program v. 2x (POP2x), by using the MISMIP+ cavity shape. Although it is an ad hoc and simple parameterization designed for the intercomparison project, the spatial pattern and magnitude is comparable to more realistic melt rate fields (Favier et al., 2019).

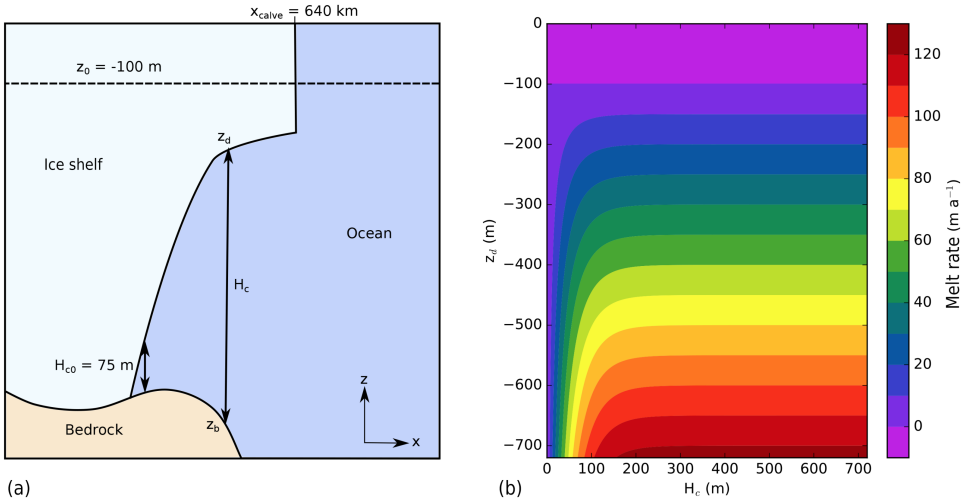

Fig. 3.3: Schematic (**a**) and melt rate (**b**) for the MISMIP+ parameterization. The ice shelf draft (z_d) and bed elevation (z_b) in **a** is shown as d and B, respectively, in Eq. 3.33. This figure is from Asay-Davis et al. (2016).

3.4.2 Depth-dependent melt rate

The second melt rate parameterization is a piecewise linear function of depth (Fig. 3.4). This type of parameterization has been used in previous ice modelling studies of PIG (Favier et al., 2014; Joughin et al., 2010). The shape of the curve given by the parameterization is based on the typical two-layer thermal structure that is observed in the Amundsen Sea (Dutrieux et al., 2014). This has a shallow cold layer overlying a deep warm layer with a rapidly changing thermocline in between. An example of this structure is shown in Fig. 2.10 for the coldest and warmest years on record in Pine Island Bay. The magnitude of melting is based on direct and indirect observations of basal melt, with values of 100 m yr^{-1} at the deep grounding lines and 20–40 m yr^{-1} under the outer ice shelf where the ice base is shallower (Bindschadler et al., 2011b; Dutrieux et al., 2013; Shean et al., 2019).

Due to its simple formulation, this parameterization is computationally efficient to run, but it has been shown to overestimate melt rates at the grounding line, when compared with melting from a more complex ocean model (Rydt and Gudmundsson, 2016). However, this parameterization is suitable for the experiments carried out in this thesis because conclusions are given about the direct influence of melting and what happens when it is removed. Furthermore, to limit any erroneous high melting at or upstream of the grounding line, all experiments apply the melt to fully floating mesh elements only (Seroussi and Morlighem, 2018).

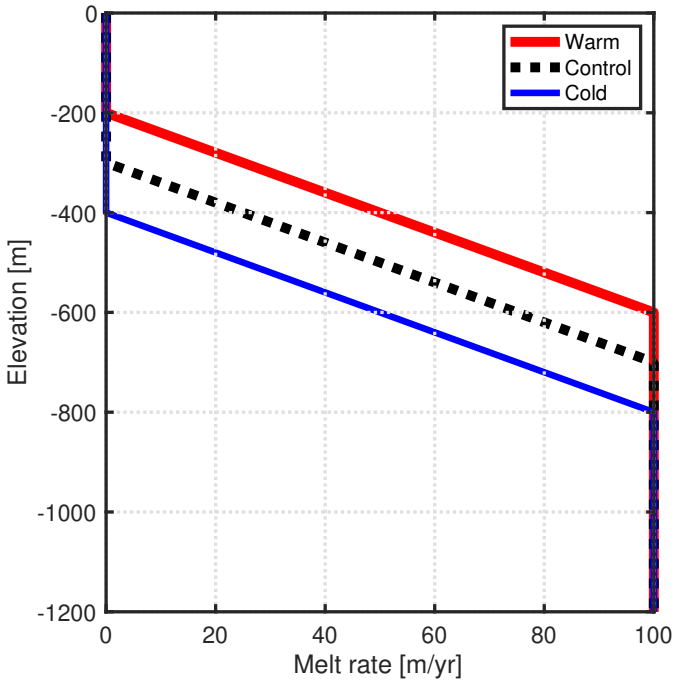

Fig. 3.4: Depth dependent melt rate parameterization.

Observations of ocean conditions in Pine Island Bay show considerable variability in the thermocline depth, with a shoaling or deepening of up to 200 m (Dutrieux et al., 2014). To represent average conditions in a control case, the thermocline in the parameterization lies between a depth of 300 m and 700 m, with the cold layer above and the warm layer below (Dutrieux et al., 2014; Rydt and Gudmundsson, 2016). This parameterization gives a melt rate of 75 m yr^{-1} at a depth of 600 m, which is similar to the MISMIP+ parameterization when the ocean cavity is not small (Fig. 3.3).

In Chapter 4 the base of the thermocline is at 700 m, as shown here, however, for the experiments in Chapters 5 and 6, the thermocline depth is lowered and raised to adjust the basal melt forcing. This captures the full range of variability that is observed in the Amundsen Sea (Dutrieux et al., 2014). An example of the cold (800 m) and warm (600 m) forcing is shown in blue and red in Fig. 3.4.

Chapter 4

Perturbations of an idealized buttressed ice sheet

4.1 Introduction

Around much of the Antarctic coastline, grounded ice flows from the interior towards the ocean and forms floating ice shelves (Bindschadler et al., 2011a). These shelves, which can be 1 km thick at their deep grounding lines (Morlighem et al., 2020), play an important role in the ice sheet's mass balance because they provide a buttressing effect on upstream ice. Lateral drag is produced as the shelves flow past slower-moving ice or stationary coastline, which causes a transmission of shear stress between the floating and grounded ice. This stress acts as a resistance against the ice flow and is enhanced when ice shelves are confined in an embayment, or in contact with the seafloor via ice rises or rumples. If there is a change in thickness or extent of an ice shelf, this can alter the stress balance at the grounding line and affect the flow of grounded ice (Gudmundsson et al., 2019).

The major glaciers in West Antarctica, such as Pine Island and Thwaites, are mostly grounded on bedrock that is below sea level and large sections of ice rest on bed which slopes upwards in the direction of flow (retrograde slope) (Morlighem et al., 2020). In the absence of lateral stresses (or ice shelf buttressing), ice flux at the grounding line increases with ice thickness, and therefore this type of bed configuration cannot support stable grounding lines (Schoof, 2007a). A perturbation of a steady state on a retrograde slope produces an unstable response until the next downward slope (prograde) is encountered. This is known as the marine ice sheet instability (MISI), and was first proposed by Weertman (1974) (see Sect. 2.3). This instability mechanism has led to concerns about the vulnerability of the WAIS and the possibility of a collapse (Favier et al., 2014; Joughin et al., 2014; Rignot et al., 2014).

The analytical results given by Schoof (2007a) were later used to judge the performance

of numerical flowline ice-sheet models in an intercomparison project (MISMIP, Pattyn et al., 2012). This project showed that some models could replicate the unstable behaviour in one horizontal dimension by stepping though an ice softness parameter in an advance and retreat phase. Once the grounding line crossed the retrograde slope, the forcing had to be significantly reversed for the ice sheet to return to its original state. For example, by decreasing the ice rate factor from $A = 5 \times 10^{-26}$ s^{-1} Pa^{-3} to $A = 2.5 \times 10^{-26}$ s^{-1} Pa^{-3} this led to an advance from the base of a trough to the downstream side of a ridge crest, but increasing the rate factor back to $A = 5 \times 10^{-26}$ s^{-1} Pa^{-3} only caused a small retreat to a steady state position, still downstream of the ridge crest. This hysteretic behaviour indicates the presence of two stable branches, with multiple steady states for the same forcing, where the final grounding line position depends on the forcing history.

A second intercomparison project, MISMIP3d (Pattyn et al., 2013), further explored grounding line dynamics during advance and retreat phases by including lateral variation on a downward sloping bed. By applying and removing a perturbation on the basal sliding, this generated a curved grounding line and some degree of buttressing. Whilst both MISMIP and MISMIP3d results showed that initial and final grounding line positions are heavily depend on the stress approximation and the horizontal resolution of the model, they did not include lateral variations in topography or strong ice shelf buttressing.

Modelling work by Gudmundsson et al. (2012) showed that an ice sheet that flowed along a narrow channel and varied in two horizontal dimensions could produce stable grounding lines on retrograde slopes if there was strong enough buttressing. Lateral stresses from the ice shelf were sufficient to stop MISI from occurring in the presence of an overdeepened bed. This showed that the stability of an ice sheet was not just dependent on the bed slope beneath, but also affected by the buttressing capacity of its ice shelf. This was also displayed for different channel widths, with stable grounding lines occurring across the entire retrograde and prograde slopes of an overdeepened bed.

Building on the results from Gudmundsson et al. (2012) and the previous community efforts (Pattyn et al., 2012; Pattyn et al., 2013), a third intercomparison project, MISMIP+ (Asay-Davis et al., 2016), was set up to investigate the impact of ice shelf ablation on the flow of upstream ice, when grounded on a retrograde slope. A loss of buttressing caused by thinning or collapsed ice shelves can induce acceleration of upstream ice and subsequent retreat of the grounding line (Gudmundsson et al., 2019; Scambos et al., 2004). Another aim of MISMIP+ was to assess the importance of how basal sliding is treated in the model, and also the effects of mesh resolution and stress approximation.

In this chapter, a series of numerical ice sheet simulations are carried out on the idealized marine ice sheet from the recent intercomparison project, MISMIP+ (Asay-Davis et al., 2016). The aims of these experiments are to: (1) assess the impact of

different sliding laws and basal melt parameterizations, (2) investigate the reversibility of a buttressed ice sheet on a retrograde slope, and (3) determine whether a hysteresis is present in response to varied forcing, for different channel widths.

4.2 Methods

In this study, two sets of experiments are presented. The first set of experiments follow the methodology of MISMIP+ (Asay-Davis et al., 2016) and investigate the effects of ocean induced thinning, and subsequent change in buttressing, on the flow of upstream ice. The second experiment builds on the original MISMIP exercise (Pattyn et al., 2012) to determine the impact of a changing ice softness on a buttressed ice sheet in two horizontal dimensions. Both sets of experiments are carried out using the MISMIP+ geometry.

4.2.1 Model description

In both sets of experiments, the ice flow model Úa (Gudmundsson et al., 2012) is used in a SSA configuration (see Ch 3). The model is run in a time-dependent mode on an unstructured mesh (Sect. 4.2.3), and a spatially uniform rate factor A is used in Glen's flow law (Eq. 3.9). In the MISMIP+ experiments, the A value suggested by Asay-Davis et al. (2016) is used, whilst in the MISMIP experiments, a series of different discrete values of A are implemented in advance and retreat stages (Sect. 4.2.5).

In the MISMIP and MISMIP+ experiments, a Weertman sliding law is used, however, three other modified power laws (Schoof, Tsai and Umbi) are also analysed in the MISMIP+ simulations. More details about the different sliding laws are given in Sect. 3.1.4. In each of the sliding laws, a spatially and temporally uniform friction coefficient C is used across the domain. The model parameters are summarized in Table 4.1.

Parameter	Value	Description
n	3	Glen's law exponent
C	1.0×10^{-3} kPa m$^{-1/3}$ a$^{1/3}$	Basal slipperiness parameter
m	3	Friction law exponent
μ_k	0.5	Coulomb coefficient of kinetic friction
g	9.81 m s^{-2}	Gravitational acceleration
a	0.3 m a^{-1}	Upper surface accumulation rate
ρ_i	918 kg m^{-3}	Ice density
ρ_s	1028 kg m^{-3}	Seawater density
S	0 m	Sea level

Table 4.1: Parameters used in the MISMIP and MISMIP+ experiments.

4.2.2 Model domain

The MISMIP+ model domain is a rectangular box, 640 km in length (x-direction) and 80 km in width (y-direction), as shown in Figure 4.1. Ice flows along a channel in the x-direction, from $x = 0$ to $x = 640$ km, where it is then removed from the domain at the fixed calving front, where ocean pressure is applied. At $x = 0$ there is a no-slip boundary condition, and at $y = 0$ and $y = 80$ km there are free-slip boundary conditions.

For the MISMIP experiments (Sect. 4.2.5), additional model simulations are carried out on domain widths of 40, 120 and 160 km. The channel width parameters (L_y and w_c) are changed accordingly, but all other model parameters remain the same as the 80 km default case.

The bedrock elevation represents a narrow, steep sided channel, and varies in both horizontal dimensions based on an earlier study by Gudmundsson et al. (2012). The elevation is given by

$$z_b(x, y) = \max\left[B_x(x) + B_y(y),\ z_{b,deep}\right], \tag{4.1}$$

where

$$B_x(x) = B_0 + B_2\tilde{x}^2 + B_4\tilde{x}^4 + B_6\tilde{x}^6 \tag{4.2}$$

$$\tilde{x} = x/\bar{x} \tag{4.3}$$

$$B_y(y) = d_c\left[\left(1 + e^{-2(y-L_y/2-w_c)/f_c}\right)^{-1} + \left(1 + e^{2(y-L_y/2+w_c)/f_c}\right)^{-1}\right] \tag{4.4}$$

The parameters in Eqs. (4.1)–(4.4) are described in Table 4.2. The bedrock elevation has a general downward slope from the ice divide ($x = 0$ km) to ice front ($x = 640$ km). There is also a shallow ridge, which causes a retrograde sloping section between $x = 390$ and $x = 506$ km. This model geometry is loosely based on the main central trunk of Pine Island Glacier, which flows along a deep channel and had been previously grounded on a subglacial ridge until earlier this century (Jenkins et al., 2010; Smith et al., 2017).

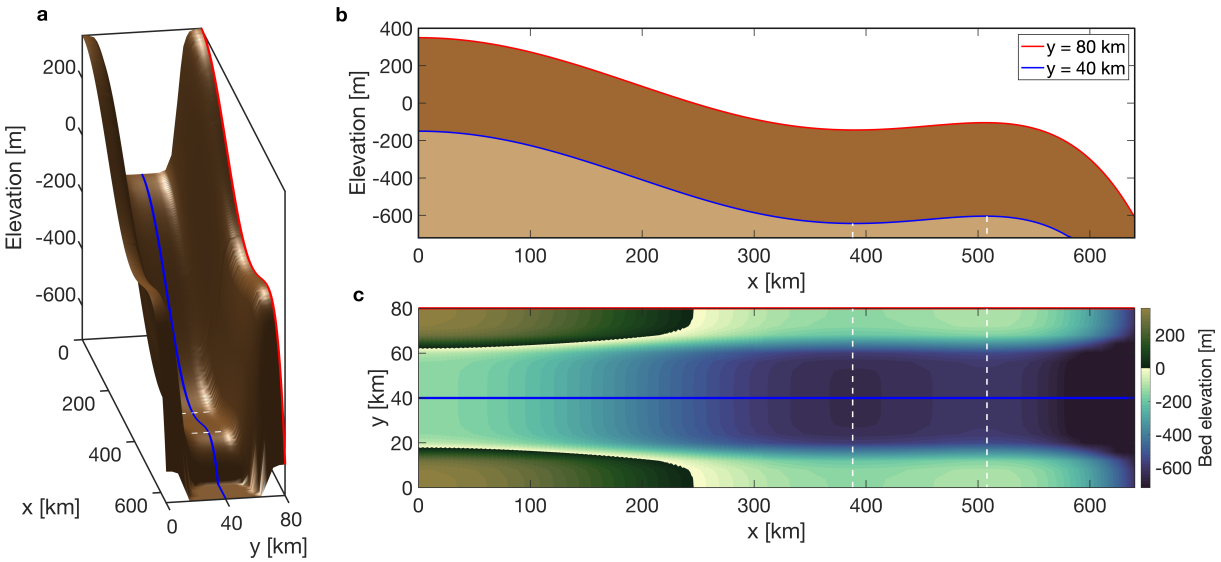

Fig. 4.1: Bedrock topography for the 80 km width MISMIP+ domain. (**a**) 3D view of the topography varying in the x and y directions, which gives a channel with high side walls, a general downward slope and an overdeepening at the lowest end. (**b**) Flowline transects through the middle $y = 40$ km (blue), and side $y = 80$ km (red) of the channel. (**c**) Plan view of the bedrock elevation. White dashed lines in all panels show the bottom and top of a retrograde slope.

Parameter	Value	Description
$z_{b,deep}$	-720 m	Maximum depth of the bedrock topography
$\bar{x}$	300 km	Characteristic along-flow length scale of the bedrock
B_0	-150 m	Bedrock topography at $x = 0$
B_2	-728.8 m	Second bedrock topography coefficient
B_4	343.91 m	Third bedrock topography coefficient
B_6	-50.57 m	Fourth bedrock topography coefficient
L_y	80 km	Width of the domain (across ice flow)
d_c	500 m	Depth of the trough compared with the side walls
w_c	24 km	Half-width of the trough
f_c	4 km	Characteristic width of the side walls of the channel

Table 4.2: Bed topography parameters used in Eqs. (4.1)–(4.4) for the standard MISMIP+ 80 km wide domain. For the other width domains in the MISMIP experiments, L_y and w_c are changed accordingly.

4.2.3 Mesh grid

In the MISMIP+ experiment, to ensure the movement of the grounding line was accurately captured a convergence analysis was carried out on the mesh resolution. Each of the meshes were generated for the entire domain using the open source Gmsh software (Geuzaine and Remacle, 2009), and were composed of linear triangular elements. A summary of the different mesh details is given in Table 4.3.

The first set of meshes have uniform sizes: 10 km, 8 km, 4 km, 2 km, 1 km. Due to computational restrictions, resolutions finer than 1 km were not possible. Therefore, to achieve finer resolution in the important grounding zone, and to run more efficiently than a uniform mesh, three additional meshes were were created with a background element size of 4 km and an additional refinement within a specified distance from the grounding line. The first is a 2 km refinement within 16 km of the grounding line. The next has a further refinement of 1 km within 8 km of the grounding line. The final mesh has another refinement level of 0.5 km within 4 km of the grounding line.

During the transient simulations, the uniform meshes were fixed and did not change in time, but the refined grounding line meshes were adapted in time to allow the refinement to follow the grounding line movement. In the refinement process, Úa interpolates the upper surface elevation, s, from the original mesh to the new mesh, and then calculates the ice thickness, h, and lower surface elevation, b, afterwards. Whilst this does not conserve the thickness, it uses the smoothness of the upper surface to avoid spurious results around bed

Name	**Background size (km)**	**Refinement size (km)** [dist to GL : refinement]	**Number of elements**	**Number of nodes**
10k	10	none	1,024	585
8k	8	none	1,600	891
4k	4	none	6,400	3,381
2k	2	none	25,600	13,161
1k	1	none	102,400	51,921
4kGL2k	4	[d16 : r2]	19,870	10,176
4kGL1k	4	[d16 : r2]; [d8 : r1]	25,586	13,029
4kGL0.5k	4	[d16 : r2]; [d8 : r1]; [d4 : r0.5]	40,582	20,528

Table 4.3: Details of the meshes with different resolutions that were compared in the MISMIP+ spin up stage. The first five are uniform and the last three have a background mesh size of 4 km and a transient refinement around the grounding line. The grounding line refinement is specified with a distance, 'd', and refinement value around the grounding line, 'r', and multiple brackets show multiple levels of refinement. The 4kGL1k mesh was used in the MISMIP experiments.

features. Although all of these meshes were used for the spin up stage of the MISMIP+ experiment, only the 4kGL1k mesh was used for the MISMIP experiments.

4.2.4 MISMIP+ experiments

The first set of experiments follow the methodology in the MISMIP+ intercomparison project (Asay-Davis et al., 2016) and were designed to investigate the impact of reduced ice shelf buttressing due to ocean-driven thinning.

Model spin up

The initial step of the MISMIP+ experiments is to have a steady state grounding line resting on the retrograde slope at $x(y = 0) = 450 \pm 10$ km. To achieve this, the model starts with a uniform ice thickness of 100 m and is run forward in time with a constant upper surface accumulation of 0.3 m a^{-1} over the entire domain, and no basal melting. The model is stopped after 10,000 years, when a steady state has been reached. The model spin up is run for all of the different mesh resolutions. The best mesh is then used for the spin up with the different sliding laws.

Following the model spin up, four experiments are carried out: control run (**Ice0**), basal melt (**Ice1r**), extended basal melt (**Ice1rr**), and no basal melt after a period of melt (**Ice1ra**). These are summarized in Table 4.4. Each of these experiments are run with four different sliding laws, as mentioned in Sect. 4.2.1.

Control run (Ice0)

The first MISMIP+ experiment is a control run (Ice0). The model starts from the final configuration of the model spin up and continues for another 100 years with no basal

Experiment	Description
Spin	Spin up of the model with no basal melt (10,000 years)
Ice0	Control run with no basal melt (100 years)
Ice1r	Basal melt run (100 years)
Ice1rr	Extended basal melt run (1000 years)
Ice1ra	100 years of basal melt + 900 years no melt (1000 years)
S-*-mis	Schoof friction with MISMIP+ melt rate
S-*-dep	Schoof friction with depth dependent melt rate

Table 4.4: Details of the MISMIP+ experiments. The first five follow the requirements of Asay-Davis et al. (2016), whilst the last two compare the different melt rate parameterizations.

melting. This is to check the initial state and ensure there is no model drift. The control run is then used as a comparison for the perturbation experiments.

Basal melting (Ice1r)

The second MISMIP+ experiment is to determine the impact of basal melting beneath the ice shelf. The spatially variable melt rate, measured as m a^{-1}, is applied across the entire shelf for 100 years (Ice1r) after the spin up phase. Then the model is run for a further 900 years to assess the impact of an extended period of melting (Ice1rr).

Following this approach, additional simulations are also run which compare two basal melt rate parameterizations. The first is from the MISMIP+ setup (Asay-Davis et al., 2016). This is dependent on ice shelf draft and water column thickness, and has a coefficient that takes into account the thermal driving and ocean friction velocity. More details about this parameterization is given in Sect. 3.4.1.

The second melt rate parameterization depends only on the ice shelf draft. This uses a simple piecewise linear function of depth, representative of ocean conditions in the Amundsen Sea. It has been used in previous ice (Favier et al., 2014) and coupled ice-ocean (Rydt and Gudmundsson, 2016) modelling studies. More details are given in Sect. 3.4.2.

Both melt rate parameterizations are applied to mesh elements that are strictly downstream of the grounding line, i.e., elements that do not contain any grounded nodes. This is to avoid melt being applied upstream of the grounding line, which can overestimate grounding line retreat if the mesh grid is not fine enough (Seroussi and Morlighem, 2018). The melt rate fields generated by the two parameterizations are shown in Fig. 4.2.

The front and sides of the ice shelf experience the lowest melt rate in both parameterizations, whilst the highest melt rates of 75 m yr^{-1} are near the grounding line over the deep bedrock. There are some key differences between the two parameterizations: (1) the MISMIP+ parameterization has a dependency on water column thickness, so the melt rate tapers to zero as the grounding line is approached; (2) the depth dependent parameterization has zero melt down to a 300 m depth; consequently, the ice shelf experiences no melt from $x = 526$ m to the ice front, where the ice shelf draft is shallower than 300 m.

Re-advance (Ice1ra)

The final MISMIP+ basal melt experiment investigates the response of the ice sheet when melting is switching off after 100 years. The model is continued for another 900 years, allowing the ice shelf to thicken. This experiment allows us to assess the rate of re-advance when the melt forcing is removed.

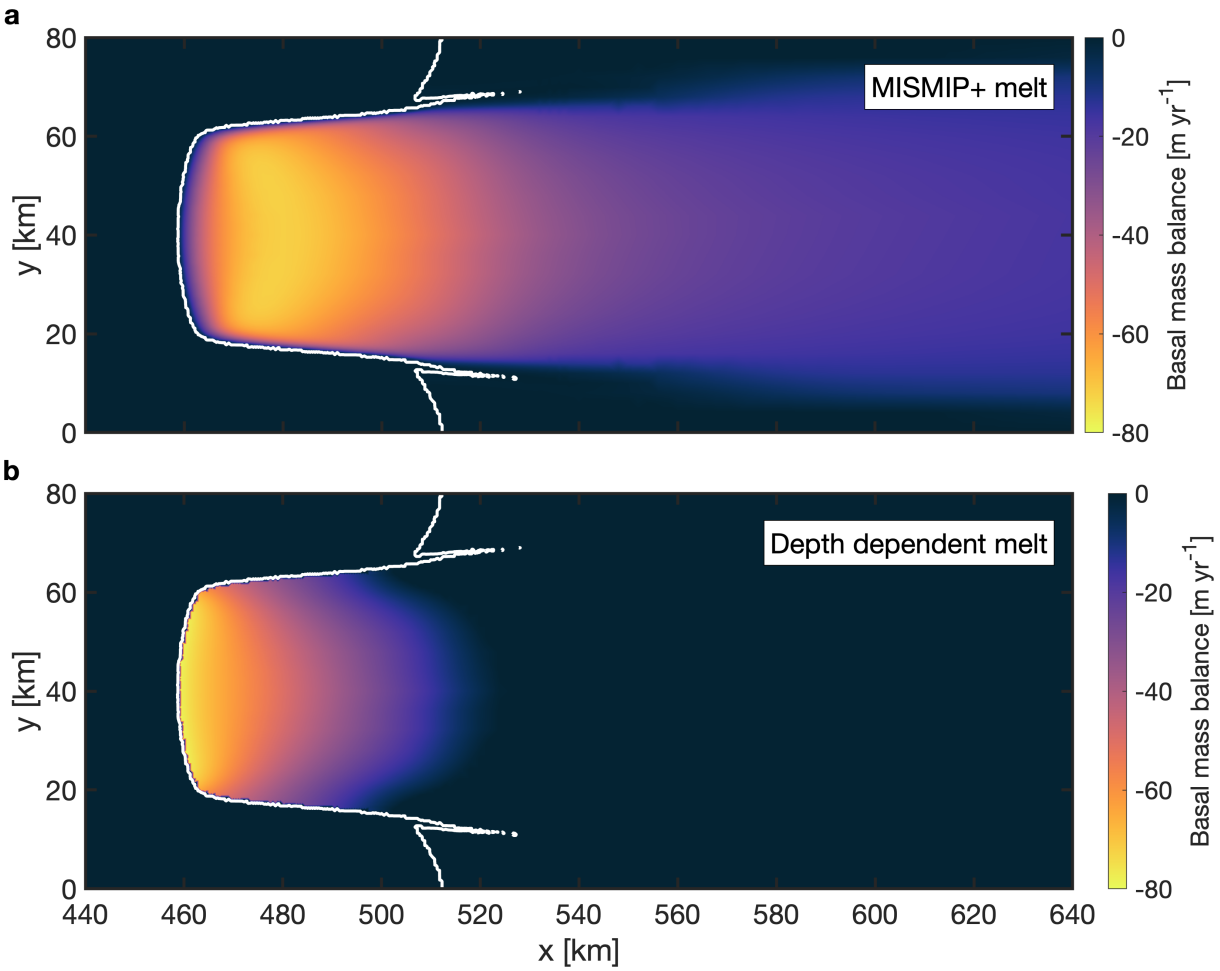

Fig. 4.2: Comparison of basal melt rate parameterizations used in the MISMIP+ Ice1r experiment. (**a**) MISMIP+ parameterization specified by Eq. 3.33. This experiment is referred to as MIS in the results section. (**b**) Depth dependent melt parameterization using a piecewise linear function. This experiment is referred to as DEP in the results section. The grounding line is shown in white.

4.2.5 MISMIP experiments

The second set of experiments in this study follows the methodology from the first marine ice sheet model intercomparison project, MISMIP (Pattyn et al., 2012), but for a two dimensional case. Here, we use the MISMIP+ geometry instead of a flowline case in the original set of experiments. In these experiments the ice softness is varied to induce advance and retreat motion across the overdeepened bed. This is to investigate whether a hysteresis is present in the system when the ice sheet is buttressed by an ice shelf. As with the MISMIP setup, the ice rate factor in Glen's flow law (Eq. 3.9) is changed to discrete values in a step-wise way, but here the experiments are not run progressively, due to computational restrictions. The ice rate factor is varied from $A = 5 \times 10^{-24}$ to $A = 5 \times 10^{-26}$ kPa^{-3} a^{-1}, which simulates a change from "soft" to "stiff" ice in an advance phase, and then reversed in a retreat phase.

These model simulations are similar to the model spin up for the MISMIP+ example described in Sect. 4.2.4. There is a constant upper surface accumulation of 0.3 m a^{-1} over the domain and no basal melting. Each model simulation was run separately for at least 10,000 years until a steady state was reached. The advance set of simulations were run from an initial ice thickness of 100 m, so that their starting grounding line was along the high side walls in the left side of the domain. The retreat simulations were all started from the final steady state configuration of the last advance run. These MISMIP experiments were also carried out for three other channel widths (40, 120 and 160 km), where the bed equation (Eq. 4.1) was adjusted accordingly.

4.3 Results

In this section the results of the MISMIP+ experiments are shown first and these are then followed by the MISMIP experiments. For the MISMIP+ section, results show the impact of mesh resolution and friction law on the model spin up and steady state position. Then the results of the control run (Ice0), basal melt (Ice1r, Ice1rr) and re-advance (Ice1ra) experiments are shown. Finally, a comparison of basal melt parameterizations is presented. In the MISMIP section, the steady state geometries for different flow rate parameters are shown, for each of the four channel widths. This is followed by a section analysing the ice shelf buttressing.

4.3.1 MISMIP+

Spin up: Mesh comparison

Figure 4.3 shows the steady state geometry after the 10,000 year spin up for different mesh resolutions. The comparison is shown for uniform meshes and mesh with grounding line refinement. In the first 2000 years, there is a rapid advance of the ice sheet for all meshes, as ice thickens with no basal melting and a constant surface accumulation. The grounding line stabilize at it reaches the retrograde slope at $x = 400$ km. After 10,000 years the model reaches a steady state with a range of central grounding line positions situated from the middle to the top of the retrograde slope. The maximum difference along the medial line ($y = 40$ km) between the steady state grounding lines is 38 km, with the least advanced (4kGL0.5k) at $x = 457$ km and the most advanced (10k) at $x = 495$ km. The grounding line appears to be converging to a similar position for the three most refined meshes (1k, 4kGL1k, 4kGL0.5k), therefore the 4kGL0.5k mesh was used for the remaining experiments.

Figure 4.4 shows the ice sheet geometry during the model spin up for the finest mesh resolution (4kGL0.5k). The model starts with an ice thickness of 100 m and an initial ice shelf forms, which is only grounded along the channel side walls. The length along the medial line of the shelf is 640 km and the length of the shelf along the edges of the domain is 340 km. After 100 years, the ice shelf grounds on the side walls at the top of the retrograde slope, and by 200 years, the ice thickens sufficiently enough at the top of the domain to fully ground across the channel. Throughout the rest of the model spin up period, the ice continues to thicken and advance, with a steepening upper surface. During this period, the grounding lines at the lateral margins gradually retreat from the prograde slope to the top of the retrograde slope. At the end of the 10,000 year spin up, the grounding line has reached a steady state position, with its central section across the middle of the retrograde slope and is most advanced along the sides of the domain at $x = 512$ km.

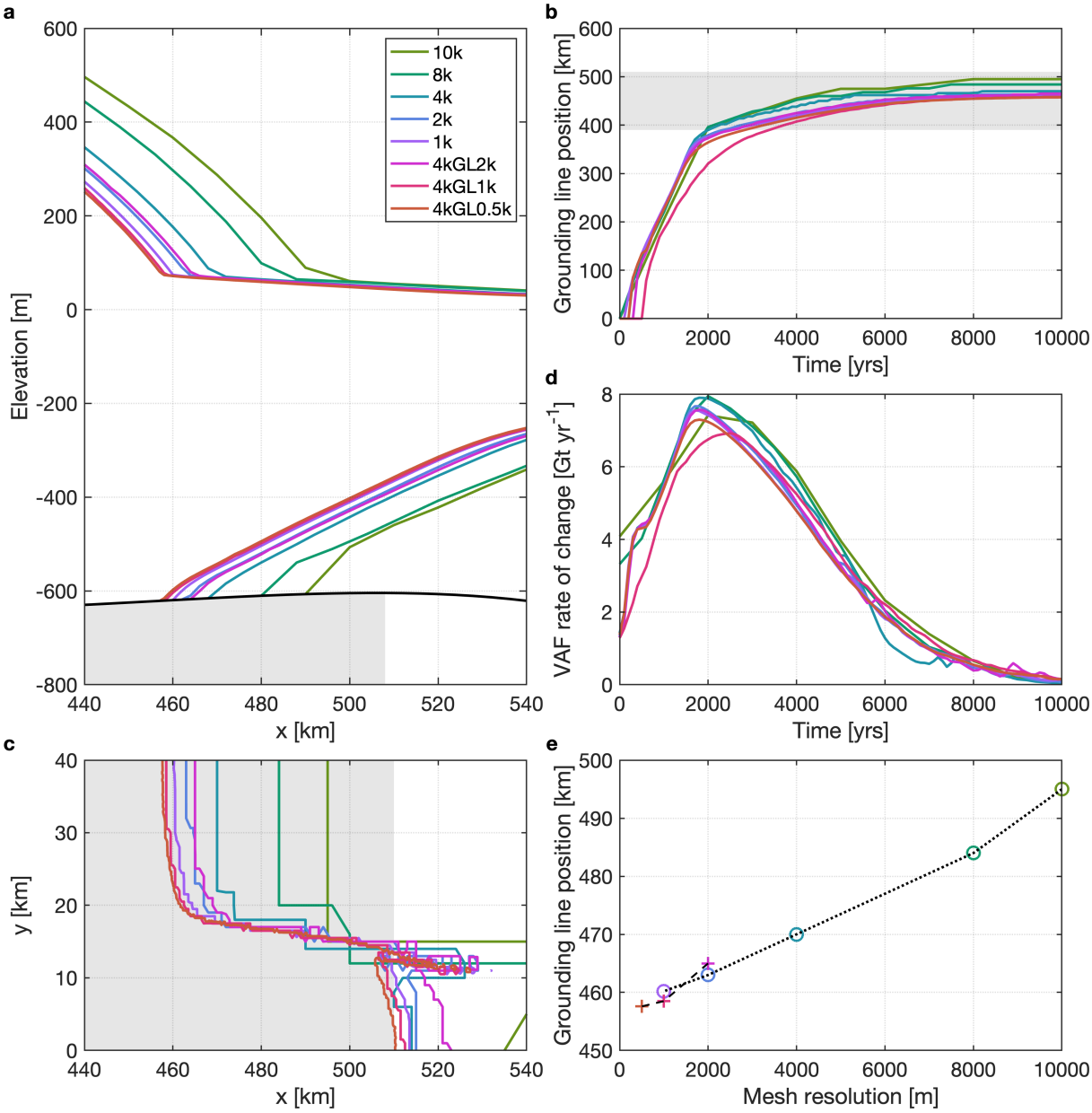

Fig. 4.3: Steady state geometry after the model spin up for meshes with different resolutions: 10k, 8k, 4k, 2k, 1k, 4kGL2k, 4kGL1k, 4kGL0.5k. The mesh details are given in Table 4.3. (**a**) Medial ($y = 40$ km) flowline profile for each mesh. Bed position is shown by the black line. (**b**) Time evolution of medial grounding lines position. (**c**) Plan view over half the channel. (**d**) Time evolution of the rate of change in volume above floatation. A value of zero indicates a steady state has been reached. (**e**) Grounding line position for each mesh resolution. Circle markers and dotted line shows the uniform meshes, whilst cross markers and dashed line shows the meshes with refinement around the grounding line. Grey shading in **a**, **b** and **c** indicates the retrograde sloping bed section.

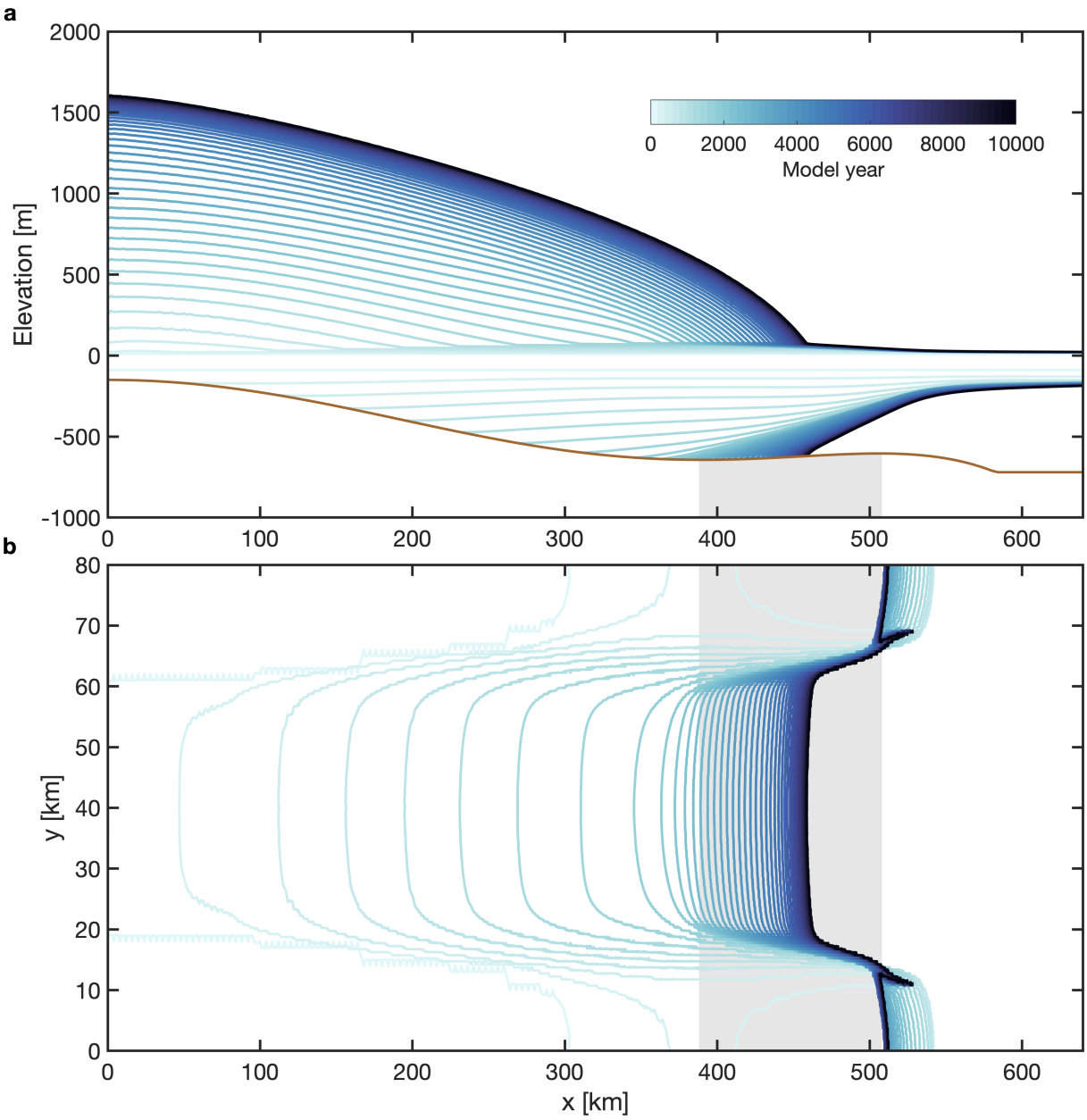

Fig. 4.4: Model spin up of 10,000 years for the mesh with a 0.5 km refinement around the grounding line. Evolution of the medial flowline profile (**a**) and plan view of the grounding line (**b**). The model results are shown for every 200 years. Grey shading indicates the retrograde sloping section of bed.

Spin up: Sliding law comparison

Figure 4.5 shows the steady state geometry after the 10,000 year model spin up for the four different sliding laws: Weertman, Schoof, Tsai and Umbi. There is a small difference between the final grounding line positions, where the Weertman power law produces the most advanced grounding line at $x = 459$ km, whilst the Tsai and Schoof modified power laws are less advanced but both produce a similar position at $x = 446$ km. The least advanced steady state grounding line position is produced by the Umbi sliding law, with $x = 443$ km. However, all sliding laws result in a central steady state grounding line across the middle of the retrograde slope.

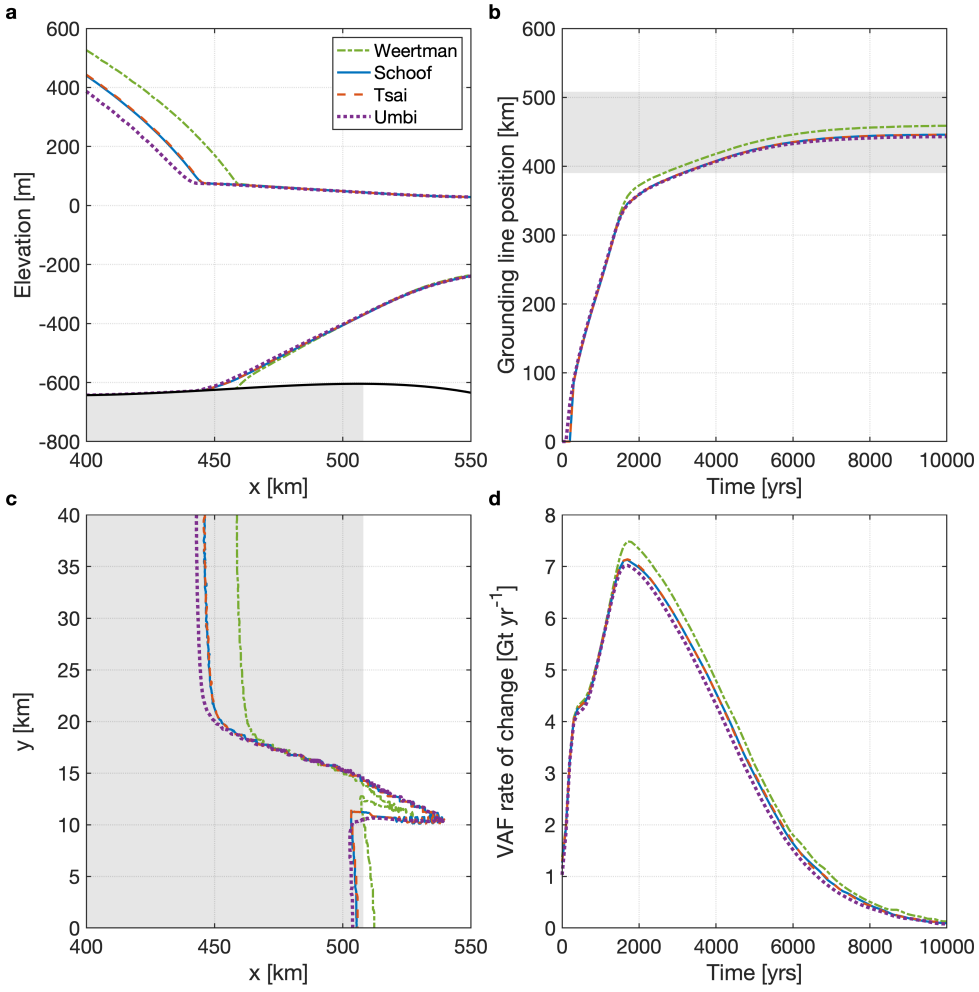

Fig. 4.5: Steady state geometry after the model spin up for different sliding laws: Weertman, Schoof, Tsai and Umbi. (**a**) Medial ($y = 40$ km) flowline profile for each mesh. Bed position is shown by the black line. (**b**) Time evolution of medial grounding lines position. (**c**) Plan view over half the channel. (**d**) Time evolution of the rate of change in volume above floatation. A value of zero indicates a steady state has been reached. Grey shading in **a**, **b** and **c** indicates the retrograde sloping bed section.

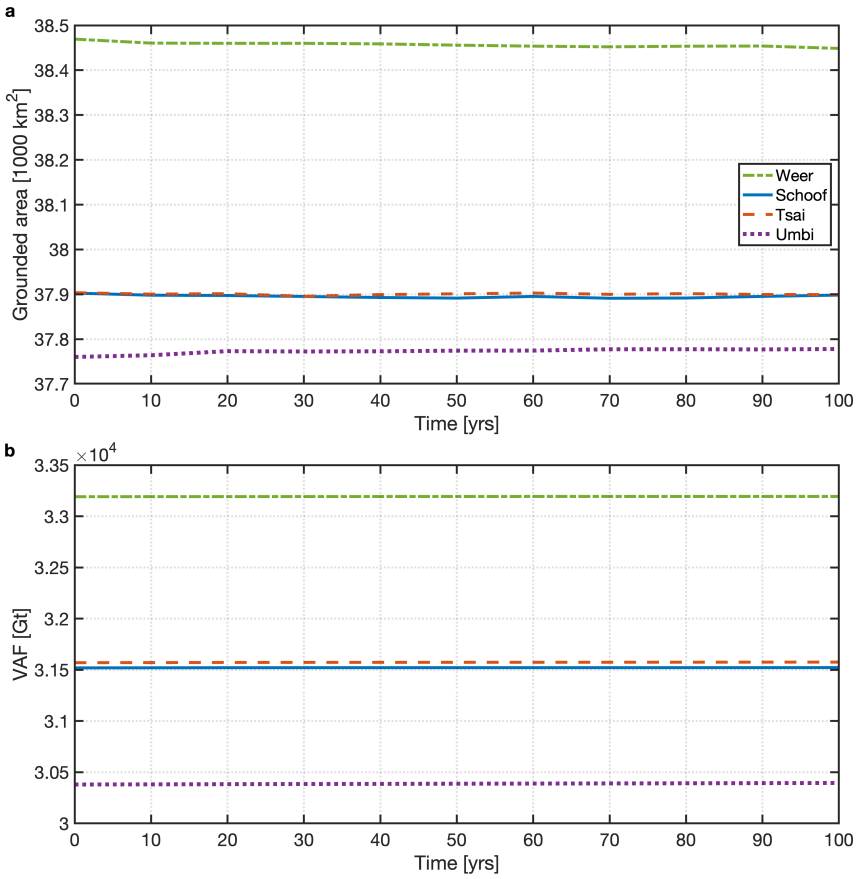

Fig. 4.6: Time evolution of the grounded area (**a**) and volume above floatation (**b**) during the control run for the four different sliding laws: Weertman (green dash-dotted), Tsai (blue solid), Schoof (orange dashed) and Umbi (purple dotted).

Control run (Ice0)

Figure 4.6 shows the result of the control run for all sliding laws, which started from their steady state configurations. At the end of the run, after 100 years of no basal melting, each of the sliding laws show very little change in grounding area and volume above floatation. The results indicate no sign of model drift and therefore can be used as control cases to compare against the perturbation experiments.

Ice1r and Ice1rr

Figures 4.7 and 4.8 show the basal melt and re-advance results for the different sliding laws. With basal melting applied for 100 years, all sliding laws produce a retreat from the initial steady state position on the retrograde slope. The model run with a Weertman sliding law retreats 39 km along the centre of the channel, and remains fully grounded on the retrograde slope. The Tsai and Schoof runs, however, retreat 63 km and the Umbi run retreats 73 km, all back onto the prograde slope. After 100 years of melting, ice shelf

thickness has halved, and its lower elevation has thinned to ∼100 m as there is no melting above this depth using the MISMIP+ melt parameterization.

The Weertman result has the slowest rate of mass loss and loses the least amount of grounded area by 100 years. At the start of the run, for all sliding laws, the ice flux across the grounding line increases sharply, from 10 Gt yr^{-1}, as the ice sheet retreats from the retrograde slope and reaches a peak at 100 years for the Umbi, Tsai, and Schoof laws. The highest ice flux after 100 years is from the Umbi result, with 47 Gt yr^{-1}, whilst the smallest is from the Weertman result with 30 Gt yr^{-1}.

When basal melt is applied for a further 900 years, the ice sheet continues to retreat for each of the sliding laws, with all of them approaching a new steady state grounding line position on the upper prograde slope. Similar to the result after 100 years, the Weertman sliding law causes the smallest overall retreat (197 km) compared to the other sliding laws, where Tsai and Schoof produce a similar retreat of 227 km, and Umbi retreats the most with 238 km.

After 100 years of melting, the grounding line ice flux for the Tsai, Schoof and Umbi results all gradually decrease until the end of the simulation, as the ice sheet retreats from the base of the prograde slope. In contrast, ice flux in the Weertman run continues to increase after 100 years, reaching a maximum of 32 Gt yr^{-1} at 250 years as it retreats from the retrograde slope. After 250 years, similar to the other results there is a gradual decrease until the end of the simulation.

During the extended period of melt, as the ice sheet retreats up the prograde slope after 100 years (Tsai, Schoof and Umbi) and 250 years (Weertman) years, the grounding line flux decrease is at a slower rate compared to the increase in the initial 50 years. The final ice flux, for all sliding laws, is higher than the starting steady state configuration.

Ice1ra

For all sliding laws, when the basal melt is switched off after 100 years and the model is run for a further 900 years, the ice sheet thickens and advances forward to the retrograde slope. However, all final grounding lines, which are close to a steady state, fail to recover their starting positions. There is a 7 km difference for the Weertman result, 13 km for Tsai and Schoof, and 15 km for Umbi.

When basal melting is stopped after 100 years, the grounding line ice flux immediately decreases at a fast rate for all sliding laws. By 200 years, the flux is almost back to the initial steady state value of 10 Gt yr^{-1}. Throughout the rest of the simulation, the ice flux continues to decrease at a much slower rate until a minimum around 500 years, and then increases gradually until the end of the run. The final grounding line flux is less than the initial steady state for all sliding laws.

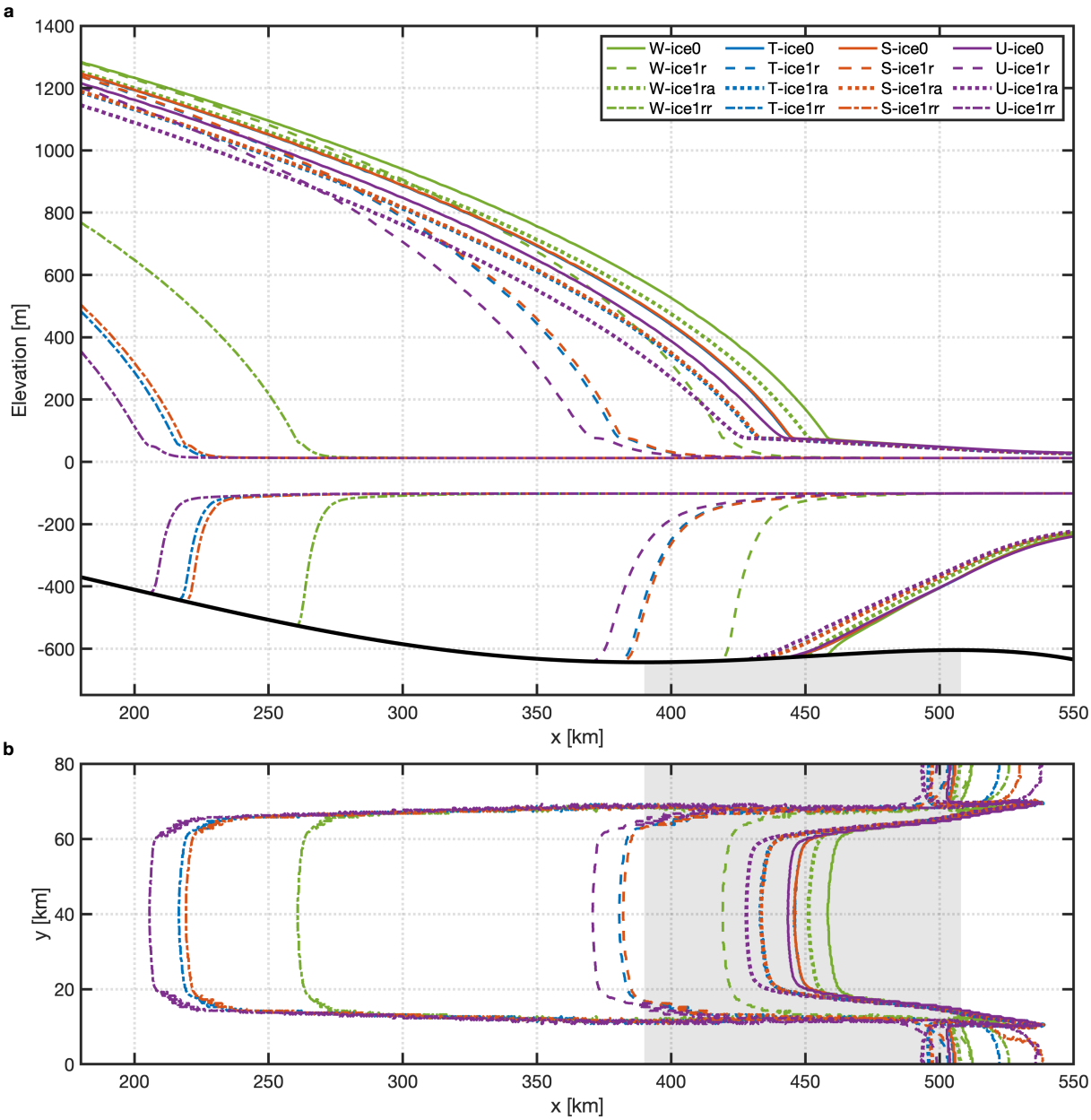

Fig. 4.7: Medial flowline profiles (**a**) and plan view grounding line position (**b**) during the MISMIP+ experiments for each of the sliding laws: Weertman (green), Tsai (blue), Schoof (orange) and Umbi (purple). Both panels show the results at the end of the Ice0 (solid line), Ice1r (dashed), Ice1ra (dotted) and Ice1rr (dash-dotted) experiments. The grey shading indicates the retrograde sloping section of bed and the black line in **a** shows the position of the bed.

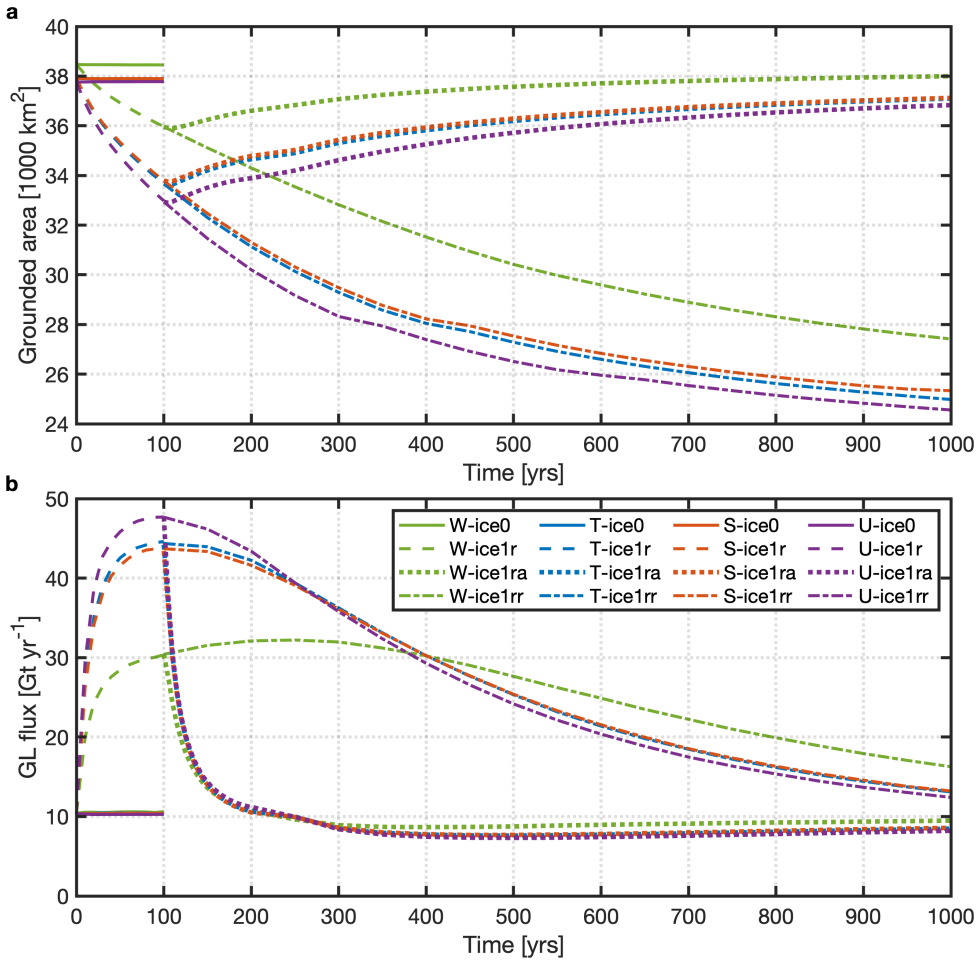

Fig. 4.8: Time evolution of grounded area (**a**) and ice flux across the grounding line (**b**) during the MISMIP+ experiments for each of the sliding laws: Weertman (green), Tsai (blue), Schoof (orange) and Umbi (purple). Both panels show the results during the Ice0 (solid line), Ice1r (dashed), Ice1ra (dotted) and Ice1rr (dash-dotted) experiments. Note, the panels do not show the full domain extent in the x-direction.

Melt parameterization comparison

Figures 4.9 and 4.10 show the basal melt and re-advance results for the two different melt parameterizations using the Schoof sliding law. The MISMIP+ result will be referred to as MIS and the depth dependent melt rate referred to as DEP. At the start of the run, thinning of the ice shelf causes a retreat in both simulations and a rapid increase in ice flux across the grounding line. After 100 years of melting, the ice flux has reached a peak in both results, but the MIS result is more than double the DEP result. Furthermore, the MIS result retreats onto the prograde slope to $x = 380$ km, whilst the DEP result remains grounded on the retrograde slope at $x = 422$ km.

A further 900 years of melting causes more retreat in both simulations, however, the MIS result retreats much further to $x = 216$ km whilst the DEP result only retreats to

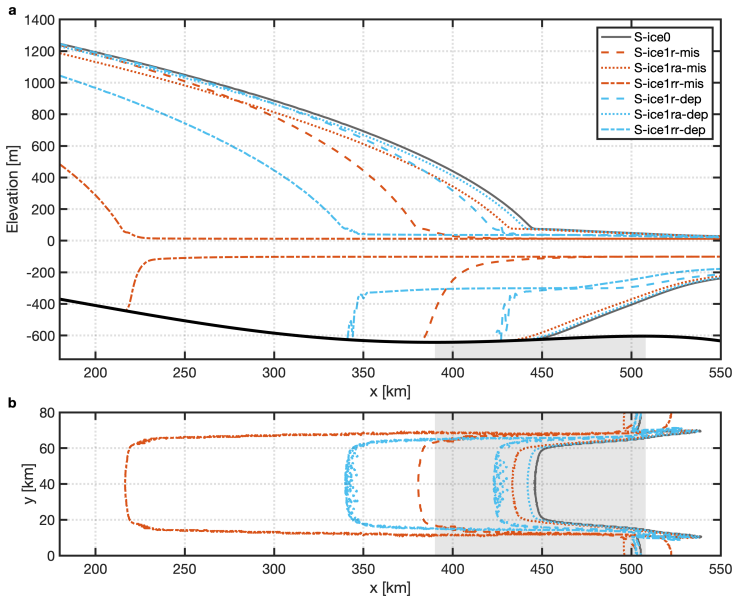

Fig. 4.9: Medial flowline profiles (**a**) and plan view grounding line position (**b**) for the MISMIP+ melt parameterization (orange) and the depth dependent parameterization (blue), both using the Schoof sliding law. Both panels show the results at the end of the Ice0 (solid line), Ice1r (dashed), Ice1ra (dotted) and Ice1rr (dash-dotted) experiments. The grey shading indicates the retrograde sloping section of bed and the black line in **a** shows the position of the bed.

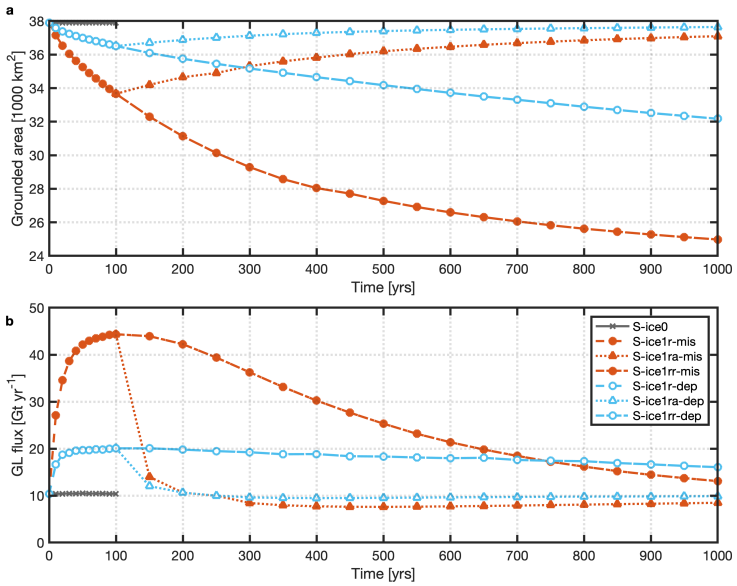

Fig. 4.10: Time evolution of grounded area (**a**) and ice flux across the grounding line (**b**) for the MISMIP+ melt parameterization (orange) and the depth dependent parameterization (blue), both using the Schoof sliding law. Both panels show the results during the Ice0 (solid line), Ice1r (dashed), Ice1ra (dotted) and Ice1rr (dash-dotted) experiments. To aid visualization, open markers are used for the depth dependent parameterization.

$x = 340$ km. There is more thinning in the MIS experiment, with an ice shelf that is less than half of its original thickness at the ice front, and less than half the thickness of the DEP result at the grounding line.

In the re-advance simulations, both parameterizations cause a thickening and advance back to the retrograde slope, however, they fail to recover their original starting positions, by a difference of 5 km in the DEP experiment and 13 km in the MIS experiment. When the melt is removed after 100 years, the ice flux in both simulations immediately decreases and by 200 years has decreased to its starting value of 10 Gt yr^{-1}. By the end of the simulation, the grounding line ice flux in the DEP result remains close to its starting value (10 Gt yr^{-1}), whilst the MIS result is 8 Gt yr^{-1}.

4.3.2 MISMIP

Figures 4.11–4.14 show the results of the MISMIP experiment for four different channel widths. In all four cases, the steady state grounding line position for the first ice rate factor value of $A = 5 \times 10^{-24}$, which corresponds to the softest or warmest ice, is between the middle and top of the prograde slope ($x = 156$ to 215 km). The ice front thickness at the end of this first simulation is 110 m for each channel width, and ice thickness at the grounding line ranges from 350 m to 500 m. As the ice rate factor is gradually reduced, representing the ice becoming colder and stiffer, the ice sheet thickens and advances further than in the previous steady state. The most advanced grounding line in all cases is produced with an ice rate factor of $A = 5 \times 10^{-26}$, and is located on the downstream prograde slope of the overdeepening. At this largest ice sheet extent, the ice front thickness ranges from 430 to 466 m and the grounding line thickness ranges from 750 m to 790 m.

In the retreat phase, as the ice rate factor is increased again, the ice sheet becomes thinner and the steady state grounding lines migrate back towards the initial starting position on the upstream prograde slope. In each of the four cases, there are steady state grounding lines positions found on all bed slopes, for each of the different A values in the advance and retreat phases.

Hysteresis

Several values of A can produce unique equilibrium positions in both the advance and retreat phases, e.g., $A = 5 \times 10^{-24}$, $A = 1 \times 10^{-24}$ and $A = 5 \times 10^{-25}$. However, there are also some values of A for which the advance and retreat steady state positions differ. This shows the presence of hysteretic behaviour for each of the four channel widths, in which multiple steady states can exist for the same value of A. The presence of a hysteresis loop indicates that there are two stable branches, which all steady states are

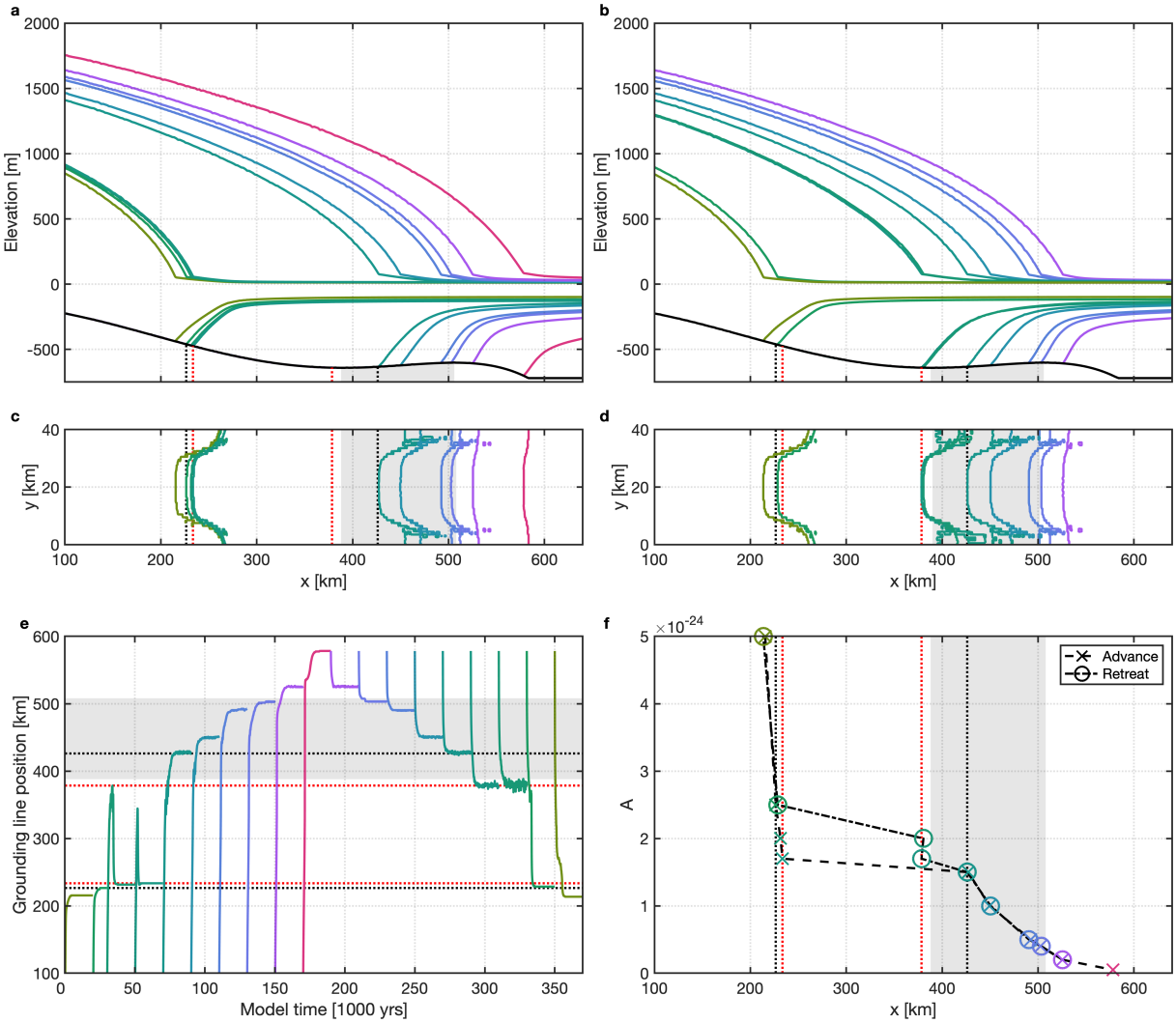

Fig. 4.11: Steady state geometry for the MISMIP 40 km experiment. Medial flowline (**a**, **b**) profiles and plan view of the grounding line (**c**, **d**) during the advance (**a**, **c**) and retreat (**b**, **d**) phases. (**e**) Time evolution of the grounding line position for each model simulation. For ease of visualization, the simulations are shown sequentially, but this is not how they were run, they were all run for 20,000 years individually. (**f**) Steady state grounding line position for each value of A. For ease of visualization, cross markers and dashed lines show the advance phase, and circle markers with the dash-dotted line show the retreat phase. The lines joining the markers are for visualization purposes only and do not show the steady state positions. The coloured lines in all panels correspond to a unique value of A which is shown in panel **f**. The grey shaded region indicates the retrograde sloping section of bed. The black dotted lines show the outer region of the hysteresis loop, as determined by panel **f** and the red dotted lines show the inner region of the hysteresis loop.

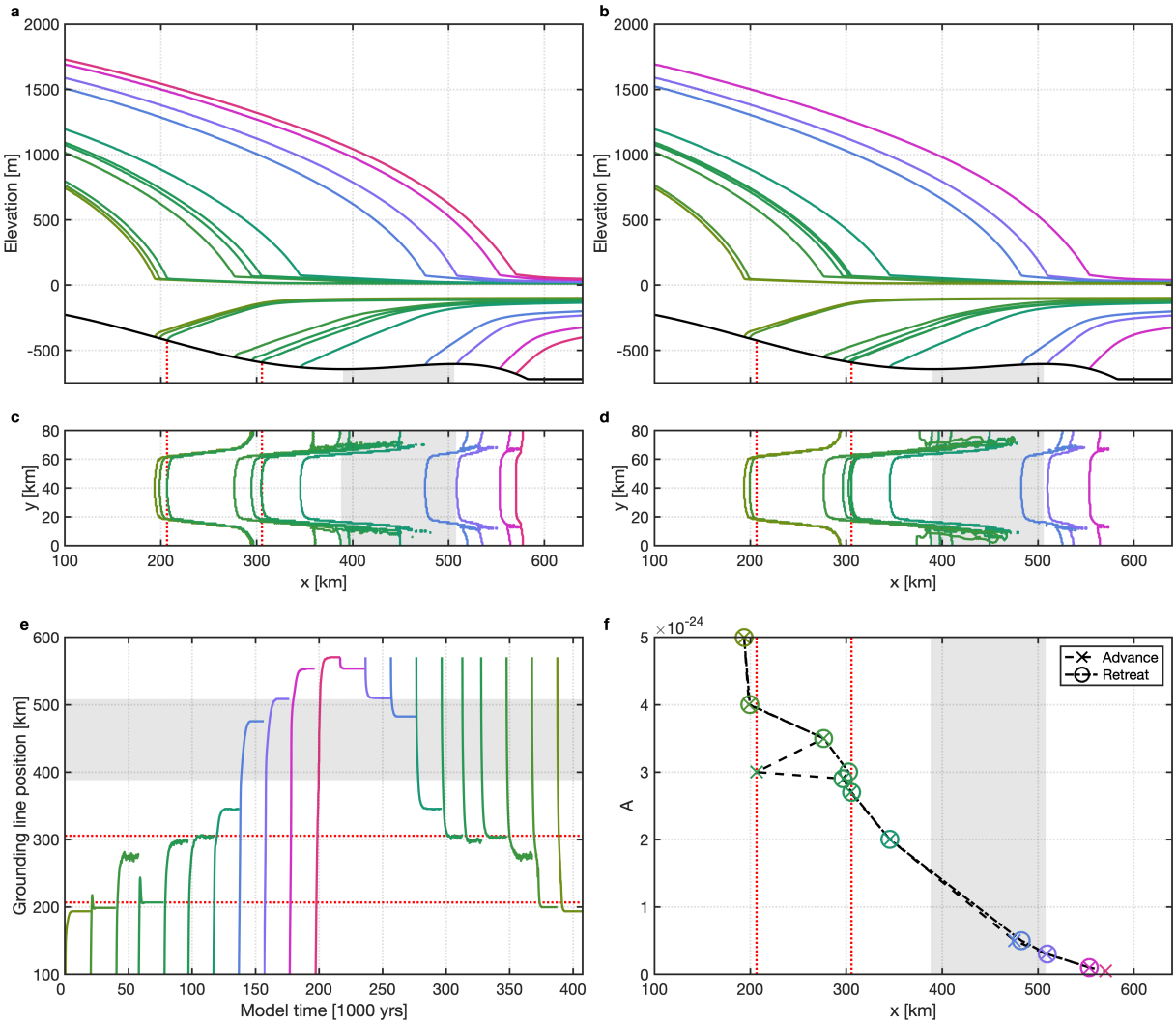

Fig. 4.12: Same as Fig. 4.11 but for the 80 km wide domain. However, there are no black dotted lines here because the outer region of the hysteresis loop is not clear.

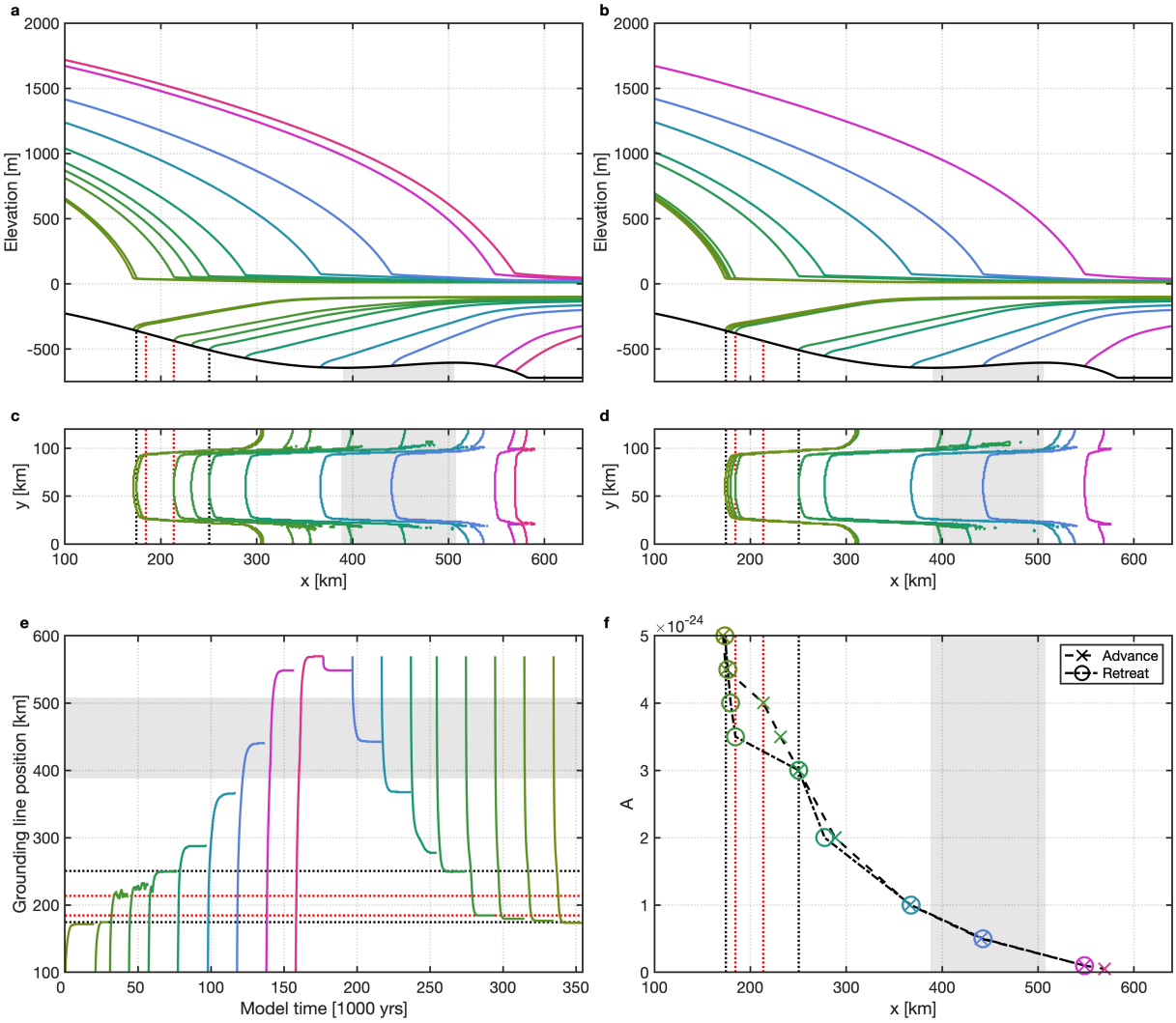

Fig. 4.13: Same as Fig. 4.11 but for the 120 km wide domain.

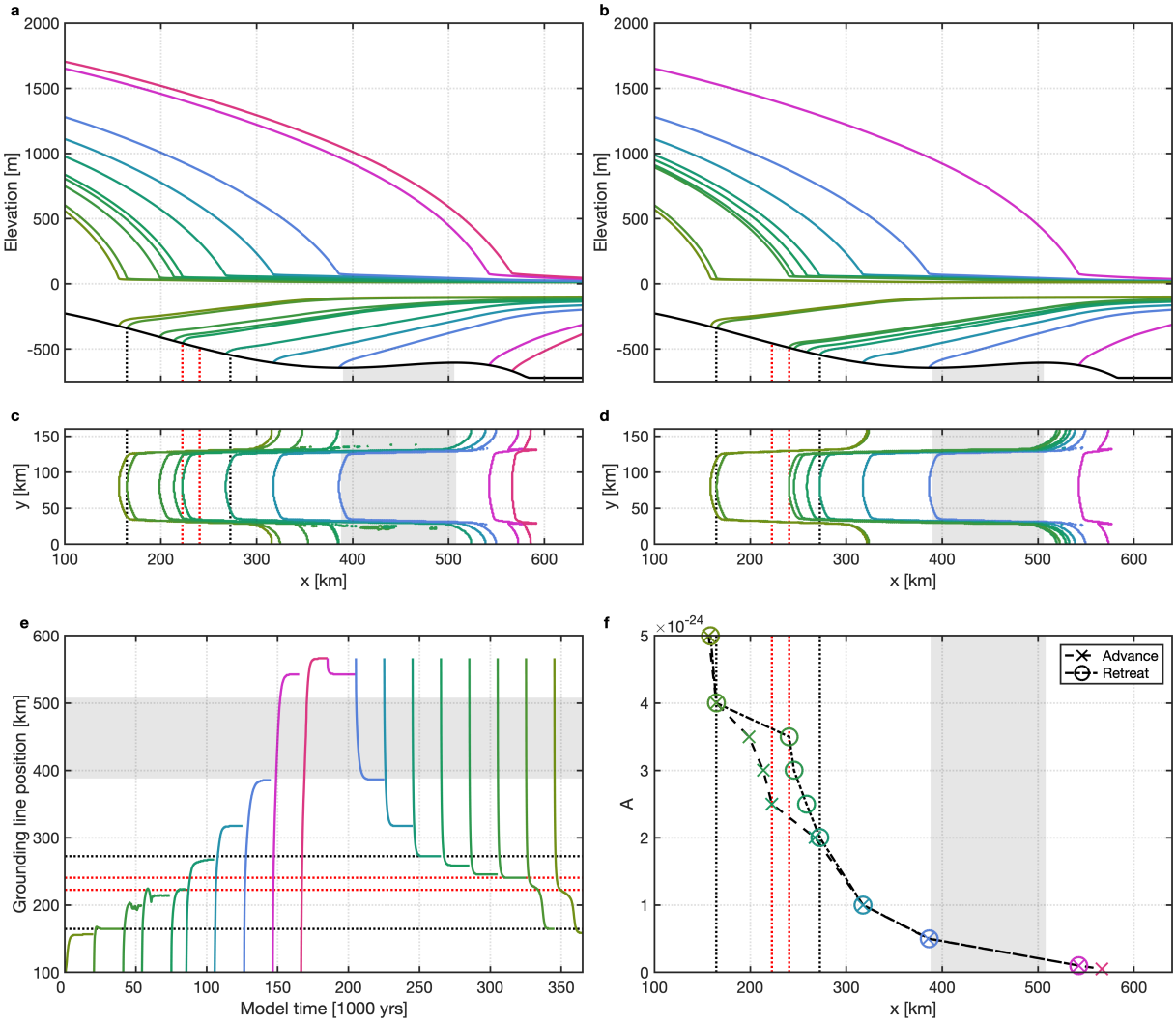

Fig. 4.14: Same as Fig. 4.11 but for the 160 km wide domain.

situated along, and an unstable region in between two tipping points. If the value of A crosses a tipping point, the ice sheet will undergo an irreversible switch from one stable branch to the other. The first stable branch corresponds to simulations which start from the upstream prograde position and advance forward, whilst the other stable branch corresponds to model simulations that start from the maximum downstream prograde position and retreat backwards. As the channel width increases, the location of the tipping points change, generally moving upstream, and the size of the hysteresis loop or unstable region becomes narrower.

In all four channel widths, when the value of A is close to a tipping point, there are several instances of the grounding line showing unusual behaviour (panel **e** in Figs. 4.11 to 4.14). Firstly, there are some spikes in grounding line position in the advance phase for the narrower channels. Here, some values of A are causing the ice sheet to initially advance forward, but then stop and retreat back again, before reaching a new steady state. This is discussed further in the next section. In other cases, for both the advance and retreat phases, the grounding line appears to reach a semi-steady state where its mean position remains the same but it fluctuates until the end of the simulation. These fluctuations are as large as 15 km in the narrowest channel. This may be a sign of critical slowing down that has been discussed in previous ice sheet tipping point experiments (Rosier et al., 2021).

Ice shelf buttressing

The results in the previous section highlighted several instances of the ice sheet advancing forward before stopping and retreating again for the same value of A. An example of this is shown in Fig. 4.15. The ice sheet starts from an upstream position, grounded only along the high side walls. As the model is run forward in time, the ice sheet steadily thickens and advances forward, before stabilizing near the base of the retrograde slope after 2000 years. Over the next 2500 years the ice sheet grounding line fluctuates in this position, reaching a maximum extent at 4000 years, and appearing to reach a new semi-steady state, similar to other examples as mentioned in the previous section. However, after 4600 years the ice sheet undergoes a large and rapid change in position, retreating from $x = 337$ km to $x = 288$ km in 100 years. After this, the ice sheet continues to retreat until it finds a new steady state midway along the upstream prograde slope ($x = 231$ km).

During the period that the ice sheet is advancing, the ice shelf area decreases because the calving front remains in a fixed position. Because of this, the ice shelf buttressing capacity is reduced. Figure 4.16 shows the degree of buttressing that is being provided by the ice shelf, as well as ice flux across the grounding line during the simulation. The normal buttressing number, K_N, is a measure of the impact that an ice shelf has on the

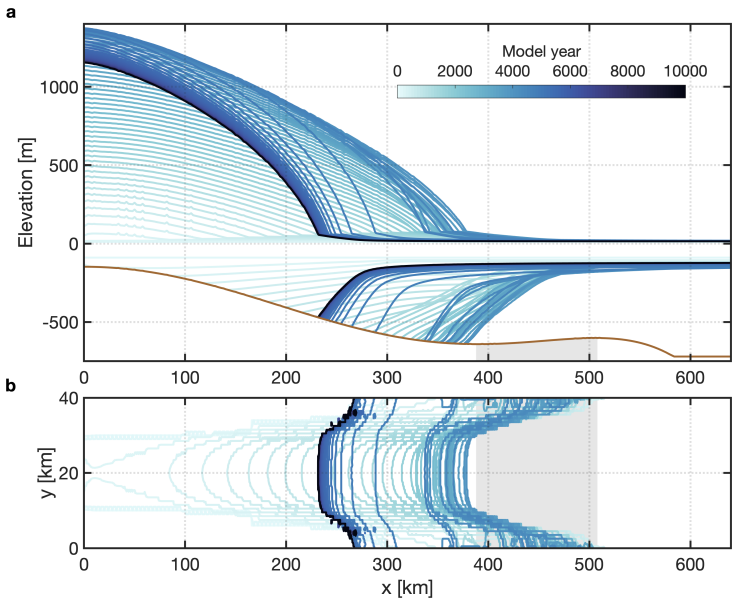

Fig. 4.15: Evolution of the 40 km wide ice sheet as it advances forward, for every 100 years. Between 4000 and 5000 years the ice sheet reaches its furthest position and starts to retreat.

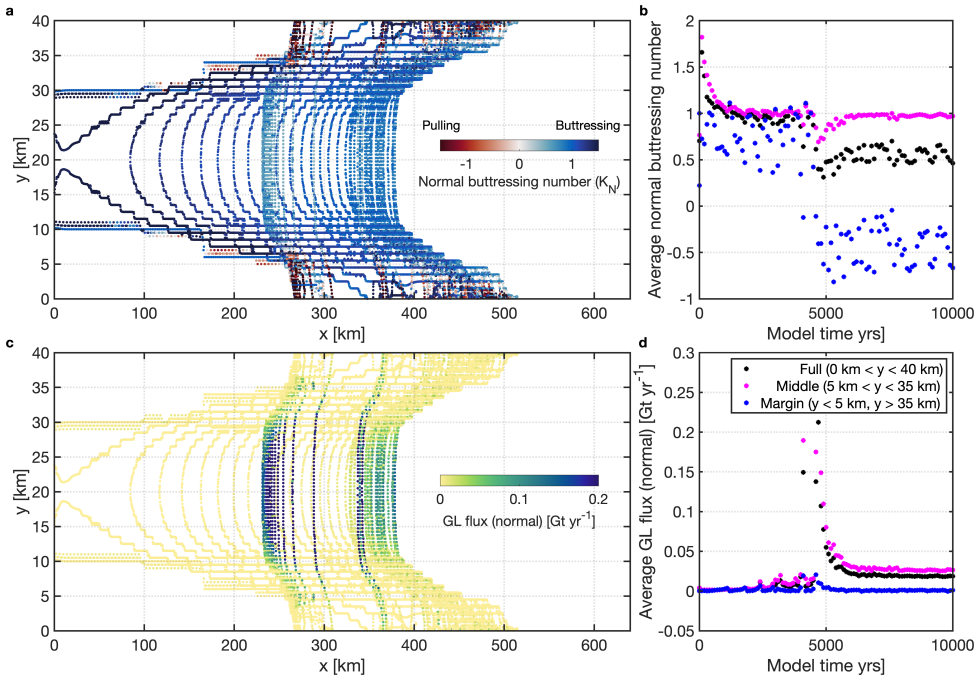

Fig. 4.16: Ice shelf buttressing response as the 40 km wide ice sheet advances forward. (**a**) Each dot shows the normal buttressing number, κ_N, along the grounding line for every 100 years. For $K_N > 0$, the ice shelf is considered to be buttressing upstream ice. For $K_N < 0$ the ice shelf can be thought of as pulling the ice at the grounding line. (**b**) Grounding line average normal buttressing number during the simulation for the full width (black), middle section (magenta) and margins (blue). (**c**) Each dot shows the ice flux normal to the grounding line for every 100 years. (**d**) Grounding line average normal ice flux during the simulation for the full width (black), middle section (magenta) and margins (blue).

stress balance at the grounding line (Gudmundsson, 2013). A value of $K_N > 0$ indicates where the ice shelf is buttressing upstream ice, whereas $K_N < 0$ shows where ice is being 'pulled' at the grounding line by the ice shelf.

In the first 4000 years, $K_N \sim 1$ around most of the grounding line and therefore the ice shelf is buttressing upstream ice and this allows the ice sheet to thicken and advance. However, after 4000 years, there is a decrease in buttressing, where $K_N \sim 0.5$ across the full grounding line, and there is a corresponding increase in ice flux. This is driven by a substantial decrease in buttressing at the ice sheet lateral margins, where $K_N < 0$, which implies those areas of the ice shelf are no longer buttressing upstream ice, but are facilitating the flow. With reduced buttressing, and increased ice flux, the ice sheet thins and retreats from its position downstream, and does not recover. This behaviour of advancing and then retreating over a considerable distance is only observed in the narrower channels, implying that shear margins have less influence on mass balance as the channel widens.

4.4 Discussion and conclusion

The aim of this chapter is to investigate the response of an idealized buttressed marine ice sheet to changes in external forcing and modelling parameters. Consequently, two sets of experiments were carried out, following the approach of previous ice sheet modelling intercomparison projects (Asay-Davis et al., 2016; Pattyn et al., 2012). The interesting feature of the geometry used in these experiments was the steady state grounding line position on a retrograde slope, which is only possible in a two-horizontal ice sheet if there is sufficient ice shelf buttressing. Therefore, the experiments were designed to assess the impact that changing forcing has on the buttressing capacity of ice shelves for an sheet grounded on a retrograde slope.

4.4.1 MISMIP+

The first set of experiments followed the approach of the most recent ice sheet model intercomparison project, MISMIP+ (Asay-Davis et al., 2016), and investigated the impact of basal melting on the ice shelf buttressing capacity. The initial mesh sensitivity analysis agrees with other studies, which show that a finer resolutions around the grounding is required to accurately model grounding line movement (Cornford et al., 2013; Seroussi and Morlighem, 2018). The model spin up with mesh resolution of 1 km or less were sufficient, and showed a convergence of grounding line position. This has also been shown with the results from other ice sheet models running the MISMIP+ experiments (Cornford

et al., 2020).

The choice of friction law which controls how basal traction is applied at the bed has been shown to influence the degree of mass loss in idealized and realistic model simulations (Brondex et al., 2017, 2019; Seroussi and Morlighem, 2018; Yu et al., 2018). Results given here support this and show that the different friction laws affect the initial steady state and how the ice sheet responds to a loss of buttressing. The Weertman friction law produced the most advanced ice sheet, whilst Umbi produced the smallest. The Tsai and Schoof laws resulted in similar steady state geometries between the Umbi and Weertman results.

Producing a steady state ice sheet on a retrograde slope is only possible due to buttressing from the ice shelf. However, when basal melting is applied beneath the shelf during the Ice1r and Ice1rr experiments, the ice sheet retreats due to the loss of buttressing and an increase in ice flux across the grounding line. Seroussi and Morlighem (2018) show the importance of refined mesh around the grounding line during these MISMIP+ melting experiments. When using the Weertman friction law, a resolution of less than 500 m is required if applying melt over partially floating elements. Due to computational limitations here, the model simulations in this chapter used a minimum mesh refinement of 500 m; however, melt is only applied to fully floating elements in the model, so this mesh size is sufficient for both Weertman and Tsai friction laws.

In the Ice1r and Ice1rr basal melting experiments the Weertman friction law causes the least amount of mass loss and has a mean rate of retreat of 0.4 km yr^{-1}. The Tsai and Schoof friction laws caused the next largest mass loss, and had similar retreat rates of around 0.6 km yr^{-1}, whilst the Umbi law causes the most mass loss, with a retreat rate of 0.7 km yr^{-1}. These rates of retreat are similar to other MISMIP+ model results (Cornford et al., 2020), and agree with other studies that show the Weertman friction law causes the least mass loss compared to other laws (Brondex et al., 2017; Yu et al., 2018).

When basal melting is removed after the ice sheet has retreated for 100 years, there is a delayed response from the ice sheet as it adjusts to the new forcing. Initially the ice sheet continues to retreat, but after 10 years it stops and starts to advance as the ice sheet thickens. The increased ice shelf thickness aids its buttressing ability, which leads to a decrease in grounding line ice flux for all sliding laws. This allows the ice sheet to re-advance towards its original starting position. After 30 years of no melting the ice sheet advances past its original 100 year retreat position. However, the rate of advance is much slower compared to the original retreat. The Weertman friction law advances at 0.03 km yr^{-1}, one order of magnitude smaller than its retreat rate. Similarly, for Tsai and Schoof (0.05 km yr^{-1}), and Umbi (0.06 km yr^{-1}). The final grounding line positions after re-advance of 900 years fails to recover the original steady state position on the retrograde

slope. This implies that more mass is lost at the margins after 100 years than can be replaced by upper surface accumulation over the entire domain for 900 years.

Melt parameterization comparison

Another set of experiments were carried out with the MISMIP+ geometry to compare two different basal melt rate parameterizations. The first parameterization (MIS), given in the MISMIP+ setup, has a dependency on ice shelf draft and water column thickness, and has a coefficient that takes into account the thermal driving and ocean friction velocity (see Sect. 3.4.1). The second parameterization (DEP) is a piecewise linear function of depth, which has been based on typical ocean temperature profiles from the Amundsen Sea (see Sect. 3.4.2).

Results in this chapter show that the MIS parameterization causes substantially more mass loss and retreat compared to the DEP parameterization (Figs. 4.9 and 4.10). In the MIS parameterization there is a tapering of the melt rate to zero at the grounding line, whereas this is where the highest melt is found for the DEP parameterization. Although this region is considered to provide much of the buttressing to upstream ice (Fürst et al., 2015; Reese et al., 2018a), it is possible that a higher integrated melt rate over the outer shelf is the dominant factor in the mass balance (Fig. 4.2).

A further possible explanation of increased mass loss in the MIS case compared to the DEP parameterization is illustrated in figure 4.17. This shows a comparison of the basal melt at the start of the simulation and after 10 years. Along the grounding line of the ice shelf shear margins, there are higher basal melt rates in the MIS experiment compared to the DEP result. This can also be seen in the average melt rates in the margins throughout the rest of the simulation, where the melting in MIS experiment is twice that in the DEP experiment. This implies that melting in the shear margins could be having a greater impact on mass loss compared to melting along the central grounding line. This agrees with the MISMIP+ results from Feldmann et al. (2022) and the adjoint melt rate sensitivities shown by Goldberg et al. (2019).

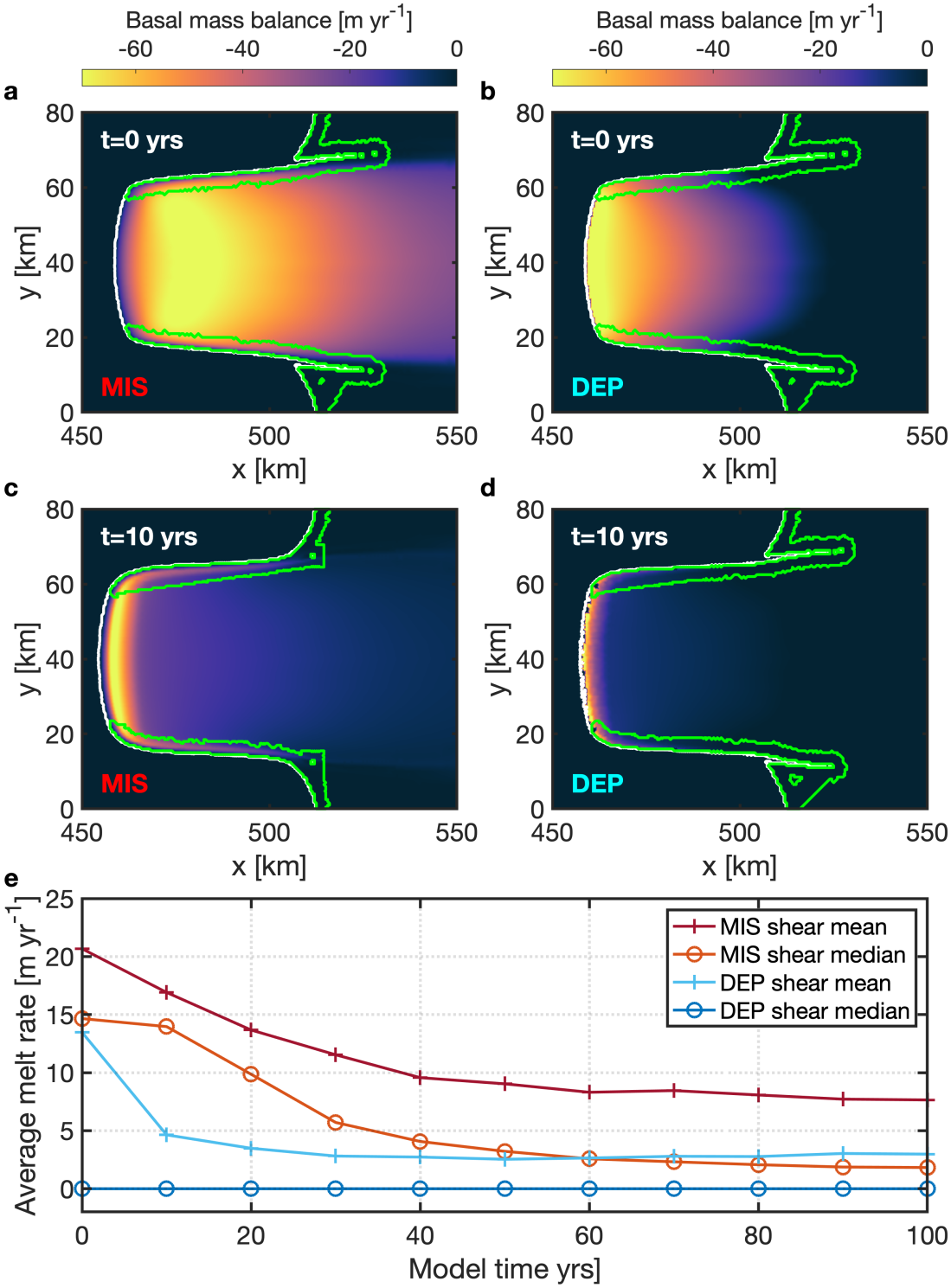

Fig. 4.17: Basal mass balance after $t = 0$ (**a**, **b**) and $t = 10$ (**c**, **d**) years in the Ice1r experiment, using the MIS (**a**, **c**) and DEP (**b**, **d**) parameterizations. The green lines around the shear margins indicate the regions used in the average melt calculation in **e**. (**e**) Average melt rates in the shear margins for the both parameterizations. Note, for visualization purposes, the average melt rates are shown in **e** rather than basal mass balance.

4.4.2 MISMIP

The final set of experiments shown in the chapter follow the approach of the first MISMIP exercise (Pattyn et al., 2012) which was to investigate the reversibility of an ice sheet. They show that by changing the ice softness parameter, a series of steady state ice sheet geometries can be generated throughout the domain. In their study, they find that due to the presence of an overdeepened bed, this leads to a hysteresis, with an unstable region over the retrograde slope, which is in agreement with the theory of MISI (Schoof, 2007a; Weertman, 1974). In this thesis chapter, those experiments from Pattyn et al. (2012) were repeated but using the three dimensional MISMIP+ geometry, which includes the effects of ice shelf buttressing. This has previously been shown to permit a stable equilibrium when a grounding line is situated on a retrograde bed (Gudmundsson et al., 2012).

Results show that in the presence of ice shelf buttressing, several examples of steady state grounding lines are possible on the retrograde sloping bed, for four different channel widths (Figs. 4.11– 4.14). When the ice softness parameter is varied, an ice sheet advances and retreat across the overdeepened bed, and leads to a hysteresis. However, the unstable region region is now not located on the retrograde slope, but instead on the prograde slope, and moving upstream as the channel widens. An in depth analysis of what is causing this behaviour was beyond the scope of this chapter, but initial tests show there is a loss of buttressing at the margins when grounding lines begin to stabilize in the unstable region. This further confirms that the shear margins are an important part of the buttressing control in this channel geometry.

Although these are just four example geometries, they show the influence of ice shelf buttressing, especially in the shear margins. Due to computational resources, the model simulations were only run to a maximum of 20,000 years. To improve these results the experiments could be run for longer to more closely approach a steady state with each value of A. Furthermore, it would be useful to have steady state geometries for more values of A, to get a more complete picture of the hysteresis loop and unstable region.

4.4.3 Lessons learnt

There have been many studies on MISI, from the theoretical concepts (Schoof, 2007a; Weertman, 1974) to ice sheet modelling experiments for idealized Pattyn et al., 2012 and realistic geometries (Favier et al., 2014; Joughin et al., 2014; Rosier et al., 2021). From the existing body of work we know that marine ice sheets can undergo irreversible phases of advance and retreat across retrograde sloping beds when there is no ice shelf buttressing. Conversely, if an ice shelf can provide enough back stress, then a stable grounding line can be supported in this previously unstable scenario (Gudmundsson et al., 2012).

The experiments presented in this chapter agree with, and build on, the results from previous studies. It was shown here that for a number of ice sheet configurations, stable grounding lines were located on retrograde slopes. However, when the ice shelf buttressing was altered through a weakening (strengthening) of the ice, this lead to irreversible phases of retreat (advance). The channel width was also varied which impacted the transient behaviour of the ice sheet and the locations of irreversible transition. For the examples showed here, the hysteresis loop, where the ice sheet transitioned from one stable state to another, occurred off the retrograde slope. This is in contrast to the previously published results. Therefore, depending on the amount of buttressing that an ice shelf provides, it can affect where an irreversible transition happens.

The buttressing analysis showed that lateral margins play an important role, particularly in narrower channels. Furthermore, the comparison of basal melt parameterization results showed that basal melt along the shear margins may have a greater impact on the mass loss compared to when melting is concentrated along the central trunk grounding line. This has implications for real world glaciers in a similar configuration such as Pine Island Glacier. Recent studies have shown that damage or weakening along its shear margins can lead to increased flow and break up (Alley et al., 2019; Lhermitte et al., 2020). On the other hand, for wider channels or where the ice shelf has little contact with coastal features, the weakening or thinning of an ice shelf, has less of an impact on the flow of upstream ice. This has been shown in a recent study for Thwaites Glacier, where a complete collapse of the ice shelf does not have a substantially impact on mass loss in the immediate future (Gudmundsson et al., 2023).

An important finding that was shown in this chapter, and in agreement with other studies, was that the choice of friction law used in an ice sheet model can impact the final result. Using the common Weertman power law produced the most advanced ice sheet when no basal melting was applied, compared with friction laws that were limited by the effective pressure (Schoof, Tsai and Umbi). For the retreat experiments, when basal melting was applied, the Weertman law caused the least amount of mass loss and grounding line retreat compared with the other laws. In future ice sheet modelling studies, there should be different sliding laws included in experiments to ensure a range of possible soolutions are found for unknown bed conditions.

Chapter 5

Recent irreversible retreat phase of Pine Island Glacier

5.1 Preface

The content in this chapter is being revised for Nature Climate Change with the following details:

> Reed, B., Green, J. A. M., Jenkins, A., and Gudmundsson, G. H. (2023), Recent irreversible retreat phase of Pine Island Glacier

5.2 Introduction

The West Antarctic Ice Sheet (WAIS) has been losing mass since at least the start of the satellite era (Mouginot et al., 2014), and has contributed almost 90% of the overall AIS mass loss since 1992 (Shepherd et al., 2018). In the Amundsen Sea sector there has been widespread thinning (Konrad et al., 2017), accelerated ice flow (Mouginot et al., 2014) and grounding-line retreat (Rignot et al., 2014), which has prompted questions about the future stability of the region (Reese et al., 2022; Urruty et al., 2022). Modelling studies have predicted further retreat under current and future climate conditions (Cornford et al., 2015; Favier et al., 2014; Joughin et al., 2014; Joughin et al., 2010; Seroussi et al., 2017), and there is a possibility of a complete collapse of the WAIS if a local destabilisation occurs (Feldmann and Levermann, 2015b). This sector alone contains 3.4 million km^3 of ice, which is a sea level equivalent of over 5 m (Morlighem et al., 2020). Due to the retrograde bed (sloping downwards in the inland direction) beneath its largest glaciers, the Amundsen Sea sector is vulnerable to a marine ice sheet instability (Schoof, 2007a; Weertman, 1974), where a small perturbation in grounding-line position could result in

irreversible mass loss and grounding-line retreat beyond a tipping point (Garbe et al., 2020; Rosier et al., 2021). The floating extensions of glaciers, known as ice shelves, provide buttressing of upstream grounded ice and can be sufficient to restore stability to an unstable grounding-line retreat (Gudmundsson, 2013; Pegler, 2018), particularly through the aid of pinning points such as ice rises and ice rumples (Favier et al., 2016; Schlegel et al., 2018). However, ice shelves are susceptible to ocean-induced melting from below (Payne et al., 2004; Pritchard et al., 2012), which can lead to thinning, weakened buttressing and accelerated ice flow (Gudmundsson et al., 2019; Joughin et al., 2021).

One of the largest glaciers in the Amundsen Sea sector is Pine Island Glacier (PIG), which has contributed more to global sea level rise in recent decades than any other glacier in Antarctica (Rignot et al., 2019). Between 1979 and 2017, PIG was responsible for 3 mm sea-level rise, which was almost a quarter of the overall contribution from the entire AIS. Thinning of the present-day ice shelf and the subsequent grounding-line retreat can be traced back to the 1940s when an ocean cavity first started to form upstream of a subglacial bedrock ridge (Smith et al., 2017). There was further grounding-line retreat and increased ice discharge in the 1970s with the ungrounding of an ice rumple over the highest part of the ridge (Jenkins et al., 2010; Mouginot et al., 2014). These events in the 1940s and 1970s coincide with notable climate anomalies in the central tropical Pacific, which has been shown to have a teleconnection with the Amundsen Sea (Lachlan-Cope and Connolley, 2006). It is possible that tropically forced wind anomalies over the continental shelf break (Holland et al., 2019) caused a shallowing of the thermocline, allowing more warm Circumpolar Deep Water to access the cavity underneath the ice shelf, leading to higher melt and enhanced thinning (Jenkins et al., 2016; Naughten et al., 2022; Steig et al., 2012; Thoma et al., 2008). Previous ice-flow modelling studies have shown that a shallower thermocline can cause irreversible retreat on an idealised representation of PIG, and this happens when there is a sufficient gap between the bedrock ridge and ice shelf (Rydt and Gudmundsson, 2016; Rydt et al., 2014).

Here, we investigate the retreat of PIG from the subglacial ridge and whether the marine ice sheet instability played a role in that retreat. We use the finite-element, vertically integrated ice-flow model Úa (Gudmundsson et al., 2012) to solve the ice dynamics equations in the shallow ice-stream approximation. We first advance a present-day PIG to a steady state position on the subglacial ridge. This is then perturbed under two scenarios: cold forcing to represent conditions prior to 1940s, and warm forcing, with a shallower thermocline, to represent conditions during a tropically forced warm period. We use a depth dependent basal melt parameterization with a piecewise linear profile in both scenarios. The final experiment explores the stability regime of the glacier by incrementally changing the thermocline depth in retreat and advance steady state simulations.

5.3 Methods

5.3.1 Ice-flow model

In this study we used the finite-element, vertically integrated ice-flow model Úa Gudmundsson et al., 2012 to solve the ice dynamics equations in the shallow ice-stream approximation (SSTREAM or SSA) (Macayeal, 1989). The model has previously been used to study tipping points and drivers of retreat of Pine Island Glacier (Rosier et al., 2021; Rydt et al., 2021), grounding-line stability and ice shelf buttressing (Gudmundsson et al., 2012; Hill et al., 2018; Reese et al., 2018a) and in a number of intercomparison projects (Cornford et al., 2020; Levermann et al., 2020; Pattyn et al., 2013).

The vertically integrated, or two horizontal dimension, momentum equations can be written in compact form as

$$\nabla_{xy} \cdot (h\boldsymbol{R}) - \boldsymbol{t}_{bh} = \rho_i g h \nabla_{xy} s + \frac{1}{2} g h^2 \nabla_{xy} \rho_i, \tag{5.1}$$

where h is the ice thickness, $\boldsymbol{t}_{bh}$ is the horizontal component of the bed-tangential basal traction $\boldsymbol{t}_b$, ρ_i is the vertically averaged ice density, g is gravitational acceleration, s is the ice upper surface elevation, and $\boldsymbol{R}$ is the resistive stress tensor defined as

$$\boldsymbol{R} = \begin{pmatrix} 2\tau_{xx} + \tau_{yy} & \tau_{xy} \\ \tau_{xy} & 2\tau_{yy} + \tau_{xx} \end{pmatrix} \tag{5.2}$$

and

$$\nabla_{xy} = (\partial_x, \partial_y)^T. \tag{5.3}$$

Here, τ_{ij} are the components of the deviatoric stress tensor. The relationship between deviatoric stresses τ_{ij} and strain-rates ϵ_{ij} is given by Glen's flow law

$$\dot{\epsilon}_{ij} = A \tau^{n-1} \tau_{ij}, \tag{5.4}$$

where τ is the second invariant of the deviatoric stress tensor

$$\tau = \sqrt{\tau_{ij}\tau_{ij}/2}, \tag{5.5}$$

A is a spatially varying ice rate factor determined using inverse methods and $n = 3$ is a creep exponent. In our main set of experiments the basal traction is given by Weertman's sliding law

$$\boldsymbol{t}_b = \mathcal{G} \beta^2 \boldsymbol{v}_b, \tag{5.6}$$

where $\mathcal{G}$ is a floating mask, with $\mathcal{G} = 1$ for grounded ice and $\mathcal{G} = 0$ otherwise and $\boldsymbol{v}_b$ is the horizontal component of the bed-tangential ice-velocity. In Eq. 5.6, β^2 is given by

$$\beta^2 = C^{-1/m} \|\boldsymbol{v}_b\|^{1/m-1}, \tag{5.7}$$

where C is a spatially varying slipperiness coefficient, determined using inverse methods, and $m = 3$ which gives a non-linear viscous relationship. Downstream of the grounding line the slipperiness coefficient is set to a constant of 0.03, which allows the ice stream to advance forward. This constant is representative of upstream slipperiness values along the fast-flowing tributaries.

In two additional experiments, a different basal sliding setup was used. Firstly, a downstream slipperiness coefficient of 0.01, representing a 'stickier' bed, was tested. Whilst in the second experiment, a modified power law was used for the basal traction, as introduced by Eq. 11 in Asay-Davis et al. (2016). This is given by

$$\boldsymbol{t}_b = \frac{\mathcal{G}\beta^2 \left\|\boldsymbol{v}_b\right\| \mu_k N}{((\mu_k N)^m + (\mathcal{G}\beta^2 \left\|\boldsymbol{v}_b\right\|)^m)^{1/m}} \frac{\boldsymbol{v}_b}{\left\|\boldsymbol{v}_b\right\|} \tag{5.8}$$

where μ_k is the coefficient of kinetic friction and is set to $\mu_k = 0.5$.

5.3.2 Model domain and mesh

The model domain includes the grounded catchment of PIG (182,000 km^2) and its floating ice shelf (Rignot et al., 2013) (Fig. 5.1). The calving front position is fixed throughout the study and corresponds approximately to the 2008/09 ice front. The average position of the calving front had been approximately constant between the 1940s and the late 2000s (Arndt et al., 2018; Rignot, 2002). For all experiments in this study, a Dirichlet boundary condition is imposed on the grounded portion of the boundary to set the velocity to zero along the ice divides, and a Neumann boundary condition arising from ocean pressure is imposed along the ice front.

An irregular, triangular mesh was generated using MESH2D (Engwirda, 2014) for the entire domain, and consisted of 58777 linear elements and 29797 nodes. The mesh was refined for ice shelf elements (1 km) and in areas of high strain rate and high strain rate gradients (0.7–1.5 km), whereas larger elements (10 km) were used for the slowest moving ice inland away from the main tributaries (Fig. 5.2). This gave a mesh with minimum, median, and maximum element sizes of 563 m, 1311 m and 11330 m respectively. For the control and warm experiments, a further grounding line mesh adaption was applied to ensure fine element sizes were used in a crucial transition area. Due to computational and time limitations, no mesh adaption was used for the reversibility experiments.

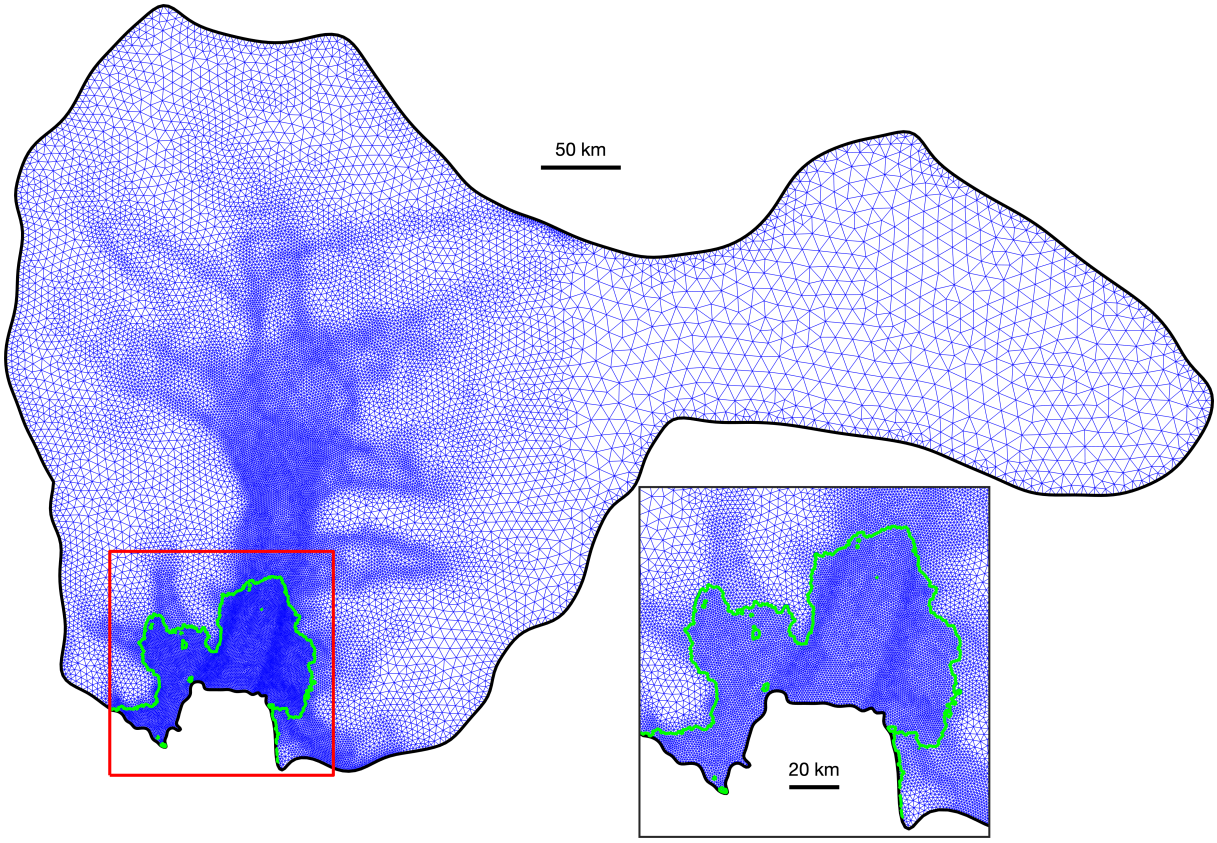

Fig. 5.1: Initial mesh for the Pine Island Glacier model domain. Catchment area is shown by the black line and the grounding line is shown in green. Blue lines indicate the linear triangular mesh elements and the red square outlines Pine Island Ice Shelf which is shown in the inset.

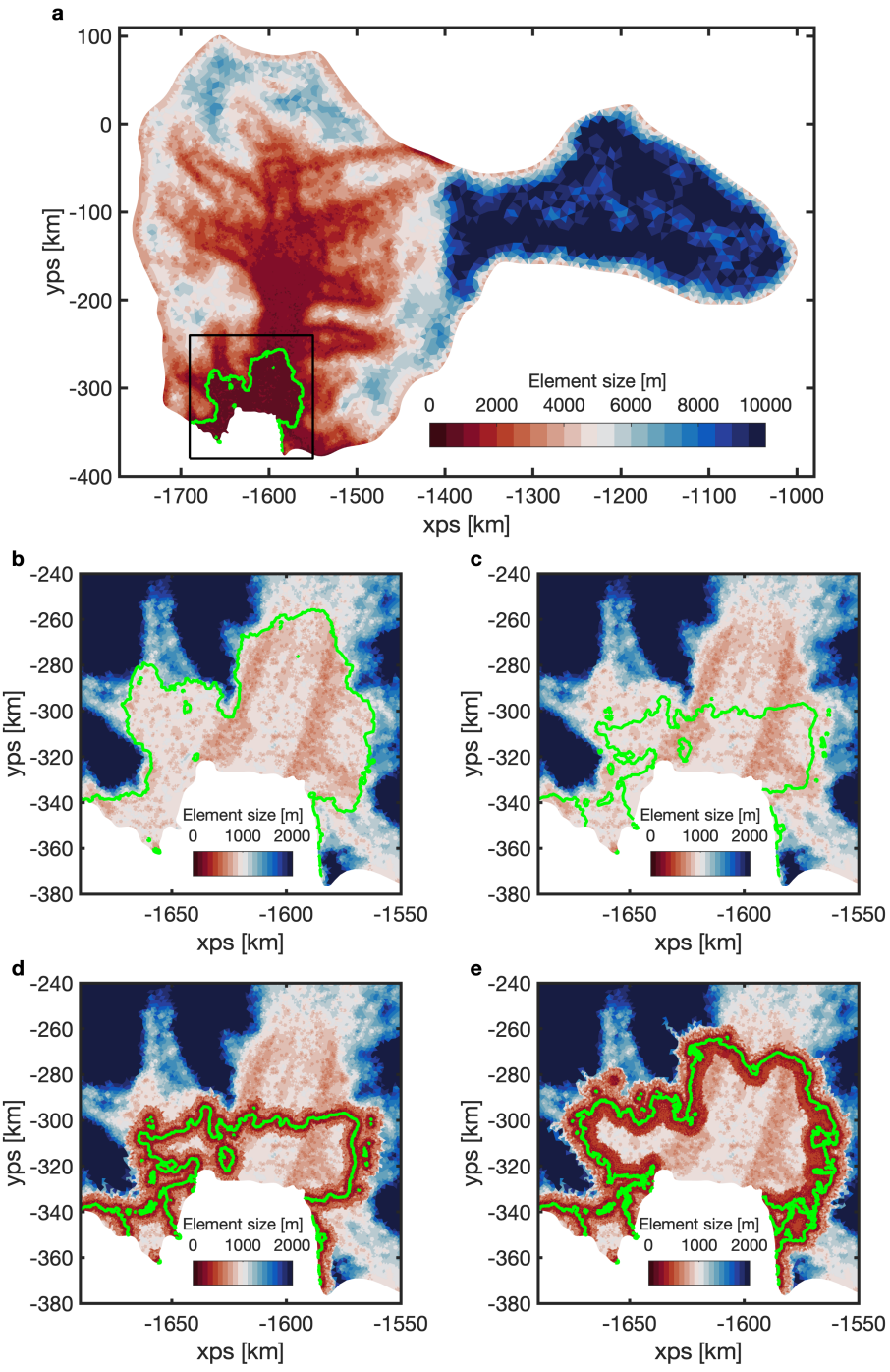

Fig. 5.2: Element sizes for the whole mesh domain (**a**) and floating ice shelf (**b**) for a present-day representation of PIG. Element sizes for the steady state geometry of PIG grounded at the subglacial ridge before grounding line mesh adaption (**c**) and after adaption (**d**). This is the starting configuration of the cold and warm experiments. (**e**) Element sizes after grounding line mesh adaption at the end of the warm experiment. The grounding line is shown as a green line in all plots and the black box in **a** shows the location of plots **b-e**.

5.3.3 Input data

This study aims to simulate the response of a 1940s PIG to a change in external forcing, however, with very little data available for that period we set up our model using present day observations and then let the model evolve in time to get an approximate configuration for 1940. The bedrock topography, ice thickness, surface elevation and ice density were taken from BedMachine Antarctica, v2 (Morlighem et al., 2020). These datasets have a resolution of 500 m and nominal data of 2015. Some local adjustments were made to the ice shelf thickness near the grounding line to ensure the hydrostatic floating condition was met. As the BedMachine data represents a recent bed geometry, we also ran an additional experiment with a lower bed to test the impact of solid-earth feedbacks. The upper surface accumulation was from given by the RACMO2.3p2 dataset (Wessem et al., 2018) and was averaged between 1979 to 2016.

5.3.4 Inversion

To initialise the model in a present-day state, we used an optimization (or inversion) process to find values for the ice rate factor, A, and the slipperiness parameter, C (Eqs 5.4 and 5.7). In Úa this is done by minimizing the misfit between modelled and observed velocities, together with a Tikhonov regularization to prevent overfitting to the observations. This method has been shown in many previous studies (e.g., Hill et al., 2021; Mitcham et al., 2022; Reese et al., 2018b). The observed ice surface velocities used in this chapter were from the MEaSUREs Annual Antarctic Ice Velocity Maps dataset (Mouginot et al., 2017a,b). More details about the optimization process are given in Sect. 3.3 and the inversion results are shown in Figure 3.2.

5.3.5 Melt rate parameterization

The basal melt rate is given by a depth dependent parameterization, similar to previous studies on the retreat of PIG (Favier et al., 2014; Joughin et al., 2010). More details about the parameterization are given in Sect. 3.4.2. The melt rate field for this geometry is shown in Fig. 5.3. Although this is a simple parameterization, the spatial melt pattern agrees well with observations, with highest melt occurring close to the deep grounding lines and lower melt on the outer shelf (Bindschadler et al., 2011b; Dutrieux et al., 2013; Shean et al., 2019). For the stability analysis, model simulations were run for 100s of years until a steady state was reached. During these runs, to avoid unrealistic retreat along the southwest tributary, close to the model domain boundary, the basal melting was set to zero for elements in this region.

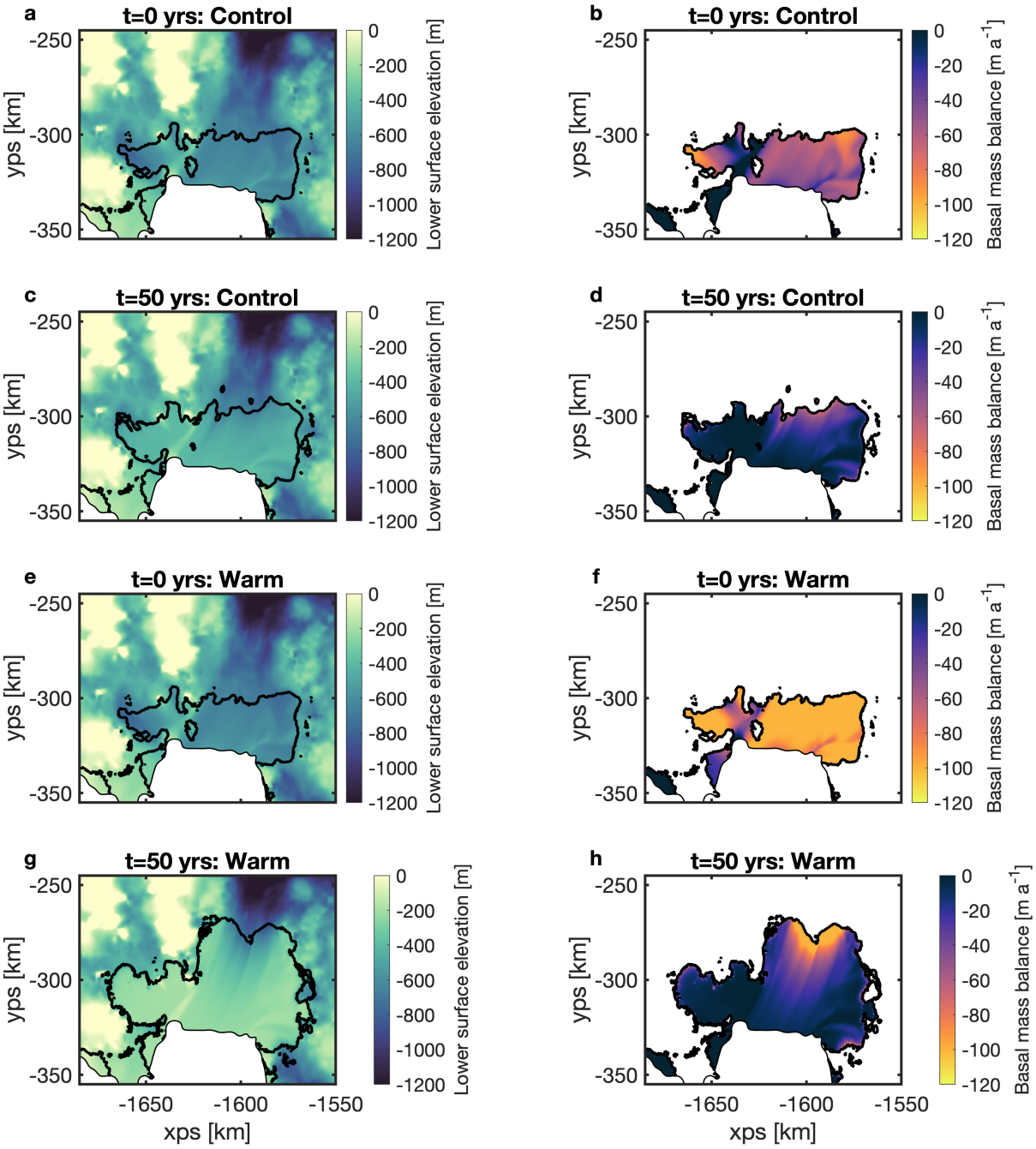

Fig. 5.3: Melt rate spatial distribution. Lower surface elevation (**a,c,e,g**) and basal mass balance (**b,d,f,h**) for the start and end of the control and warm simulations.

5.4 Results

In this section the results of the initial model spin up are first presented. This gives the pre-1940s PIG configuration in a steady state on the ridge. This is presented alongside the results of the cold perturbation experiment. Following this is a more in-depth look at the warm perturbation experiment. Finally, the results of a stability analysis are given, which show the impact of incremental step changes in thermocline depth in retreat and advance phases.

5.4.1 Pre 1940s Pine Island Glacier

The model starts from a present-day representation of PIG, with the grounding line of the main central trunk sitting on a 1200 m deep section of bedrock, 45 km upstream of the subglacial ridge crest (Fig. 5.4). It is then run for 500 years, with no basal melting applied, allowing a new steady state to be reached. During this period, the ice stream thickens and advances forward, reduces in speed, and grounds at the ridge crest front. The initial response is effectively finished within the first 150 years, and there is no further change in the main central grounding line position in the following years (Fig. 5.5). Using the total grounding line length and the change in grounded area we find that the mean migration rate of the grounding line is less than 3 m yr^{-1} by the end of the 500 years, showing that the system is effectively in a steady state. The final grounding-line ice flux is 67 Gt yr^{-1}, which is almost within the error range of the earliest observed grounding-line flux, when PIG was still grounded on the ridge (Mouginot et al., 2014). It is also similar to the overall surface mass balance of the PIG basin (Rignot et al., 2019), showing the glacier is close to a balanced state. The ice flux is calculated along the present day grounding-line position (dotted purple in Fig. 5.4) and this flux gate is used for the flux calculations hereafter. This final configuration is the starting point for the following cold and warm perturbations.

For the following experiments, we apply a simple depth-dependent melt-rate parameterization (Sect. 3.4.2), which follows a similar approach in a previous PIG study (Favier et al., 2014). The parameterization represents a two-layer ocean, typically used for conditions in Pine Island Bay (Dutrieux et al., 2014; Rydt and Gudmundsson, 2016), with zero melting at shallow depths and maximum melting in the deeper areas. Between the two layers is a linearly changing melt rate which represents the ocean thermocline. We first run a control simulation, which represents cold conditions, such as those observed in 2012 (Dutrieux et al., 2014). This has a maximum melt rate of 100 m yr^{-1} below a depth of 800 m (Bindschadler et al., 2011b; Dutrieux et al., 2013; Rydt and Gudmundsson, 2016),

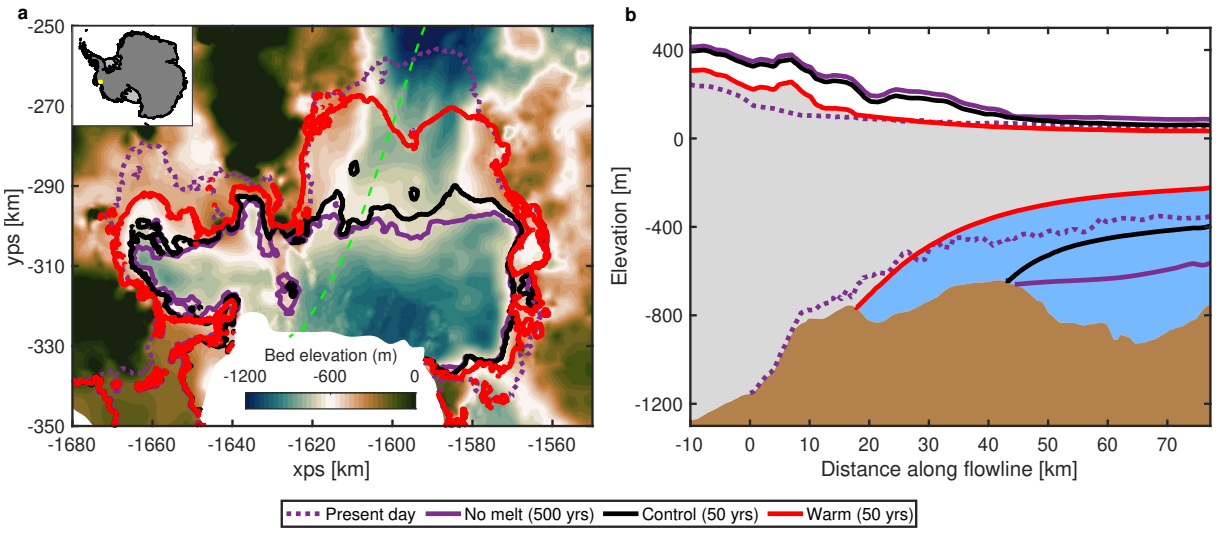

Fig. 5.4: Pine Island Ice Shelf. Bedrock elevation with overlain grounding lines (**a**) and flowline profiles (**b**) for the initial model setup, control and warm simulations. The flowline position is shown in dashed green in **a**. In both panels, the present-day geometry is shown in dotted purple and the steady state geometry for no basal melting after 500 years is shown in solid purple. The solid black line shows the geometry after 50 years of control forcing and the red line shows the geometry after 50 years of warm forcing. The zero position along the flowline corresponds to the present-day grounding line.

decreasing to zero melt at 400 m. We refer to this as having a thermocline depth of 800 m to be consistent with other studies. The highest melt rate in this model run is below the depth of the ridge crest, and hence, most of the ice shelf is exposed to lower melt rates (Fig. 5.3).

At the start of the run, the integrated melt rate across the ice shelf is 98 Gt yr^{-1}, the mean melt rate is 40 m yr^{-1} and ice flux across the grounding line is 67 Gt yr^{-1}. After 50 years of control forcing, the ice stream reaches a new steady state and has thinned a little, sped up by 8-10 % and retreated 2-3 km. However, importantly, it remains grounded along the middle of the ridge crest (Fig. 5.4). The mean melt rate decreases to 15 m yr^{-1} and the integrated melt rate decreases to 32 Gt yr^{-1} as the ice shelf lower surface becomes shallower, which agrees well with observations for a typical cold year (Dutrieux et al., 2014). Due to faster flowing ice, the grounding-line ice flux increases to 74 Gt yr^{-1}, which is close to the earliest recorded observation (Mouginot et al., 2014). The final configuration of the control case is an estimation of how PIG was situated prior to the 1940s.

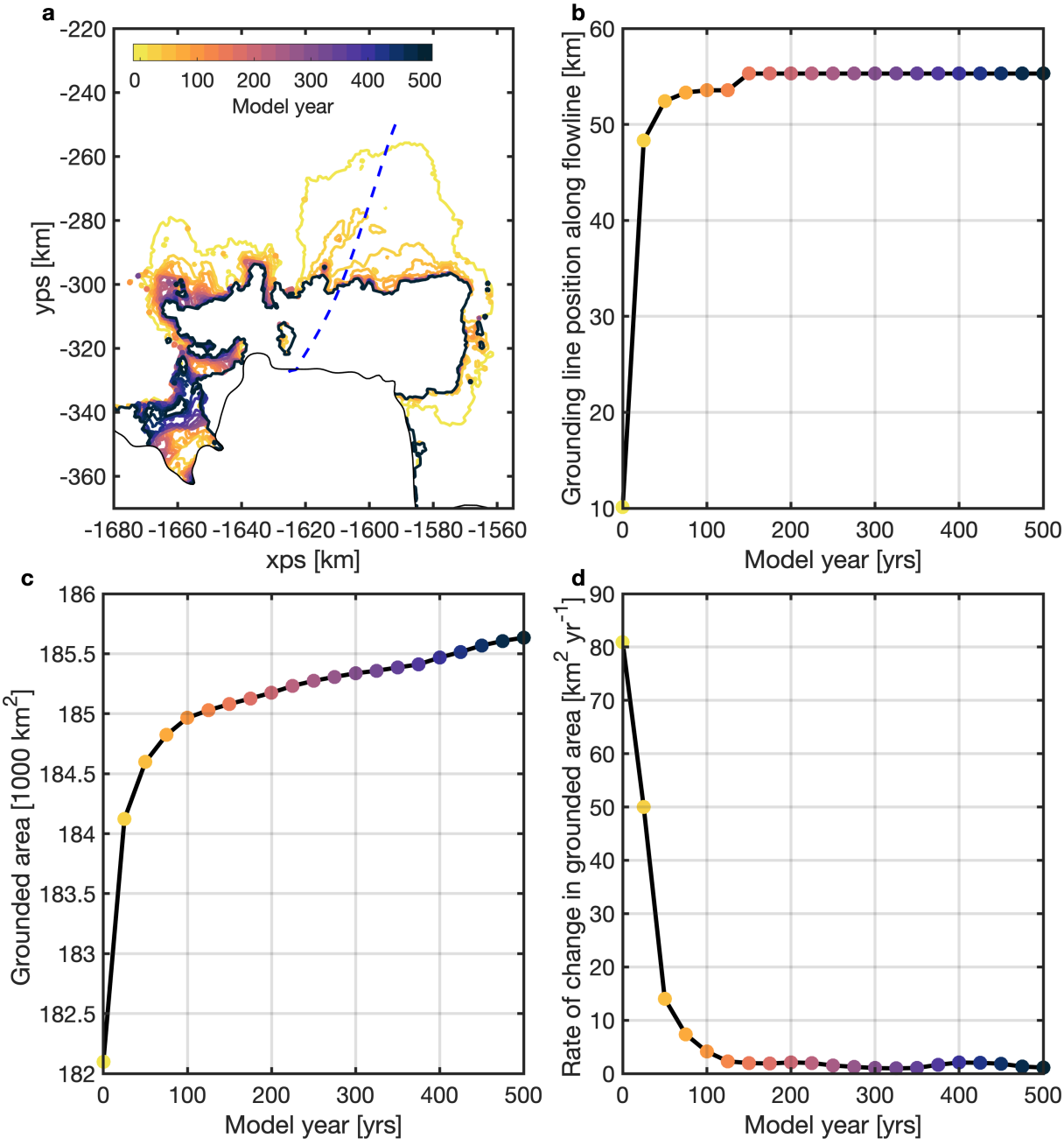

Fig. 5.5: **a**) Grounding line for every 25 years during the 500 year advance model simulation. The thin black line shows the model boundary. (**b**) Grounding line position along the blue dashed flowline shown in **a**. Grounded area (**c**) and rate of change in grounded area (**d**) during the simulation.

5.4.2 Rapid retreat from a subglacial ridge

To simulate the response of PIG to warmer ocean conditions when grounded at the ridge, we raise the melt-rate profile by 200 m so that the maximum melt rate is below a depth of 600 m and decreases to zero at 200 m. This is representative of the warmest temperature profiles that were observed in 2009 (Jacobs et al., 2011), and this step change in forcing is similar to other studies (Bradley et al., 2022; Rydt and Gudmundsson, 2016). In this experiment the highest melt rate is above the depth of the ridge crest, which compared to the control case results in an almost doubling of the starting mean melt rate (77 m yr^{-1}) and integrated melt rate (180 Gt yr^{-1}) across the ice shelf (Fig. 5.3).

Figure 5.6 shows the transient behaviour of the glacier during the warm forcing experiment. After 50 years of warm forcing, there is extensive thinning of grounded and floating ice, the ice stream accelerates by 50 %, and there is a 30 km grounding-line retreat from the ridge crest to the next raised section of bedrock. By the end of the experiment, the mean melt rate decreases to 20-30 m yr^{-1} and the integrated melt rate decreases below 100 Gt yr^{-1}. The grounding-line ice flux at the end of the warm forcing simulation is 107 Gt yr^{-1}, which is comparable to the 1996 observation, when PIG was grounded in a similar position.

The temporal changes in total melt and ice flux reveal four different stages of the retreat (Fig. 5.6), similar to a previous idealised study of PIG (Rydt and Gudmundsson, 2016). During the first stage, for approximately 5 to 10 years, there is a gradual retreat from the front of the ridge crest, as the ice shelf rapidly thins in response to the high melt rate, transforming the profile of the ice shelf lower surface from convex to concave. The slowest rate of retreat occurs from the north end of the ridge, where the bedrock is shallow and wide, whilst the fastest retreat occurs from the south, along the deep bedrock channel (Fig. 5.6a). There is a sharp decrease in integrated melt rate, from 180 Gt yr^{-1} down to 84 Gt yr^{-1}, as the ice shelf thins and becomes shallower, experiencing lower melting. During this period, there is a gradual increase in ice flux across the grounding line.

During the second stage, from 10 to approximately 32 years, the grounding-line retreats gradually across the ridge crest, with occasional jumps across small retrograde slopes (Figs. 5.7–5.9), before slowing down towards the back of the ridge crest. There is a little ice shelf thinning, a gradual decrease in integrated melt rate, a slowdown in retreat and a continued gradual increase in grounding-line ice flux. During this period, two isolated subglacial lakes start to form upstream of the ridge beneath the gradually thinning ice shelf, but they remain disconnected from the main outer ice shelf cavity, so they do not experience any melting.

The third stage, between 32–40 years, is illustrated by rapid grounding-line retreat

across several areas of retrograde bed on the landward side of the ridge, and the upstream lakes merge with the main cavity via the deep southern channel. An ice rumple forms over the highest part of the ridge in the North, and then the ice shelf ungrounds completely around 40 years. This stage of retreat shows a sharp increase in integrated melt rate as the grounding line enters a deeper section of the bedrock and experiences higher melting. This leads to a notable increase in grounding-line flux.

For the fourth and final stage, from 40 years until the end of the simulation, there is a gradual retreat of the grounding line onto the next prominent section of prograde bedrock, and the ice stream begins to approach a new steady state. There is a gradual decrease in integrated melt rate and ice flux as the ice shelf continues to slowly thin and stabilize.

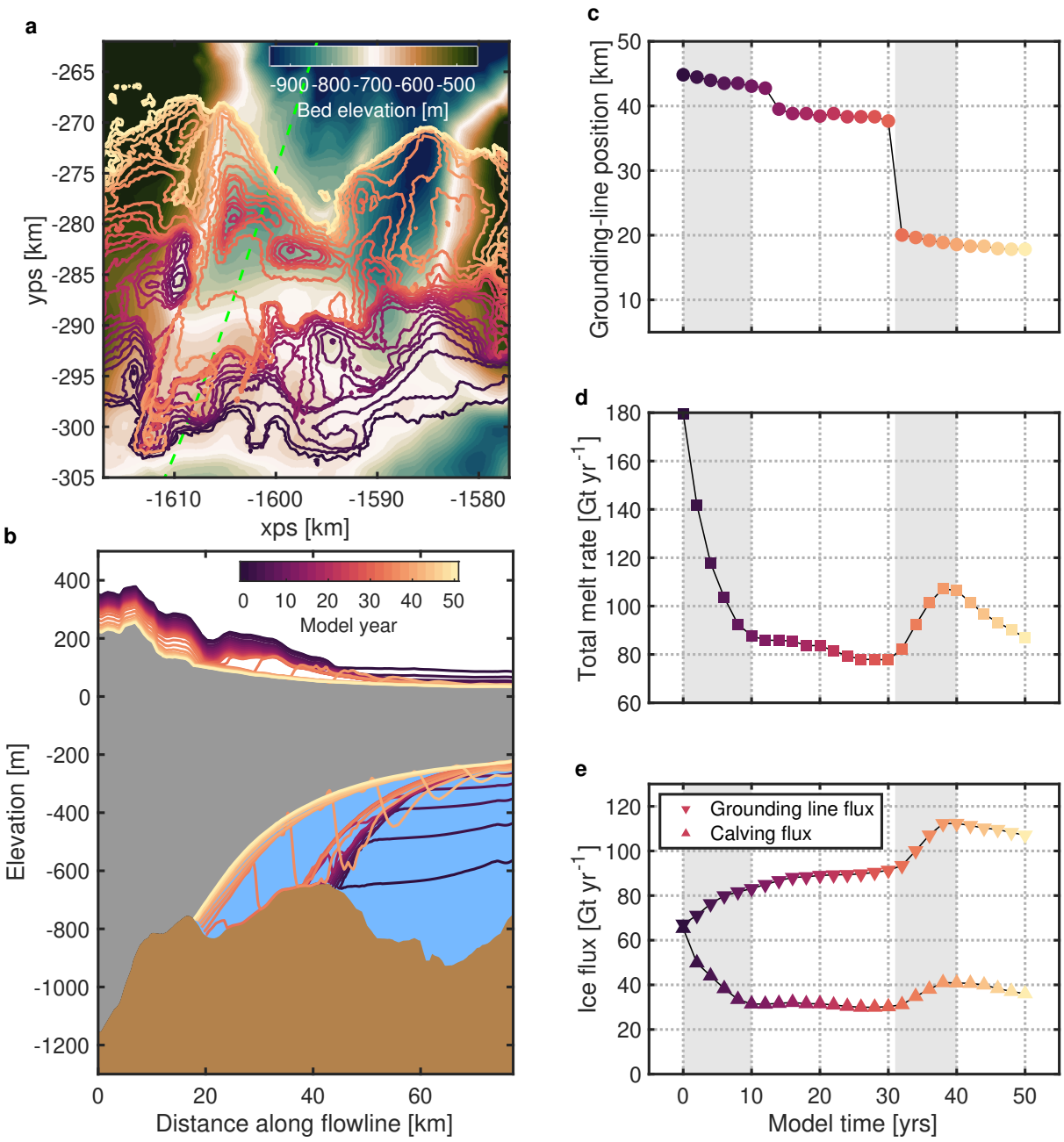

Fig. 5.6: Warm forced retreat. **a**,**b**, Bedrock elevation with overlain grounding lines (**a**) and flowline profiles (**b**) during the warm forcing experiment. The zero position along the flowline corresponds to the present-day grounding line. Grounding-line position during the model simulation (**c**) along the dashed green flowline which is shown in **a**. Total integrated melt rate over the entire ice shelf (**d**), and grounding-line flux and calving flux (**e**) during the experiment. The grounding-line flux is calculated along the present day grounding-line position (dotted purple in Fig. 5.4) for all timesteps. The colour of grounding lines, profiles and plot markers in all panels show the model year during the experiment (increment of 2 years). Shaded and unshaded regions in **c**-**e** indicate four different stages of retreat.

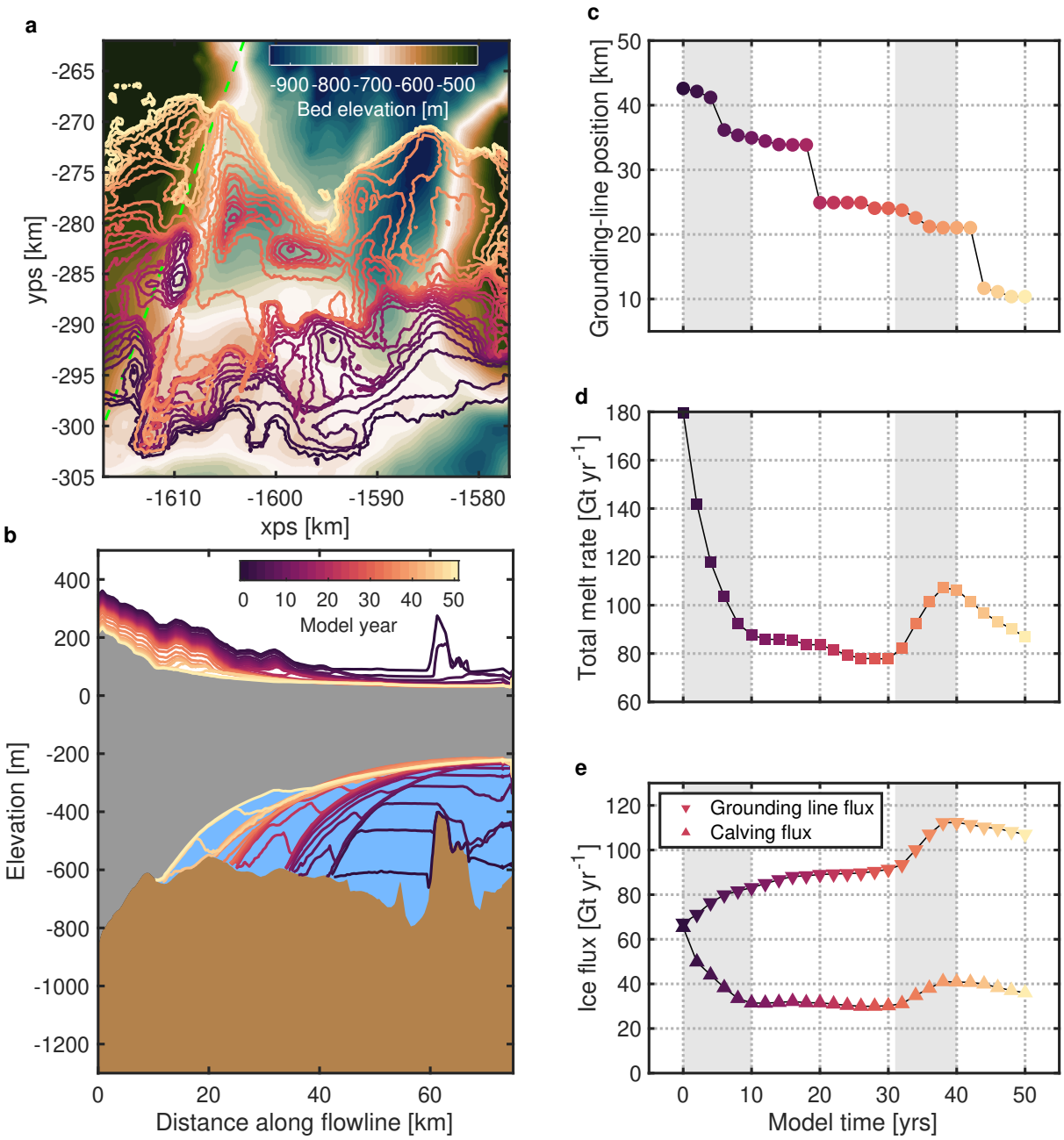

Fig. 5.7: Warm forced retreat. Same as Fig. 5.6 but for a northern flowline which is shown in **a** as a green dashed line.

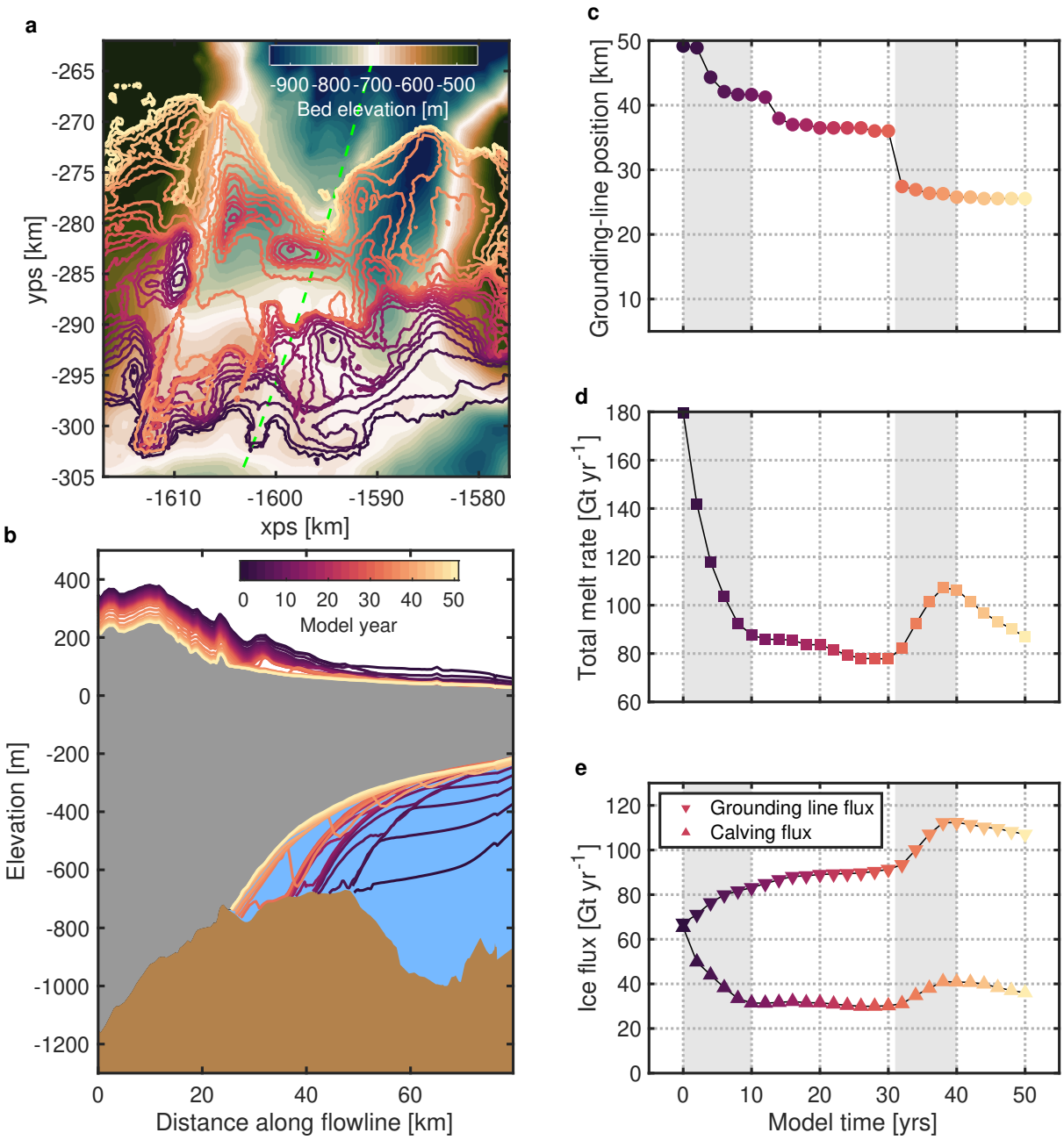

Fig. 5.8: Warm forced retreat. Same as Fig. 5.6 but for a central flowline which is shown in **a** as a green dashed line.

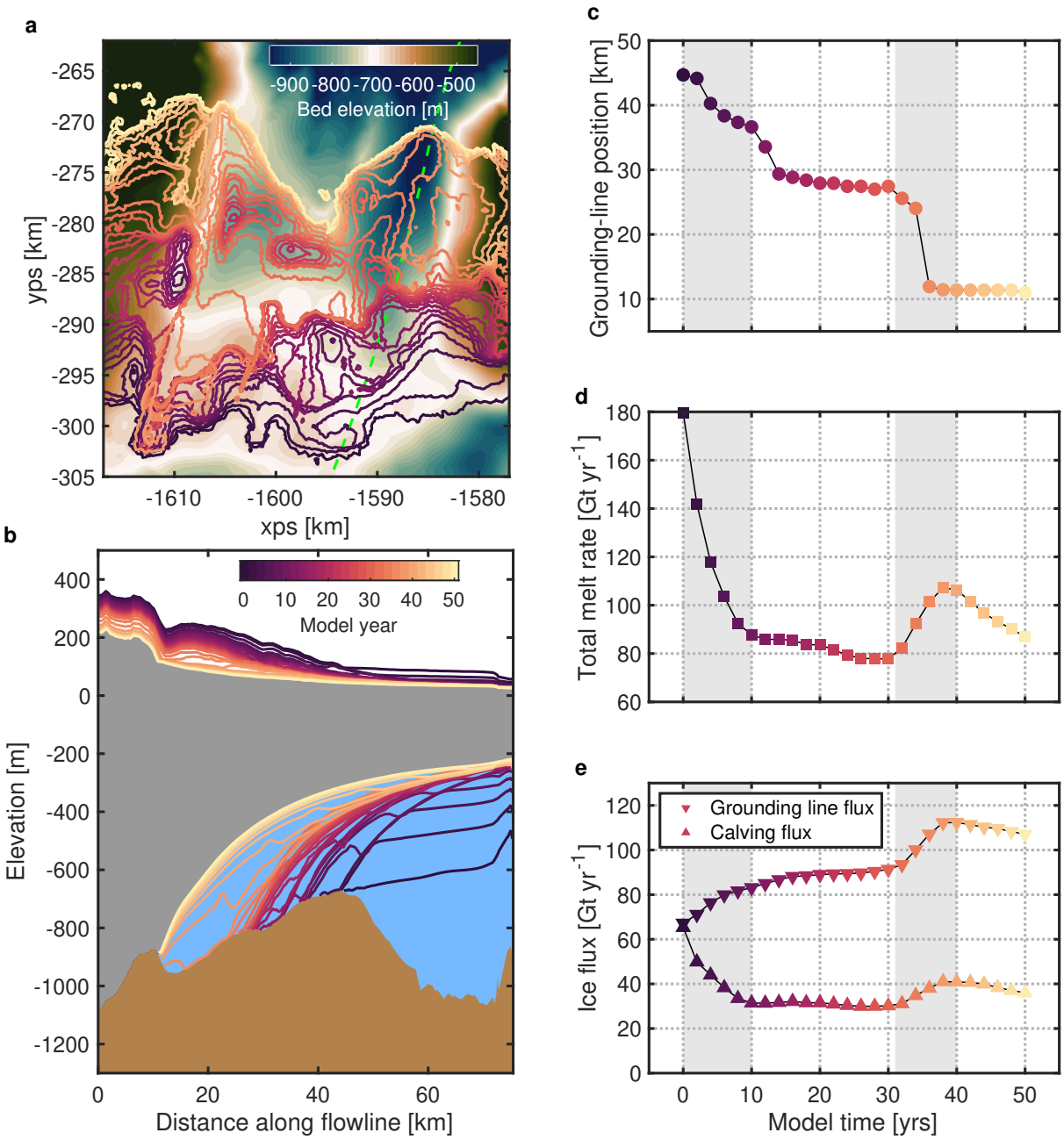

Fig. 5.9: Warm forced retreat. Same as Fig. 5.6 but for a southern flowline which is shown in **a** as a green dashed line.

5.4.3 Marine Ice Sheet Instability

The warm forcing experiment showed several instances of rapid grounding-line retreat across retrograde sloping bedrock in response to increased melting. However, this may not have necessarily been an unstable or irreversible response. To assess whether the retreat crossed a tipping point, whereby the ice sheet displays hysteretic behaviour and enters a new state, we perform a stability analysis. This involves additional model simulations to show the impact of incremental changes in thermocline depth (Fig. 5.10). The experiment consists of 38 separate simulations, with 19 comprising a retreat group and 19 a subsequent advance group. The retreat simulations all start from the no-melt steady state solution at the ridge, approximately 45 km downstream of the present-day grounding line (Fig. 5.4). The advance simulations all start from the final steady state solution of the last model run in the retreat group, which is approximately 10 km from the present-day grounding line. All model simulations in the two groups have a different thermocline depth, which ranges from 1300 m to 400 m (Fig. 5.10), and each is run to a steady state, indicating how far the grounding line can move under each forcing.

The first six retreat simulations, with thermocline depths between 1300 m and 1050 m, do not cause any thinning of the ice shelf because the highest melt rates are deeper than the ridge crest and lower ice surface. The maximum melt rate from the warmest of these runs is 34 m yr^{-1}, whilst the mean is 2 m yr^{-1} and the median is 0 m yr^{-1}. As the thermocline is raised above 1050 m, the steady state solutions show a gradual, continual thinning of the ice shelf and retreat of the grounding line from the front of the ridge crest to the back (Fig. 5.10). Once the thermocline is raised above 700 m, the steady state grounding-line retreats a further 20 km from the ridge crest down the retrograde slope to the next prominent high point in the bed. For thermocline depths above 650 m there is only a further 5 km of retreat, with the final steady state grounding line resting on an upstream prograde section of bedrock.

The large transition in grounding-line position in response to the small change in thermocline depth above 700 m does not necessarily mean a tipping point has been crossed. To examine whether this retreat has become irreversible we perform an opposite set of simulations, in the advance direction, and incrementally lower the thermocline, creating progressively colder conditions with lower melt rates. As the thermocline is lowered from a depth of 400 m to 1000 m, there is a gradual thickening of the ice shelf and a total grounding-line advance of 8 km from the upstream prograde slope of the bed rise. The thermocline must be lowered below 1000 m for the melt rates to become small enough to allow for sufficient thickening of the ice shelf and regrounding on the subglacial ridge. There is no change in ice shelf thickness or grounding line once the thermocline is lowered

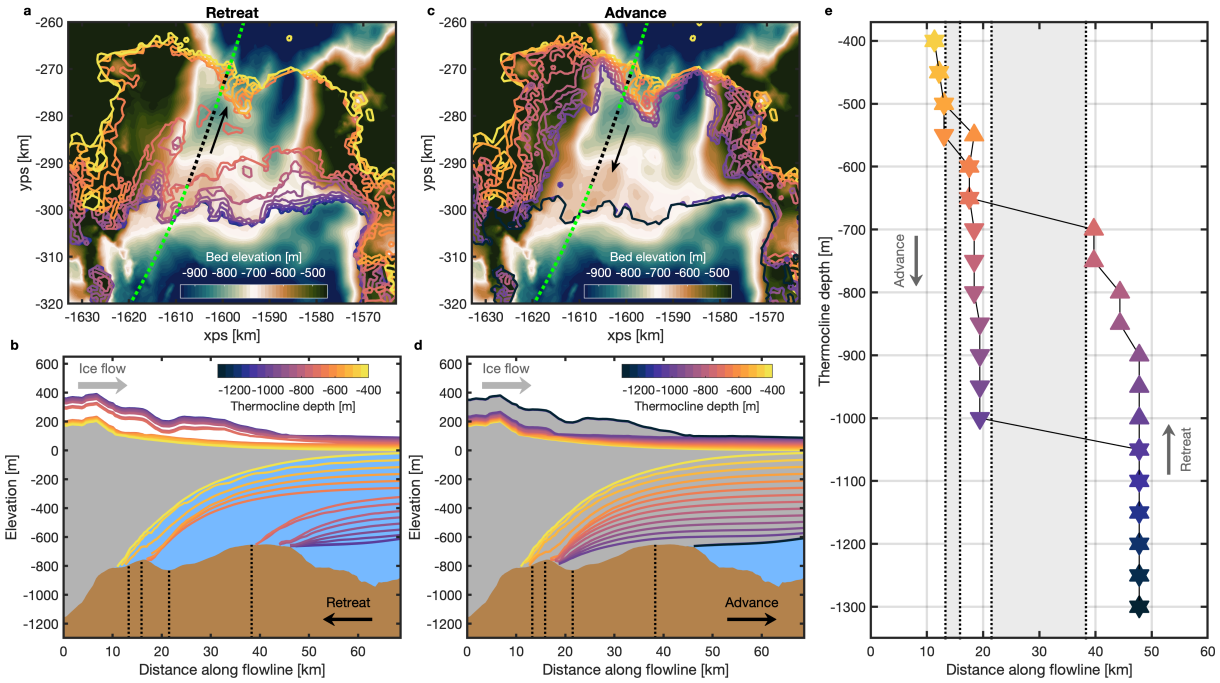

Fig. 5.10: Reversibility experiments. **a-d**, Final steady state grounding lines (**a**,**c**) and flowline profiles (**b**,**d**) for model simulations with different thermocline depths. The thermocline depths for each simulation are shown in **e** as corresponding colours. **e**, Flowline grounding-line position as a function of thermocline depth for each model simulation. Upward pointing triangles indicate the final grounding-line position for simulations which start at the subglacial ridge in the retreat group. Downward pointing triangles indicate the final grounding-line position for simulations which start at the upstream position in the advance group. The advance simulations all start from the final grounding-line position from the last retreat simulation (approx. 11 km along flowline). Note the solid black lines between markers in **e** are not results of model runs but are for visual purposes only. The grey shaded region in **e** corresponds to steep retrograde sections of bed, which are also indicated by black dotted lines in all panels. The location of the flowline is shown as a dotted line in **a** and **c**.

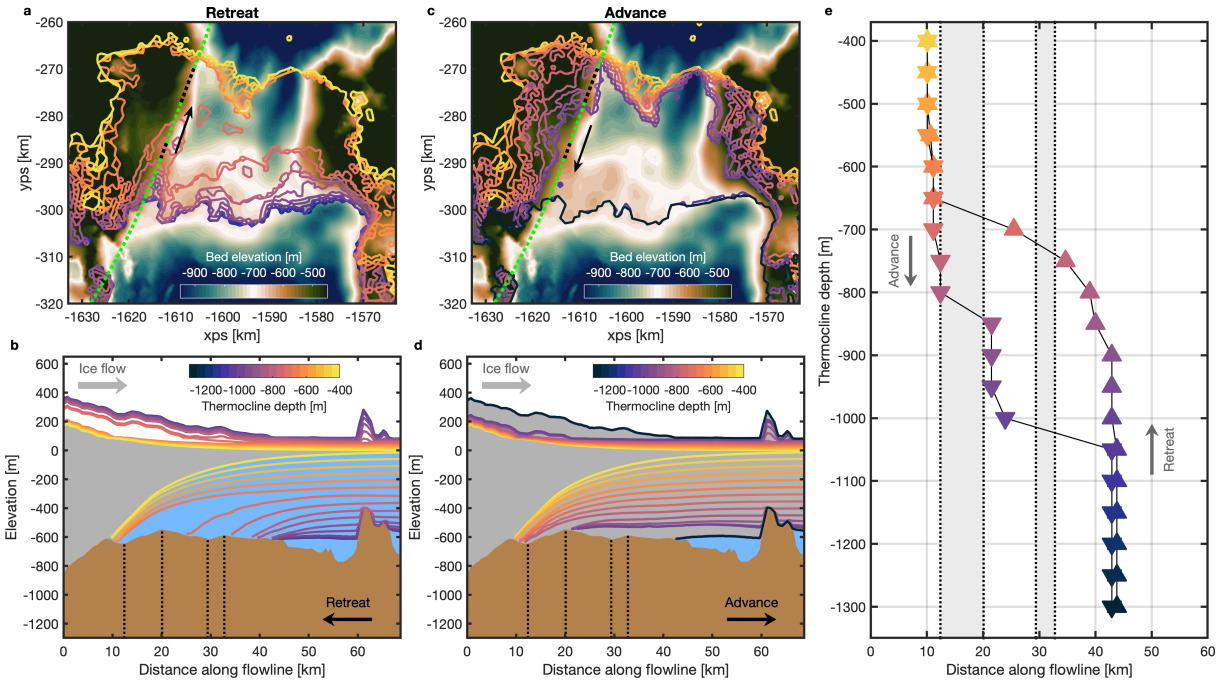

Fig. 5.11: Reversibility experiments. Same as Figure 5.10 but for a northern flowline which is shown in **a** and **c** as a green dashed line.

beneath a depth of 1050 m and the steady state position coincides with the original starting position, 45 km from the present-day grounding line.

It is evident from this experiment that a hysteretic behaviour exists when PIG is forced with a changing thermocline depth. The final position of the steady state grounding line depends on the history of forcing applied, whether the glacier has been retreating or advancing. There are two threshold thermocline depths at 700 m and 1000 m, that when crossed, lead to irreversible grounding-line motion. These are irreversible transitions because the thermocline depth must be changed more than the forcing in the opposite direction to achieve the same grounding-line position. Furthermore, there are no steady state grounding lines on the steep retrograde slope behind the central section of bedrock ridge, except for two isolated lakes where there is no melting. These results imply that PIG experienced a marine ice sheet instability retreat as it began to lose contact with the subglacial bedrock ridge after the 1940s climate anomaly. Figure 5.10 shows the main region of instability along one of the central flowlines as the steep, landward (retrograde) slope of the ridge, which is also seen in other flowlines across the shelf (Figs. 5.11–5.13).

Additional experiments were also carried out to test the dependency of our results on the selected model parameters and the choice of bedrock state. The first experiment used a smaller slipperiness coefficient in the Weertman sliding law (Eq. 5.7) to account for a different sediment profile beneath the glacier (Muto et al., 2016). The second experiment used a modified power law for the basal traction (Eq. 5.8), which has been shown to

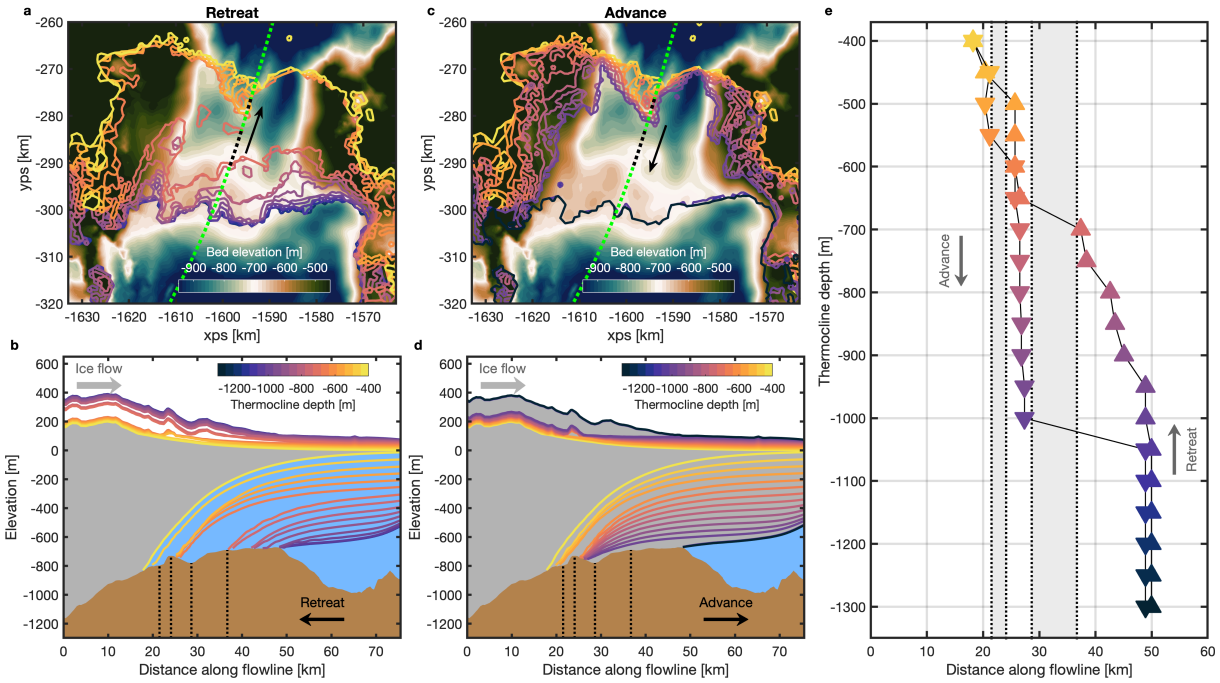

Fig. 5.12: Reversibility experiments. Same as Figure 5.10 but for a central flowline which is shown in **a** and **c** as a green dashed line.

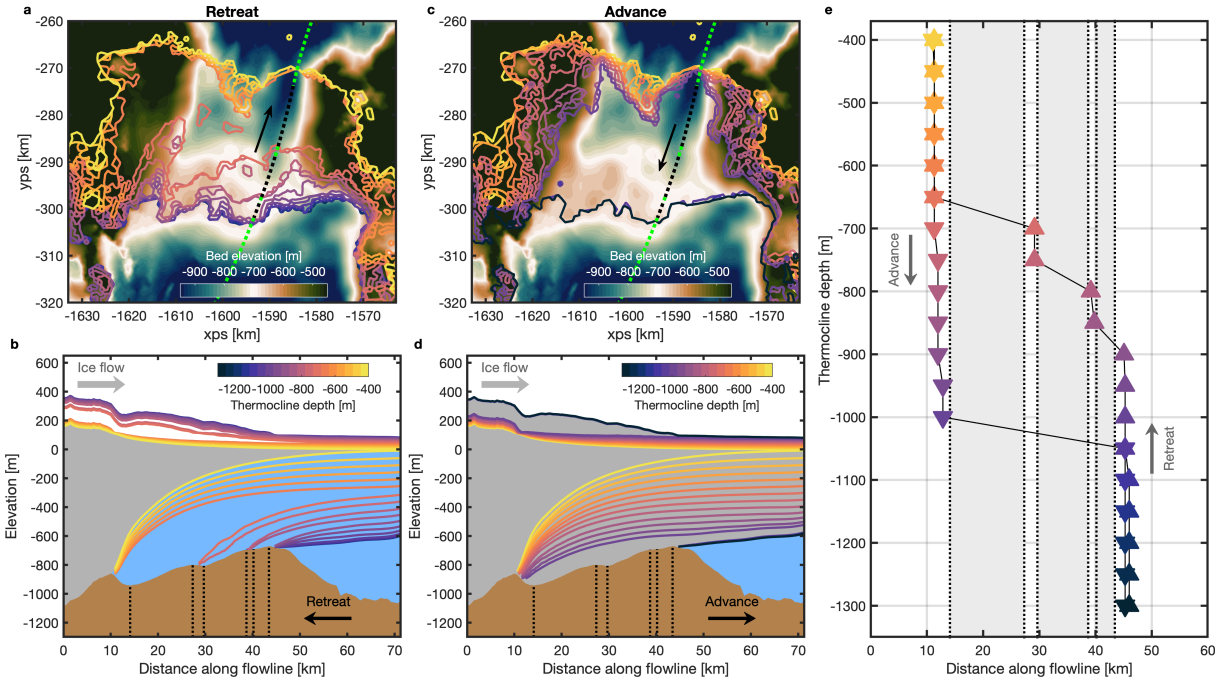

Fig. 5.13: Reversibility experiments. Same as Figure 5.10 but for a southern flowline which is shown in **a** and **c** as a green dashed line.

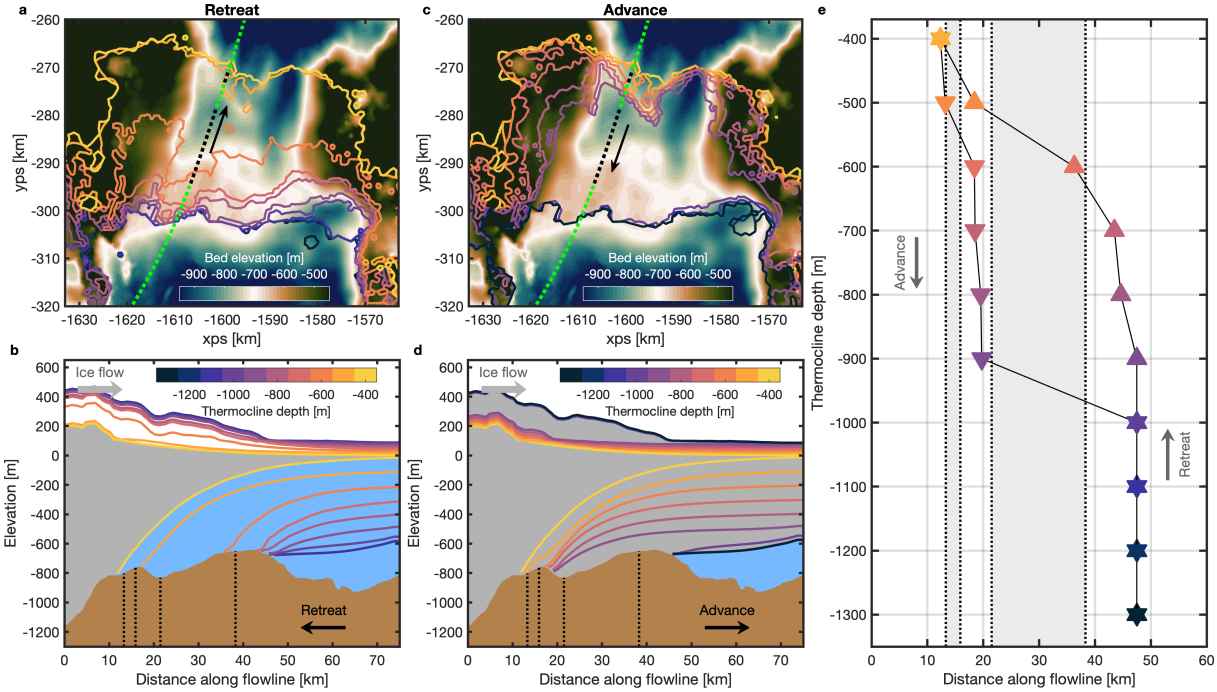

Fig. 5.14: Reversibility experiments. Same as Figure 5.10 but for the experiment which uses a slipperiness coefficient of $C = 0.01$. See Methods section for further details.

affect grounding line retreat and the rate of mass loss (Brondex et al., 2017, 2019; Yu et al., 2018). Finally, the third experiment was run on a lower bed to test the impact of solid-earth feedbacks. For this simulation the bed was lowered by 10 m at the start of the run, where we had assumed a high uplift rate of 20 cm yr^{-1} for our entire model period (Barletta et al., 2018). In all three experiments a hysteresis was present in response to the changing melt forcing (Figs. 5.14–5.16). For the smaller slipperiness case, there is a change in the onset of irreversible transitions, where they now occur at shallower thermocline depths in the melt parameterization. Whilst in the modified sliding law experiment and for the lower bed, there is a small change to the retreat tipping point, which occurs for a deeper thermocline than in the main experiment.

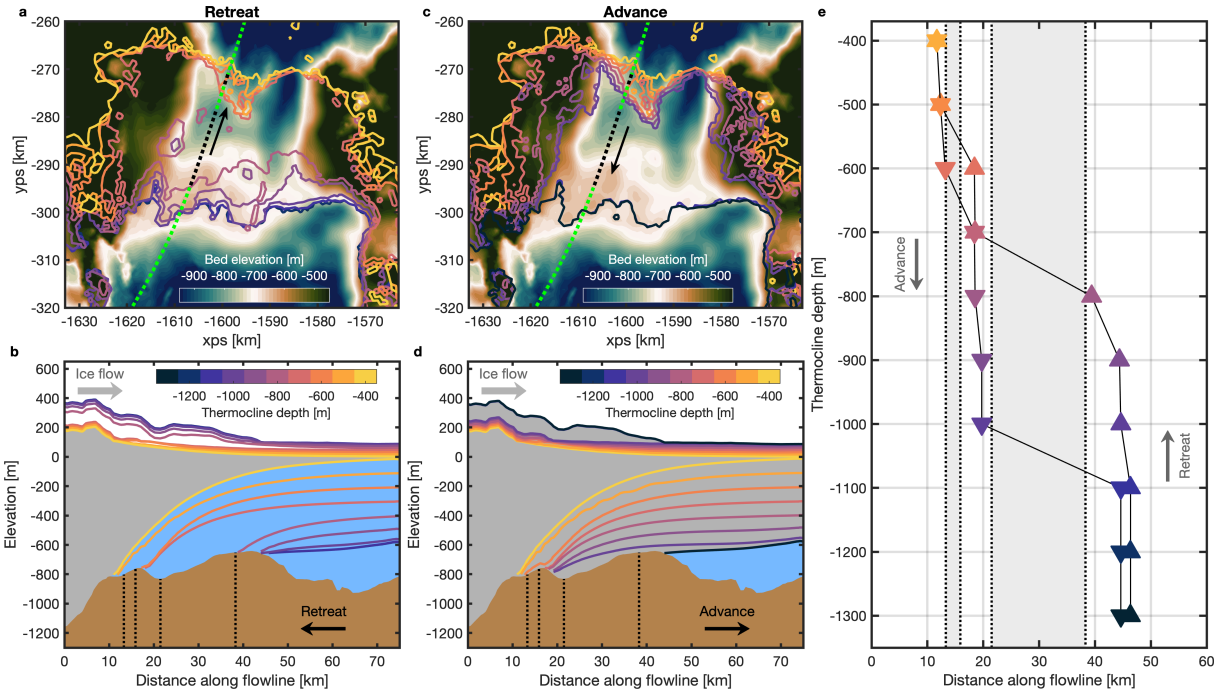

Fig. 5.15: Reversibility experiments. Same as Figure 5.10 but for the experiment using a modified sliding law for the basal traction. See Methods section for further details.

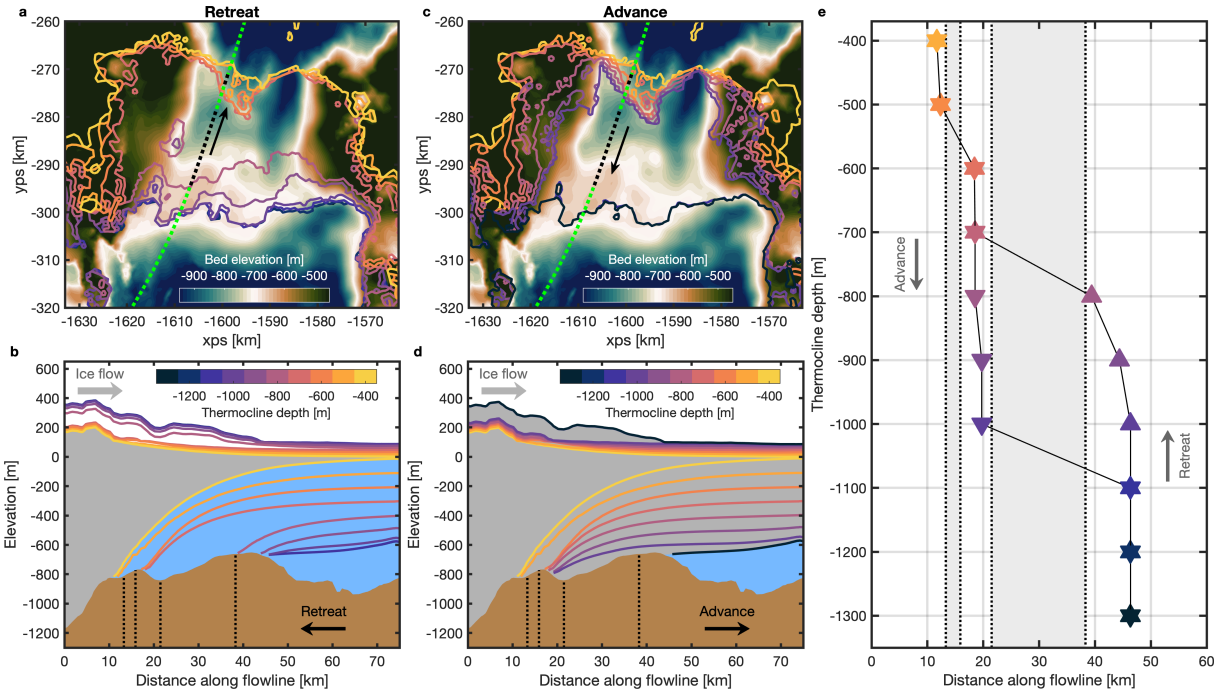

Fig. 5.16: Reversibility experiments. Same as Figure 5.10 but for the experiment which uses a bed that was lowered by 10 m. See Methods section for further details.

5.5 Discussion

Prior to the 1940s, it is likely that PIG had been grounded in a stable position on a subglacial ridge 45 km downstream from its present-day position (Smith et al., 2017). Then, following notable climate anomalies, and probably warmer basal conditions, in the 1940s and 1970s (Jenkins et al., 2016; Jenkins et al., 2018), a pre-existing cavity beneath the ice shelf became connected with the open ocean and the glacier started to retreat from the ridge crest (Jenkins et al., 2010; Smith et al., 2017). In the subsequent decades, PIG failed to recover its original position on the ridge, despite periods of cool ocean conditions which should have caused less melting and more thickening (Jenkins et al., 2016). A decadal variability in local ocean conditions, largely driven by changes in the tropical Pacific Ocean (Jenkins et al., 2016), is not reflected in the near monotonic increase in ice discharge that has been observed since the start of the satellite period in the 1970s (Mouginot et al., 2014). By the early 1990s, the PIG grounding line had completely retreated off the ridge, across the retrograde bed, stabilizing at an ice plain 30 km upstream (Park et al., 2013) (Fig. 5.17). This raises the question of whether its retreat from the ridge was an induced instability in response to the initial perturbation.

Using a vertically integrated ice-flow model and a depth-dependent melt rate parameterization, we investigated the aspect of the retreat from the subglacial ridge that was due to internal dynamics of the system rather than changes in external forcing. The ocean forcing in this experiment is therefore simplified as we focus solely on whether the marine ice sheet instability played a role in the retreat of PIG from the ridge. Prior to the warm simulation, the grounding line is in a stable position at the ridge crest. After a step change in forcing, the grounding line retreats initially slowly across the ridge, before undergoing a rapid retreat down the retrograde slope with the merging of upstream lakes. Although we used a simple melt rate parameterization, the initial behaviour of retreat, the speed at which it progresses and the final ungrounding of a pinning point above the ridge are all comparable with satellite observations and sediment records from the 1940s and 1970s (Jenkins et al., 2010; Smith et al., 2017). The same key features of retreat also occurred when we used a more realistic parameterization which tapered the melt rate down to zero at the grounding line (Figs. 5.18 and 5.19).

Our stability analysis suggests that by the early 1970s, when PIG had already started retreating from the ridge (Jenkins et al., 2010), a tipping point had been crossed, whereby further retreat was inevitable despite a return to cooler conditions (Jenkins et al., 2016). This irreversible phase comes to a halt as the grounding line reaches a new steady state on the next bed high point (Fig. 5.10 and Fig. 5.20). This location coincides with its early 1990s position, when PIG was grounded at an ice plain (Corr et al., 2001; Park

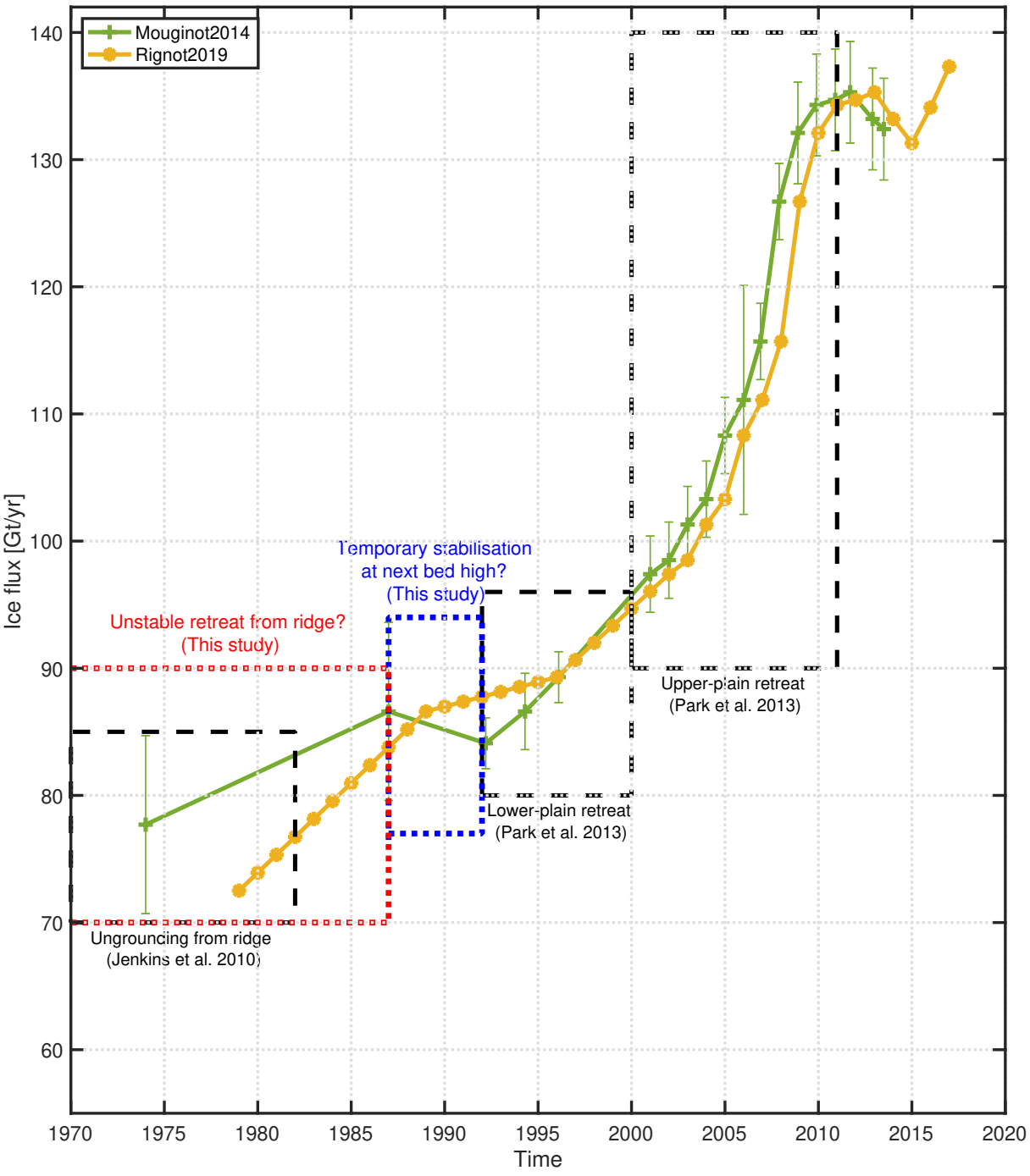

Fig. 5.17: History of Pine Island Glacier retreat. Grounding line ice flux (discharge) between 1974 and 2017 from Mouginot et al. (2014) [green] and Rignot et al. (2019) [yellow]. Black dashed boxes show times of grounding line retreat according to different studies. The red dotted box shows the estimated period of unstable retreat from the ridge and the blue dotted box shows the estimated period of stabilisation at the next bed high point, using results from our study.

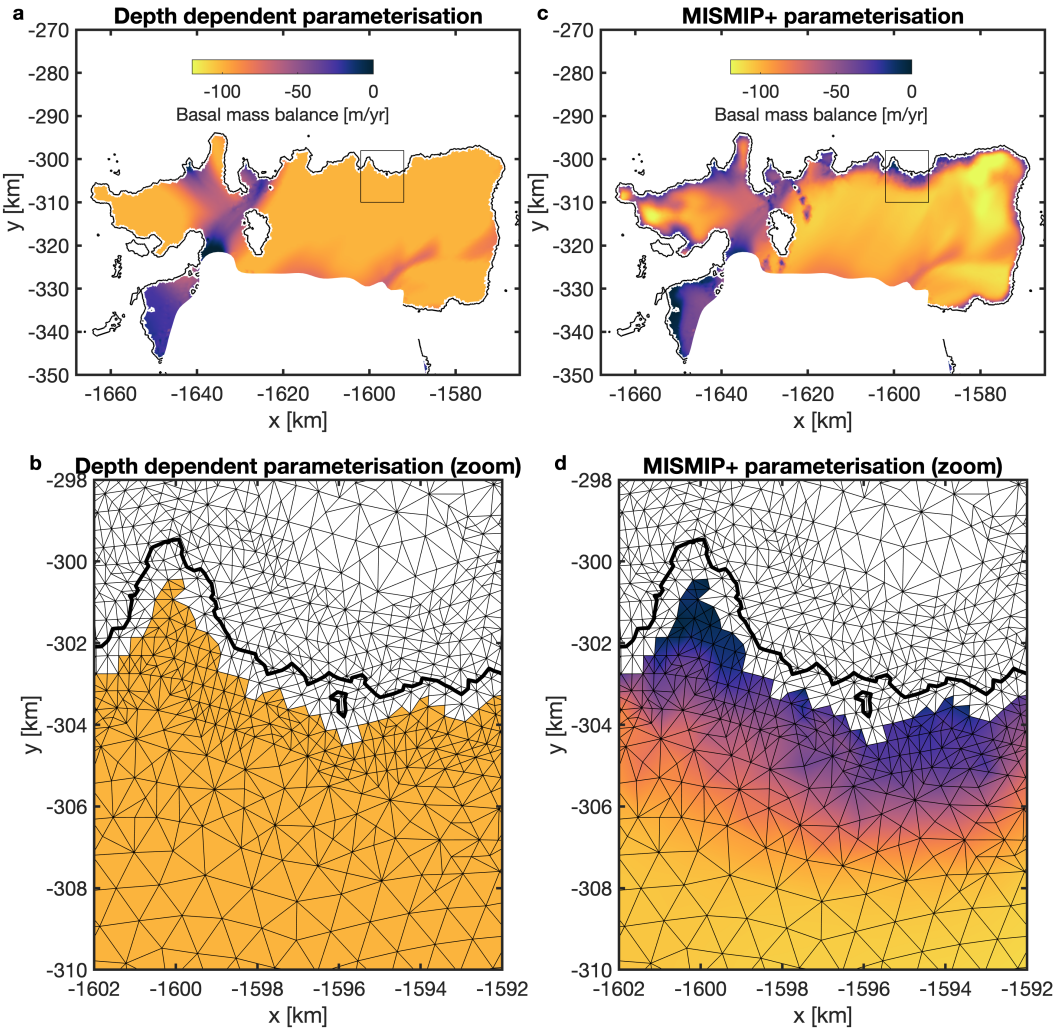

Fig. 5.18: Comparison of melt rate parameterizations. **a**,**c**, Basal mass balance given by the depth dependent parameterization that is used in this study (**a**) and the parameterization from the MISMIP+ intercomparison project (Asay-Davis et al., 2016) (**b**). **b**,**d**, Zoomed in section of ice shelf for the area indicated by black boxes in **a** and **c**, overlain with the model mesh in thin black lines and the grounding line in thick black.

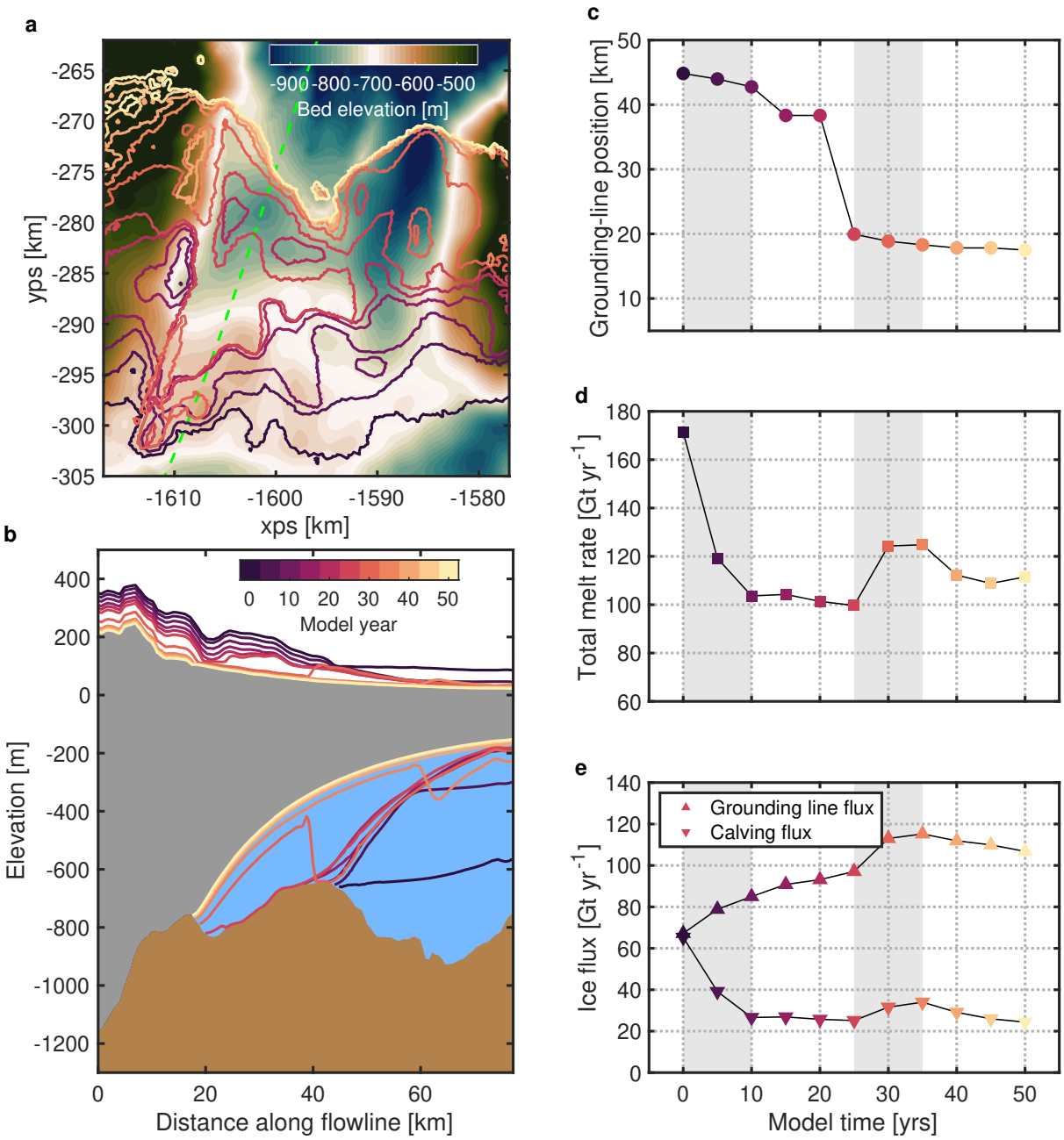

Fig. 5.19: Warm forced retreat using MISMIP+ melt parameterization. Same as Figure 5.6 but using the melt rate parameterization from the MISMIP+ intercomparison project (Asay-Davis et al., 2016).

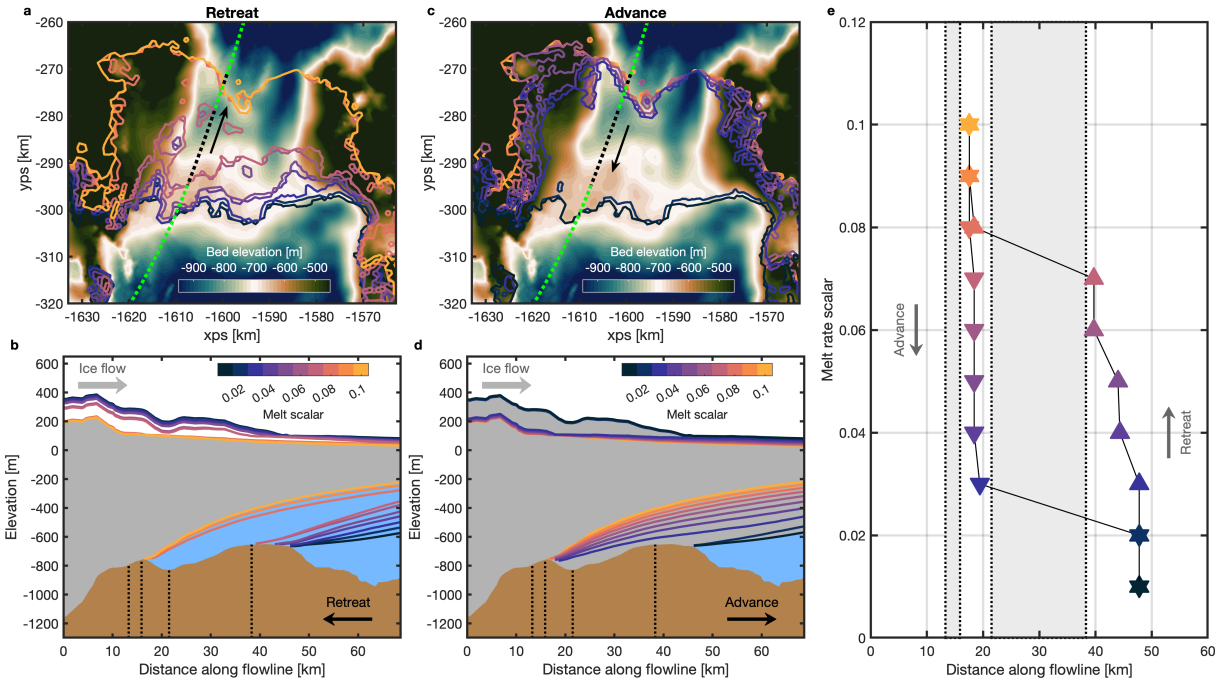

Fig. 5.20: Reversibility experiments using MISMIP+ melt parameterization. Same as Figure 5.10 but using the melt rate parameterization from the MISMIP+ intercomparison project (Asay-Davis et al., 2016). The vertical axis in **e** differs from Figure 5.10 and shows a varying melt rate scalar from equation 17 in Asay-Davis et al. (2016).

et al., 2013). During the suspected period of rapid retreat from the 1970s to the early 1990s, PIG was responsible for a third of the mass loss from West Antarctica, and almost 13 % of the overall Antarctic Ice Sheet mass loss (Rignot et al., 2019). Despite its basin comprising of only 1.5 % of the entire ice sheet area, PIG was the largest contributor to sea level rise during those years, adding 0.34 mm in total (Rignot et al., 2019).

Climate change is likely to cause further upstream migration of grounding lines of WAIS. In the Amundsen Sea, as local wind trends change in response to internal and external forcing (Holland et al., 2019, 2022), this may deliver more warm water to the continental shelf (Steig et al., 2012; Thoma et al., 2008), leading to increased basal melt (Jourdain et al., 2022) and ice shelf thinning. Previous modelling studies of the behaviour of Amundsen Sea glaciers have suggested the existence of multiple tipping points within the ice sheet and the onset of irreversible mass loss at some point in the future (Joughin et al., 2014; Rosier et al., 2021). This marine ice sheet instability is theoretically well understood (Schoof, 2007a; Weertman, 1974), and robustly replicated in numerical models (Favier et al., 2014; Joughin et al., 2014; Pattyn et al., 2012; Rosier et al., 2021), however, the hypothesis has hitherto had little direct observational support. This is in part due to the long timescales involved and the sparsity of relevant observations. Here, we have now shown that the recent observed grounding-line retreat of PIG, in the period from the 1940s

to 1990s, was irreversible and thereby provided the first observational validated example of the marine ice sheet instability. Our ice-flow model is based on the same physical assumptions used in those previous future simulations (Joughin et al., 2014; Rosier et al., 2021) and therefore this greatly strengthens our confidence in the capability of ice sheet models and their ability to simulate and predict highly nonlinear behaviours of large ice sheets. Furthermore, the results presented here are robust and insensitive to our choice of model parameters. These simulations suggest that the recent retreat phase of PIG may have been primarily internally driven, as opposed to external forced. While ocean-induced melt may have been the initial trigger, the retreat phase was driven by internal ice-dynamical processes leading to irrevocable loss of ice that will not be recovered by a reversal in external climatic condition. The implications for the future are clear: What has happened in the recent past, can happen again and, as predicted by ice-flow models, future ice loss from the WAIS may become self sustaining, amplified and irreversible as the ice-sheets enter unstable phases of retreat.

Chapter 6

Melt sensitivity of irreversible retreat of Pine Island Glacier

6.1 Preface

The content in this chapter is to be submitted to The Cryosphere with the following details:

> Reed, B., Green, J. A. M., Jenkins, A., and Gudmundsson, G. H. (2023), Melt sensitivity of irreversible retreat of Pine Island Glacier

6.2 Introduction

The Antarctic Ice Sheet has been losing mass in the last four decades. Much of this mass loss has originated in the Amundsen Sea Embayment (ASE) sector in West Antarctica (Rignot et al., 2019; Shepherd et al., 2018), where glaciers have undergone rapid acceleration (Mouginot et al., 2014), inland thinning (Konrad et al., 2017) and widespread grounding line retreat (Rignot et al., 2014). Between 1979 and 2017, ASE glaciers contributed over 7 mm to sea-level rise, which accounted for over half of the overall contribution from the entire Antarctic Ice Sheet (Rignot et al., 2019). This mass loss has led to concerns about the current stability (Urruty et al., 2022) and future evolution of the region (Alevropoulos-Borrill et al., 2020; Cornford et al., 2015). Glaciers here are susceptible to the marine ice sheet instability (MISI) (Schoof, 2007a; Weertman, 1974) due to the retrograde bed that lies beneath them. Under future climate conditions, an instability in this region has the potential to destabilize and collapse the sector (Feldmann and Levermann, 2015b; Reese et al., 2022), which contains 3.4 million km^3 of ice, or a sea level equivalent of over 5 m (Morlighem et al., 2020). Whilst modelling studies have

predicted possible MISI episodes occurring in ASE in the near future (Favier et al., 2014; Seroussi et al., 2017), there has not yet been a study that shows a MISI retreat in the recent history.

The mass imbalance and accelerated ice flow in ASE has been attributed to reduced buttressing along coastal margins, where floating ice shelves have thinned due to ocean-driven melting (Paolo et al., 2015; Pritchard et al., 2012). Along the Amundsen Sea coastline, warm modified Circumpolar Deep Water (CDW) flows onto the continental shelf and into ice shelf cavities (Dutrieux et al., 2014; Jacobs and Hellmer, 1996), causing the highest basal melt rates around Antarctica (Adusumilli et al., 2020). The influx of CDW, and therefore available heat content beneath the ice, varies on seasonal to decadal timescales (Dutrieux et al., 2014; Jenkins et al., 2016; Jenkins et al., 2018; Webber et al., 2017), and is strongly influenced by local wind forcing, natural climate variability and anthropogenic forcing (Holland et al., 2019; Steig et al., 2012; Thoma et al., 2008).

Changes in the thickness of the CDW layer impact the depth of the thermocline and corresponding melt rates, and therefore affect the flow of ASE glaciers (Dutrieux et al., 2014; Gudmundsson et al., 2019; Jenkins et al., 2018). A shallow thermocline in the mid to late 2000s coincided with rapid acceleration (Mouginot et al., 2014), enhanced thinning (Konrad et al., 2017) and widespread grounding line retreat (Rignot et al., 2014). Conversely, a deep thermocline in 2012, following a strong La Niña event in 2011, caused the lowest basal melt rates recorded in the ASE and likely caused a sector wide slow down (Dutrieux et al., 2014; Mouginot et al., 2014). Although these shifts in oceanic forcing had simultaneous impacts across the region, glaciers have been shown to respond differently depending on their local geometry and bed topography (Scheuchl et al., 2016).

In the mid to late 1990s, while the flow of most ASE glaciers had steadied, possibly in response to cooler conditions (Dutrieux et al., 2014; Mouginot et al., 2014; Naughten et al., 2022), Pine Island Glacier (PIG) continued accelerating (Mouginot et al., 2014; Rignot et al., 2002), thinning (Shepherd et al., 2001; Wingham et al., 2009) and retreating (Park et al., 2013). The glacier had been retreating down the landward side of a seabed rise since the early 1990s, possibly caused by a tropically forced warm anomaly, and it continued losing mass despite a deepening of the thermocline in 2000 and likely lower melt rates (Dutrieux et al., 2014; Naughten et al., 2022). Hence, whilst it may have been an increase in basal melt that initiated the retreat, it was likely that the local geometry and bed slope controlled the flow once conditions returned to normal.

Sediment cores recovered from beneath Pine Island ice shelf indicate a similar sequence of events occurring in the 1940s, when PIG was grounded on a subglacial ridge, 40 km downstream of its present-day position (Smith et al., 2017). Following a climate anomaly in West Antarctica (Schneider and Steig, 2008), possibly caused by the 1939–42 El Niño

event, a pre-existing cavity beneath the ice shelf became connected with the open ocean. In the subsequent years, when conditions returned to pre-anomaly levels (Schneider and Steig, 2008), the cavity connection remained open and the grounding line continued to retreat down the landward, retrograde slope of the ridge. Whilst we have no observations of ocean conditions in the Amundsen Sea prior to 1994, modelling results suggest there was a similar variability that we observe today (Dutrieux et al., 2014; Naughten et al., 2022). Therefore, despite likely periods of colder forcing, the glacier has not recovered to its original position on the ridge. This suggests that the retreat had entered an unstable and irreversible phase after the 1940s climate anomaly, which finished when the glacier stabilized on an ice plain in the early 1990s (Mouginot et al., 2014; Park et al., 2013; Reed et al., 2022; Rydt and Gudmundsson, 2016).

In this study we investigate the transient response of PIG to changes in basal melting when it is grounded on a submarine ridge, 40 km downstream from its present-day position. We extend the work of Reed et al. (2022) to address the following questions: (1) Could a short period of increased basal melt initiate retreat from the ridge? (2) Once PIG is retreating, does a return to colder conditions with lower melt stop the retreat and allow for recovery back to the ridge? (3) What is the sensitivity of irreversibility to different basal melt rates? By answering these questions, we can assess how local geometry and external forcing may have impacted the retreat of PIG from the ridge in the 1940s. In Sect. 6.3, we give a description of the model and domain used in this study and explain the experiment setup. In Sect. 6.4 we present the results from each of the experiments and discuss the findings in Sect. 6.5.

6.3 Methods

For this study, we use the finite-element, vertically integrated ice-flow model Úa (Gudmundsson et al., 2012) to solve the shallow ice-stream approximation (SSA) (see Chapter 3) for a regional configuration of PIG. Úa has been used in several studies from diagnostic (Mitcham et al., 2022; Reese et al., 2018a) to transient (Hill et al., 2021; Jones et al., 2021) investigations, tipping point analysis (Reed et al., 2022; Rosier et al., 2021), ice-ocean coupled experiments (Rydt and Gudmundsson, 2016) and intercomparison projects (Cornford et al., 2020; Levermann et al., 2020; Pattyn et al., 2013).

6.3.1 Model domain and mesh

The model domain encompasses the entire grounded catchment of PIG (Mouginot and Rignot., 2017) and its floating ice shelf, a total of $\sim 188,000$ km^2 (Fig. 5.1). The calving

front position, from BedMachine Antarctica, v2 (Morlighem et al., 2020), corresponds approximately to the 2008/09 front and remains fixed throughout the experiments. Aerial photographs show the 1940s calving front to be in a similar position (Rignot, 2002). Dirichlet boundary conditions are imposed on the grounded section of the boundary with a zero velocity along the ice divides, and Neumann boundary conditions are imposed along the ice front using ocean pressure.

For the model inversion (Sect. 6.3.4) and setup of the approximate 1940s geometry (Sect. 6.3.5), a fixed irregular triangular mesh was used that was generated with MESH2D (Engwirda, 2014). This consisted of 29797 nodes and 58777 linear elements and had refinement on the ice shelf elements (∼0.5 to 1 km) and areas of high strain rate and strain rate gradients (∼1 to 2 km). A coarser mesh size was used for the slowest moving ice far from the main tributaries, with elements sizes of ∼10 km (Fig. 5.2). The minimum, median, and maximum element sizes for the fixed mesh were 563 m, 1311 m and 11330 m respectively.

For the cold and warm transient experiments (Sect. 6.3.6) a further time-dependent mesh refinement was applied around the grounding line, adapting as it moved, to ensure element sizes were less than 500 m in the area of transition from grounded to floating ice (Fig. 5.2). The grounding line in Úa is defined by the floatation condition and closely matches its present-day position (Mouginot and Rignot., 2017).

6.3.2 Input data

The aim of this study is to model the response of a 1940s PIG to changes in basal melting, but very little data is available prior to the satellite observation period, which began in the 1970s. To overcome this, we start from a present-day PIG configuration and let the ice stream evolve in time, without any basal melting applied, so it advances forward to the subglacial ridge downstream (Fig. 6.1). The present-day ice thickness, surface elevation, bedrock topography and ice density were supplied from BedMachine Antarctica, v2 (Morlighem et al., 2020). These geometry variables have a nominal date of 2015 and a resolution of 500 m, and they each were linearly interpolated onto the model mesh. Some adjustments were made to the ice shelf thickness near the grounding line to ensure the hydrostatic floating condition was met for our geometry. The upper surface accumulation was given by RACMO2.3p2 and averaged between 1979 to 2016 (Wessem et al., 2018).

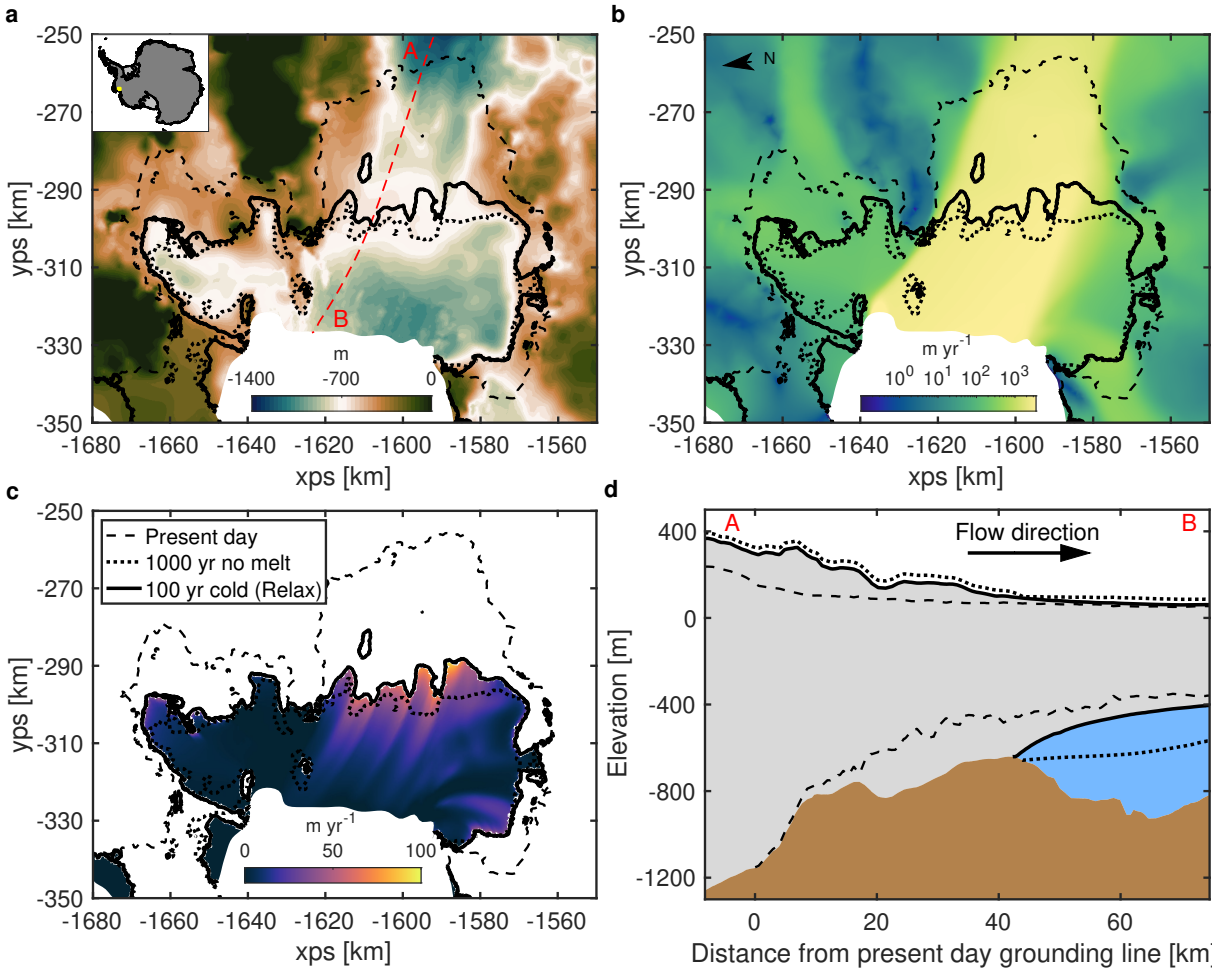

Fig. 6.1: Bedrock elevation (**a**), ice surface speed (**b**) and basal melt rate (**c**) with overlain grounding lines for the initial model setup of the present-day configuration (black dashed), the steady state geometry after 1000 years of no basal melting (black dotted) and the steady state result of the relaxation run after 100 years of cold forcing (black solid). The speed in **b** and the melt rate in **c** are from the end of the relaxation simulation. The isolated grounding line upstream of the ridge in **a**, **b** and **c** indicates a lake that forms where ice has thinned above deep bedrock. (**d**) Corresponding flowline profiles for the location shown in dashed red in **a**, with the flow direction from A to B.

6.3.3 Basal melt parameterization

To simulate changes in ocean conditions in the perturbation experiments (Sect. 6.3.6) we use a depth-dependent melt rate parameterization applied beneath the ice shelf (Fig. 6.2b). The parameterization represents typical conditions in Pine Island Bay, which has a shallow cold layer, a deep warm layer and a rapidly changing thermocline between them (Dutrieux et al., 2014). More details about the parameterization are given in Sect. 3.4.2.

In the cold experiment, the shallow, zero melt layer extends down to 400 m depth and the deep layer begins at 800 m depth. We refer to this cold parameterization as having a thermocline depth of 800 m to keep consistent with previous studies (Favier et al., 2014; Reed et al., 2022; Rydt and Gudmundsson, 2016).

In the warm experiment, the thermocline is shifted upwards 200 m, so has a depth of 600 m. These cold and warm thermocline depths have been observed in Pine Island Bay

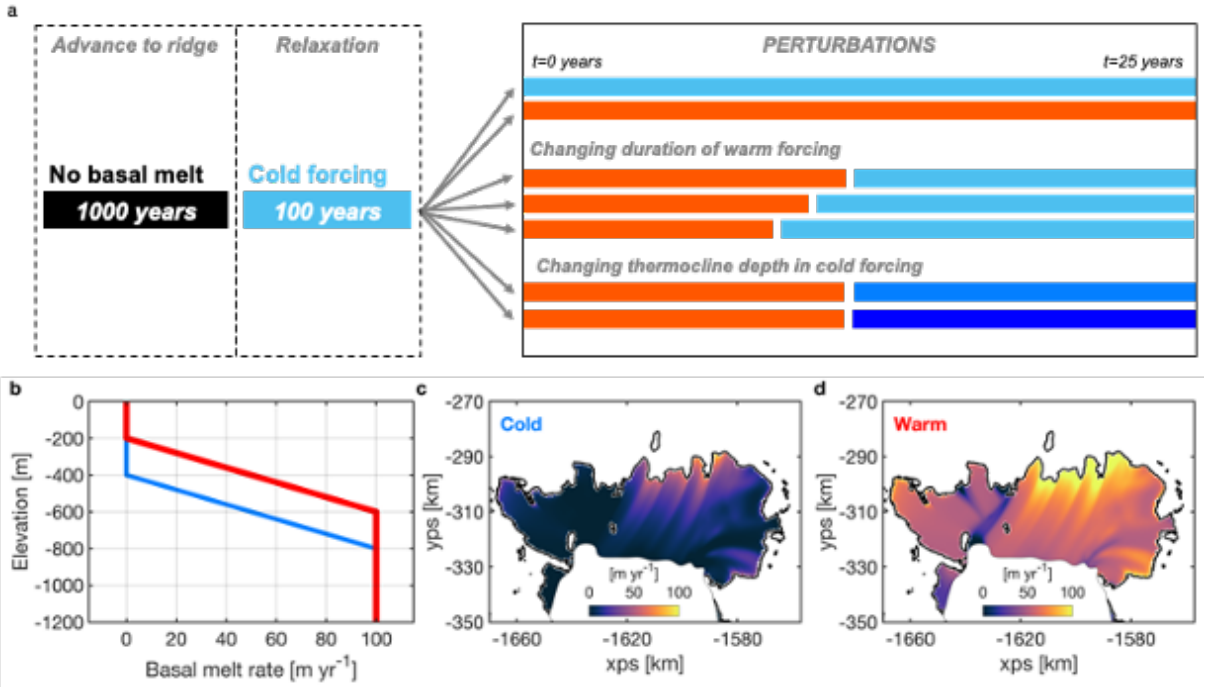

Fig. 6.2: (**a**) Schematic of the experiment setup. For the initial phase, the model is run for 1000 years with no basal melting to allow for a steady state to be reached on the subglacial ridge. This is followed by 100 years of cold forcing to put the model into a new steady state using basal melting beneath the ice shelf. This represents an approximate configuration of Pine Island Glacier prior to the 1940s retreat from the ridge and provides the starting point for the perturbation experiments. Different periods of warm forcing are then applied, followed by cold forcing, until 25 years is reached. (**b**) Depth dependent basal melt parameterization for the cold (blue) and warm (red) forcing. Basal melt at the start of the perturbation experiments for the cold parameterization (**c**) and the warm parameterization (**d**).

following La Niña and El Niño events, respectively (Dutrieux et al., 2014; Jenkins et al., 2016). Although this is a simplified parameterization, and does not capture feedbacks between ice and ocean, it allows us to draw conclusions about the direct effect of basal melting, which varies on a decadal scale with the changing ocean conditions. The basal melt was applied to mesh elements that were strictly downstream of the grounding line, and fully floating, to ensure we did not overestimate mass loss (Seroussi and Morlighem, 2018).

6.3.4 Model inversion

The initial conditions for a present-day PIG configuration were generated using an inverse methodology. By making use of Úa's optimization capabilities, we estimated the unknown model parameters of basal slipperiness (C) and ice rate factor (A) using known velocity measurements from the MEaSUREs Annual Antarctic Ice Velocity Maps dataset (Mouginot et al., 2017a,b). Further details of the inversion process are given in Sect. 3.3, with the final results shown in Fig. 3.2. There is a good fit between modelled and observed velocities, with only large differences where there were missing measurements near the ice front. The mean difference, excluding these large discrepancies, is 0.94 m yr^{-1}, with typical differences within 30 m yr^{-1} in all the main tributaries.

6.3.5 Advance to ridge and relaxation

To generate an approximate 1940s PIG configuration at the ridge we start from the present-day setup obtained in Sect. 6.3.4, which is shown by the dashed line in Fig. 6.1. PIG has several tributaries flowing into the landward sides of its ice shelf, with the main central trunk flowing the fastest in a north-west direction. The grounding line of the main trunk is located at a depth of 1200 m on the bottom section of a retrograde slope, 45 km upstream from the subglacial ridge. From this present-day configuration, we run the model with no basal melting for 1000 years to allow a new steady state to be reached. The ice stream thickens, advances forward and reduces in speed, with its grounding line coming to rest at the front of the ridge crest, at a depth of approximately 700 m. It takes less than 25 years for the ice shelf to initially ground on the landward side of the ridge, after an advance of 40 km, and then only advances a further 5 to 10 km by the end of the simulation. Hence, the subglacial ridge provides a stable position for PIG, which does not advance beyond it despite the absence of basal melting. This is also aided by the fixed calving front, which is not far from its 1940s position (Arndt et al., 2018; Rignot, 2002).

After setting up the new steady state on the ridge we relax the geometry to get an approximate 1940s PIG configuration. This is done by running the model with the cold

basal melt parameterization described in Sect. 6.3.3, which has a thermocline depth of 800 m and therefore the maximum melt is deeper than the crest of the ridge. However, at the start of the transient simulation, the ice shelf draft has a convex shape, which initially causes high melt rates, with a mean of 40 m yr^{-1} and integrated melt of 97 Gt yr^{-1}. We run the model for 100 years to allow the ice stream to adjust to the updated forcing and reach a new steady state with basal melting (Fig. 6.1). Within the first five years the melt decreases by almost 50 %, and by 15 years the mean melt rate has dropped below 18 m yr^{-1} and the integrated melt is below 40 Gt yr^{-1}, remaining at approximately this level until the end of the simulation. This melt is typical for cold years in Pine Island Bay (Dutrieux et al., 2014). At the end of the simulation, both grounded and floating ice have thinned and the ice stream has sped up by 6 to 8 %. This causes a 2 to 4 km retreat along the main trunk from the shallowest section of ridge, and up to 10 km along the deeper southern channel. However, the ice stream remains fully grounded along the top of the ridge, as shown in Fig. 6.1a, with no connection being established between the outer open ocean and the inner region upstream of the ridge. This new steady state represents the approximate situation prior to the warm anomaly in the 1940s (Smith et al., 2017) and is the starting configuration for the perturbation experiments (Sect. 6.3.6).

6.3.6 Perturbation experiments

Following the model setup and relaxation, we ran a suite of perturbation experiments with different warm and cold forcing. A summary of these experiments is given in Table 6.1 and a schematic is shown in Fig. 6.2a. These experiments were designed to assess the sensitivity of a 1940s PIG to changes in basal melt, over a 25 year period, by varying the forcing history on a near-decadal timescale. This would help us to better understand the reversibility of retreat from the subglacial ridge in the 1940s.

Before investigating the reversibility, we first ran two experiments with fixed forcing for 25 years (COLD25 and WARM25). We used these simulations as control cases to compare the time varying perturbation experiments against. We do not expect these extended periods of forcing to be realistic, but they act as lower and upper estimates of the dynamical response of PIG.

The second set of experiments compared the impact of different durations of warm forcing on the retreat of PIG from the ridge (WARM10–12). The aim of these is to determine whether short warm anomalies are sufficient to force PIG off the ridge and initiate a retreat. We applied cold forcing after each of the warm anomalies, until 25 years, to assess the reversibility of retreat.

The third set of perturbation experiments tested the impact of different cold forcing that follows the warm anomaly (COLD800–1200). The aim of these simulations is to

Name	Warm duration (t_w) [yrs]	Warm thermocline (d_w) [m]	Cold duration (t_c) [yrs]	Cold thermocline (d_c) [m]
COLD25	0	n/a	25	800
WARM25	25	600	0	n/a
WARM10	**10**	600	15	800
WARM11	**11**	600	14	800
WARM12	**12**	600	13	800
COLD800	12	600	13	**800**
COLD1000	12	600	13	**1000**
COLD1200	12	600	13	**1200**
WARMvar	**0–50**	**400:50:700**	50	800
COLDvar	12	600	**0–50**	**800:50:1200**

Table 6.1: A summary of the forcing durations and thermocline depths for the basal melt parameterization in the perturbation and sensitivity experiments (Sect. 6.3.6). Bold numbers indicate the parameter being changed. The first eight experiments are individual simulations and are illustrated in the schematic in Fig. 6.2. Note that WARM12 and COLD800 are the same test but are shown twice for comparison purposes. The final two experiments (WARMvar and COLDvar) test a range of parameter values.

explore whether typical cold conditions are sufficient to stop an already retreating PIG and allow it to recover back to the ridge, or whether more extreme forcing is needed. To adjust the cold conditions, we lowered the depth of the thermocline in the melt rate parameterization to 1000 m and 1200 m. The colder forcing was applied once PIG had already started retreating from the ridge and melting had begun upstream of the ridge. This is to replicate the known situation in the 1940s (Schneider and Steig, 2008; Smith et al., 2017).

The final set of experiments test the sensitivity of irreversible retreat to a wider set of cold and warm basal conditions (WARMvar and COLDvar). All model simulations started at the ridge and consisted of a period of warm forcing, followed by cold forcing. This allowed us to test whether any retreat was irreversible or not. We first experimented with the warm anomaly, by changing the duration of forcing (0 to 50 years) and the thermocline depth (400 to 700 m), where each of the experiments was followed by a 50 year period of cold forcing with 800 m thermocline depth. Then we varied the cold forcing, after an initial warm anomaly, by changing the cold duration (0 to 50 years) and the thermocline depth (800 to 1200 m). The warm forcing for these cold model runs was the same in each simulation, with a 600 m thermocline and run for 12 years, so that melting had started upstream of the ridge.

6.4 Results

In this section the results of the perturbation experiments are shown. Firstly, the constant cold and warm forcing experiments are given. This is followed by the reversibility experiments. The impact of different durations of warm forcing is followed by the effect of varied cold forcing. Finally, results for a wider set of warm and cold forcing parameters are shown.

6.4.1 Constant forcing

The first experiment, COLD25, reveals that 25 years of cold forcing, after the initial relaxation run, makes no impact on the ice thickness, speed or grounding line position of PIG. The glacier remains in a steady state, with a balance between the mass gained over the entire domain and mass lost through the calving front and to basal melting. Throughout the experiment, the mean melt rate remained at approximately 14 m yr^{-1} and integrated melt was 33 Gt yr^{-1}.

In contrast to the constant cold run, when warm forcing was applied for 25 years, in the WARM25 experiment, the ice shelf thinned by 100 to 400 m and accelerated by 1000 m yr^{-1} (Fig. 6.3). Due to a loss of buttressing, ice upstream of the grounding line thinned by up to 100 m and the grounding line retreated 20 to 30 km. Over the 25 years, as the ice shelf thinned, mean melt rates decreased by 50%, from 57 m yr^{-1} at the start of the run down to 25 m yr^{-1} at the end. Integrated melt was initially high at 158 Gt yr^{-1}, but this rapidly decreases to a minimum of 84 Gt yr^{-1} after 10 years (Fig. 6.4e). There is a jump in integrated melt as the upstream cavity opens after 12 years but as the glacier reaches its final position the melt drops again to 93 Gt yr^{-1}. The melt values from five years onwards are typical for a warm year in Pine Island Bay (Dutrieux et al., 2014).

In the first 5 to 10 years, there is little retreat across the top of the ridge, but there is an inland propagation of thinning and acceleration along the main trunk (Fig. 6.5). This leads to an increase in ice flux across the grounding line (Fig. 6.4c), and further thinning over a depression in the bed causes two isolated lakes to form upstream of the grounding line (Fig. 6.3). After two more years of melting, the lakes merge with each other and then connect with the outer cavity via the southern channel, causing basal melting upstream of the ridge.

Once high basal melting occurs upstream of the ridge, and is sustained, the grounding line continues to retreat down the retrograde sloping bed (Fig. 6.3). An ice rumple begins to form after 12 years and ice flux rapidly increase as the ice thins and retreats across the deeper parts of the bed. The ice rumple becomes more isolated and reduces

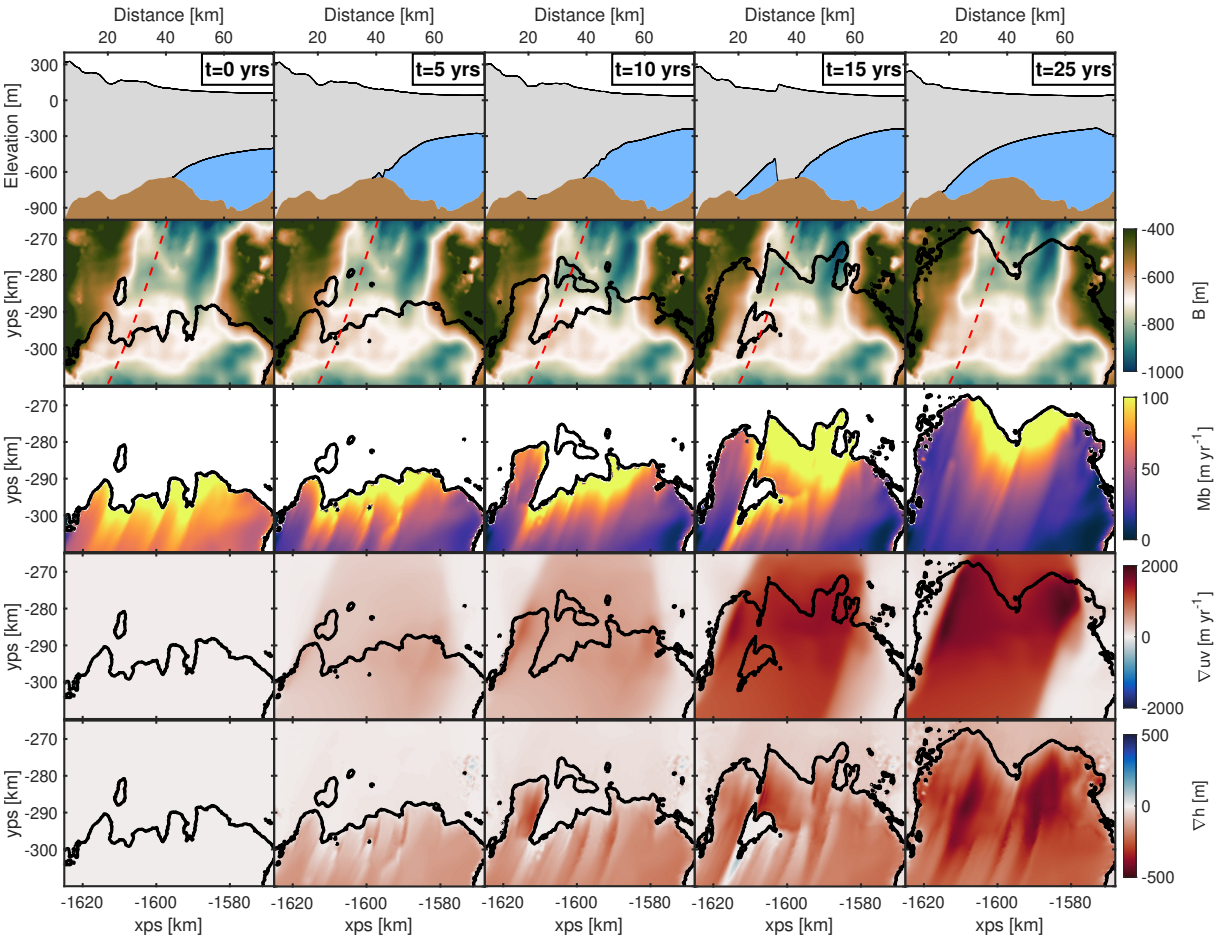

Fig. 6.3: Evolution of flowline profiles (**top row**), grounding line position over bed elevation (**second row**), basal melt rate (third row), change in ice speed (**fourth row**) and change in ice thickness (**bottom row**) during the WARM25 experiment. The columns from left to right show results after t =0, 6, 9, 12, 15 years. Changes in speed and thickness are with respect to $t = 0$ years.

in size, leaving only a small region of the ice shelf still grounded on the ridge. This is the sequence of events that happened in the 1970s (Jenkins et al., 2010; Mouginot et al., 2014). Eventually, after 18 years, the ice shelf completely detaches from the ridge and the grounding line stabilizes on the prograde slope of a seabed rise 20 to 30 km upstream of the ridge (Fig. 6.6). The glacier stops accelerating and there is a gradual decrease in ice flux across the grounding line as the glacier approaches a new stable state (Fig. 6.4c). This is consistent with observations of PIG stabilizing at an ice plain in the 1990s (Mouginot et al., 2014; Park et al., 2013).

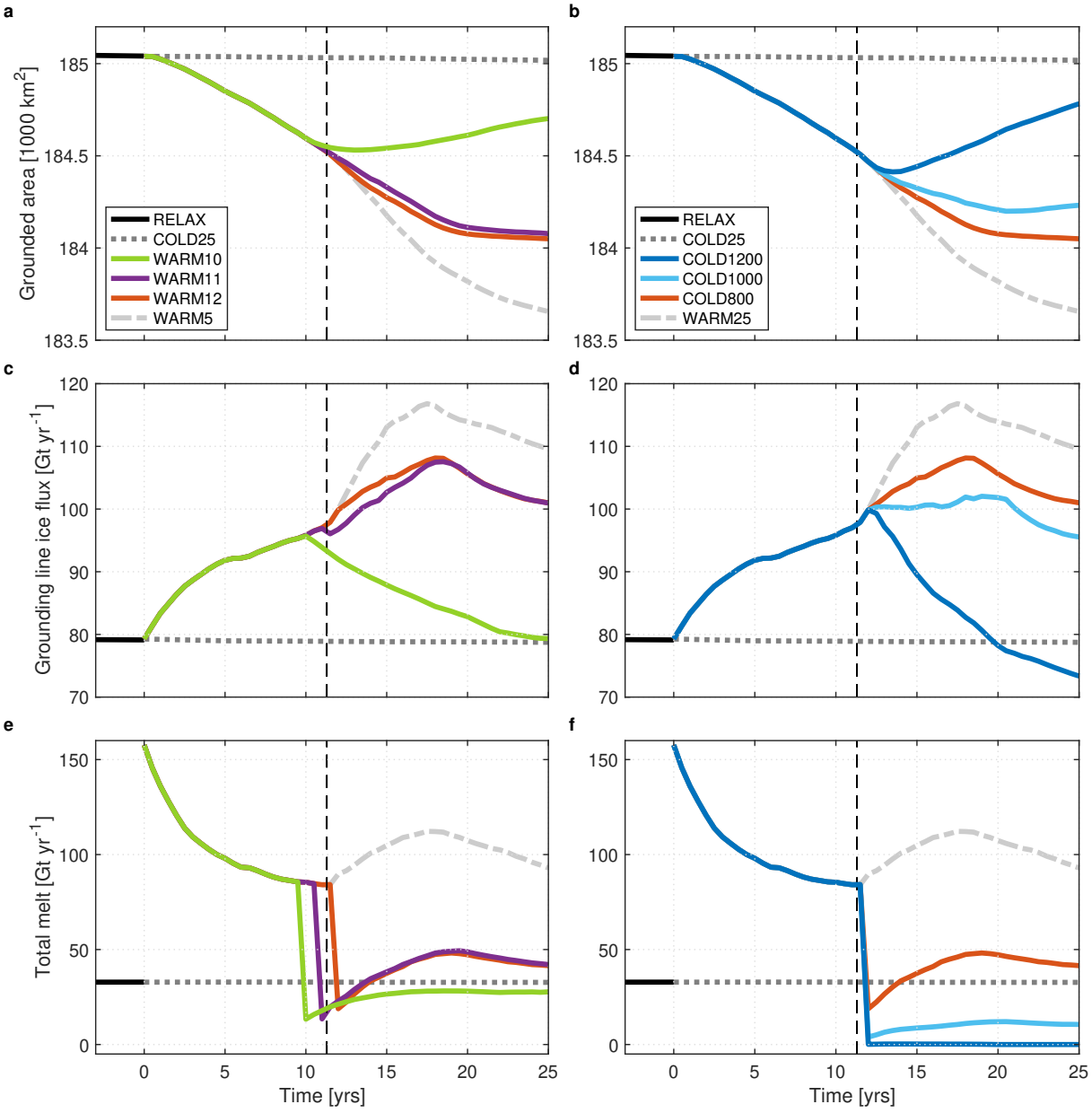

Fig. 6.4: Time evolution of the total grounded area (**a,b**), ice flux across the grounding line (**c,d**) and integrated basal melt rate (**e,f**) for the reversibility experiments. The final three years of the relaxation run using cold forcing is shown in solid black, and the two control runs with continuous cold and warm forcing for 25 years are shown in dark grey dotted and light grey dash-dotted, respectively. The green, purple and red solid lines in **a**, **c**, and **e** show warming for 10, 11 and 12 years respectively, with cold forcing thereafter. The dark blue, light blue and red solid lines in **b**, **d**, and **f** show warming for 12 years followed by cold forcing using thermocline depths of 1200 m, 1000 m and 800 m respectively. The vertical black dashed line indicates the time of melting starting upstream of the ridge (11.3 yrs). Note, the WARM12 and COLD800 show the same result in both sets of panels. Details of these perturbations experiments are summarized in Table 6.1.

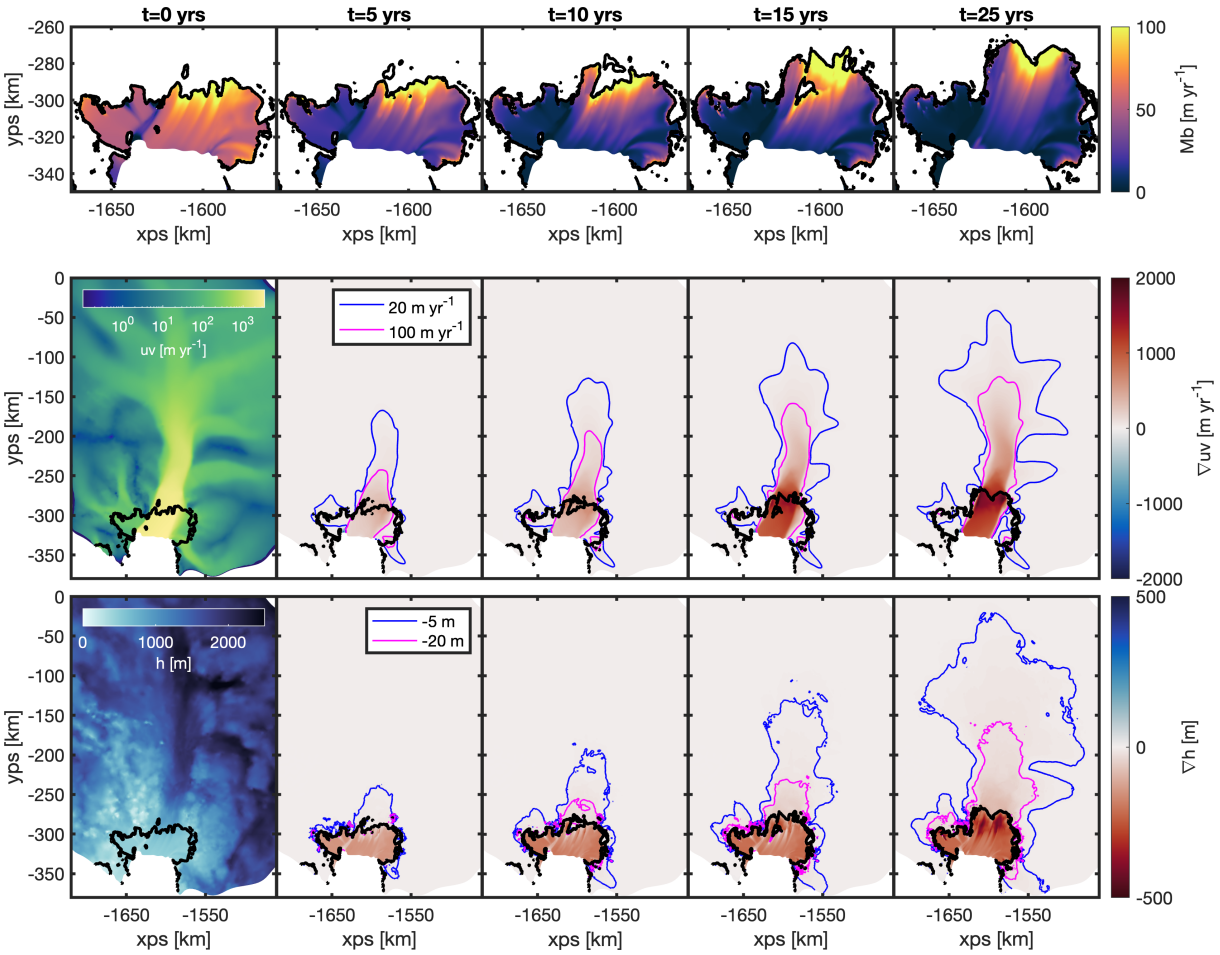

Fig. 6.5: Time evolution of ice shelf basal melt rate (Mb; **top row**), surface ice speed changes (∇uv; **middle row**) and ice thickness changes (∇h; **bottom row**) during the WARM25 experiment, after $t = 0, 5, 10, 15, 25$ years. The changes in speed and thickness are relative to $t = 0$, which is shown in the first column. Contours are shown in the middle and bottom rows to indicate the spreading of acceleration and thinning inland.

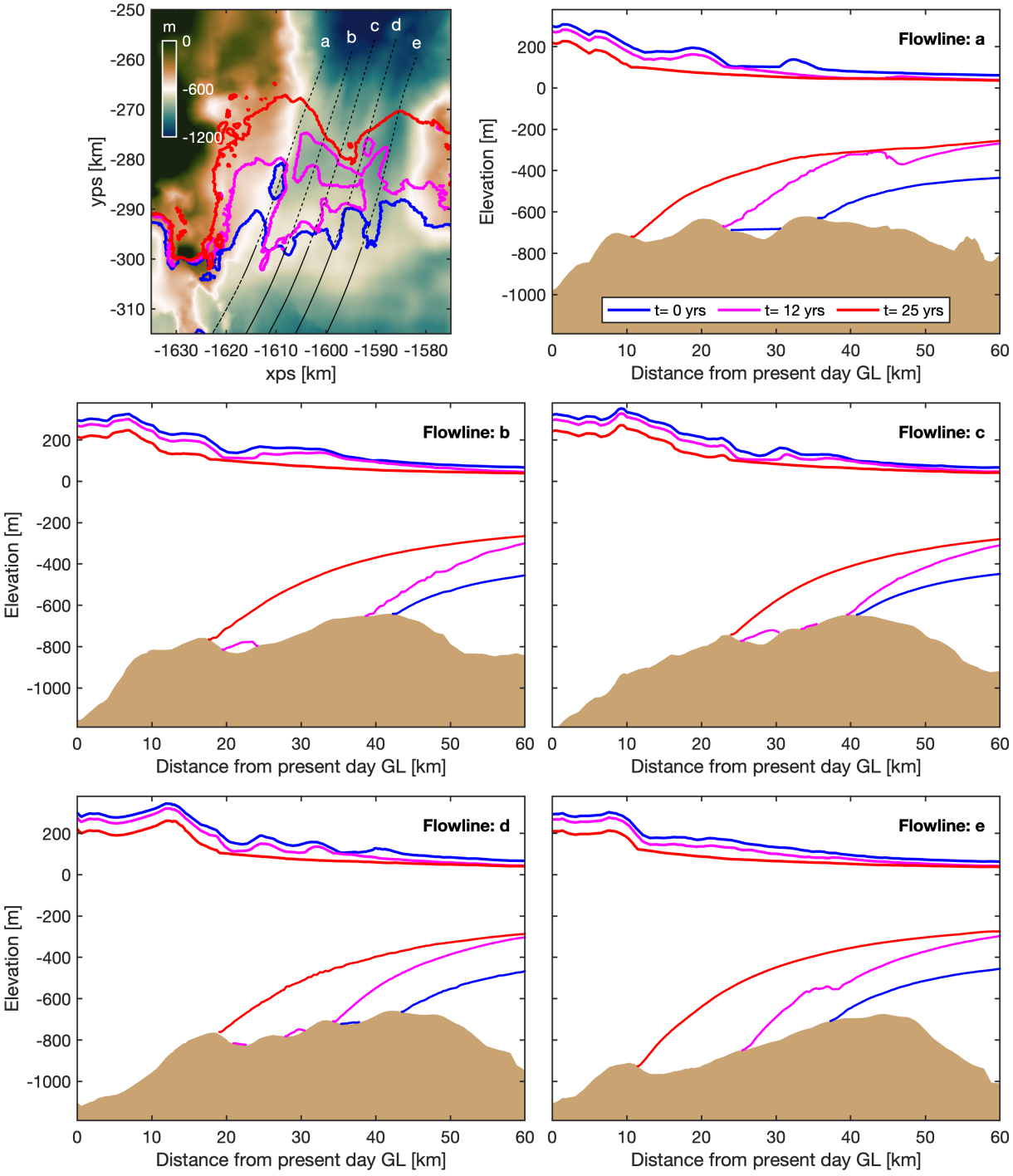

Fig. 6.6: Flowline profiles after $t = 0, 12, 25$ years during the WARM25 experiment. All profile lines start at the present-day grounding line position, as shown on the bed elevation plot.

6.4.2 Duration of warm forcing

The constant forcing experiment showed that sustained warming leads to substantial thinning and acceleration, causing a 20 to 30 km retreat. Our second set of experiments tests whether shorter, more realistic warm anomalies would also be sufficient to force PIG off the ridge and initiate a retreat. To best represent the 1940s situation, we first applied warming for 12 years to ensure melting occurs upstream of the ridge. This then represents the oceanic connection being established between the inner and outer cavities (Smith et al., 2017). After the warming we subsequently applied cold forcing for 25 years to represent the shift back to normal conditions after the 1940s El Niño event (Schneider and Steig, 2008).

Figure 6.7 shows that despite stopping the warm anomaly after 12 years, the grounding line continues to retreat to the ice plain upstream, without any additional forcing. Following the warm anomaly, when cold forcing is re-applied, mean melt rate immediately decreases from 31 m yr^{-1} to 11 m yr^{-1}. Integrated melt decreases from 84 Gt yr^{-1} to 19 Gt yr^{-1}, which is lower than at the end of the constant cold simulation (Fig. 6.4). This is because the ice shelf is thinner than when it is grounded on the ridge. Despite this drop in overall melt, it is insufficient to stop the increase in ice flux or reverse the grounding line retreating.

We also ran shorter warm anomalies of 10 and 11 years, where a switch to cold forcing occurs before the melting starts upstream of the ridge. Figure 6.4a,c,e shows that after 11 years of warming, there is continued retreat with a loss of grounded area, increased ice flux and the final configuration coinciding with the 12 year simulation. When we stopped warm forcing after 10 years, at least a year before there is melting upstream, this allowed the ice shelf to thicken leading to an increase in buttressing. Consequently, upstream thinning was reduced, and there was no connection between the upstream lakes and the outer cavity. There was a decrease in ice flux and a re-advance of the grounding line, eventually recovering its original position on the ridge.

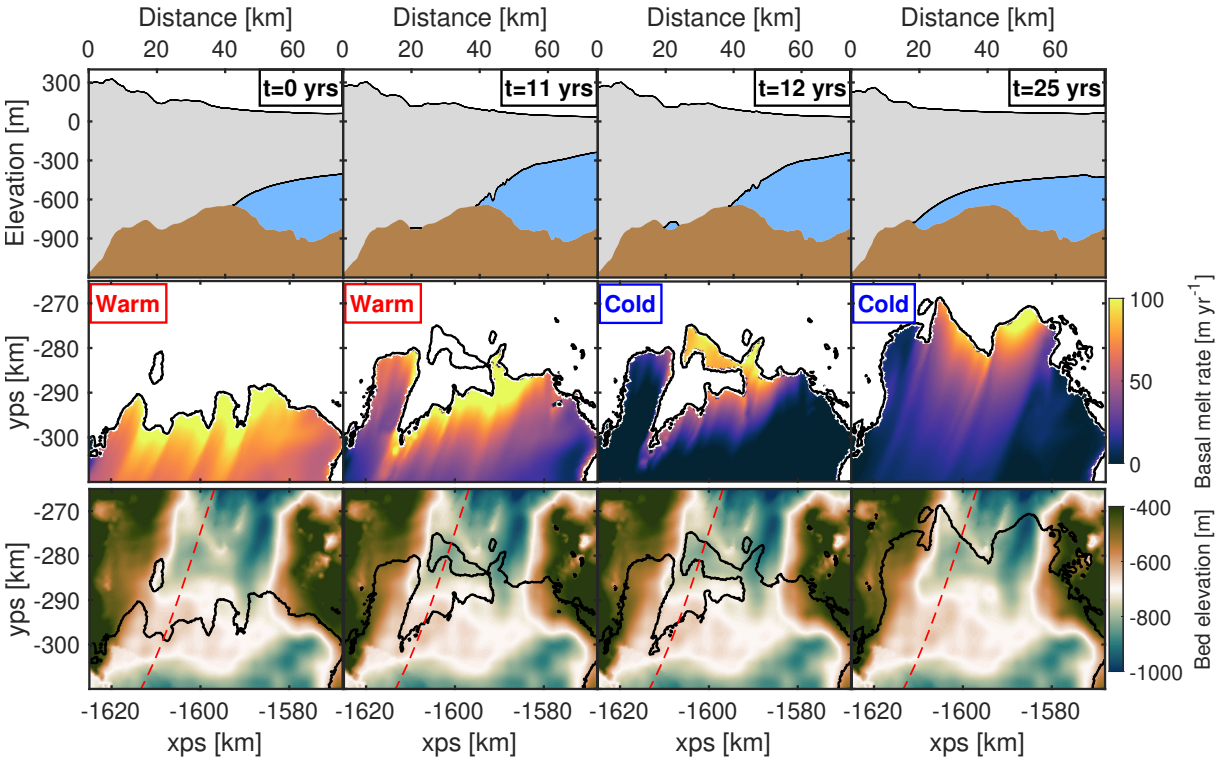

Fig. 6.7: Evolution of flowline profiles (**top row**), basal melt rate (**middle row**) and grounding line position on bedrock elevation (**bottom row**) for the WARM12 experiment. Warm forcing is applied for 12 years, until melting occurs upstream of the ridge, then cold forcing is applied thereafter to test for reversibility.

6.4.3 Magnitude of cold forcing

The third set of perturbation experiments shows that only extreme cold forcing, which causes much lower melt, can stop and reverse the retreat of PIG from the ridge (Fig. 6.4b,d,f). After a warm anomaly for 12 years, we lower the thermocline in the melt parameterization to 1200 m, so the bottom of the upper cold layer is at 800 m, and therefore below the depth of the cavity grounding line. This causes the overall melt to decrease to almost zero for the rest of the simulation. This was enough to stop the mass loss and decline in grounded area, and reverse the retreat. A more realistic cold parameterization, with a thermocline depth of 1000 m, gives mean melt rates of 2 to 5 m yr^{-1} and integrated melt of 4 to 12 Gt yr^{-1}, which is a third of the original cold forcing. However, this is not sufficient to stop the already retreating grounding line.

6.4.4 Sensitivity of reversibility

The previous experiments showed that the response of a 1940s PIG to changes in basal melting varies according to the duration of warm forcing and the magnitude of cold forcing

that follows. To extend these results we ran further tests, which cover a wider parameter space, to assess the impact of different forcing. Figure 6.8 shows that a shorter period of only 2 to 5 years of warmer forcing, with thermocline depths 400 to 550 m, can cause an irreversible retreat back to the ice plain, despite 50 years of cold forcing after the warm anomaly. Whereas, melting caused by a deeper thermocline of at least 700 m, during the warm period, has to be applied for at least 40 years to cause an unstable response.

After a period of warming for 12 years, once the upstream lakes connect with the outer cavity and the grounding line starts to retreat, cold forcing with thermocline depths of 1000 m and above are not sufficient to stop the retreat or allow recovery back to the ridge, despite being applied for at least 50 years. Whereas, deeper thermocline depths of 1050 m and below can cause re-grounding and a complete re-advance to the ridge, after at least eight years of cold forcing.

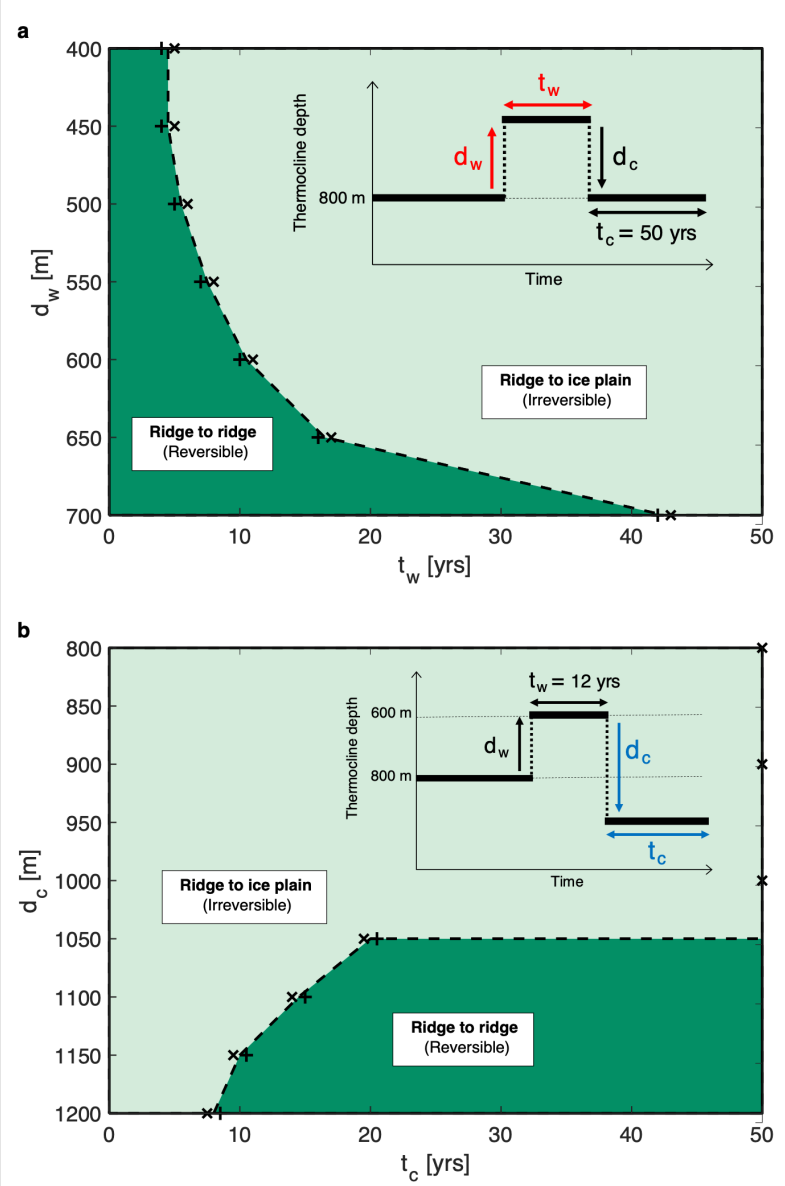

Fig. 6.8: Reversibility of PIG depending on the duration of forcing (t_w, t_c) and the thermocline depth (d_w, d_c) in the separate warm and cold stages. The green areas illustrate two different final grounding line positions (ridge and ice plain) after a period of warm forcing followed by cold forcing, with a starting position at the ridge. Dark green areas indicate parameters that lead to a final position at the ridge, and light green regions encompass all parameter combinations which lead to irreversible retreat back to the ice plain. (**a**) Warm forcing is varied, then cold forcing is applied for 50 years with a 800 m deep thermocline. (**b**) Cold forcing is varied, after an initial warm anomaly of 12 years with a 600 m thermocline. Inset in each panel is a schematic of the model forcing setup. The dashed line between the two areas indicates the approximate change in behaviour between reversible and irreversible simulations, where we have used a discrete number of model simulations (markers) to generate this parameter space.

6.5 Discussion

6.5.1 Cold forced stability

Our modelling results show that the subglacial ridge beneath present-day PIG ice shelf provides a steady and stable grounding line position after the glacier advances forward with no basal melting (Fig. 6.1). The glacier remains grounded on the ridge when forced with cold ocean conditions, despite some thinning of grounded and floating ice, and finds a new steady state on small prograde or flat sections along the ridge crest (Fig. 6.6). It remains in this position because the highest basal melt rates, which correspond to the warm Circumpolar Deep Water, are limited to below the depth of the ridge crest, resulting in little thinning (Fig. 6.2). This modelling result is consistent with sediment core observations that suggest PIG had been grounded on the ridge since the early Holocene (Smith et al., 2017).

6.5.2 Warm forced retreat

The first of our aims was to determine if a warm anomaly could initiate a PIG retreat from its stable position on the ridge, which is likely what happened in the 1940s (Schneider and Steig, 2008; Smith et al., 2017). To replicate warmer ocean conditions we applied a step change in forcing, which corresponded to a shallower thermocline and therefore higher basal melt rates (Fig. 6.2). During the first 10 years of warming there was thinning and acceleration (Fig. 6.3), which propagated far inland along the main trunk (Fig. 6.5), leading to an increase in ice discharge across the grounding line (Fig. 6.4). Ice shelf thinning is known to have upstream effects, through a loss of buttressing, especially where thinning is concentrated near to the grounding line or margins (Fürst et al., 2016; Reese et al., 2018a). A similar scenario was observed for PIG and other neighbouring glaciers in the mid to late 2000s when thinning, acceleration and mass loss followed a period of warm ocean conditions in the Amundsen Sea (Dutrieux et al., 2014; Jenkins et al., 2018; Konrad et al., 2017; Mouginot et al., 2014). Our modelling results combined with observations demonstrate that glacier flow and mass loss can be sensitive to changes in ocean conditions, when grounded on a topographic high, and this can happen simultaneously across multiple glaciers.

The thinning and acceleration of grounded ice in our warm experiment led to the formation and merging of two lakes just upstream of the ridge (Fig. 6.3). The location and evolution of these lakes are where the ice becomes marginally afloat over the deep lying bedrock, and this has also been shown in a previous idealized modelling study (Rydt and Gudmundsson, 2016). If warm forcing continues until 12 years, the lakes connect with

the outer cavity on the south side of the shelf, where there is faster grounding line retreat down a steep retrograde bed (Fig. 6.6). This connection between the inner and outer main cavity leads to high basal melting upstream of the ridge. We can interpret this as the opening of the inner cavity to warm ocean waters (Smith et al., 2017), which causes thinning and grounding line retreat in the central trunk. When this happens, an ice rumple forms on the shallower bedrock and the glacier is no longer in a stable state.

6.5.3 Unstable response

The second aim of this study was to determine whether the retreat of PIG from the ridge could be stopped by removing the warm anomaly and returning to normal or cold basal conditions. This was motivated by the variable ocean conditions that are observed in the Amundsen Sea, which directly influence basal melt rates inside the ice shelf cavity (Dutrieux et al., 2014). Our reversibility experiments show that removing the warm forcing after 12 years, or when high basal melting is already occurring upstream of the ridge, does not stop the retreating grounding line or ongoing mass loss (Fig. 6.7). After a connection is established between the inner and outer cavities, there is a sharp increase in grounded and floating ice velocities and greater ice flow across the grounding line. This is likely due to a loss of buttressing as the ice shelf continues to thin and unground from the ridge (Gudmundsson et al., 2019). With a greater drawdown of upstream ice, there is further thinning and retreat, signalling a change in behaviour and the possible crossing of a tipping point (Reed et al., 2022; Rydt and Gudmundsson, 2016).

The increase in grounding line ice flux as the ice thins and retreats across the deep sections of bed agrees with observations of PIG ice shelf becoming detached from the ridge between 1975 and 1982 (Jenkins et al., 2010; Mouginot et al., 2014). A surface impression on the ice shelf disappears as contact is lost with the bed, consistent with observed behaviour in the 1970s (Jenkins et al., 2010). Following the ungrounding, our results show that the glacier stabilizes on the prograde slope of a seabed rise 20 to 30 km upstream of the ridge and there is a gradual decrease in ice flow. This is likely what occurred in the late 1980s to early 1990s, when PIG was grounded in a similar position at an “ice plain” (Corr et al., 2001; Park et al., 2013). This period may also have coincided with cold ocean conditions (Dutrieux et al., 2014; Jenkins et al., 2016; Thoma et al., 2008), which would have facilitated the stabilization.

These results suggest that PIG underwent an unstable retreat from the subglacial ridge in the 1940s (Smith et al., 2017), which could have been initiated by a temporary increase in basal melt. The change in melt was possibly due to a shoaling thermocline, following a tropically forced climate anomaly in West Antarctic (Schneider and Steig, 2008). The irreversible retreat would have been unaffected by a reverse of ocean conditions in the

following years and continued losing mass through the 1970s and 1980s (Jenkins et al., 2010; Mouginot et al., 2014). The glacier then stabilized when it reached an ice plain in the 1990s. This demonstrates that although an increase in basal melt is the initial cause of mass imbalance and retreat, it can be the dynamical response to bed geometry that becomes the dominant driver of mass loss once the forcing is removed.

6.5.4 Sensitivity of irreversibility

The final aim of this study was to investigate the sensitivity of irreversible retreat to different basal melt forcing. We know from observations that ocean conditions in the Amundsen Sea vary on interannual to decadal timescales (Dutrieux et al., 2014; Jenkins et al., 2016; Jenkins et al., 2018), which is partly influenced by the varying strength of westerly winds over the continental shelf break (Steig et al., 2012; Thoma et al., 2008). Future predictions under a high emissions scenario show persistent shelf break mean westerlies by 2100, which suggests there could be more prevalent warm ocean conditions in the Amundsen Sea (Holland et al., 2019). Therefore, these sensitivity experiments were designed as hypothetical scenarios to gauge the influence of more extreme ocean conditions on the retreat of a glacier from a prominent seabed ridge.

Our modelling results show that a 12 year period of typical present-day warm conditions, which uses a basal melt parameterization with a 600 m deep thermocline, is sufficient to cause irreversible retreat from the ridge (Fig. 6.8a). This same basal melt parameterization applied for 10 years or less can still lead to the formation of upstream lakes. However, they do not merge with the outer cavity and thus the glacier is able to thicken and re-advance. Our shallowest thermocline results, above 550 m, show that if there is a thicker layer of CDW on the shelf, it is possible that an unstable response could be triggered in just two to five years. This suggests that a future phase of irreversible retreat could be initiated with just a short period of increased melting, and it is therefore not necessary for there to be either a sustained period of melting or an additional event after the initial anomaly has finished. Model simulations suggest that shelf temperatures and basal melting have increased over the past century, which if continues, could lead to this increased melting beneath the ice shelf (Naughten et al., 2022).

We also show that once PIG is retreating from the ridge after a warm anomaly, only extreme cold conditions, where melt decreases to zero very quickly, can stop the retreat (Figs. 6.4b,d,f and 6.8b). This indicates that a hysteretic behaviour exists in response to varying basal melt, where much lower melt is required to advance the glacier back to its original position (Favier et al., 2014; Reed et al., 2022). Lower melt is possible if the ridge blocks the deepest warm waters (Dutrieux et al., 2014; Rydt et al., 2014), but the melt parameterization that is used here does not take that into account. However, in support

of the results here, a coupled modelling study has shown that a switch to pre-anomaly conditions is not necessarily sufficient to stop a retreat from the ridge, despite blocking at the ridge (Rydt and Gudmundsson, 2016).

The timescales of irreversible retreat that we show with these results should be treated with caution and not used as an exact prediction for future retreat. We have used a depth dependent melt rate parameterization which only captures the first order response to melting, and neglects any ocean-ice feedbacks or topographic influences. More realistic simulations using a coupled ice-ocean model would further improve these results, and allow us to identify the additional influence that topography has on the ocean forcing, as has been shown in previous idealized experiments (Rydt and Gudmundsson, 2016; Rydt et al., 2014).

We have also used present-day input data, such as ice velocities and geometry, to generate spatially varying slipperiness and ice rate factor fields that are unlikely to model the exact evolution of a 1940s PIG (Rydt et al., 2021). However, this study shows the melt sensitivity of an approximate 1940s glacier as it retreats from the ridge. Whilst PIG may now be in a more stable position compared to recent years (Urruty et al., 2022), these modelling results give us an insight into the dynamical behaviour of a glacier that is forced with changing basal melt when grounded on a topographic high.

6.6 Conclusion

This study set out to investigate the melt sensitivity of the historical retreat of PIG from a subglacial ridge 40 km downstream from its present-day grounding line position. Our ice sheet modelling results show that the ridge provides a stable position for the glacier when there is either low or zero basal melting due to cold ocean conditions. We found that an increase in basal melt rates, which are observed during typical warm years in the Amundsen Sea, can cause substantial thinning and acceleration and are sufficient to force the glacier off the ridge, initiating a retreat. After 12 years of warm forcing, once high melting occurs upstream of the ridge, the retreat becomes irreversible despite a removal of the warm anomaly and a return to cooler conditions. Much lower melt is required to stop the retreat and allow a recovery back to the ridge, which indicates there is a hysteresis in response to basal melting. Melt sensitivity experiments show that shorter, sub-decadal, warm anomalies with higher melt rates can also lead to irreversible retreat. We have used a simplified depth dependent melt rate for these experiments, but this has shown the direct effect of variable basal melt on the retreat of PIG from the ridge. These results demonstrate that as warm conditions become more prevalent in the Amundsen Sea, an unstable response of glaciers in a similar configuration cannot be ruled out. Future

modelling experiments that use more realistic ocean forcing, taking into consideration the effects of topography, will increase certainty of the effects of changing melt on PIG and the wider West Antarctic Ice Sheet.

Chapter 7

Discussion and conclusions

The purpose of this thesis was to improve the current understanding of the transient evolution of Pine Island Glacier (PIG) during the last 80 years. It is likely that prior to the 1940s, PIG had been grounded in a stable position on a subglacial ridge 45 km downstream from its present-day position for a long period of time (Smith et al., 2017). Following a notable climate anomaly in the 1940s (Jenkins et al., 2016; Schneider and Steig, 2008), a pre-existing cavity beneath the glacier became connected to the open ocean and the glacier started to retreat from the ridge crest (Jenkins et al., 2010; Smith et al., 2017). By the early 1990s, the ice shelf had detached from the ridge and the grounding line had stabilized at an ice plain 30 km upstream of the ridge (Park et al., 2013). Questions remain about what initially caused the retreat from the ridge, and why it continued to retreat despite subsequent periods of cool ocean conditions (Dutrieux et al., 2014; Jenkins et al., 2018).

Consequently, the first aim of the thesis was to investigate how an idealized buttressed ice sheet responds to changes in external forcing, including ocean-driven basal melting and variations in ice flow parameters. The second aim was to apply this knowledge to a realistic case and determine whether a change in ocean forcing could have been responsible for the retreat of PIG from a subglacial ridge in the 1940s. Tied to this was the investigation of why, once PIG was retreating, it did not recover in the years that followed. The final aim was to explore the impact of different ocean driven basal melt on PIG when it was grounded on the ridge.

The following sections summarise the key findings from each research chapter, which were designed to answer the aims mentioned above. The limitations of the work is also discussed and how these issues might be addressed and extended in future research.

7.1 Chapter 4 summary

The aim of Chapter 4 was to investigate the response of a marine ice sheet to changes in ice shelf buttressing. The modelling experiments were carried out on an idealized three-dimensional ice sheet from a recent model intercomparison project, MISMIP+ (Asay-Davis et al., 2016). The bedrock topography consisted of a narrow channel on an incline with an overdeepening at the base. The model was spun up from an initial ice thickness of 100 m and run until a steady state was reached. The first modelling result showed that in the presence of ice shelf buttressing, a steady state grounding line was possible on the retrograde slope of the overdeepening. This is in agreement with previous studies that show the importance of lateral stresses on preventing the marine ice sheet instability (MISI) from occurring (Goldberg et al., 2009; Gudmundsson et al., 2012).

When basal melting was applied, the ice shelf thinned, which reduced its buttressing capacity. This led to an increase in ice flux across the grounding line, and subsequent thinning and retreat of grounded ice. Furthermore, results showed that the rate of retreat and mass loss was affected by how basal traction was implemented. The Weertman power law caused the slowest rate of retreat, whilst the Umbi, Schoof and Tsai laws, which incorporate an effective pressure term, led to the fastest retreat and rate of mass loss. This is consistent with other modelling results from other idealized and realistic studies (Brondex et al., 2017, 2019; Seroussi and Morlighem, 2018; Yu et al., 2018).

When basal melting is removed after 100 years, the ice sheet initially continues to retreat as it adjusts to the new forcing. However, eventually the thickening ice shelf, and resulting buttressing, is sufficient to cause an advance back towards to its initial steady state. This happens for all sliding laws. During the subsequent 900 years of imposing no melting, the rate of advance is an order of magnitude lower than the retreat rate. At the end of the 1000 year simulation, the grounding line does not recover its original position on the retrograde slope; mass lost due to basal melting over 100 years is not completely replaced by surface accumulation over the domain during the remaining 900 years.

Results from a comparison of melt parameterizations showed that elevated melting along the shear grounding lines may be responsible for greater mass loss and retreat compared to melting concentrated along the central grounding line. This implies that shear margins can have a dominating role in the mass balance of a glacier, which is consistent with results from a recent MIMISP+ study (Feldmann et al., 2022).

The final set of experiments examined whether a hysteresis was present in a buttressed marine ice sheet when subject to a changing flow parameter. This followed the same approach as in an earlier intercomparison project, MISMIP, which investigated a flowline example with no buttressing (Pattyn et al., 2012). Results in Chapter 4 show that by

varying the ice rate factor (ice softness) for a number of different channels widths, the ice sheet undergoes a hysteresis. Consequently, multiple steady states exist for the same forcing. The hysteresis loops implied that an unstable region exists on the prograde slope, and that this region moves further upstream as the channel widens. An analysis of the ice shelf buttressing further highlighted the importance of shear margins. In the narrower channels, where the side walls cover a larger fraction of the width, mass balance is largely controlled by the level of buttressing in the margins.

This chapter showed the impact that changes in ice shelf buttressing and flow properties can have on the flow of upstream ice. Further work could be undertaken to extend these results. For example, the mesh convergence analysis could also include meshes which have refinement in regions other than the grounding line, for example, in areas of high shear strain or high shear gradients, particular along the lateral margins. The mesh sensitivity could also show the effect of other sliding laws during the model spin up and basal melting stages.

In the MISMIP experiments a fixed calving front was used, which constrains the size of the ice shelf. This will likely impact the ice shelf buttressing when the ice sheet advances forward and may give biased results during the hysteresis. Further modelling experiments could allow the ice shelf to grow as the ice sheet thickens. The hysteresis experiments should also be repeated using other friction laws, as this has been shown to impact the rate of mass loss. The results at the end of this chapter could be investigated further to understand the cause of the hysteresis and the complex response of ice shelf buttressing in different channels widths.

7.2 Chapter 5 summary

The aim of the research presented in Chapter 5 was to extend the work from the previous chapter to a realistic case: could ocean driven changes in ice shelf thickness, and therefore buttressing, lead to the ungrounding and subsequent retreat of PIG from a subglacial ridge 80 years ago? If this was the case, why has PIG not recovered back to the ridge during the periods of cooler ocean conditions that followed?

Starting from a present day PIG configuration, the model was spun up with no basal melting until a steady state was established on the ridge. Once this was achieved, PIG was subjected to two separate periods of low and high melt, using the depth dependent melt rate parameterization. The melt rate was representative of cool and warm ocean conditions which have been observed in Pine Island Bay since the mid 1990s.

After 50 model years, both periods of forcing led to contrasting results. The low melt scenario resulted in some thinning and acceleration but only a small retreat across the

ridge crest, and a new steady state was found still grounded on the ridge. The high melt, on the other hand, led to substantial acceleration, thinning and retreat from the ridge. A key finding during the warm forced retreat was the formation and merging of upstream subglacial lakes as the grounded ice thinned over deep bedrock. This has been discussed as a precursor to the retreat by Smith et al. (2017) and also observed in coupled ice-ocean modelling of an idealized representation of PIG (Rydt and Gudmundsson, 2016). The results in Chapter 5 show that once the merged lakes connect with the outer cavity, there is a rapid retreat back to the next topographic high point.

During the warm forcing, there are several instances of fast retreat over sections of retrograde bed, prompting the question of whether MISI played any role in the recent retreat of PIG. However, a rapid retreat is not necessarily an indication of an unstable response and a stability analysis was carried out to assess whether the retreat from the ridge may have crossed a stability threshold. Individual model simulations, each with higher basal melting than the previous, were run to a steady state from an initial position on the ridge. This produced several equilibrium positions from the ridge to the upstream topographic high point. Another set of simulations, starting from the upstream position, were run with the reverse forcing (melt lowering). A comparison of the equilibrium positions in both sets of runs (retreat and advance) showed that a hysteresis was present, with an unstable region across the retrograde landward slope of the ridge. This shows that after the grounding line retreats to the upstream topographic high, a large reverse in forcing conditions is required to achieve the same steady state position back on the ridge.

The stability analysis in Chapter 5 suggests that by the early 1970s, when PIG had already started retreating from the ridge (Jenkins et al., 2010), a tipping point had been crossed, whereby further retreat was inevitable despite a return to cooler conditions (Jenkins et al., 2016). The irreversible phase of retreat came to a halt when the grounding line stabilized upstream at an ice plain in the early 1990s (Park et al., 2013). These results show, for the first time, a MISI occurring which is validated by observations.

A limitation of these results is the use of a simplified melt parameterization to represent ocean conditions beneath PIG. A repeated analysis using the MISMIP+ parameterization, which has more physical constraints, showed the same outcome. However, neither parameterization take into account the impacts of topography such as blocking of deep warm water by the ridge (Dutrieux et al., 2014) or ice-ocean feedbacks when fresh water enters the cavity due to basal melting (Rydt and Gudmundsson, 2016; Rydt et al., 2014). Despite the use of a simplified melt parameterization, the initial behaviour of retreat, the speed at which it progresses, and the final ungrounding of a pinning point above the ridge are all comparable with satellite observations and sediment records from the 1940s and 1970s (Jenkins et al., 2010; Smith et al., 2017).

7.3 Chapter 6 summary

The previous chapter established the presence of a hysteresis and a possible tipping point that had been crossed during the recent retreat of PIG from a subglacial ridge. This was achieved by incrementally changing the melt rate and running the ice sheet model to a steady state to see how far the grounding line would move under each forcing. However, in reality, ocean conditions of importance to ice sheet stability vary on seasonal to decadal timescales (Dutrieux et al., 2014; Jenkins et al., 2016), and if a climatic anomaly was responsible for the initial retreat of PIG in the 1940s, it would only have been a temporary change to the average conditions (Schneider and Steig, 2008). Therefore the aim of Chapter 6 was to investigate the impact of shorter warm anomalies on the retreat of PIG, and whether reversibility could be achieved once it had already started retreating.

These basal melt experiments were run following a model spin up and relaxation to establish an approximate 1940s PIG grounded on the ridge. After applying high basal melting for just 5 years, this caused an inland propagation of thinning and acceleration along the central trunk, subsequently leading to an increase in grounding line ice flux. A similar event was recently observed throughout the Amundsen Sea Embayment in the late 2000s, when PIG and neighbouring glaciers experienced thinning, acceleration and mass loss following a short period of warm ocean conditions (Dutrieux et al., 2014; Jenkins et al., 2018; Konrad et al., 2017; Mouginot et al., 2014).

Similar to the previous chapter, the thinning and acceleration of grounded ice led to the formation and merging of two lakes just upstream of the ridge. This occurs in the first ten years of high melting, and after another two years they connect with the outer cavity. Once this happens, there is high basal melting of the deeper grounding line upstream of the ridge, and this represents the opening of the inner cavity to warm ocean waters (Rydt and Gudmundsson, 2016; Smith et al., 2017).

The previous chapter showed that once the grounding line starts to retreat across the retrograde slope, it undergoes an unstable response and crosses a tipping point. This is supported by the reversibility experiments in Chapter 6. Reverting to cold forcing after the lakes merge with the outer cavity does not stop the retreating grounding line or ongoing mass loss. The glacier continues to retreat, with only a small region of the ice shelf in contact with the ridge, which leads to the formation of an ice rumple on the shallower bedrock. This agrees with satellite imagery in the 1970s of a lightly grounded ice shelf over the ridge (Jenkins et al., 2010). During this period there is an increase in flux across the grounding line, which is likely due to a loss of buttressing as the ice shelf continues to thin and unground from the ridge (Gudmundsson et al., 2019). This increased ice flux is consistent with observations of the PIG ice shelf becoming detached

from the ridge between 1975 and 1982 (Jenkins et al., 2010; Mouginot et al., 2014).

After the ice shelf ungrounds from the ridge, the modelling results show the glacier stabilizing on the prograde slope of a topographic high 20–30 km upstream of the ridge. This agrees with observations of a decrease in ice flux in the early 1990s when PIG was grounded in a similar position at an "ice plain" (Corr et al., 2001; Park et al., 2013). This period may also have coincided with cold ocean conditions (Dutrieux et al., 2014; Jenkins et al., 2016; Thoma et al., 2008), which would have facilitated the stabilization.

The modelling results in Chapter 6 suggest that PIG underwent an unstable retreat from the subglacial ridge in the 1940s (Smith et al., 2017), which could have been initiated by a temporary increase in basal melt. The irreversible retreat would have been unaffected by a reverse of ocean conditions in the following years and PIG continued losing mass through the 1970s and 1980s (Jenkins et al., 2010; Mouginot et al., 2014). This demonstrates that although an increase in basal melt could have been the initial cause of mass imbalance and retreat, it is likely that the dynamical response to bed geometry became the dominant driver of mass loss once the melt forcing was reduced.

The final results in Chapter 6 show the sensitivity of irreversible retreat to different basal melt forcing. Ten years of warm forcing leads to the formation of upstream lakes but no connection with the outer cavity, which means no high melting or unstable retreat. However, a shallower thermocline could lead to an irreversible retreat in less than 10 years. Once PIG is retreating from the ridge, a much lower thermocline depth (thus exposing the ice shelf to less melt) is needed to stop the retreat due to the deep upstream grounding lines. This indicates that a hysteretic behaviour exists in response to varying basal melt, where much colder forcing is required to advance the glacier back to its original position (Favier et al., 2014; Reed et al., 2022).

The timescales of irreversible retreat that are shown in these results should be treated with caution and not used as an exact prediction for future retreat. As mentioned in the previous chapters, a simple depth dependent melt rate parameterization was used, which only captures the first order response to melting, and neglects any ocean-ice feedbacks or topographic influences. This is important because the ridge can block deep warm waters, which can impact the melting of deep grounding lines upstream of the ridge (Dutrieux et al., 2014). More realistic simulations using a coupled ice-ocean model would further improve these results, and allow us to identify the additional influence that topography has on the ocean forcing, which has been shown in previous idealized experiments (Rydt and Gudmundsson, 2016; Rydt et al., 2014).

A further limitation of these results was the use of present day input data to generate the spatially varying ice rate factor and slipperiness fields. This is unlikely to model the exact evolution of a 1940s PIG as has been discussed by Rydt et al. (2021). Further

research could use input data that is from a closer time period, or test different rate factor and slipperiness fields to make these results more robust. It would also be useful to repeat these experiments with different friction laws, as the results in Chapter 4 showed that mass loss can depend on the representation of basal traction at the bed.

The results in Chapter 6 show the melt sensitivity of an approximate 1940s glacier as it retreats from the subglacial ridge. Whilst PIG may now be in a more stable position compared to recent years (Urruty et al., 2022), these modelling results give us an insight into the dynamical behaviour of a glacier that is forced with changing basal melt when grounded on a topographic high.

7.4 Concluding remarks

This thesis used an ice flow model to investigate the response of PIG to changes in ice shelf basal melting when it was grounded on a bedrock ridge 40 km downstream from its present day position. The aim of this was to determine whether the marine ice sheet instability played any role in its retreat following a tropically forced perturbation in the 1940s.

Modelling experiments on an idealized representation of PIG showed that ocean induced ice shelf melting can cause a buttressed ice sheet to accelerate and retreat when grounded in a stable position on a retrograde slope. The rate of mass loss is affected by how the basal traction is treated in the model, with the commonly used Weertman nonlinear power law causing the least retreat. Experiments showed that the ice sheet undergoes hysteretic behaviour in response to variations in ice softness, and buttressing along its shear margins is an important control on the flow of upstream ice.

This work was extended to a 1940s PIG and its response to basal melting. Ice flow modelling results show that a sustained increase in melting beneath the ice shelf causes rapid mass loss due to the loss of buttressing. Thinning of grounded ice causes the glacier to retreat from a stable position on a bedrock ridge to an upstream ice plain. Steady state model simulations suggest that an unstable region exists on the landward retrograde slope of the ridge, and therefore the retreat of PIG had already crossed a tipping point by the early 1970s. Further modelling results show that a 12 year period of warm conditions can lead to irreversible retreat unless basal melt is reduced to near-zero which closes the connection between upstream subglacial lakes and the outer cavity.

These modelling results suggest that PIG experienced an induced instability in response to a perturbation in the 1940s, following a climate anomaly in West Antarctica. Once PIG started to unground from the ridge and enter deeper water, a return to cooler conditions was not sufficient to stop its inevitable retreat to the next bed rise. To extend

these results, future work should make use of more realistic ocean forcing and feedbacks, such as in coupled ice-ocean models. This would take into account the effects of topography and potential blocking of deep warm waters that is lacking in the melt parameterizations used here. This will help to better understand the competing effects of bed profile, ocean forcing and ice dynamics in retreating ASE glaciers.

References

Adusumilli, S., Fricker, H. A., Medley, B., Padman, L. and Siegfried, M. R. (2020) Interannual variations in meltwater input to the Southern Ocean from Antarctic ice shelves. *Nature Geoscience*, 1–5.

Alevropoulos-Borrill, A., Nias, I., Payne, A., Golledge, N. and Bingham, R. (2020) Ocean forced evolution of the Amundsen Sea catchment, West Antarctica, by 2100. *The Cryosphere Discussions*, **14**, 1245–2020.

Alley, K. E., Scambos, T. A., Alley, R. B. and Holschuh, N. (2019) Troughs developed in ice-stream shear margins precondition ice shelves for ocean-driven breakup. *Science Advances*, **5** (10).

Arndt, J. E., Larter, R. D., Friedl, P., Gohl, K., Höppner, K., Afanasyeva, V., Bickert, T., Bohaty, S., Dziadek, R., Ebermann, B., Ehrmann, W., Esper, O., Frederichs, T., Freudenthal, T., Gebhardt, C., Hillenbrand, C. D., Hochmuth, K., Klages, J., Küssner, K., Najman, Y., Pälike, H., Riefstahl, F., Ronge, T., Scheinert, M., Pereira, P. S., Smith, J., Uenzelmann-Neben, G., van de Flierdt, T. and Zundel, M. (2018) Bathymetric controls on calving processes at Pine Island Glacier. *Cryosphere*, **12** (6), 2039–2050.

Asay-Davis, X. S., Cornford, S. L., Durand, G., Galton-Fenzi, B. K., Gladstone, R. M., Gudmundsson, G. H., Hattermann, T., Holland, D. M., Holland, D., Holland, P. R., Martin, D. F., Mathiot, P., Pattyn, F. and Seroussi, H. (2016) Experimental design for three interrelated marine ice sheet and ocean model intercomparison projects: MISMIP v. 3 (MISMIP+), ISOMIP v. 2 (ISOMIP+) and MISOMIP v. 1 (MISOMIP1). *Geosci. Model Dev*, **9**, 2471–2497.

Barletta, V. R., Bevis, M., Smith, B. E., Wilson, T., Brown, A., Bordoni, A., Willis, M., Khan, S. A., Rovira-Navarro, M., Dalziel, I., Smalley, R., Kendrick, E., Konfal, S., Caccamise, D. J., Aster, R. C., Nyblade, A. and Wiens, D. A. (2018) Observed rapid bedrock uplift in Amundsen Sea Embayment promotes ice-sheet stability. *Science*, **360**(6395), 1335–1339.

Barnes, J. M., Santos, T. D. D., Goldberg, D., Gudmundsson, G. H., Morlighem, M. and Rydt, J. D. (2021) The transferability of adjoint inversion products between different ice flow models. *Cryosphere*, **15** (4), 1975–2000.

Bindschadler, R., Choi, H., Wichlacz, A., Bingham, R., Bohlander, J., Brunt, K., Corr, H., Drews, R., Fricker, H., Hall, M., Hindmarsh, R., Kohler, J., Padman, L., Rack, W., Rotschky, G., Urbini, S., Vornberger, P. and Young, N. (2011a) Getting around Antarctica: new high-resolution mappings of the grounded and freely-floating boundaries of the Antarctic ice sheet created for the International Polar Year. *The Cryosphere*, **5**(3), 569–588.

Bindschadler, R., Vaughan, D. G. and Vornberger, P. (2011b) Variability of basal melt beneath the Pine Island Glacier ice shelf, West Antarctica. *Journal of Glaciology*, **57** (204), 581–595.

Blatter, H. (1995) Velocity and stress fields in grounded glaciers: a simple algorithm for including deviatoric stress gradients. *Journal of Glaciology*, **41**(138), 333–344.

Bradley, A. T., Bett, D. T., Dutrieux, P., Rydt, J. D. and Holland, P. R. (2022) The Influence of Pine Island Ice Shelf Calving on Basal Melting. *Journal of Geophysical Research: Oceans*, **127** (9), 1–32.

Brondex, J., Gagliardini, O., Gillet-Chaulet, F. and Durand, G. (2017) Sensitivity of grounding line dynamics to the choice of the friction law. *Journal of Glaciology*, **63** (241), 854–866.

Brondex, J., Gillet-Chaulet, F. and Gagliardini, O. (2019) Sensitivity of centennial mass loss projections of the Amundsen basin to the friction law. *The Cryosphere*, **13**. the Weertman law systematically predicts the lowest mass losses. In addi- tion, because of its particular dependence on effective pres- sure, the Budd friction law induces significantly different grounding-line retreat patterns than the other laws and predicts significantly higher mass losses., 177–195.

Budd, W. F., Keage, P. L. and Blundy, N. A. (1979) Empirical Studies of Ice Sliding. *Journal of Glaciology*, **23**(89), 157–170.

Bueler, E. and Brown, J. (2009) Shallow shelf approximation as a "sliding law" in a thermomechanically coupled ice sheet model. *Journal of Geophysical Research*, **114**(F3).

Bulthuis, K., Arnst, M., Sun, S. and Pattyn, F. (2019) Uncertainty quantification of the multi-centennial response of the Antarctic Ice Sheet to climate change. *The Cryosphere*, **13**, 1349–1380.

Burgard, C., Jourdain, N. C., Reese, R., Jenkins, A. and Mathiot, P. (2022) An assessment of basal melt parameterisations for Antarctic ice shelves. *The Cryosphere*, **16**(12), 4931–4975.

Cornford, S. L., Martin, D. F., Payne, A. J., Ng, E. G., Brocq, A. M. L., Gladstone, R. M., Edwards, T. L., Shannon, S. R., Agosta, C., Broeke, M. R. V. D., Hellmer, H. H., Krinner, G., Ligtenberg, S. R., Timmermann, R. and Vaughan, D. G. (2015) Century-scale simulations of the response of the West Antarctic Ice Sheet to a warming climate. *The Cryosphere*, **9** (4), 1579–1600.

Cornford, S. L., Martin, D. F., Graves, D. T., Ranken, D. F., Brocq, A. M. L., Gladstone, R. M., Payne, A. J., Ng, E. G. and Lipscomb, W. H. (2013) Adaptive mesh, finite volume modeling of marine ice sheets. *Journal of Computational Physics*, **232** (1), 529–549.

Cornford, S. L., Seroussi, H., Asay-Davis, X. S., Gudmundsson, G. H., Arthern, R., Borstad, C., Christmann, J., Santos, T. D. D., Feldmann, J., Goldberg, D., Hoffman, M. J., Humbert, A., Kleiner, T., Leguy, G., Lipscomb, W. H., Merino, N., Durand, G., Morlighem, M., Pollard, D., Rückamp, M., Williams, C. R. and Yu, H. (2020) Results of the third Marine Ice Sheet Model Intercomparison Project (MISMIP+). *Cryosphere*, **14** (7), 2283–2301.

Corr, H. F., Doake, C. S., Jenkins, A. and Vaughan, D. G. (2001) Investigations of an "ice plain" in the mouth of Pine Island Glacier, Antarctica. *Journal of Glaciology*, **47** (156), 51–57.

DeConto, R. M. and Pollard, D. (2016) Contribution of Antarctica to past and future sea-level rise. *Nature*, **531** (7596), 591–597.

DeConto, R. M., Pollard, D., Alley, R. B., Velicogna, I., Gasson, E., Gomez, N., Sadai, S., Condron, A., Gilford, D. M., Ashe, E. L., Kopp, R. E., Li, D. and Dutton, A. (2021) The Paris Climate Agreement and future sea-level rise from Antarctica. *Nature*, **593** (7857), 83–89.

Depoorter, M. A., Bamber, J. L., Griggs, J. A., Lenaerts, J. T. M., Ligtenberg, S. R., Broeke, M. R. V. D. and Moholdt, G. (2013) Calving fluxes and basal melt rates of Antarctic ice shelves. *Nature*, **502** (7469), 89–92.

Dupont, T. K. and Alley, R. B. (2005) Assessment of the importance of ice-shelf buttressing to ice-sheet flow. *Geophysical Research Letters*, **32**, L04503.

Durand, G., Gagliardini, O., Zwinger, T., Meur, E. L. and Hindmarsh, R. C. (2009) Full Stokes modeling of marine ice sheets: Influence of the grid size. *Annals of Glaciology*, **50** (52), 109–114.

Dutrieux, P., Vaughan, D. G., Corr, H. F., Jenkins, A., Holland, P. R., Joughin, I. and Fleming, A. H. (2013) Pine Island glacier ice shelf melt distributed at kilometre scales. *Cryosphere*, **7** (5), 1543–1555.

Dutrieux, P., Rydt, J. D., Jenkins, A., Holland, P. R., Ha, H. K., Lee, S. H., Steig, E. J., Ding, Q., Abrahamsen, E. P. and Schröder, M. (2014) Strong sensitivity of Pine Island ice-shelf melting to climatic variability. *Science*, **343** (6167), 174–178.

Engwirda, D. B. T. (2014) Locally optimal Delaunay-refinement and optimisation-based mesh generation.

Favier, L., Durand, G., Cornford, S. L., Gudmundsson, G. H., Gagliardini, O., Gillet-Chaulet, F., Zwinger, T., Payne, A. J. and Brocq, A. M. L. (2014) Retreat of Pine Island Glacier controlled by marine ice-sheet instability. *Nature Climate Change*, **4** (2), 117–121.

Favier, L., Jourdain, N. C., Jenkins, A., Merino, N., Durand, G., Gagliardini, O., Gillet-Chaulet, F. and Mathiot, P. (2019) Assessment of sub-shelf melting parameterisations using the ocean-ice-sheet coupled model NEMO(v3.6)-Elmer/Ice(v8.3). *Geoscientific Model Development*, **12** (6), 2255–2283.

Favier, L., Pattyn, F., Berger, S. and Drews, R. (2016) Dynamic influence of pinning points on marine ice-sheet stability: A numerical study in Dronning Maud Land, East Antarctica. *Cryosphere*, **10** (6), 2623–2635.

Feldmann, J., Albrecht, T., Khroulev, C., Pattyn, F. and Levermann, A. (2014) Resolution-dependent performance of grounding line motion in a shallow model compared with a full-Stokes model according to the MISMIP3d intercomparison. *Journal of Glaciology*, **60** (220), 353–360.

Feldmann, J. and Levermann, A. (2015a) Interaction of marine ice-sheet instabilities in two drainage basins: Simple scaling of geometry and transition time. *Cryosphere*, **9** (2), 631–645.

Feldmann, J. and Levermann, A. (2015b) Collapse of the West Antarctic Ice Sheet after local destabilization of the Amundsen Basin. *Proceedings of the National Academy of Sciences*, **112** (46), 14191–14196.

Feldmann, J., Reese, R., Winkelmann, R. and Levermann, A. (2022) Shear-margin melting causes stronger transient ice discharge than ice-stream melting in idealized simulations. *The Cryosphere*, **16**(5), 1927–1940.

Flament, T. and Rémy, F. (2012) Dynamic thinning of Antarctic glaciers from along-track repeat radar altimetry. *Journal of Glaciology*, **58** (211), 830–840.

Fox-Kemper, B., Hewitt, H., Xiao, C., Aðalgeirsdóttir, G., Drijfhout, S., Edwards, T., Golledge, N., Hemer, M., Kopp, R., Krinner, G., Mix, A., Notz, D., Nowicki, S., Nurhati, I., Ruiz, L., Sallée, J.-B., Slangen, A. and Yu, Y. (2021) Ocean, Cryosphere and Sea Level Change. In: *Climate Change 2021: The Physical Science Basis. Contribution of Working Group I to the Sixth Assessment Report of the Intergovernmental Panel on Climate Change*. Edited by V. Masson-Delmotte, P. Zhai, A. Pirani, S. Con-

nors, C. Péan, S. Berger, N. Caud, Y. Chen, L. Goldfarb, M. Gomis, M. Huang, K. Leitzell, E. Lonnoy, J. Matthews, T. Maycock, T. Waterfield, O. Yelekçi, R. Yu and B. Zhou. Cambridge University Press, Cambridge, United Kingdom and New York, NY, USA, pages 1211–1362.

Fürst, J. J., Durand, G., Gillet-Chaulet, F., Merino, N., Tavard, L., Mouginot, J., Gourmelen, N. and Gagliardini, O. (2015) Assimilation of Antarctic velocity observations provides evidence for uncharted pinning points. *Cryosphere*, **9** (4), 1427–1443.

Fürst, J. J., Durand, G., Gillet-Chaulet, F., Tavard, L., Rankl, M., Braun, M. and Gagliardini, O. (2016) The safety band of Antarctic ice shelves. *Nature Climate Change*, **6** (5), 479–482.

Garbe, J., Albrecht, T., Levermann, A., Donges, J. F. and Winkelmann, R. (2020) The hysteresis of the Antarctic Ice Sheet. *Nature*, **585** (7826), 538–544.

Gardner, A. S., Moholdt, G., Scambos, T., Fahnstock, M., Ligtenberg, S., Broeke, M. V. D. and Nilsson, J. (2018) Increased West Antarctic and unchanged East Antarctic ice discharge over the last 7 years. *The Cryosphere*, **12** (2), 521–547.

Geuzaine, C. and Remacle, J. F. (2009) Gmsh: A 3-D finite element mesh generator with built-in pre- and post-processing facilities. *International Journal for Numerical Methods in Engineering*, **79** (11), 1309–1331.

Gill, A. E. (1973) Circulation and bottom water production in the Weddell Sea. *Deep-Sea Research and Oceanographic Abstracts*, **20** (2), 111–140.

Goldberg, D. N., Gourmelen, N., Kimura, S., Millan, R. and Snow, K. (2019) How Accurately Should We Model Ice Shelf Melt Rates? *Geophysical Research Letters*, **46** (1), 189–199.

Goldberg, D., Holland, D. M. and Schoof, C. (2009) Grounding line movement and ice shelf buttressing in marine ice sheets. *Journal of Geophysical Research: Earth Surface*, **114**, F04026.

Gudmundsson, G. H. (2013) Ice-shelf buttressing and the stability of marine ice sheets. *The Cryosphere*, **7** (2), 647–655.

Gudmundsson, G. H., Krug, J., Durand, G., Favier, L. and Gagliardini, O. (2012) The stability of grounding lines on retrograde slopes. *The Cryosphere*, **6** (6), 1497–1505.

Gudmundsson, G. H., Barnes, J. M., Goldberg, D. N. and Morlighem, M. (2023) Limited Impact of Thwaites Ice Shelf on Future Ice Loss From Antarctica. *Geophysical Research Letters*, **50**(11).

Gudmundsson, G. H. (2020) *GHilmarG/UaSource: Ua2019b*. Version v2019b.

Gudmundsson, G. H., Paolo, F. S., Adusumilli, S. and Fricker, H. A. (2019) Instantaneous Antarctic ice sheet mass loss driven by thinning ice shelves. *Geophysical Research Letters*, **46** (23), 13903–13909.

Hanna, E., Pattyn, F., Navarro, F., Favier, V., Goelzer, H., van den Broeke, M. R., Vizcaino, M., Whitehouse, P. L., Ritz, C., Bulthuis, K. and Smith, B. (2020) Mass balance of the ice sheets and glaciers – Progress since AR5 and challenges. *Earth-Science Reviews*, **201**, 102976.

Hill, E. A., Gudmundsson, G. H., Carr, J. R., Stokes, C. R. and King, H. M. (2021) Twenty-first century response of Petermann Glacier, northwest Greenland to ice shelf loss. *Journal of Glaciology*, **67** (261), 147–157.

Hill, E. A., Gudmundsson, G. H., Carr, J. R. and Stokes, C. R. (2018) Velocity response of Petermann Glacier, northwest Greenland, to past and future calving events. *Cryosphere*, **12** (12), 3907–3921.

Hindmarsh, R. C. A. (2004) A numerical comparison of approximations to the Stokes equations used in ice sheet and glacier modeling. *Journal of Geophysical Research: Earth Surface*, **109**(F1).

Holland, P. R., Bevan, S. L. and Luckman, A. J. (2023) Strong Ocean Melting Feedback During the Recent Retreat of Thwaites Glacier. *Geophysical Research Letters*, **50**(8).

Holland, P. R., Bracegirdle, T. J., Dutrieux, P., Jenkins, A. and Steig, E. J. (2019) West Antarctic ice loss influenced by internal climate variability and anthropogenic forcing. *Nature Geoscience*, **12** (9), 718–724.

Holland, P. R., O'Connor, G. K., Bracegirdle, T. J., Dutrieux, P., Naughten, K. A., Steig, E. J., Schneider, D. P., Jenkins, A. and Smith, J. A. (2022) Anthropogenic and internal drivers of wind changes over the Amundsen Sea, West Antarctica, during the 20th and 21st centuries. *The Cryosphere*, **16** (12), 5085–5105.

Hughes, T. (1973) Is the West Antarctic Ice Sheet disintegrating? *Journal of Geophysical Research*, **78** (33), 7884–7910.

Hughes, T. J. (1981) The Weak Underbelly of the West Antarctic Ice-Sheet. *Journal of Glaciology*, **27** (97), 518–525.

Hutter, K. (1983) *Theoretical glaciology: material science of ice and the mechanics of glaciers and ice sheets*. Volume 1. Springer.

Jacobs, S. S., Hellmer, H. H., Doakea, C. S. M., Jenkins, A. and Frolich, R. M. (1992) Melting of ice shelves and the mass balance of Antarctica. *Journal of Glaciology*, **38** (130), 375–387.

Jacobs, S., Giulivi, C., Dutrieux, P., Rignot, E., Nitsche, F. and Mouginot, J. (2013) Getz Ice Shelf melting response to changes in ocean forcing. *Journal of Geophysical Research: Oceans*, **118** (9), 4152–4168.

Jacobs, S. S. (1991) On the nature and significance of the Antarctic Slope Front. *Marine Chemistry*, **35** (1-4), 9–24.

Jacobs, S. S. and Hellmer, H. H. (1996) Antarctic Ice Sheet melting in the southeast Pacific. *Geophysical Research Letters*, **23** (9), 957–960.

Jacobs, S. S., Jenkins, A., Giulivi, C. F. and Dutrieux, P. (2011) Stronger ocean circulation and increased melting under Pine Island Glacier ice shelf. *Nature Geoscience*, **4** (8), 519–523.

Jenkins, A., Dutrieux, P., Jacobs, S., Steig, E. J., Gudmundsson, G. H., Smith, J. and Heywood, K. J. (2016) Decadal ocean forcing and Antarctic Ice Sheet response: Lessons from the Amundsen Sea. *Oceanography*, **29** (4), 106–117.

Jenkins, A., Dutrieux, P., Jacobs, S. S., McPhail, S. D., Perrett, J. R., Webb, A. T. and White, D. (2010) Observations beneath Pine Island Glacier in West-Antarctica and implications for its retreat. *Nature Geoscience*, **3** (7), 468–472.

Jenkins, A., Shoosmith, D., Dutrieux, P., Jacobs, S., Kim, T. W., Lee, S. H., Ha, H. K. and Stammerjohn, S. (2018) West Antarctic Ice Sheet retreat in the Amundsen Sea driven by decadal oceanic variability. *Nature Geoscience*, **11** (10), 733–738.

Jones, R. S., Gudmundsson, G. H., Mackintosh, A. N., McCormack, F. S. and Whitmore, R. J. (2021) Ocean-Driven and Topography-Controlled Nonlinear Glacier Retreat During the Holocene: Southwestern Ross Sea, Antarctica. *Geophysical Research Letters*, **48** (5).

Joughin, I., Smith, B. E. and Medley, B. (2014) Marine ice sheet collapse potentially under way for the Thwaites Glacier Basin, West Antarctica. *Science*, **344** (6185), 735–738.

Joughin, I., Rignot, E., Rosanova, C. E., Lucchitta, B. K. and Bohlander, J. (2003) Timing of recent accelerations of Pine Island Glacier, Antarctica. *Geophysical Research Letters*, **30** (13).

Joughin, I., Shapero, D., Dutrieux, P. and Smith, B. (2021) Ocean-induced melt volume directly paces ice loss from Pine Island Glacier. *Science Advances*, **7** (43).

Joughin, I., Smith, B. E. and Holland, D. M. (2010) Sensitivity of 21st century sea level to ocean-induced thinning of Pine Island Glacier, Antarctica. *Geophysical Research Letters*, **37** (20), n/a–n/a.

Joughin, I., Smith, B. E. and Schoof, C. G. (2019) Regularized Coulomb Friction Laws for Ice Sheet Sliding: Application to Pine Island Glacier, Antarctica. *Geophysical Research Letters*, **46** (9), 4764–4771.

Jourdain, N. C., Mathiot, P., Burgard, C., Caillet, J. and Kittel, C. (2022) Ice shelf basal melt rates in the Amundsen Sea at the end of the 21 st century (May), 1–14.

Kachuck, S. B., Martin, D. F., Bassis, J. N. and Price, S. F. (2020) Rapid Viscoelastic Deformation Slows Marine Ice Sheet Instability at Pine Island Glacier. *Geophysical Research Letters*, **47**(10).

Kimura, S., Jenkins, A., Regan, H., Holland, P. R., Assmann, K. M., Whitt, D. B., Wessem, M. V., van de Berg, W. J., Reijmer, C. H. and Dutrieux, P. (2017) Oceanographic Controls on the Variability of Ice-Shelf Basal Melting and Circulation of Glacial Meltwater in the Amundsen Sea Embayment, Antarctica. *Journal of Geophysical Research: Oceans*, **122** (12), 10131–10155.

Kirchner, N., Hutter, K., Jakobsson, M. and Gyllencreutz, R. (2011) Capabilities and limitations of numerical ice sheet models: A discussion for Earth-scientists and modelers. *Quaternary Science Reviews*, **30** (25-26), 3691–3704.

Konrad, H., Gilbert, L., Cornford, S. L., Payne, A., Hogg, A., Muir, A. and Shepherd, A. (2017) Uneven onset and pace of ice-dynamical imbalance in the Amundsen Sea Embayment, West Antarctica. *Geophysical Research Letters*, **44** (2), 910–918.

Konrad, H., Shepherd, A., Gilbert, L., Hogg, A. E., McMillan, M., Muir, A. and Slater, T. (2018) Net retreat of Antarctic glacier grounding lines. *Nature Geoscience*, **11** (4). Between 2010-2016 there was overall 59.4% GL retreat in the Amundsen Sea Sector (but ... Retreat at Pine Island Glacier appears to have stagnated around 2011), 258–262.

Lachlan-Cope, T. and Connolley, W. (2006) Teleconnections between the tropical Pacific and the Amundsen-Bellinghausens Sea: Role of the El Niño/Southern Oscillation. *Journal of Geophysical Research Atmospheres*, **111** (23).

Levermann, A., Winkelmann, R., Albrecht, T., Goelzer, H., Golledge, N. R., Greve, R., Huybrechts, P., Jordan, J., Leguy, G., Martin, D., Morlighem, M., Pattyn, F., Pollard, D., Quiquet, A., Rodehacke, C., Seroussi, H., Sutter, J., Zhang, T., Breedam, J. V., Calov, R., Deconto, R., Dumas, C., Garbe, J., Gudmundsson, G. H., Hoffman, M. J., Humbert, A., Kleiner, T., Lipscomb, W. H., Meinshausen, M., Ng, E., Nowicki, S. M., Perego, M., Price, S. F., Saito, F., Schlegel, N. J., Sun, S. and Wal, R. S. V. D. (2020) Projecting Antarctica's contribution to future sea level rise from basal ice shelf melt using linear response functions of 16 ice sheet models (LARMIP-2). *Earth System Dynamics*, **11** (1), 35–76.

Lhermitte, S., Sun, S., Shuman, C., Wouters, B., Pattyn, F., Wuite, J., Berthier, E. and Nagler, T. (2020) Damage accelerates ice shelf instability and mass loss in Amundsen Sea Embayment. *Proceedings of the National Academy of Sciences of the United States of America*, **117** (40), 24735–24741.

Macayeal, D. R. (1989) Large-scale ice flow over a viscous basal sediment: theory and application to ice stream B, Antarctica. *Journal of Geophysical Research*, **94** (134), 4071–4087.

MacAyeal, D. R. (1993) A tutorial on the use of control methods in ice-sheet modeling. *Journal of Glaciology*, **39**(131), 91–98.

McMillan, M., Shepherd, A., Sundal, A., Briggs, K., Muir, A., Ridout, A., Hogg, A. and Wingham, D. (2014) Increased ice losses from Antarctica detected by CryoSat-2. *Geophysical Research Letters*, **41** (11), 3899–3905.

Mercer, J. H. (1978) West Antarctic ice sheet and C02 greenhouse effect: a threat of disaster. *Nature*, **271** (5643), 321–325.

Mercer, J. H. (1968) Antarctic ice and Sangamon sea level. *International Association of Scientific Hydrology*, **79**, 217–225.

Milillo, P., Rignot, E., Rizzoli, P., Scheuchl, B., Mouginot, J., Bueso-Bello, J. L., Prats-Iraola, P. and Dini, L. (2022) Rapid glacier retreat rates observed in West Antarctica. *Nature Geoscience*, **15** (1), 48–53.

Mitcham, T., Gudmundsson, G. H. and Bamber, J. L. (2022) The instantaneous impact of calving and thinning on the Larsen C Ice Shelf. *The Cryosphere*, **16** (3), 883–901.

Morlighem, M., Rignot, E., Binder, T., Blankenship, D., Drews, R., Eagles, G., Eisen, O., Ferraccioli, F., Forsberg, R., Fretwell, P., Goel, V., Greenbaum, J. S., Gudmundsson, H., Guo, J., Helm, V., Hofstede, C., Howat, I., Humbert, A., Jokat, W., Karlsson, N. B., Lee, W. S., Matsuoka, K., Millan, R., Mouginot, J., Paden, J., Pattyn, F., Roberts, J., Rosier, S., Ruppel, A., Seroussi, H., Smith, E. C., Steinhage, D., Sun, B., den Broeke, M. R., Ommen, T. D., van Wessem, M. and Young, D. A. (2020) Deep glacial troughs and stabilizing ridges unveiled beneath the margins of the Antarctic ice sheet. *Nature Geoscience*, **13** (2), 132–137.

Mouginot, J., Rignot, E. and Scheuchl, B. (2014) Sustained increase in ice discharge from the Amundsen Sea Embayment, West Antarctica, from 1973 to 2013. *Geophysical Research Letters*, **41** (5), 1576–1584.

Mouginot, J., Rignot, E., Scheuchl, B. and Millan, R. (2017a) Comprehensive Annual Ice Sheet Velocity Mapping Using Landsat-8, Sentinel-1, and RADARSAT-2 Data. *Remote Sensing 2017, Vol. 9, Page 364*, **9** (4), 364.

Mouginot, J., Scheuchl, B. and Rignot, E. (2017b) MEaSUREs Annual Antarctic Ice Velocity Maps, Version 1. *NASA National Snow and Ice Data Center Distributed Active Archive Center*.

Mouginot and Rignot., E. (2017) MEaSUREs Antarctic Boundaries for IPY 2007-2009 from Satellite Radar, Version 2.

Muto, A., Peters, L. E., Gohl, K., Sasgen, I., Alley, R. B., Anandakrishnan, S. and Riverman, K. L. (2016) Subglacial bathymetry and sediment distribution beneath Pine Island Glacier ice shelf modeled using aerogravity and in situ geophysical data: New results. *Earth and Planetary Science Letters*, **433**, 63–75.

Naughten, K. A., Holland, P. R., Dutrieux, P., Kimura, S., Bett, D. T. and Jenkins, A. (2022) Simulated Twentieth-Century Ocean Warming in the Amundsen Sea, West Antarctica. *Geophysical Research Letters*, **49** (5).

Naughten, K. A., Meissner, K. J., Galton-Fenzi, B. K., England, M. H., Timmermann, R. and Hellmer, H. H. (2018) Future Projections of Antarctic Ice Shelf Melting Based on CMIP5 Scenarios. *Journal of Climate*, **31** (13), 5243–5261.

Naughten, K. A., Rydt, J. D., Rosier, S. H., Jenkins, A., Holland, P. R. and Ridley, J. K. (2021) Two-timescale response of a large Antarctic ice shelf to climate change. *Nature Communications*, **12** (1), 1–10.

Nick, F., Veen, C. V. D., Vieli, A. and Benn, D. (2010) A physically based calving model applied to marine outlet glaciers and implications for the glacier dynamics. *Journal of Glaciology*, **56**(199), 781–794.

Nowicki, S., Goelzer, H., Seroussi, H., Payne, A. J., Lipscomb, W. H., Abe-Ouchi, A., Agosta, C., Alexander, P., Asay-Davis, X. S., Barthel, A., Bracegirdle, T. J., Cullather, R., Felikson, D., Fettweis, X., Gregory, J. M., Hattermann, T., Jourdain, N. C., Munneke, P. K., Larour, E., Little, C. M., Morlighem, M., Nias, I., Shepherd, A., Simon, E., Slater, D., Smith, R. S., Straneo, F., Trusel, L. D., van den Broeke, M. R. and van de Wal, R. (2020) Experimental protocol for sea level projections from ISMIP6 stand-alone ice sheet models. *The Cryosphere*, **14**(7), 2331–2368.

Padman, L., Siegfried, M. R. and Fricker, H. A. (2018) Ocean Tide Influences on the Antarctic and Greenland Ice Sheets. *Reviews of Geophysics*, **56** (1), 142–184.

Paolo, F. S., Padman, L., Fricker, H. A., Adusumilli, S., Howard, S. and Siegfried, M. R. (2018) Response of Pacific-sector Antarctic ice shelves to the El Niño/Southern Oscillation. *Nature Geoscience*, **11** (2), 121–126.

Paolo, F. S., Fricker, H. A. and Padman, L. (2015) Volume loss from Antarctic ice shelves is accelerating. *Science*, **348** (6232). Using 18 years of continuous satellite radar altimeter observations, we have computed decadal-scale changes in ice-shelf thickness...
...average ice-shelf volume change accelerated, 327–331.

Park, J. W., Gourmelen, N., Shepherd, A., Kim, S. W., Vaughan, D. G. and Wingham, D. J. (2013) Sustained retreat of the Pine Island Glacier. *Geophysical Research Letters*, **40** (10), 2137–2142.

Pattyn, F., Schoof, C., Perichon, L., Hindmarsh, R. C., Bueler, E., Fleurian, B. D., Durand, G., Gagliardini, O., Gladstone, R., Goldberg, D., Gudmundsson, G. H., Huybrechts, P., Lee, V., Nick, F. M., Payne, A. J., Pollard, D., Rybak, O., Saito, F. and Vieli, A. (2012) Results of the marine ice sheet model intercomparison project, MISMIP. *Cryosphere*, **6** (3), 573–588.

Pattyn, F. (2003) A new three-dimensional higher-order thermomechanical ice sheet model: Basic sensitivity, ice stream development, and ice flow across subglacial lakes. *Journal of Geophysical Research*, **108**(B8).

Pattyn, F. (2018) The paradigm shift in Antarctic ice sheet modelling. *Nature Communications*, **9** (1), 2728.

Pattyn, F., Perichon, L., Durand, G., Favier, L., Gagliardini, O., Hindmarsh, R. C., Zwinger, T., Albrecht, T., Cornford, S., Docquier, D., Fürst, J. J., Goldberg, D., Gudmundsson, G. H., Humbert, A., Hütten, M., Huybrechts, P., Jouvet, G., Kleiner, T., Larour, E., Martin, D., Morlighem, M., Payne, A. J., Pollard, D., Rückamp, M., Rybak, O., Seroussi, H., Thoma, M. and Wilkens, N. (2013) Grounding-line migration in plan-view marine ice-sheet models: Results of the ice2sea MISMIP3d intercomparison. *Journal of Glaciology*, **59** (215), 410–422.

Payne, A. J., Vieli, A., Shepherd, A. P., Wingham, D. J. and Rignot, E. (2004) Recent dramatic thinning of largest West Antarctic ice stream triggered by oceans. *Geophysical Research Letters*, **31** (23), 1–4.

Pegler, S. S. (2018) Suppression of marine ice sheet instability. *J. Fluid Mech*, **857**, 648–680.

Pollard, D. and Deconto, R. M. (2009) Modelling West Antarctic ice sheet growth and collapse through the past five million years. *Nature*, **458** (7236), 329.

Pritchard, H., Ligtenberg, S. R. M., Fricker, H. A., Vaughan, D. G., Broeke, M. R. V. D. and Padman, L. (2012) Antarctic ice-sheet loss driven by basal melting of ice shelves. *Nature*, **484** (7395), 502–505.

Ranganathan, M., Minchew, B., Meyer, C. and Gudmundsson, G. H. (2020) A new approach to inferring basal drag and ice rheology in ice streams, with applications to West Antarctic ice streams. *Journal of Glaciology*, 1–14.

Reed, B., Green, J. A. M., Jenkins, A. and Gudmundsson, G. H. (2022) Recent irreversible retreat of Pine Island Glacier. *Research Square Platform [preprint]*.

Reese, R., Garbe, J., Hill, E. A., Urruty, B., Naughten, K. A., Gagliardini, O., Durand, G., Gillet-Chaulet, F., Chandler, D., Langebroek, P. M. and Winkelmann, R. (2022) The stability of present-day Antarctic grounding lines – Part B: Possible commitment of regional collapse under current climate. *The Cryosphere Discussions*, **2022**, 1–33.

Reese, R., Gudmundsson, G. H., Levermann, A. and Winkelmann, R. (2018a) The far reach of ice-shelf thinning in Antarctica. *Nature Climate Change*, **8** (1), 53–57.

Reese, R., Winkelmann, R. and Gudmundsson, G. H. (2018b) Grounding-line flux formula applied as a flux condition in numerical simulations fails for buttressed Antarctic ice streams. *Cryosphere*, **12** (10), 3229–3242.

Rignot, E. J. (1998) Fast recession of a West Antarctic glacier. *Science*, **281** (5376). Between 1992-1996 hinge line retreated mean rate of 1.2 +-0.3 km/yr; thinning 3.5m/yr at hinge line; basal melting 50m/yr near hinge and 24m/yr between hinge and front, 549–551.

Rignot, E., Jacobs, S., Mouginot, J. and Scheuchl, B. (2013) Ice-shelf melting around antarctica. *Science*, **341** (6143), 266–270.

Rignot, E., Mouginot, J., Morlighem, M., Seroussi, H. and Scheuchl, B. (2014) Widespread, rapid grounding line retreat of Pine Island, Thwaites, Smith, and Kohler glaciers, West Antarctica, from 1992 to 2011. *Geophysical Research Letters*, **41** (10), 3502–3509.

Rignot, E., Mouginot, J. and Scheuchl, B. (2011) Ice flow of the antarctic ice sheet. *Science*, **333** (6048), 1427–1430.

Rignot, E. (2002) Ice-shelf changes in Pine Island Bay, Antarctica, 1947-2000. *Journal of Glaciology*, **48** (161), 247–256.

Rignot, E., Mouginot, J., Scheuchl, B., van den Broeke, M., van Wessem, M. J. and Morlighem, M. (2019) Four decades of Antarctic Ice Sheet mass balance from 1979–2017. *Proceedings of the National Academy of Sciences*, **116** (4), 1095–1103.

Rignot, E., Vaughan, D. G., Schmeltz, M., Dupont, T. and MacAyeal, D. (2002) Acceleration of Pine Island and Thwaites Glaciers, West Antarctica. *Annals of Glaciology*, **34**, 189–194.

Robel, A. A., Seroussi, H. and Roe, G. H. (2019) Marine ice sheet instability amplifies and skews uncertainty in projections of future sea-level rise. *Proceedings of the National Academy of Sciences*, 201904822.

Rosier, S. H. R., Bull, C. Y. S., Woo, W. L. and Gudmundsson, G. H. (2023) Predicting ocean-induced ice-shelf melt rates using deep learning. *The Cryosphere*, **17**(2), 499–518.

Rosier, S. H., Reese, R., Donges, J. F., Rydt, J. D., Gudmundsson, G. H. and Winkelmann, R. (2021) The tipping points and early warning indicators for Pine Island Glacier, West Antarctica. *Cryosphere*, **15** (3), 1501–1516.

Rydt, J. D. and Gudmundsson, G. H. (2016) Coupled ice shelf-ocean modeling and complex grounding line retreat from a seabed ridge. *Journal of Geophysical Research F: Earth Surface*, **121**, 865–880.

Rydt, J. D., Gudmundsson, G. H., Rott, H. and Bamber, J. L. (2015) Modeling the instantaneous response of glaciers after the collapse of the Larsen B Ice Shelf. *Geophysical Research Letters*, **42** (13), 5355–5363.

Rydt, J. D., Holland, P. R., Dutrieux, P. and Jenkins, A. (2014) Geometric and oceanographic controls on melting beneath Pine Island Glacier. *Journal of Geophysical Research: Oceans*, **119** (4), 2420–2438.

Rydt, J. D., Gudmundsson, G. H., Nagler, T., Wuite, J. and King, E. C. (2018) Recent rift formation and impact on the structural integrity of the Brunt Ice Shelf, East Antarctica. *Cryosphere*, **12** (2), 505–520.

Rydt, J. D., Reese, R., Paolo, F. S. and Gudmundsson, G. H. (2021) Drivers of Pine Island Glacier speed-up between 1996 and 2016. *Cryosphere*, **15** (1), 113–132.

Santos, T. D. D., Morlighem, M., Seroussi, H., Devloo, P. R. B. and Simões, J. C. (2019) Implementation and performance of adaptive mesh refinement in the Ice Sheet System Model (ISSM v4.14). *Geoscientific Model Development*, **12** (1), 215–232.

Scambos, T. A., Bohlander, J. A., Shuman, C. A. and Skvarca, P. (2004) Glacier acceleration and thinning after ice shelf collapse in the Larsen B embayment, Antarctica. *Geophysical Research Letters*, **31**, L18402.

Scheuchl, B., Mouginot, J., Rignot, E., Morlighem, M. and Khazendar, A. (2016) Grounding line retreat of Pope, Smith, and Kohler Glaciers, West Antarctica, measured with Sentinel-1a radar interferometry data. *Geophysical Research Letters*, **43** (16), 8572–8579.

Schlegel, N. J., Seroussi, H., Schodlok, M. P., Larour, E. Y., Boening, C., Limonadi, D., Watkins, M. M., Morlighem, M. and Broeke, M. R. V. D. (2018) Exploration of Antarctic Ice Sheet 100-year contribution to sea level rise and associated model uncertainties using the ISSM framework. *Cryosphere*, **12** (11), 3511–3534.

Schmidtko, S., Heywood, K. J., Thompson, A. F. and Aoki, S. (2014) Multidecadal warming of Antarctic waters. *Science*, **346** (6214), 1227–1231.

Schneider, D. P. and Steig, E. J. (2008) Ice cores record significant 1940s Antarctic warmth related to tropical climate variability. *Proceedings of the National Academy of Sciences of the United States of America*, **105** (34), 12154–12158.

Schoof, C. and Hindmarsh, R. C. A. (2010) Thin-Film Flows with Wall Slip: An Asymptotic Analysis of Higher Order Glacier Flow Models. *The Quarterly Journal of Mechanics and Applied Mathematics*, **63**(1), 73–114.

Schoof, C. (2005) The effect of cavitation on glacier sliding. *Proceedings of the Royal Society A: Mathematical, Physical and Engineering Sciences*, **461**(2055), 609–627.

Schoof, C. (2007a) Ice sheet grounding line dynamics: Steady states, stability, and hysteresis. *Journal of Geophysical Research: Earth Surface*, **112** (F3).

Schoof, C. (2007b) Marine ice-sheet dynamics. Part 1. The case of rapid sliding. *Journal of Fluid Mechanics*, **573**, 27–55.

Schrama, E. J. O., Wouters, B. and Rietbroek, R. (2014) A mascon approach to assess ice sheet and glacier mass balances and their uncertainties from GRACE data. *Journal of Geophysical Research: Solid Earth*, **119**(7), 6048–6066.

Seroussi, H., Nakayama, Y., Larour, E., Menemenlis, D., Morlighem, M., Rignot, E. and Khazendar, A. (2017) Continued retreat of Thwaites Glacier, West Antarctica, controlled by bed topography and ocean circulation. *Geophysical Research Letters*, **44** (12), 6191–6199.

Seroussi, H., Morlighem, M., Larour, E., Rignot, E. and Khazendar, A. (2014) Hydrostatic grounding line parameterization in ice sheet models. *Cryosphere*, **8** (6). Good summary of mesh refinement in Intro, 2075–2087.

Seroussi, H. and Morlighem, M. (2018) Representation of basal melting at the grounding line in ice flow models. *Cryosphere*, **12** (10), 3085–3096.

Seroussi, H., Nowicki, S., Payne, A. J., Goelzer, H., Lipscomb, W. H., Abe-Ouchi, A., Agosta, C., Albrecht, T., Asay-Davis, X., Barthel, A., Calov, R., Cullather, R., Dumas, C., Galton-Fenzi, B. K., Gladstone, R., Golledge, N. R., Gregory, J. M., Greve, R., Hattermann, T., Hoffman, M. J., Humbert, A., Huybrechts, P., Jourdain, N. C., Kleiner, T., Larour, E., Leguy, G. R., Lowry, D. P., Little, C. M., Morlighem, M., Pattyn, F., Pelle, T., Price, S. F., Quiquet, A., Reese, R., Schlegel, N. J., Shepherd, A., Simon, E., Smith, R. S., Straneo, F., Sun, S., Trusel, L. D., Breedam, J. V., Wal, R. S. V. D., Winkelmann, R., Zhao, C., Zhang, T. and Zwinger, T. (2020) ISMIP6 Antarctica: A multi-model ensemble of the Antarctic ice sheet evolution over the 21st century. *Cryosphere*, **14** (9), 3033–3070.

Shean, D. E., Joughin, I. R., Dutrieux, P., Smith, B. E. and Berthier, E. (2019) Ice shelf basal melt rates from a high-resolution digital elevation model (DEM) record for Pine Island Glacier, Antarctica. *Cryosphere*, **13** (10), 2633–2656.

Shepherd, A., Ivins, E., Rignot, E., Smith, B., Broeke, M. V. D., Velicogna, I., Whitehouse, P., Briggs, K., Joughin, I., Krinner, G., Nowicki, S., Payne, T., Scambos, T., Schlegel, N., Geruo, A., Agosta, C., Ahlstrøm, A., Babonis, G., Barletta, V., Blazquez, A., Bonin, J., Csatho, B., Cullather, R., Felikson, D., Fettweis, X., Forsberg, R., Gallee, H., Gardner, A., Gilbert, L., Groh, A., Gunter, B., Hanna, E., Harig, C., Helm, V., Horvath, A., Horwath, M., Khan, S., Kjeldsen, K. K., Konrad, H., Langen, P., Lecavalier, B., Loomis, B., Luthcke, S., McMillan, M., Melini, D., Mernild, S., Mohajerani, Y., Moore, P., Mouginot, J., Moyano, G., Muir, A., Nagler, T., Nield, G., Nilsson, J., Noel, B., Otosaka, I., Pattle, M. E., Peltier, W. R., Pie, N., Rietbroek, R., Rott, H., Sandberg-Sørensen, L., Sasgen, I., Save, H., Scheuchl, B., Schrama, E., Schröder, L., Seo, K. W., Simonsen, S., Slater, T., Spada, G., Sutterley, T., Talpe, M., Tarasov, L., Berg, W. J. V. D., Wal, W. V. D., Wessem, M. V., Vishwakarma, B. D., Wiese, D.

and Wouters, B. (2018) Mass balance of the Antarctic Ice Sheet from 1992 to 2017. *Nature*, **558** (7709), 219–222.

Shepherd, A., Wingham, D. J. and Mansley, J. A. D. (2002) Inland thinning of the Amundsen Sea sector, West Antarctica. *Geophysical Research Letters*, **29** (10), 2–1–2–4.

Shepherd, A., Wingham, D. J., Mansley, J. A. and Corr, H. F. (2001) Inland thinning of Pine Island Glacier, West Antarctica. *Science*, **291** (5505), 862–864.

Shepherd, A., Wingham, D., Payne, T. and Skvarca, P. (2003) Larsen Ice Shelf Has Progressively Thinned. *Science*, **302**(5646), 856–859.

Shepherd, A., Wingham, D. and Rignot, E. (2004) Warm ocean is eroding West Antarctic Ice Sheet. *Geophysical Research Letters*, **31** (23), 1–4.

Smith, J. A., Andersen, T. J., Shortt, M., Gaffney, A. M., Truffer, M., Stanton, T. P., Bindschadler, R., Dutrieux, P., Jenkins, A., Hillenbrand, C. D., Ehrmann, W., Corr, H. F., Farley, N., Crowhurst, S. and Vaughan, D. G. (2017) Sub-ice-shelf sediments record history of twentieth-century retreat of Pine Island Glacier. *Nature*, **541** (7635), 77–80.

Steig, E. J., Ding, Q., Battisti, D. S. and Jenkins, A. (2012) Tropical forcing of circumpolar deep water inflow and outlet glacier thinning in the amundsen sea embayment, west antarctica. *Annals of Glaciology*, **53** (60), 19–28.

Sutterley, T. C., Velicogna, I., Rignot, E., Mouginot, J., Flament, T., Broeke, M. R. V. D., Wessem, J. M. V. and Reijmer, C. H. (2014) Mass loss of the Amundsen Sea Embayment of West Antarctica from four independent techniques. *Geophysical Research Letters*, **41** (23). - mass loss due to increased glacier flow, 8421–8428.

Sverdrup, H. U. (1954) The Currents off the Coast of Queen Maud Land. *Norsk Geografisk Tidsskrift - Norwegian Journal of Geography*, **14**(1-4), 239–249.

Thoma, M., Jenkins, A., Holland, D. and Jacobs, S. (2008) Modelling Circumpolar Deep Water intrusions on the Amundsen Sea continental shelf, Antarctica. *Geophysical Research Letters*, **35** (18), 2–7.

Thomas, R. H. (1979) The dynamics of marine ice sheets. *Journal of Glaciology*, **24** (90), 167–177.

Thomas, R. H. and Bentley, C. R. (1978) A model for Holocene retreat of the West Antarctic Ice Sheet. *Quaternary Research*, **10** (2), 150–170.

Tsai, V. C., Stewart, A. L. and Thompson, A. F. (2015) Marine ice-sheet profiles and stability under Coulomb basal conditions. *Journal of Glaciology*, **61** (226), 205–215.

Urruty, B., Hill, E. A., Reese, R., Garbe, J., Gagliardini, O., Durand, G., Gillet-Chaulet, F., Gudmundsson, G. H., Winkelmann, R., Chekki, M., Chandler, D. and Langebroek, P. M. (2022) The stability of present-day Antarctic grounding lines – Part A: No

indication of marine ice sheet instability in the current geometry. *The Cryosphere Discussions*, **2022**, 1–34.

Vieli, A. and Payne, A. J. (2005) Assessing the ability of numerical ice sheet models to simulate grounding line migration. *Journal of Geophysical Research: Earth Surface*, **110** (1), F01003.

Wåhlin, A. K., Kalén, O., Arneborg, L., Björk, G., Carvajal, G. K., Ha, H. K., Kim, T. W., Lee, S. H., Lee, J. H. and Stranne, C. (2013) Variability of Warm Deep Water Inflow in a Submarine Trough on the Amundsen Sea Shelf. *Journal of Physical Oceanography*, **43**(10), 2054–2070.

Wåhlin, A. K., Yuan, X., Björk, G. and Nohr, C. (2010) Inflow of warm Circumpolar Deep Water in the central Amundsen shelf. *Journal of Physical Oceanography*, **40** (6), 1427–1434.

Walker, D. P., Brandon, M. A., Jenkins, A., Allen, J. T., Dowdeswell, J. A. and Evans, J. (2007) Oceanic heat transport onto the Amundsen Sea shelf through a submarine glacial trough. *Geophysical Research Letters*, **34** (2), L02602.

Walker, D. P., Jenkins, A., Assmann, K. M., Shoosmith, D. R. and Brandon, M. A. (2013) Oceanographic observations at the shelf break of the Amundsen Sea, Antarctica. *Journal of Geophysical Research: Oceans*, **118**(6), 2906–2918.

Webber, B. G., Heywood, K. J., Stevens, D. P., Dutrieux, P., Abrahamsen, E. P., Jenkins, A., Jacobs, S. S., Ha, H. K., Lee, S. H. and Kim, T. W. (2017) Mechanisms driving variability in the ocean forcing of Pine Island Glacier. *Nature Communications*, **8**.

Weertman, J. (1974) Stability of the junction of an ice sheet and an ice shelf. *Journal of Glaciology*, **13** (67), 3–11.

Weertman, J. (1957) On the Sliding of Glaciers. *Journal of Glaciology*, **3**(21), 33–38.

Wessem, J. M. V., Berg, W. J. V. D., Noël, B. P., Meijgaard, E. V., Amory, C., Birnbaum, G., Jakobs, C. L., Krüger, K., Lenaerts, J. T., Lhermitte, S., Ligtenberg, S. R., Medley, B., Reijmer, C. H., Tricht, K. V., Trusel, L. D., Ulft, L. H. V., Wouters, B., Wuite, J. and Broeke, M. R. V. D. (2018) Modelling the climate and surface mass balance of polar ice sheets using RACMO2 - Part 2: Antarctica (1979-2016). *Cryosphere*, **12** (4), 1479–1498.

Wingham, D. J., Wallis, D. W. and Shepherd, A. (2009) Spatial and temporal evolution of Pine Island Glacier thinning, 1995-2006. *Geophysical Research Letters*, **36** (17), L17501.

Yu, H., Rignot, E., Seroussi, H. and Morlighem, M. (2018) Retreat of Thwaites Glacier, West Antarctica, over the next 100 years using various ice flow models, ice shelf melt scenarios and basal friction laws. *The Cryosphere*, **12** (12), 3861–3876.